



HAL
open science

Development of methods and tools for the design and optimisation of Brushless Doubly-Fed Induction Machines for variable speed application in Hydro-generation

Nicolas Moisson Franckhauser

► **To cite this version:**

Nicolas Moisson Franckhauser. Development of methods and tools for the design and optimisation of Brushless Doubly-Fed Induction Machines for variable speed application in Hydro-generation. Electric power. Université Grenoble Alpes, 2018. English. NNT: 2018GREAT031 . tel-01883608

HAL Id: tel-01883608

<https://theses.hal.science/tel-01883608>

Submitted on 28 Sep 2018

HAL is a multi-disciplinary open access archive for the deposit and dissemination of scientific research documents, whether they are published or not. The documents may come from teaching and research institutions in France or abroad, or from public or private research centers.

L'archive ouverte pluridisciplinaire **HAL**, est destinée au dépôt et à la diffusion de documents scientifiques de niveau recherche, publiés ou non, émanant des établissements d'enseignement et de recherche français ou étrangers, des laboratoires publics ou privés.

THÈSE

Pour obtenir le grade de

DOCTEUR DE LA COMMUNAUTE UNIVERSITE GRENOBLE ALPES

Spécialité : **Génie Electrique**

Arrêté ministériel : 25 mai 2016

Présentée par

Nicolas MOISSON-FRANCKHAUSER

Thèse dirigée par **Frédéric WURTZ**, Directeur de Recherche,
G2Elab, et

codirigée par **Lauric GARBUIO**, Maître de Conférences, **G2Elab**

préparée au sein du **Laboratoire G2Elab**
dans **l'École Doctorale Electronique, Electrotechnique,
Automatique et Traitement du Signal (EEATS)**

Development of Methods and Tools for the Design and Optimization of Brushless Doubly-Fed Induction Machines for Variable Speed Applications in Hydro-Generation

Thèse soutenue publiquement le **13 avril 2018**,
devant le jury composé de :

Georges, BARAKAT

Directeur du GREAH au Havre, Rapporteur, Président

Thomas, LUGAND

Senior Engineer, GE Switzerland, Birr, Examineur

Xavier, ROBOAM

Directeur de Recherches au LAPLACE à Toulouse, Examineur

Abdelmounaim, TOUNZI

Professeur au L2EP à Lille, Rapporteur

Frédéric, WURTZ

Directeur de Recherche au G2Elab à Grenoble, Directeur de Thèse

Lauric, GARBUIO

Enseignant Chercheur au G2Elab à Grenoble, Co-Directeur de Thèse



**DEVELOPMENT OF METHODS AND TOOLS FOR THE DESIGN AND
OPTIMIZATION OF BRUSHLESS DOUBLY-FED INDUCTION MACHINES
FOR VARIABLE SPEED APPLICATIONS IN HYDRO-GENERATION**

A Dissertation Presented

by

Nicolas MOISSON-FRANCKHAUSER

Prepared with: the Electrical Laboratory of Grenoble, G2Elab, France
The Ph.D. school EEATS: Electronique, Electrotechnique, Automatique et Signal.
and the Technology department, General Electric Renewable Energy, Birr Switzerland.
in partial fulfillment of the requirements for the degree of

DOCTOR OF THE UNIVERSITY OF GRENOBLE

April 2018

© Copyright by Nicolas MOISSON-FRANCKHAUSER 2018

All Rights Reserved

ACKNOWLEDGMENTS

Dear reader,

Depending on your name, I am aware that this part of my work may be the only one that you will read. If you are my mom or my grandparents, you might even require the help of your children or grandchildren to enjoy these few lines. However, be advised that this is far from being the only interesting part of this thesis. Several compelling ideas can be found after the table of contents in those couple hundred pages. Even in the appendices...

During these three years of work, I went through many stages. I was sometimes thrilled by positive results and frustrated on other occasions by aberrant ones. I had both optimistic and pessimistic periods. I experienced moments when I was happy to develop, and moments I was bored to keep writing (especially when I had to put a lot of what I had done in the appendix section). I learned a lot, about physics, about electrical machines, and about myself. What dominates now is that: I am happy to be here, proud of the accomplished work, glad to share, and eager to move forward.

I would like to thank all the people that helped me going through this work. They are many; and if you are reading this part, dear reader, you might probably be one of them. I hope you will find yourself.

If you are Xavier ROBOAM, thank you for accepting to be the president of the Jury. If you are Georges BARAKAT or Abdelmounaim TOUNZI, thank you for consenting to the examiner roles. If you are Frédéric WURTZ, thank you for being my thesis director. If you are Lauric GARBUIO, thank you for being vice-director. I am grateful for all the tips both of you gave me, the wisdom you shared with me, your help, and the time you took for the meetings. If you are Grace, I appreciate that you were always giving a bit of extra time to Lauric and I during these meetings.

If you are Alexander SCHWERY or Thomas LUGAND, thank you for allowing me to do this work in GE. To Thomas LUGAND, some special thanks for all the help and support you gave me in GE, and for the awesome boss you are. I appreciated and still appreciate to work with you.

If you are part of GE Switzerland Birr and know me, thank you for all the good things during these three years. Among all, thanks for the barbecues, for the football matches during the world cup, for the karting sessions, for the climbing sessions or for the good buggers shared together.

If you are Laurie-ann SELIGER, thank you for Figure III-1.

If you are a Swiss friend: Silvia, Géraldine, Ronnie, Robin, Markus, Christian, Adrian or Vali, thank you to be there to help me escape from my work from times to times. I appreciated doing sport with you since this is where I met most of you.

If you are Franck and Gaëlla, Thomas and Chelsea, Valentin and Laura, or Charles and Saulainne, oh sorry Solenne, you are the friends I met during my years as an ENSE3 student. I had so many good times with you too. We are not living nearby anymore, but I hope we will continue seeing each other regularly. I cannot wait Solenne for you to be pregnant, so that we can play the socks game all together!

If your name is Liming, Arnaud, Quentin, Bertrand, Jonathan and Savana, Vincent, Lyes, Guilherme, Lucas, Mateus, Thiago or Tiago, Tamiris, Juliana, Kathleen and Théo, Andressa, Lou, Zakariya, Camille, Simon, Thomas, Marie, Mylène, Pranshu or Amit, you are my friends from the laboratory. I was lucky to meet you all, coming from around the world. I cannot have a specific word here for each of you, I am not doing a thesis on the friendships developed in the G2Elab. I hope to stay in touch with you all.

If you did not find yourself in the previous lists, but consider yourself to be my friend, I also consider you to be my friend. I am sorry I forgot you, you are probably not the only one, and I hope you will forgive me.

If you are part of my close family, my mother, my father, one of my brothers, my sister, or even my brother in law or sister in law. Thank you for all those years. I have had a happy life so far, and this is mostly because of you. I am happy that you are all doing well. I am happy to become an uncle soon (some family people should not read this too early). I hope this happy life will go on. If you are the youngest of my brothers, some special thanks for all the science discussions that we have had and still have and for your help.

If you are part of my big family: grandparents, great grandparents (I still have some), cousins, uncles and aunts or even further, thank you for being who you are. I am surprised and glad you read thus far.

If you are Sophie and love me, a massive thank you, my love, for being there with me. For all the help you gave me during this PhD. For your patience, for your smile, for your love, and all the happy moments we lived together. I hope this will continue, and maybe one day, we will, well, you know ... together.

Finally, if you do not belong in the lists above, it is surprising that you read all the acknowledgment section. Thank you dear¹ for opening and reading this thesis. Now that you went thus far, I would strongly advise you to read CHAPTER I if you like electronics and electrical machines, CHAPTER II if you prefer optimizations, or CHAPTER III if you are curious about how to adapt simulation and optimization methods to the BDFM. It will surely be much more delicate to understand than acknowledgments, but I did my best to make it accessible.

Yours Faithfully,

Nicolas

¹ : A bright new concept : “The PhD where you are the reader!” You can dear reader, dedicate this thesis to yourself by writing you name in the appropriate area.

ACKNOWLEDGMENTS	III
LIST OF FIGURES	IX
LIST OF TABLES	XV
NOMENCLATURE	XIX
ACRONYMS	XXIII
ABSTRACTS	1
GENERAL INTRODUCTION	3
CHAPTER I. BENEFITS OF VARIABLE SPEED WITH PUMPED-STORAGE POWER PLANT, AND STATE OF THE ART OF VARIABLE SPEED GENERATORS.....	5
I.1. Introduction.....	7
I.2. Regulation of the electric grid while renewable energy production increases implies a growing need for storage capacity.....	7
I.3. Pumped-storage power plants: currently the only storage solution at the scale level needed for the grid.....	9
I.3.1. Hydraulic advantages of variable speed in pumped-storage power plants.....	11
I.3.2. Improved regulation of the power in pump mode: a big plus for grid balancing	11
I.3.3. Higher hydraulic efficiency in turbine mode	12
I.3.4. Faster stabilization after a perturbation	12
I.4. Variable speed implies variable frequency: state of the art of power inverters	12
I.4.1. Different designs of power converters.....	14
I.4.2. Highest power outputs achieved by VSC or CSC and their prices	17
I.4.3. Future of the converter technology	18
I.5. Different technologies of variable speed machines.....	18
I.5.1. Fully-Fed, full speed range that implies fully rated power converters	19
I.5.2. Doubly-Fed Induction Machine: DFIM, a variable speed machine with a small power converter but with brushes	20
I.5.3. New kind of Doubly-Fed Machines: BDFM and BDFRM, the advantage of doubly-fed machines without the brushes.....	20
I.6. Conclusion	37
CHAPTER II. SIMULATIONS METHODS, DESIGN AND OPTIMIZATION OF ROTATING MACHINES FOR HIGH POWER GENERATION: STATE OF THE ART, EXAMPLE, AND LIMITS TOWARD A SIMILAR APPLICATION FOR THE BDFM.....	41
II.1. Introduction.....	43

II.2.	Simulations methods, design, and optimization of rotating machines for high power generation	43
II.2.1.	Multiphysics problems imply Multiphysics models.....	43
II.2.2.	Optimization methods: with analytical and semi-analytical models or with Finite-Element Methods (FEM)	44
II.2.3.	Optimization example of an IM using first an analytical iterative method, followed by a semi-analytical 1 st order optimization.....	52
II.3.	Limits to apply the previous methods to the new kind of doubly-fed machines.....	64
II.3.1.	Empirical knowledge for a first sizing.....	64
II.3.2.	Semi-analytical models to be paired with a 1 st order optimizations do not exist yet...	65
II.3.3.	Finite-element methods: for experimental research plan. FE simulations are much more time consuming for a BDFM than for usual rotating machines because of the different frequencies of the stator windings	68
II.4.	Conclusion	70
CHAPTER III. METHODS AND TOOLS DEVELOPED FOR THE DESIGN AND THE OPTIMIZATION OF THE BRUSHLESS DOUBLY-FED INDUCTION MACHINE		73
III.1.	Introduction.....	75
III.2.	Verification of analytical results and better understanding of the BDFM thanks to harmonic analysis with FE magneto-transient simulations.....	76
III.2.1.	Geometry of the BDFM used for the FE magneto-transient harmonic analyses	76
III.2.2.	Results of the BDFM FE magneto-transient harmonic analyses	78
III.3.	New equivalent circuit model developed for the BDFM.....	85
III.3.1.	Reasons to develop a new equivalent circuit model of the BDFM	85
III.3.2.	From the equivalent circuit of the IM to the equivalent circuit of the BDFM	86
III.3.3.	Determination of the equivalent circuit parameters with electrical tests inspired by a common method used for induction machines	97
III.3.4.	Implementation in a 1 st order analytical optimization software (CADES) of the method to determine the equivalent parameters.....	98
III.3.5.	Taking saturation and iron losses into account in the equivalent scheme	99
III.3.6.	Results comparison between the new model, previous models, and FE methods	100
III.4.	Development of a fast model: FE based coupled-circuit method, using the expressions of the mutual inductances as functions of the rotor position.....	104
III.4.1.	An FE based method inspired by the analytical coupled-circuit method	104

III.4.2.	Advantages and disadvantages of the FE based coupled-circuit method over the analytical coupled-circuit method.....	105
III.4.3.	Validation of the FE based coupled-circuit method and applications in this work.....	106
III.5.	A model that considers saturation based on FE magneto-harmonic simulations	107
III.5.1.	Principles of FE magneto-harmonic simulations in Flux2D	107
III.5.2.	Computation of the equivalent permeability.....	108
III.5.3.	Idea to use FE magneto-harmonic simulations with two different frequencies.....	111
III.5.4.	Magneto-harmonic simulations for the BDFM technology, a method to compute the mutual interactions	111
III.5.5.	Saturation consideration in the new magneto-harmonic method with two sources at different frequencies.....	113
III.5.6.	Summary of the iterative process of the magneto-harmonic method for the BDFM with saturation	115
III.5.7.	Comparison of the magneto-harmonic method developed for the BDFM with magneto-transient simulations.....	115
III.6.	Perspectives towards a complete semi-analytical model of the BDFM to implement optimizations with a 1 st order algorithm.....	117
III.7.	Conclusion	118
CHAPTER IV.	EXAMPLE OF A BDFM SIZING FOR A GIVEN SET OF CHARACTERISTICS USING THE KNOWLEDGE AND METHODS OF THE PREVIOUS CHAPTERS AND FOUND IN THE LITERATURE.	121
IV.1.	Introduction.....	123
IV.2.	The Typical Tidal Project (TTP) specifications.....	123
IV.3.	An analytical method for a first design of the BDFM	124
IV.3.1.	Step 1: Choice of the number of poles.....	124
IV.3.2.	Step 2: Choice of the bore diameter	135
IV.3.3.	Step 3: Choice of the number of stator and rotor slots	138
IV.3.4.	Step 4: Magnetic loading and number of turns in series for each stator winding.....	141
IV.3.5.	Step 5: The stator currents, and the size and proportion of the slots	145
IV.3.6.	Step 6: Determination of the airgap radial length	149
IV.3.7.	Step 7: Determination of the rotor and stator yoke heights followed by the external diameter of the machine.....	150
IV.3.8.	Step 8: Determination of the stacking factor, and the number and width of ventilation ducts.....	151

IV.3.9. Summary of the first analytical sizing of the BDFM on the specifications of the Typical Tidal Project (TTP)	152
IV.4. FE simulation of the analytical design, and improvement of the design through an iterative process	154
IV.4.1. FE load simulation of the analytical design with a magneto-transient application	154
IV.4.2. Iterative process to improve the BDFM design with an FE magneto-harmonic model.....	154
IV.5. Conclusion	156
GENERAL CONCLUSION	157
APPENDICES.....	161
APPENDIX A. Stator of Radial Machines with Three-Phase Distributed Winding Design	163
APPENDIX B. Synchronous Machines.....	171
APPENDIX C. Induction Machines	175
APPENDIX D. Speed Control with Induction Machines: Wound Rotors, Rheostat, and Doubly-Fed Induction Machines	181
APPENDIX E. Principles and Determination of a Reluctance Network	185
APPENDIX F. Semi-Analytical Model of an Asynchronous Machine Used for Sizing with a First Order Optimization Method in Cades	189
APPENDIX G. Example of Improvements Using FEM and a Method Comparable to Design of Experiment for an Induction Machine Design.....	217
APPENDIX H. From imaginary to real machines using the Semi-Analytical model presented in APPENDIX F and a 1 st order optimization.....	221
APPENDIX I. Harmonic analyses of a BDFM.....	235
APPENDIX J. Determination of the Parameters of the Equivalent Circuit of an Induction Machine Using No-Load and Blocked Rotor Tests.	243
APPENDIX K. Determination of the equivalent circuit parameters of the BDFM from electrical tests.....	247
APPENDIX L. Computation of the power state of the BDFM through the electrical state of the equivalent scheme.	255
APPENDIX M. An iterative process for the improvement of the BDFM design with FE magneto-harmonic simulations	261
Bibliography.....	263

LIST OF FIGURES

Figure I-1: Wind Power production in 2009 in Denmark [5]	8
Figure I-2: Comparison of different technologies of energy storage on: the rated power, the energy capacity, the cycle efficiency and the discharge time.....	9
Figure I-3: Comparison between variable speed with four DFIM (power variation: 70% - 100% for speed variation of $\pm 15\%$) and fixed speed with four synchronous machines for a PSP with four 100 MW pumps (inspired from [5])	11
Figure I-4: Comparison of the hydraulic efficiency of a Francis-type turbine for fixed and variable speed operation [14].....	12
Figure I-5: Scheme of a Current Source Converter with the rectifier stage, the DC energy storage <i>LDC</i> , the inverter stage, and the capacity filters <i>CF, inp</i> and <i>CF, out</i> [15]	15
Figure I-6: Scheme of a Voltage Source Converter with the rectifier stage, the DC energy storage <i>CDC</i> , and the inverter stage: currently the state of the art to drive motors and generators. <i>LB</i> are the inductances of the grid; the VSC often does not need additional filters to meet grid compliance [15]	16
Figure I-7: Scheme of an Indirect Matrix Converter (left) and a Direct Matrix Converter (Right) [15].	17
Figure I-8 : Topologies of fixed speed machines and different technologies of variable speed machines. The DFIM has one stator fed at the grid frequency and a rotor fed at variable frequency through a partial scale Power Converter. BDFM and BDFRM have two stator windings: the Power Winding (PW) fed at the grid frequency, and the Command Winding (CW) fed at variable frequency through a partial scale Power Converter.	19
Figure I-9: Different designs of reluctance rotors, (from [41]).....	23
Figure I-10: Scheme of a BDFM rotor with <i>pg + pc</i> nested-loops; left: isolated from each other's, right: with a common ring	33
Figure I-11: Per phase equivalent circuit of a Brushless Doubly-Fed Induction Machine expressed on the side of the PW as generally found in the bibliography [50].....	36
Figure II-1: Reasonable expectations from the three big categories of models in terms of speed and intricacy [53].....	44
Figure II-2 Pareto curve for two objectives	47
Figure II-3: Local and global optimums with the results that 1 st order deterministic algorithms would probably get depending on the starting point	48
Figure II-4: Reluctance network for one stator tooth and its respective slot [41]	51
Figure II-5: Comparison of the sum of the magnetizing reactance and the stator leakage reactance $X_m + X_s$ between the semi-analytical model and FE2D simulations. The IM used for this comparison was obtained in APPENDIX G after a DOE with FE simulations. It is designed to operate at a nominal stator voltage of 6600 V	59
Figure II-6: Parametrized optimization: maximum efficiency reached after each optimization as a function of the imposed teeth flux density for the specifications of the TTP.....	62
Figure II-7: Pareto curve: maximum efficiency reached after optimizations as a function of the maximum length of the machine for the specifications of the TTP and for a maximum flux density in the teeth of 1.7 T	63

Figure II-8: Per phase equivalent circuit of the BDFM with a mutual inductance representation from [26] 66

Figure II-9: Rotor representation of the BDFRM with a reluctance network, from [41]..... 67

Figure III-1: Nested loops rotor of a BDFM with 10 nests and 6 loops per nest. The rotor on the left is the usual nested-loops design. The rotor on the right was designed to diminish the centrifugal forces on the end windings, especially for the outermost loops. These 3D representations and the centrifugal stress computation were performed by the mechanical R&D team of GE renewable hydro. 78

Figure III-2: Per phase equivalent scheme of the Induction Machine with rotor terminals accessible 87

Figure III-3: Mutual inductance. Notice that the right and left representations are equivalent and yield the same equations. 88

Figure III-4: Equivalence between the transformer representation and the mutual inductance representation..... 89

Figure III-5: Per phase equivalent circuit of the Induction Machine with a transformer representation and rotor terminals accessible 90

Figure III-6: Per phase equivalent circuit of the Command Winding Induction Machine with a transformer representation and rotor terminals accessible. The pulsations have been inverted because $-\omega r2 = \omega r1$ 93

Figure III-7: Per phase equivalent circuit of a BDFM using a transformer representation 93

Figure III-8: Per phase equivalent circuit of a BDFM using a transformer representation and with a pulsation $\omega 1$ 96

Figure III-9: Equivalent circuit of the BDFM in the PW reference frame. Watch out, as explained with equation (70) and (76), the power that goes into the equivalent circuit is not the power that goes into the BDFM. The power that goes into the BDFM is calculated with $ReV2eq''I2eq''$ * as demonstrated in APPENDIX L, p 255. 97

Figure III-10: Adaption of Figure III-8 with the addition of the resistances of the iron losses, in parallel to the magnetizing inductances 100

Figure III-11: Amplitude of the PW current, for load tests, depending on the phase of the PW feeding voltage at $t = 0$ 101

Figure III-12: Amplitude of the CW current, for load tests, depending on the phase of the PW feeding voltage at $t = 0$ 101

Figure III-13: Amplitude of the PW current, for load tests, depending on the phase of the CW feeding voltage at $t = 0$ 102

Figure III-14: Amplitude of the CW current, for load tests, depending on the phase of the CW feeding voltage at $t = 0$ 102

Figure III-15: Amplitude of the PW current, for load tests, depending on the position of the rotor at $t = 0$ 103

Figure III-16: Amplitude of the CW current, for load tests, depending on the position of the rotor at $t = 0$ 103

Figure III-17: Phase of the CW current, for load tests, depending on the position of the rotor at $t = 0$ 104

Figure III-18: Saturation B(H) curve of a material and equivalent permeability of each mesh element for the first iteration during the solving of a magneto-harmonic simulation.....	108
Figure III-19: Absolute flux density in one mesh element of a rotating machine during an electrical period	109
Figure III-20: The coenergy (area in blue): the magnetic energy covered per cycle, per volume, for the mesh element being considered if the material was not linear, from the maximal absolute flux density computed	109
Figure III-21: The coenergy of the linear material (area in yellow): The magnetic energy covered per cycle, per volume, for the mesh element being considered if the material was not linear, from the maximal absolute flux density computed	110
Figure III-22: Absolute flux density in one mesh element of a BDFM during an electrical period, PW at 100 Hz, CW at 25 Hz.....	113
Figure III-23: Comparison of the sum of the PW and CW reactive powers for the magneto-harmonic method with saturation, the magneto-harmonic method without saturation, and the magneto-transient application.	116
Figure III-24: Comparison of the sum of the PW and CW active powers for the magneto-harmonic method with saturation, the magneto-harmonic method without saturation, and the magneto-transient application.	117
Figure IV-1: Active Power of the Power Winding (PW: discs), Control Winding (CW: squares), and BDFM (PW+CW: black curve) depending on the total number of pole pairs ($p_p + p_c$) and the mechanical speed of the rotor.	129
Figure IV-2: Comparison of the potential cross-coupling factors of all the possible combinations of p_g and p_c for a total sum $p_g + p_c = 76$	131
Figure IV-3: Mechanical speed of the rotor and forbidden speeds as a function of the mechanical speed for the combination with $p_g = 32$, $p_c = 48$. From equations (101) and (94).	135
Figure IV-4: Evolution of the power factor of the BDFM designs during the iterative process starting from the analytical design at iteration 0	155
Figure A-1: Section view of the stator of an 8 poles 48 slots three-phase machine.....	163
Figure A-2: Slot with 2 winding layers (2 bars), 4 conductors per slot (so 2 conductors per bar) and 32 strands per slot (which gives 8 strands per conductor)	164
Figure A-3: Three different configurations of windings layout. The top one has one parallel path and the two others two parallels paths.	166
Figure A-4: Winding of a 2-pole 12-slot 3-phase machine with a single layer per slot. $q=2$ and the coil span is full pitch (6 slots)	167
Figure A-5: Winding of a 2-pole 12-slot 3-phase machine with two layers per slot (double-layer winding). The coil span is reduced by one slot pitch ($coil\ span = 5\ slots$ instead of $oil\ span = 6\ slots$).	168
Figure A-6: Winding of a 2-pole 12-slot 3-phase machine with double-layer winding. The coil span is reduced by two slots pitch ($coil\ span = 4\ slots$ instead of $oil\ span = 6\ slots$).	168
Figure A-7: Fractional slot winding of a 2-pole 9-slot 3-phase machine with a double-layer winding.....	168
Figure B-1: Section view of a salient pole synchronous machine	171

Figure B-2: Section view of a turbomachine: a synchronous machine with a wound rotor	172
Figure B-3: Different kind of radial flux rotors with permanent magnets [94]	173
Figure C-1: Section view of a squirrel cage asynchronous machine	175
Figure C-2: Squirrel cage of an induction machine. The conductor bars are inclined or skewed	176
Figure C-3: Per phase equivalent circuit of an asynchronous machine with rotor losses resistance and rotor conversion resistance separated	176
Figure C-4: Torque of an asynchronous machine in function of the slip [95]	177
Figure C-5: Impact of rotor resistance on the torque of an asynchronous machine	178
Figure C-6: Rotor shape and slot shape of a squirrel cage machine with a double cage to increase the torque starting current [97]	179
Figure D-1: Per phase equivalent circuit of an asynchronous machine with a slip power recovery system referred to as sub-synchronous cascade or a DFIM (sub-synchronous cascade, voltage in phase with currents, DFIM: voltage can have a phase shift with currents). The rotor losses resistance and rotor conversion resistance are separated.	182
Figure D-2: Scheme of an induction machine with a wound rotor and slip power recovery SPR [98]	183
Figure E-1: A tube of flux and the equivalent flux tube associated with it	185
Figure E-2: Reluctance network in the airgap able to consider the rotor rotation of one stator tooth pitch from [41].....	187
Figure E-3: Definition of the MMF of each rotor tooth from the fundamental harmonic of the MMF created by the stator [101]	188
Figure E-4: Definition of the MMF of each rotor tooth with a discrete method and most of the spatial harmonics considered	188
Figure G-1: View on Flux2D of one pole of the initial design obtained by an optimization with the semi-analytical model of APPENDIX F. The flux density is visualized for sectors with high saturation: between 1.6 and 2.01 Tesla.....	218
Figure G-2: View on Flux2D of one pole of the final design obtained after 17 iterations of FE simulations with the variation of a few parameters. The flux density is visualized for sectors with high saturation: between 1.6 and 2.01 Tesla.	218
Figure H-1: Parametrized optimization: maximum efficiency reached after optimizations as a function of the imposed teeth flux density for the specifications of the TTP	223
Figure H-2: Evolution of two discrete parameters (p and q) of the imaginary machines of the parametrized optimization from Figure H-1	223
Figure H-3: Evolution of two discrete parameters (p and q) for the imaginary machines and real machines of the parametrized optimization from Figure H-5	224
Figure H-4: Evolution of the feeding voltage for the imaginary machines and real machines of the parametrized optimization from Figure H-5	224
Figure H-5: Parametrized optimization: maximum efficiency reached after optimizations as a function of the imposed teeth flux density for the specifications of the TTP (identical to Figure II-6)	225
Figure H-6: Evolution of the power factor of the IM depending on the iteration of the optimization. The red line is the upper limit constraint and the blue line is the lower limit constraint.	232

Figure H-7: Evolution of the slip of the IM depending on the iteration of the optimization. The red line is the upper limit constraint and the blue line is the lower limit constraint.....	232
Figure H-8: Evolution of the efficiency of the IM depending on the iteration of the optimization. The red line is the upper limit constraint and the blue line is the lower limit constraint.	233
Figure J-1: Equivalent circuit of an Induction Machine with a squirrel cage rotor	243
Figure J-2: Simplified equivalent scheme of an Induction Machine during a no-load test ($s = 0$). ...	244
Figure J-3 Simplified equivalent scheme of an IM during a blocked-rotor test ($s = 1$).	245
Figure K-1: Per phase equivalent scheme of a BDFM operating in cross-coupling mode. All the parameters, the voltages, and the currents are expressed on the power winding side. Identical to Figure III-9, p 97.....	247
Figure K-2 : Equivalent circuit of the BDFM at no load conditions.	249
Figure K-3: Equivalent circuit of the BDFM for a blocked rotor test with the control winding short-circuited and with the cross-coupling condition of the BDFM met.	250
Figure K-4: Equivalent circuit of the BDFM with blocked rotor a control winding short-circuited. Equivalent impedance 1.....	251
Figure K-5: Equivalent circuit of the BDFM with blocked rotor a control winding short-circuited. Equivalent impedance 2.....	251
Figure K-6: Equivalent circuit of the BDFM with blocked rotor a control winding short-circuited. Equivalent impedance 3.....	251
Figure L-1: Per phase equivalent scheme of a BDFM operating at the cross-coupling speed. All the parameters are expressed on the power winding side. This equivalent scheme and the expression of the parameters on the power winding side was already presented in Figure I.....	255
Figure L-2: Equivalent scheme of the BDFM expressed in the power winding reference frame.	256

LIST OF TABLES

Table I-1: Typical emission of greenhouse gases for the electricity production depending on the source of energy. (Value from EDF, a French utility company) [3].	8
Table I-2: Different cases of interactions between the fundamental harmonics and the sidebands harmonics of the BDFRM with the related conditions on the number of rotor saliencies and the mechanical speed.	27
Table II-1: Electric and Magnetic analogy [63] and [64].	50
Table II-2: Major specifications of each electrical machines (12 identical) to be installed in the Typical Tidal Project (TTP)	53
Table II-3: Inputs and outputs of the sizing analytical model implemented in MATLAB, equations can be found in [71]	55
Table III-1: Characteristics of the BDFM used for CHAPTER III FE and analytical studies	77
Table III-2: Harmonic analysis of the flux density in the airgap due to the PW (more harmonics in Table I-1, p 235)	79
Table III-3: Harmonic analysis of the flux density in the airgap due to the CW (more harmonics in Table I-2, p 235)	79
Table III-4: Harmonic analysis of the flux density in the airgap due to the PW and nested-loop interactions (more harmonics in Table I-3, p 235)	80
Table III-5: Harmonic analysis of the flux density in the airgap due to the CW and nested-loop interactions (more harmonics in Table I-4, p 236)	80
Table III-6: Harmonic analysis of the flux density in the airgap due to the PW with the CW in cascaded mode through the nested-loops (more harmonics in Table I-5, p 236)	80
Table III-7: Harmonic analysis of the flux density in the airgap due to the CW with the PW in cascaded mode through the nested-loops (more harmonics in Table I-6, p 237)	80
Table III-8: Harmonic analysis of the flux density in the airgap during a load case without saturation of the BDFM (more harmonics in Table I-7, p 237)	81
Table III-9: Harmonic analysis of the flux density in the airgap due to the PW. Rotor position at $t = 0$ is rotated by $+13^\circ$ (more harmonics in Table I-8, p 238)	81
Table III-10: Harmonic analysis of the flux density in the airgap due to the CW. Rotor position at $t = 0$ is rotated by $+13^\circ$	81
Table III-11: Harmonic analysis of the flux density in the airgap due to the PW and nested-loops interaction. Rotor position at $t = 0$ is rotated by $+13^\circ$ (more harmonics in Table I-9, p 238)	82
Table III-12: Harmonic analysis of the flux density in the airgap due to the CW and nested-loops interaction. Rotor position at $t = 0$ is rotated by $+13^\circ$ (more harmonics in Table I-10, p 238)	83
Table III-13: Harmonic analysis of the flux density in the airgap due to the PW with the CW in cascaded mode through the nested-loops. Rotor position at $t = 0$ is rotated by $+13^\circ$ (more harmonics in, Table I-11 p 239)	83
Table III-14: Harmonic analysis of the flux density in the airgap due to the CW with the PW in cascaded mode through the nested-loops. Rotor position at $t = 0$ is rotated by $+13^\circ$ (more harmonics in, Table I-12, p 239)	83

Table III-15: Harmonic analysis of the flux density in the airgap during a load case without saturation of the BDFM. Rotor position at $t = 0$ is rotated by $+13^\circ$ (more harmonics in Table I-13, p 240).....	84
Table III-16: Harmonic analysis of the flux density in the airgap during a BDFM load case without saturation (more harmonics in Table I-14, p 241).....	85
Table III-17: Harmonic analysis of the flux density in the airgap during a BDFM load case without saturation (more harmonics in Table I-15, p 241).....	85
Table III-18: Results of the equivalent circuit parameter extraction of the BDFM presented in Table III-1. The results are presented in Ohms, at the frequency of 50 Hz for the equivalent scheme in Figure III-8 without saturation.....	99
Table III-19: Validation of the FE based coupled-circuit method. Comparison, for a linear load case of the phase-neutral voltages, currents amplitudes, and phase of the currents for the phase A of the PW and CW	106
Table III-20: Comparison, for a linear load case of a BDFM, between the FE magneto-harmonic method, the FE based coupled-circuit method, and the FE magneto-transient method. Voltage and currents amplitudes per phase, and phase of the currents for the phase A of the PW and CW.	112
Table III-21: Different voltage scenarios used for the comparison between the magneto-harmonic method and the magneto-transient method.....	116
Table IV-1: Major specifications of each electrical machine (among 12) to be installed in the TTP ..	124
Table IV-2: Different possible configurations of pole pairs with the greatest common divisor between the pole pairs of the two stator windings. All these configurations meet the criteria of a judicious sum of pole pairs $pg + pc > 75$, and a good potential cross-coupling factor.	132
Table IV-3: Maximum, minimum and rated feeding frequency of the control winding corresponding to the different speed of the BDFM	133
Table IV-4: Comparison of the forbidden speeds due to the natural speed and the synchronism speed of the power winding for two different pole configurations	134
Table IV-5: Some possibilities of the choice of parallel paths, conductors in series and voltages for the control winding of the BDFM based on a first sizing on the specification of a Typical Tidal Project (TTP).	145
Table IV-6: Characteristics of the analytical design of the BDFM on the specifications of the TTP....	153
Table IV-7: Results of a load test of the analytical BDFM design with FE magneto-transient simulations. Verifications of the phase-neutral voltage amplitudes, current amplitudes, and phase of the currents for the phase A of the PW and CW. Verification of the active power per phase, reactive power per phase and power factor.	154
Table G-1: Comparison of the initial and final IM design after 17 iterations of FE simulations with the variation of a few parameters.....	217
Table G-2: Parameters of the final design fed with 6600 V supply at 9.6 Hz and a rotor slip of 3% for the results of Table G-1. This design will be used for the comparison between FEM and the semi-analytical model (see II.2.3.6, p 58).....	219
Table H-1: Inputs parameters of an optimization with the semi-analytical model of APPENDIX F. In gray, the parameters that were fixed, in red, the parameters that reached the constraint upper limit, and in blue the parameters that reached the constraint lower limit.	226

Table H-2: Outputs parameters of an optimization of the semi-analytical model of APPENDIX F. In red. the parameters that reached the constraint upper limit. and in blue the parameters that reached the constraint lower limit.	227
Table I-1: Harmonic analysis of the flux density in the airgap due to the PW, an extension of Table III-2, p 79.....	235
Table I-2: Harmonic analysis of the flux density in the airgap due to the CW, an extension of Table III-3, p 79.....	235
Table I-3: Harmonic analysis of the flux density in the airgap due to the PW and nested-loops interactions, an extension of Table III-4, p 80.....	235
Table I-4: Harmonic analysis of the flux density in the airgap due to the CW and nested-loops interactions, an extension of Table III-5, p 80.....	236
Table I-5: Harmonic analysis of the flux density in the airgap due to the PW with the CW in cascaded mode through the nested-loops, an extension of Table III-6, p 80.....	236
Table I-6: Harmonic analysis of the flux density in the airgap due to the CW with the PW in cascaded mode through the nested-loops, an extension of Table III-7, p 80.....	237
Table I-7: Harmonic analysis of the flux density in the airgap during a load case without saturation of the BDFM, an extension of Table III-8, p 81.	237
Table I-8: Harmonic analysis of the flux density in the airgap due to the PW, an extension of Table III-9, p 81.....	238
Table I-9: Harmonic analysis of the flux density in the airgap due to the PW and nested-loops interactions. Rotor position at $t = 0$ is rotated by $+13^\circ$. Extension of Table III-11, p 82.....	238
Table I-10: Harmonic analysis of the flux density in the airgap due to the CW and nested-loops interactions. Rotor position at $t = 0$ is rotated by $+13^\circ$. Extension of Table III-12, p 83.....	238
Table I-11: Harmonic analysis of the flux density in the airgap due to the PW with the CW in cascaded mode through the nested-loops. Rotor position at $t = 0$ is rotated by $+13^\circ$. Extension of Table III-13, p 83.....	239
Table I-12: Harmonic analysis of the flux density in the airgap due to the CW with the PW in cascaded mode through the nested-loops. Rotor position at $t = 0$ is rotated by $+13^\circ$. Extension of Table III-14, p 83.....	239
Table I-13: Harmonic analysis of the flux density in the airgap during a load case without saturation of the BDFM. Rotor position at $t = 0$ is rotated by $+13^\circ$. Extension of Table III-15, p 84.....	240
Table I-14: Harmonic analysis of the flux density in the airgap during a load case without saturation of the BDFM. Extension of Table III-16, p 85.....	241
Table I-15: Harmonic analysis of the flux density in the airgap during a load case without saturation of the BDFM. Extension of Table III-17, p 85.....	241
Table M-1: Evolution of the optimized parameters and results of the no saturation load test of the BDFM during the iterative process to improve upon the analytical design (iteration 0).	261

NOMENCLATURE

List of Indices

X_{ag}	Airgap
$X_{c/2}$	Control (= Command) winding for the BDFM
X_{cl}	Classical
X_{enc}	Enclosed
X_{ex}	Excess
$X_{g/1}$	Grid (= Power) winding for the BDFM
X_{hyst}	Hysteresis
X_{max}	Maximal
X_{min}	Minimal
X_r	Rotor
X_s	Stator
X_{tot}	Total
X^{-1}	Inverse
X^T	Transpose
X^*	Conjugate of a complex
\vec{X}	Vector
\hat{X}	Amplitude for a harmonic
$X_{x,y}$	Element matrix X at x^{th} row and y^{th} column

List of Greek Symbols

Γ	Torque
η	Efficiency
Θ	Magnetomotive Force (Magnetic Potential)
θ_{ag}	Position in the airgap in the reference frame of the stator
θ_{agR}	Position in the airgap in the reference frame of the rotor
Θ_j	The rotor moment of inertia
θ_{rm}	Mechanical position of the rotor in the reference frame of the stator
δ_{ag}	Radial airgap length
Λ_{ag}	Permeance of the airgap
μ_0	Vacuum Permeability
μ_R	Relative Magnetic Permeability
σ	Electric Conductivity of the material
σ_v	Harmonic wave direction
ϕ	Flux through a given section
ω_c	Electrical pulsation of the control winding
ω_g	Electrical pulsation of the grid winding
ω_n	Natural speed of the rotor for the BDFM
ω_r	Electrical pulsation of the rotor
ω_{rm}	Mechanical pulsation of the rotor
ω_s	Electrical pulsation of the stator

List of Latin Symbols

A	Surface area
\vec{B}	Flux density
B_r	Remanent Induction

C	Esson factor
D	Diameter
D_{ag}	Diameter of the averaged airgap
$D_{b,s}$	Bore diameter (internal diameter of the bore)
\vec{E}	Electric Field
E	Electro-Motive Force Amplitude
e	Instantaneous Electro-Motive Force
f	Frequency
G	Inverse of the radial airgap length
\vec{H}	Magnetic Field
H_{CB}	Coercive Magnetic Field of the induction
H_{CJ}	Coercive Magnetic Field of the polarization
h_{slot}	Height of a slot
h_{spacer}	Height of the spacer in the slot
h_{wedge}	Height of the wedge in the slot
\Im	Imaginary part of a complex
I	Current amplitude
i	Instantaneous current
\vec{J}	Current density
\vec{j}	Magnetic polarization
J_r	Remanent polarization
K_e	Excess coefficient in Bertotti's model
K_{cs}	Filling coefficient of the stator slot
K_{cr}	Filling coefficient of the rotor slot
K_h	Hysteresis coefficient in Bertotti's model
k_d	Distribution factor
k_p	Pitch factor or coil span factor
k_{pc}	Cross-coupling factor of the BDFM between the grid and the control
k_s	Skew factor
$k_{stacking}$	Stacking factor
k_w	Winding factor
k_{Θ}	The inertia factor
L	Inductance
L_{core}	Length of the active material
L_f	Inductance of the fundamental
L_m	Magnetic length of a given circuit or Magnetizing inductance
L_{σ}	Leakage inductance comprising the inductance of the harmonics
M	Magnetomotive Force
\vec{M}	Magnetizing vector
M_v	Bulk density of the sheet
m	Magnetic moment or Number of phases of a machine
m_{rot}	Mass of the rotor
m_{stat}	Mass of the stator
N_{cond}	Number of conductors per slot
N_{ducts}	Number of ventilation ducts
$N_{loops/nest}$	Number of loops per nest for the BDFM
N_{pp}	Number of parallel paths
N_r	Number of rotor nests for the BDFM
N_s	Number of turns in series in the stator

$N_{s,c}$	Number of turns in series in the control winding of the BDFM
$N_{s,g}$	Number of turns in series in the grid winding of the BDFM
$N_{slot,r}$	Rotor slot number
$N_{slot,s}$	Stator slot number
n_{rm}	Rotational speed of the rotor
n_s	Synchronism speed of the rotor
P	Active Power
P	Number of poles
P	Permeance
P_{cl}	Power of classical losses for iron
P_e	Total Power transmitted from the stator to the rotor
P_{ex}	Power of excess losses for iron
P_{hyst}	Power of hysteresis losses for iron
P_{JR}	Rotor Joule losses
P_{JS}	Stator Joule losses
p	Number of pole pairs
Q	Reactive Power
q	Number of slots per pole and phase
\Re	Real part of a complex
R	Resistance or Reluctance
S	Section area
S_r	Number of saliencies of the rotor for the BDFRM
s	Slip
s_{coil}	Coil span
s_{red}	Reduction of the coil span
s_{turn}	Turn span
T	Period
V	Voltage potential
V_{mag}	Magnetic Potential
V_ϕ	Feeding voltage per phase
W	Energy (expressed in Wh or kWh)
w_{duct}	Width of a ventilation duct
w_{slot}	Width of a slot
w_{stack}	Width of a stack of iron
X	Reactance
Z	Impedance

Mathematical symbol

\angle	Angle of a complex value
----------	--------------------------

ACRONYMS

List of Acronyms

BDFM	Brushless Doubly-Fed Induction Machine
BDFRM	Brushless Doubly-Fed Reluctance Machine
BGCT	Bi-mode Gate Commutated Thyristor
BIGT	Bi-Mode Insulated Gate Transistor
CMC	Conventional Matrix Converter
CSC	Current Source Converter
CSI	Current Source Inverter
CSR	Current Source Rectifier
CW	Command Winding or Control Winding (for a BDFM or BDFRM)
DC	Direct Current
DFIM	Doubly-Fed Induction Machine
DOE	Design of Experiments
DSIM	Double Stator Induction Machine
FE	Finite-Element
FEA	Finite-Element Analysis
FEM	Finite-Element Method
FFT	Fast Fourier Transform
GCD	Greatest Common Divisor
GDP	Growth Domestic Product
HVDC	High Voltages Direct Current
IGBT	Insulated-Gate Bipolar Transistor
IGCT	Integrated Gate-Commutated Thyristor
IM	Induction Machine
IMC	Indirect Matrix Converter
LCC	Line Commutated Converter
MMC	Modular Multilevel Converter
MMF	Magnetomotive Force
MOSFET	Metal-Oxide-Semiconductor Field-Effect Transistor
PSP	Pumped-Storage Plants
pu	Per Unit
PW	Power Winding or Grid Winding (for a BDFM or BDFRM)
PWM	Pulse Width Modulation
RMS	Root Mean Squared
rpm	Revolutions per minute
SM	Synchronous Machine

SPR	Slip Power Recovery
SPSM	Salient Pole Synchronous Machine
SQP	Sequential Quadratic Programming
THD	Total Harmonic Distortion
TTP	Typical Tidal Project
VSC	Voltage Source Converter
VSI	Voltage Source Inverter
VSR	Voltage Source Rectifier

ABSTRACTS

English version:

Pumped-hydro storage plants (PSP) are important assets to stabilize electric grids.

Variable speed technologies can improve the cycle efficiency and the power adjustability of PSPs. Current technologies such as fully-fed machines or Doubly-Fed Induction Machines (DFIM) have drawbacks. In this work, the focus will be on an unconventional design of variable speed machine: the Brushless Doubly-Fed Induction Machine (BDFM). The objectives are to better understand the working principles of this machine to size it, optimize it, and compare it to other types of variable speed machines.

Following a review of sizing and optimization techniques for conventional machines, similar approaches are investigated for the BDFM. Two different methods for faster Finite-Element (FE) simulations of the BDFM are presented: a fast one without saturation considerations and another one based on the principle of magneto-harmonic simulations. A careful harmonic analysis combined with a comparison of cross-coupling tests between FE simulations and results of equivalent circuit found in the literature will lead to a modification of the BDFM equivalent circuit. A new method to determine the parameters of this equivalent circuit from electrical tests is presented. The parameters determination from the geometry will also be considered for the elaboration of a derivable semi-analytical model. Such a model, paired with a 1st order optimization algorithm could be extremely powerful during the sizing of a BDFM. The potential of such an approach is shown in this work with the example of the optimization of an Induction Machine.

Version Française :

Les Stations de Transfert d'Énergie par Pompage (STEP) sont des structures importantes pour stabiliser le réseau électrique.

Les technologies à vitesse variable peuvent améliorer l'efficacité et la souplesse d'utilisation des STEPs. Les technologies actuelles telles que les machines alimentées à fréquence variable, ou les Machines Asynchrone à Double Alimentations (MADA) présentent des inconvénients. Dans ce travail, nous nous concentrons sur une structure non conventionnelle de machine à vitesse variable : la Machine à Induction à Double Alimentation sans Balais (BDFM). Les objectifs sont de mieux comprendre le fonctionnement de cette machine pour la dimensionner, l'optimiser et finalement la comparer aux structures existantes.

Après un examen des techniques de dimensionnement et d'optimisation des machines classiques, des approches similaires sont étudiées pour les BDFM. Deux méthodes différentes pour des simulations éléments finis plus rapides de la BDFM sont présentées : une première, la plus rapide mais qui ne considère pas le phénomène de saturation et une seconde basée sur le principe des simulations magnéto-harmoniques. Une analyse harmonique minutieuse combinée à une comparaison de cas en charges (couplage-croisés) entre des simulations FE et les résultats obtenus avec des schémas équivalents obtenus dans la littérature conduit à une modification du circuit équivalent de la BDFM. Une nouvelle méthode pour déterminer les paramètres de ce circuit grâce à des essais électriques est ensuite présentée. La détermination des paramètres à partir de la géométrie est également abordée pour aboutir à un modèle semi-analytique dérivable. Un tel modèle, couplé à un algorithme d'optimisation du 1er ordre pourrait être extrêmement puissant lors du dimensionnement d'une BDFM. Le potentiel d'une telle approche est montré dans ce travail grâce à l'optimisation d'une machine à induction.

GENERAL INTRODUCTION

The worldwide electrical energy consumption steadily increases due to different factors such as economic and population growth among others. This growing need has to be satisfied in combination with a decrease in the emissions of greenhouse gases to mitigate future climate change. This challenge can be met with the development of renewable energy production in future electrical grids. An important technical challenge will be to maintain the stability of these networks.

Energy storage will have a bigger and bigger role to play in the stability of future Grids. In CHAPTER I, Pumped-hydro Storage Plants (PSPs) will be compared to other energy storage systems. Due to their advantages over other energy storage solutions, PSPs already play a considerable stabilization role in developed countries. There is still some place for new installations in emerging countries and for retrofitting the aging fixed speed installations with variable speed technologies. The advantages of variable speed machines over fixed speed machines will be presented in CHAPTER I. A review of the state of the art of variable speed machines will follow. In the end, two new doubly-fed technologies will be introduced: the Brushless Doubly-Fed Reluctance Machine (BDFRM) and the Brushless Doubly-Fed Induction Machine (BDFM). These technologies have advantages and disadvantages over the current technologies of Doubly-Fed Induction Machines (DFIM) or the technologies of fully-fed machines. The advantages of the BDFM and the BDFRM still need further investigations before planning to introduce them in future PSP projects. At the end of CHAPTER I, it will be decided to study further the BDFM because the BDFM rotor seems easier to manufacture and appears to have better mechanical characteristics than the BDFRM rotor.

0 will present the methods to simulate, design and optimize rotating machines. The example of the Induction Machine (IM) will be taken to illustrate these methods. A fully-fed IM will be optimized for the specifications of a Typical Tidal Project (TTP). Thanks to this example, three groups of methods will be identified: the analytical methods, the semi-analytical methods, and the numerical methods. The advantages and disadvantages, and the use of these methods will be discussed. The limits to apply the illustrated methods to the BDFM will be shown at the end of CHAPTER II. In particular, the fact that FE simulations take much longer for a BDFM than for other rotating machines, and the need to create new analytical methods for the BDFM.

CHAPTER III will be dedicated to the development and improvement of existing methods for faster simulations and optimizations of the BDFM. First, a new equivalent scheme that better works with cross-coupling tests than the equivalent schemes available in literature will be introduced. Then two FE methods, much faster than the FE magneto-transient method to simulate steady-state load tests for the BDFM, will be presented. The first method: the coupled-circuit FE based method will be the fastest but will not consider saturation. The second FE method will be an adaptation of the magneto-harmonic application for the BDFM. It will consider saturation, will be much faster than FE magneto-transient applications, but slower than the coupled-circuit based on FE method.

Finally, in CHAPTER IV, a BDFM will be designed and optimized for the same specifications as the IM of CHAPTER II. This design will show the limits of the current analytical design method for the BDFM and the power of the new FE model methods developed in CHAPTER III.

CHAPTER I. BENEFITS OF VARIABLE SPEED WITH PUMPED-STORAGE POWER PLANT, AND STATE OF THE ART OF VARIABLE SPEED GENERATORS

I.1.	Introduction.....	7
I.2.	Regulation of the electric grid while renewable energy production increases implies a growing need for storage capacity.....	7
I.3.	Pumped-storage power plants: currently the only storage solution at the scale level needed for the grid.....	9
I.3.1.	Hydraulic advantages of variable speed in pumped-storage power plants.....	11
I.3.2.	Improved regulation of the power in pump mode: a big plus for grid balancing.....	11
I.3.3.	Higher hydraulic efficiency in turbine mode.....	12
I.3.4.	Faster stabilization after a perturbation.....	12
I.4.	Variable speed implies variable frequency: state of the art of power inverters.....	12
I.4.1.	Different designs of power converters.....	14
I.4.1.1.	Current Source Converter.....	14
I.4.1.2.	Voltage Source Converter.....	15
I.4.1.3.	Indirect Matrix Converter (IMC) and Conventional/Direct Matrix Converter (CMC)	16
I.4.2.	Highest power outputs achieved by VSC or CSC and their prices.....	17
I.4.3.	Future of the converter technology.....	18
I.4.3.1.	Modular Multilevel Converters.....	18
I.4.3.2.	Semiconductors with SiC and GaN.....	18
I.5.	Different technologies of variable speed machines.....	18
I.5.1.	Fully-Fed, full speed range that implies fully rated power converters.....	19
I.5.2.	Doubly-Fed Induction Machine: DFIM, a variable speed machine with a small power converter but with brushes.....	20
I.5.3.	New kind of Doubly-Fed Machines: BDFM and BDFRM, the advantage of doubly-fed machines without the brushes.....	20
I.5.3.1.	Origin and history of the BDFM and BDFRM.....	20
I.5.3.2.	Advantages and disadvantages in comparison to the DFIM.....	20
I.5.3.3.	Differences between BDFM and BDFRM, advantages - disadvantages.....	21
I.5.3.4.	The Brushless Doubly-Fed Reluctance Machine: BDFRM.....	22

1.5.3.4.1.	Topology	22
1.5.3.4.2.	Different kind of reluctance rotors	22
1.5.3.4.3.	Analytical expression of the airgap flux densities from the two stator windings	23
1.5.3.4.4.	Harmonic coupling in a BDFRM for torque creation.....	25
1.5.3.4.5.	Torque of the BDFRM.....	28
1.5.3.5.	The Brushless Doubly-Fed Induction Machine: BDFM	28
1.5.3.5.1.	Analytical expression of the airgap flux densities of the two stator windings ...	29
1.5.3.5.2.	Special Nested-Loop rotor.....	32
1.5.3.5.3.	Comparison between nested-loop rotors and other rotor designs for BDFM....	33
1.5.3.5.4.	Natural speed, slip, and power	34
1.5.3.5.5.	The equivalent circuit of the BDFM.....	35
1.5.3.5.6.	Torque expression derived from the equivalent circuit.....	36
1.5.3.5.7.	Relationship between grid winding and control winding power, and sizing of the power converter	36
1.5.3.5.8.	The biggest BDFM to date	37
1.6.	Conclusion	37

I.1. Introduction

In this chapter, the focus will be on energy storage technology. First, the benefits of storage technologies considering the growing renewable energy production will be reminded. A comparison between the different existing storage technologies will be made. This will help us understand why Pumped Storage Power Plants (PSPs) are currently making most of the storage capacity for electric grids worldwide.

We will then focus on the technology of PSPs, and discuss the advantages of variable speed generators over fixed speed ones. The working principles of variable speed generators will be explained, from the power electronics to different existing technologies; fully-fed and doubly-fed. The advantages and disadvantages of these different designs will be discussed.

In the last part of this chapter, two new designs of doubly-fed variable speed machines will be highlighted. Their mode of operation will be explained and the expected advantages and drawbacks of these new designs in comparison to the currently used Doubly-Fed Induction Machine (DFIM). One of these designs, the Brushless Doubly-Fed Induction Machine (BDFRM) will be selected to be further studied in the following chapters of this thesis.

I.2. Regulation of the electric grid while renewable energy production increases implies a growing need for storage capacity

The renewable energy sector is growing. It has been growing at an exponential rate for more than a decade now, and it can be expected to continue growing fast. In December 2015, delegations from 195 countries gathered in Paris at COP21 to discuss future efforts to mitigate global warming. According to [1], as of the beginning of 2017, 196 countries representing 99.75% of the emissions of greenhouse gases signed the agreement. On June 1, 2017, Donald Trump declared that the United States was not part of the agreement anymore. At that time, the United States represented 17.89% of the emissions of greenhouse gases.

With this agreement and with previous ones, many countries took on ambitious challenges to reduce the emissions of greenhouse gases. In Europe for example, the goal is to reduce greenhouse gases emissions by 40% by 2030 in comparison to 1990 and by 80 to 95% by 2050 [2]. China will try to reduce its CO₂ emissions by 60 to 65% per GDP points before 2030 in comparison to 2005.

Since the world population is still increasing, and since most of the population in developing countries will consume more energy per capita in the future, most of the reduction of greenhouse gases will have to be made through a shift in the energy sector: from fossil fuel to renewable energy. As it can be seen in Table I-1, according to EDF, a French electric utility company, a total shift in electricity production from non-renewable to renewable would not completely reduce the greenhouse gases emissions to zero. But the different renewable energy sources produce around 99% fewer greenhouse gases than current fossil fuel energy sources. The only fossil fuel that does not produce a lot of greenhouse gases in comparison to renewable is nuclear. But nuclear has other drawbacks.

Table I-1: Typical emission of greenhouse gases for the electricity production depending on the source of energy. (Value from EDF, a French utility company) [3].

Source of Electricity	Greenhouse gas emissions (equivalent g of CO ₂ /kWh)
Nuclear	4
Hydraulic on the river	6
Hydraulic – dams	6
Wind turbines	14
PV	18 – 180
Gas Combined Cycle	499
Diesel	870
Coal 600 MW with desulphurization	1029

In Europe-28, in 2014, renewable energy sources accounted for 16 % of the gross inland energy consumption. Still, in EU-28, 27.5% of the gross electricity consumption was generated from renewable energy [4]. These figures will have to keep going up fast to achieve the goals set for 2030 and 2050.

One of the major issues with some renewable energy like wind and solar is the unpredictability and the fluctuation of power generation. This can be seen in Figure I-1 with the production of wind power in Denmark over one year.

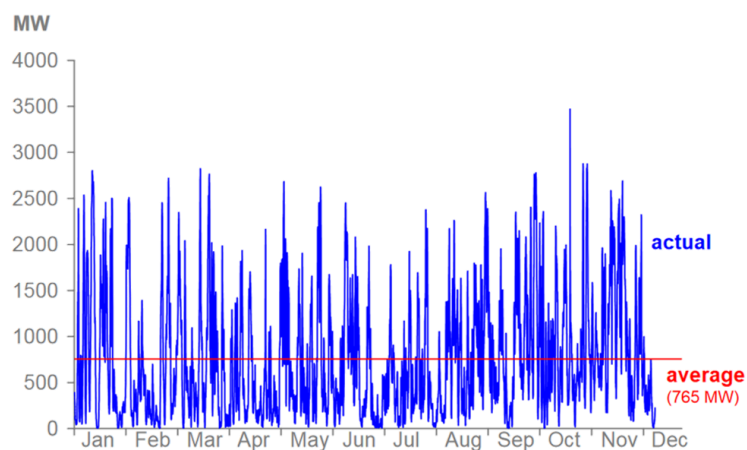


Figure I-1: Wind Power production in 2009 in Denmark [5]

To maintain a good quality of current, the grid needs to be balanced: the supply must match the demand at any time on the network. The electricity generated needs to be immediately consumed. Not matching the demand can affect the voltage and the frequency of the network. With a surplus of energy, the frequency of the grid will increase. A deficiency of energy will slow down the frequency. With renewable energy as solar and wind, the other sources of energy will have to adapt their production depending on the demand but also the production of solar and wind. Moreover, both power consumption and renewable energy production are only roughly predictable. To do so, energy sources that can quickly change their power output are needed, like hydro, gas petrol and coal power plant. In this context, being able to store energy when there is too much available on the network is a plus. Energy storage enables further integration of renewable energies on the electrical grid and helps to reduce the emission of greenhouse gases for electrical production.

I.3. Pumped-storage power plants: currently the only storage solution at the scale level needed for the grid

There are many technologies used to store energy. Some of them transform electrical energy into mechanical or chemical and then back to electrical when needed. Others are purely electrical. Most of these technologies can fit under the following list:

- Capacitors: electrical or chemical.
- Super or supra conductor energy storage.
- Flywheel energy storage.
- Compressed air storage.
- Synthetic natural gas.
- Hydrogen storage.
- Different technologies of batteries.
- Hydro storage: Pumped Storage Power plant (PSP).

The most relevant factors to compare these technologies for grid applications are:

- The power output.
- The response time.
- The energy capacity per cycle.
- The efficiency per cycle.
- The price of the installation.
- The lifetime in years and cycles.

Figure I-2 compares the group of technologies listed above. The data for the different technologies come from [6] from 2011. The Li-ion battery data has been updated in the light of the new developments of Tesla batteries.

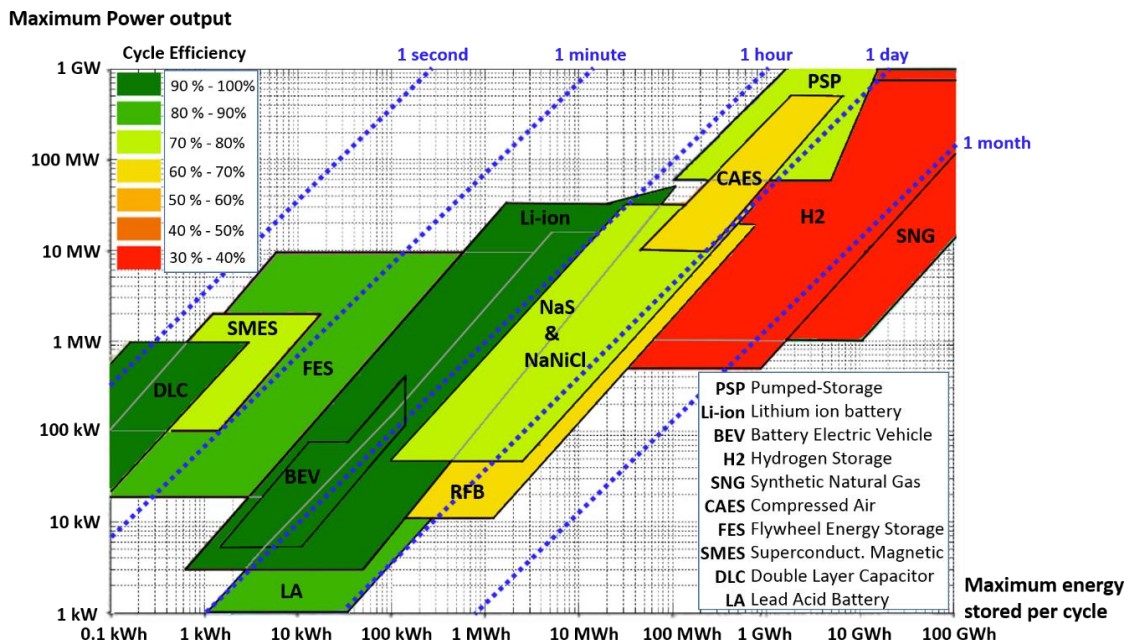


Figure I-2: Comparison of different technologies of energy storage on: the rated power, the energy capacity, the cycle efficiency and the discharge time

For a storage system to make sense at the level of the grid, the energy storage is expected to be in the range of GWh and the rated power in the range of GW with an efficiency of let's say at least 70%. As it can be seen in Figure I-2, the only technology that currently meets these expectations is pumped storage hydro. Hydrogen and Synthetic Natural Gas currently have cycle efficiencies below 50% and Lithium-ion batteries have not yet reached PSPs in terms of energy storage and rated power.

To this day, the biggest lithium-ion battery project in the world was won by Tesla. The project of 100 MW/129 MWh Powerpack system was completed on November 24, 2017; less than 100 days after the project was first talked about. It was built in South Australia. The cost of this project was not revealed, but some information leaked in big media with a price around \$50M according to CNBC [7], Reuters [8], Forbes [9], and other.

The previous biggest project was a 20 MW/80 MWh, also delivered by Tesla, commissioned on January 30, 2017; 88 days after the order with an estimated cost of \$38M [10]. It was built at the Southern California Edison Mira Loma substation.

In comparison, according to the U.S. Department of Energy [11], in 2016 PSP already had a worldwide capacity of 142 GW with an additional 34 GW under development. In terms of rated power, thousands of Lithium-Ion batteries 100 MW projects would be needed for Lithium-Ion to catch up on PSPs.

Still, for comparison purposes, a big PSP project like the one of Grand Maison in France, has a rated power of 1820 MW, an energy storage capacity of 30 GWh with a cycle efficiency of 78%.

Still according to [11] in 2016, 98% of the grid-storage capacity comes from PSPs.

It is interesting to compare the price of a lithium-ion project with the price of the variable speed technology and turbines of PSP plants without the infrastructure cost. In fact, there are many dams in the world, which were built in the past with two water reservoirs. These dams would be able to operate as PSPs if they were fitted with variable speed technology and reversible turbines (in many cases replace Peltier turbines by Francis or Kaplan turbines). The cost of variable speed generators and reversible turbines is only a fraction of the total infrastructure cost of a dam. The infrastructure cost of a new PSP may make it uncompetitive in the future in comparison to a lithium-ion storage project. However, in a lot of cases, the infrastructure is already built, especially in Europe. In these cases, the cost of upgrading the hydroelectric production to a PSP is a lot lower than building a new one. From experience, the cost of the power electronics, the turbine, and the copper generally makes about 30% of the cost of a PSP. The rest, over 70% is infrastructure cost: building the dam, digging tunnels, etc. Under these conditions, the PSP technology can be considered much more competitive.

Even if the price of new PSPs with their infrastructures may be high, it still has some advantages over lithium-ion storage projects. For example, powerful electrical machines provide system/grid services to the grid. In terms of stabilizing power per cost, rotating machines are currently still unbeatable.

I.3.1. Hydraulic advantages of variable speed in pumped-storage power plants

Several papers and at least one Ph.D. from GE employees (previously ALSTOM) have already explained the advantages of variable speed in PSPs, for example: [5], [12], [13] and [14]. In this section, the explanations given in the previous publications will be summarized. To get extended information, one can refer to the previous publications.

Today, most of the PSPs are still working at fixed speed since they are directly fed at the network frequency. The technology used is generally salient pole synchronous machines with a reversible Francis-type turbine. To accelerate switching between turbine mode and pump mode, some PSPs are equipped with a separate turbine and pump. The advantages of variable speed will be given in comparison to this technology.

I.3.2. Improved regulation of the power in pump mode: a big plus for grid balancing

In turbine mode, both active and reactive power can be controlled. The active power is controlled by the opening of the guide vanes. The reactive power with the rotor winding current (or field winding current). In pump mode, the active power only varies in a small range. With fixed speed, the active power is a function of the head (the height between the surfaces of the two water storages). The active power cannot be controlled by the operator of the PSP. Variable speed allows regulating this power taken from the grid.

With the regulation of the active power in pump mode, PSPs can play a role to balance the grid. It also allows storing more energy and it reduces the number of starts and stops. In Figure I-3, a comparison between variable speed is done for a PSP with 4 100 MW pumps. For the variable speed case, the range of power attainable by the pumps was set to vary from 70% to 100% of the nominal power.

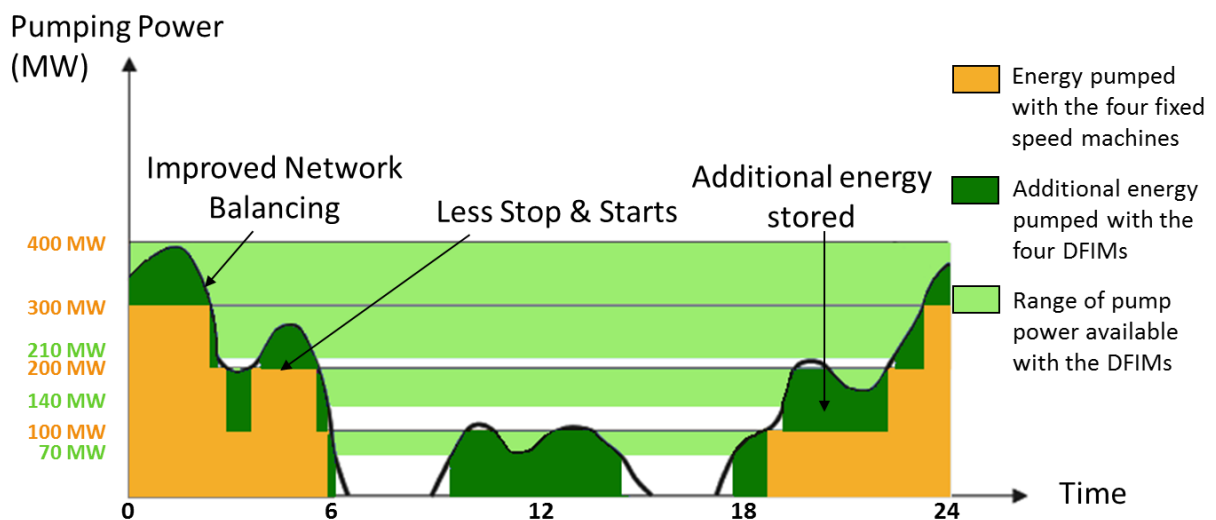


Figure I-3: Comparison between variable speed with four DFIM (power variation: 70% - 100% for speed variation of $\pm 15\%$) and fixed speed with four synchronous machines for a PSP with four 100 MW pumps (inspired from [5])

I.3.3. Higher hydraulic efficiency in turbine mode

In turbine mode, the hydraulic efficiency of the turbine depends on the head, the flow and the speed of the turbine. During operation at constant speed, the maximum efficiency for a given head and flow cannot be reached (the turbine is generally designed for a good efficiency in pump mode). Variable speed allows the turbines to operate at the best efficiency possible for any head/flow characteristic. Figure I-4 compares the hydraulic efficiency of a Francis-type turbine operating at fixed speed and operating under variable speed. As it can be seen, in this example, variable speed increases the hydraulic efficiency of the turbine by approximately 1.5% across the whole range of load.

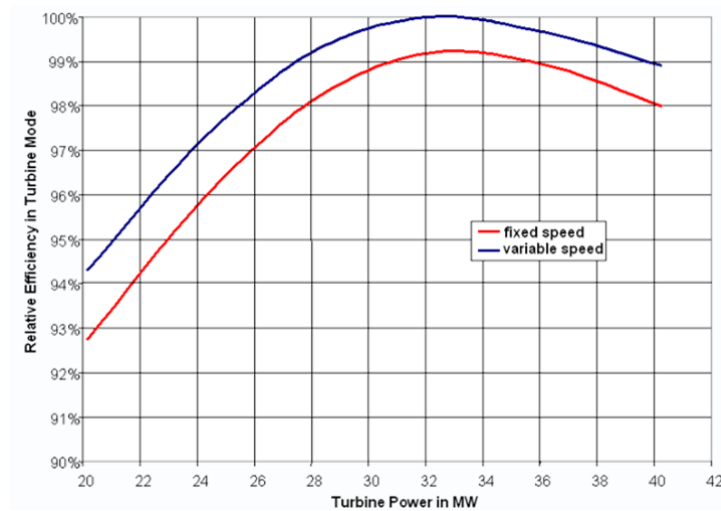


Figure I-4: Comparison of the hydraulic efficiency of a Francis-type turbine for fixed and variable speed operation [14]

I.3.4. Faster stabilization after a perturbation

This advantage may depend on the technology of variable speed used. In the case of Doubly-Fed Induction Machine (DFIM), the rotor currents can be controlled: phase shift and amplitudes. These degrees of freedom allow re-stabilizing the network faster after a perturbation [14].

I.4. Variable speed implies variable frequency: state of the art of power inverters

In general, an electrical machine with a given number of pole pairs fed by a fixed frequency will rotate at a fixed speed. This is a basic rule well known by all machinists even if some exceptions may exist depending on the considered technology. This rule is linked to the fact that an electrical machine works through the interaction of two magnetic fields. This interaction can result in an exchange of electrical/magnetic energy to mechanical energy or the inverse. For this exchange of energy not to be null, the two fields need to have the same number of poles. For the exchange of energy not to be null over a period, the two fields need to rotate at the same speed.

For large generators, the magnetic field of the stator will generally be created by a three-phase winding. The winding will impose the number of poles of the magnetic field. The rotational speed of this magnetic field is related to both the number of poles and the feeding frequency as seen in the following expression:

$$n_{stat_field} = \frac{\omega_s}{p} \times \frac{60}{2\pi} \quad (1)$$

n_{stat_field} is the rotating speed of the magnetic field created by the stator in revolution per minute.

ω_s is the feeding pulsation of the stator.

p is the number of pole pairs.

From equation (1), it is obvious that if the feeding frequency is fixed, then the rotating speed of the magnetic field for a given topology is fixed.

In synchronous machines, the magnetic field of the rotor does not rotate in the rotor reference frame. It is generally created by a winding fed by direct current, or by permanent magnets. The rotor will rotate at the speed of the stator magnetic field. The rotating speed of the stator field will be defined as the synchronous speed: $n_s = n_{stat_field}$.

In asynchronous machines, the magnetic field of the rotor will rotate in the rotor reference frame. In the case of induction machines, the rotor magnetic field is created by induced currents. For that reason, the rotor will not rotate at the synchronism speed.

The slip is defined as the difference between the synchronism speed and the rotor rotational speed:

$$s = \frac{n_s - n_m}{n_s} = \frac{\omega_s - p \omega_m}{\omega_s} \quad (2)$$

n_s synchronism speed equal to the rotating speed of the stator magnetic field.

n_m is the mechanical rotating speed of the rotor.

s is the slip.

As shown in APPENDIX C about induction machines, the rotor efficiency cannot be greater than $\eta_{rotor} = 1 - s$, see equation (166).

The faster the rotor magnetic field will rotate in the rotor reference frame, the less efficient the machine will be. Because of that and for powerful applications (>5 MW), the slip of the machine is not higher than a few percent under load operation. For that reason, the slip of asynchronous machines cannot be used in big generators to vary the rotor speed. As for synchronous machines, under load condition, the rotation speed of the rotor of asynchronous machines is fixed close to the synchronous speed which is fixed by the feeding frequency.

From the previous considerations, it can be understood that variable speed can be obtained through the variation of the feeding frequency. This can be done with a power inverter which must be sized for the full apparent power of the machine. Such solutions are referred to as fully-fed machines see I.5.1.

The fully-fed solution can be very expensive because of the converter price. Other solutions referred to as doubly-fed machines can be preferred. With doubly-fed machines, the converter only needs to be sized for a fraction of the machine apparent power. The converter can feed the rotor winding, to be able to change the slip of an induction machine without a loss in efficiency. This technology is referred to as a Doubly-Fed Induction Machine (or DFIM). Another idea, to avoid the brushes of a DFIM is to add another stator winding and feed it through the converter to impact the behavior of the machine, as in the Brushless Doubly-Fed Induction Machine (BDFM) or the Brushless Doubly-Fed Reluctant Machine (BDFRM). For visualization, the topologies of fully fed machines, DFIM, BDFM, and BDFRM are shown in Figure I-8, p 19. With such technologies, it is possible to reach speed around the synchronous speed plus or minus 10% with a power inverter rated at only 10% of the machine power output. See I.5.2.

I.4.1. Different designs of power converters

The technology of the power inverters has a great impact on the choice of variable speed solutions chosen for each project. For that reason, the following section of this chapter will discuss the current state of the art of power inverter.

I.4.1.1. Current Source Converter

A Current Source Converter (CSC) is designed with a large inductor (L_{DC} in Figure I-5) to keep the direct current (DC) constant. The power flow's direction is imposed by the polarity of the DC voltage that depends on the operation of the semiconductors.

The semiconductors used in a CSC are generally thyristors, they can be closed but cannot be opened by command. Thus, there is only one degree of freedom referred to as the firing angle. This degree of freedom allows choosing when the thyristors are set on and become conductors.

Thyristors have a natural commutation: they are set off when the current flowing through them becomes negative. For that reason, a CSC can also be called a Line Commutated Converter (LCC). A schematic of such a converter is given in Figure I-5.

Some main advantages of the CSC technology can be cited:

- For a given power output, it is cheaper than a Voltage Source Converter.
- The inductance of the DC line has a longer lifespan than the capacitors of a Voltage Sourced Converter presented in I.4.1.2.

Because of these advantages, most of the High Voltages Direct Current connection systems (HVDC) built in the past were based on these types of converters.

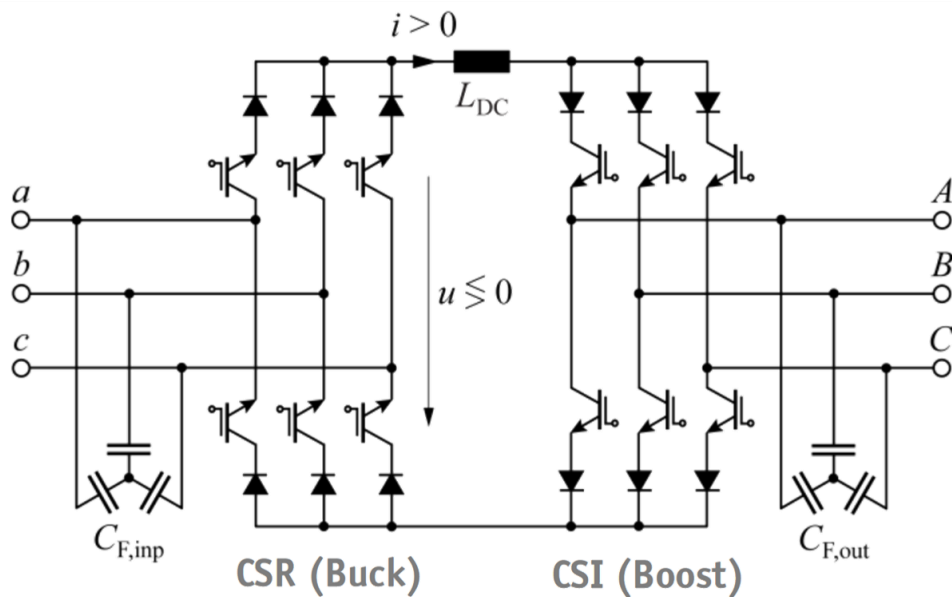


Figure I-5: Scheme of a Current Source Converter with the rectifier stage, the DC energy storage L_{DC} , the inverter stage, and the capacity filters $C_{F,inp}$ and $C_{F,out}$ [15]

I.4.1.2. Voltage Source Converter

A Voltage Source Converter (VSC) is designed with a large capacitance (C_{DC} in Figure I-6) to keep its voltage constant.

A VSC generally uses semiconductors that can be controlled to be opened or closed. Depending on the application these semiconductors can be, IGBT, IGCT, BIGT or BGCT. These types of semiconductors give a second degree of freedom. For that reason, a VSC can sometimes be referred to as a Self-Commutated Converter (SCC).

This additional controllability has several advantages:

- The semiconductors can be switched on and off several times per cycle. This allows operating the system with Pulse Width Modulation (PWM). The Total Harmonic Distortion (THD) of such system is greatly improved.
- This controllability also allows to manage the reactive power locally in both AC terminals of the converter.

Because of these advantages, a VSC does not need as much harmonics filters as a CSC.

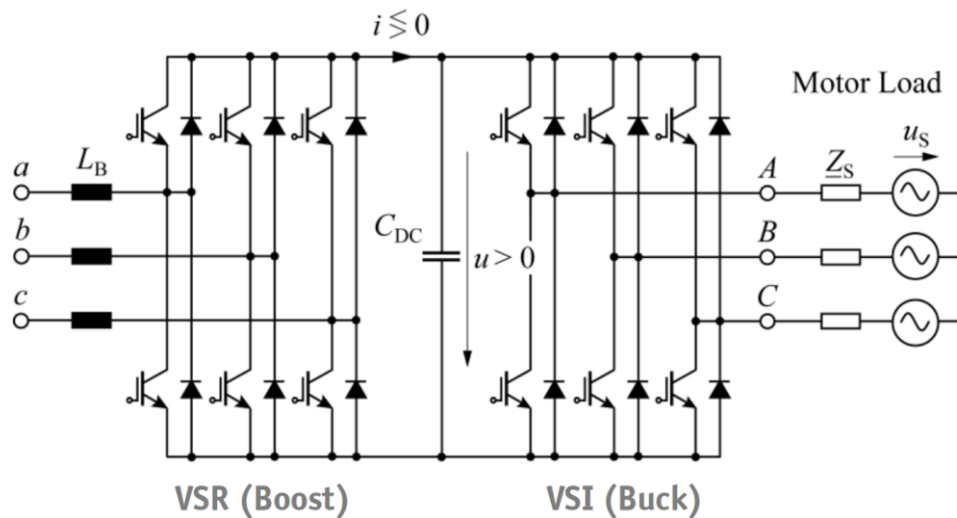


Figure I-6: Scheme of a Voltage Source Converter with the rectifier stage, the DC energy storage C_{DC} , and the inverter stage: currently the state of the art to drive motors and generators. L_B are the inductances of the grid; the VSC often does not need additional filters to meet grid compliance [15]

From a design point of view, it could be possible to build voltage source converters with thyristors and thus have a line commutated voltage source converter. It could also be possible to build a Current Source Converter with transistors to obtain a self-commutated current source converter. Very few applications are built with these kinds of configurations. Once again, this is the reason why current source converters are often designated as line commutated converters and voltage source converters are often mentioned as self-commutated converters.

A VSC for high power applications is often based on multi-level modules. This technology is referred to as Modular Multilevel Converter (MMC). Thanks to semiconductors in series, the converter can operate at higher voltages. Semiconductors available today are generally not rated higher than 6600V.

As explained in [16] and [17], the MMC has also improved output waveforms, reduced filter size, lowered electromagnetic interference, lowered THD in comparison to a conventional VSC. The disadvantage being that the number of power electronic elements augments with the number of levels.

I.4.1.3. Indirect Matrix Converter (IMC) and Conventional/Direct Matrix Converter (CMC)

Voltage Source and Current Source Inverters have an intermediate energy storage: a capacitor for the voltage source and an inductor for the current source. Indirect Matrix Converter and Conventional Matrix Converter do not have an intermediate energy storage. This gives them some advantages: they are more compact and more reliable. Currently, they are not broadly used in the industry because of the complexity of their control.

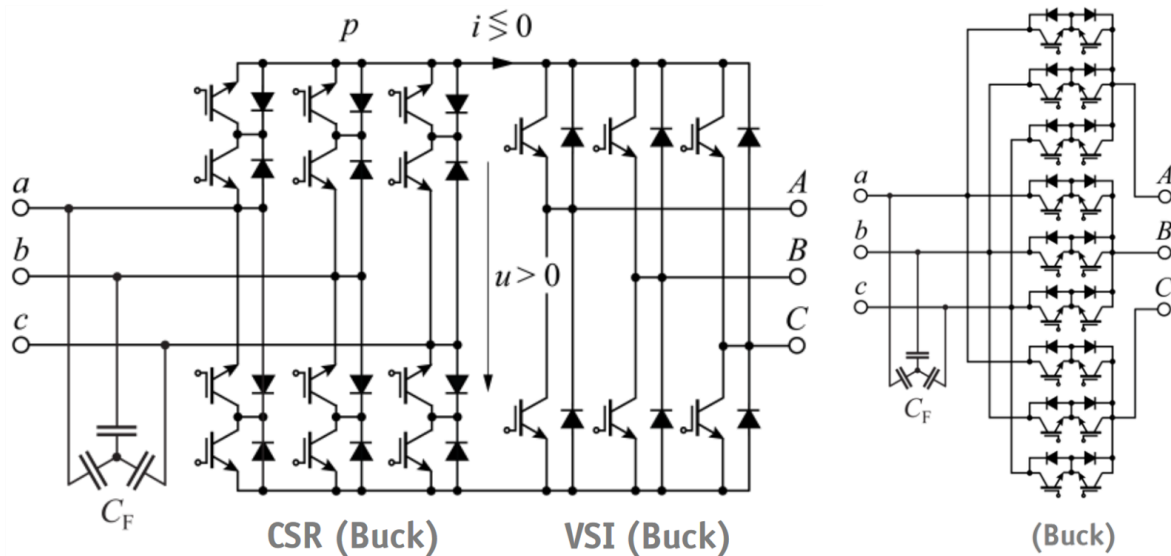


Figure I-7: Scheme of an Indirect Matrix Converter (left) and a Direct Matrix Converter (Right) [15]

I.4.2. Highest power outputs achieved by VSC or CSC and their prices

In [18], the authors mention the largest fully-fed synchronous machine currently in operation with a 100 MW VSC. The converter was commissioned in Grimseil by ABB. The authors are also reporting that the largest existing Load-Commutated Inverter (LCI) has a 100 MW capacity.

Higher power output VSCs have already been commissioned in HVDC connections for offshore wind power plants. In [19], the authors describe VSCs with ratings up to 900 MW at $\pm 320kV$.

The price of big power inverters is not publicly advertised in articles. From various sources, a rough estimate of VSC prices can be given to be around \$ 0.10 per W. Thus, the price of a 100 MW converter can be estimated in the range of \$10 million.

In [20], an economic study made in 2012 for large solar farms showed that it could be financially interesting to operate hundreds or thousands of small voltage inverters in parallel rather than a big one. The advantage is that the inverters in the 10kW range are produced in industrial quantities. The author arrived at a cost reduction in the range of 50 % over the lifetime of the 10 MW solar farm (25 years). For this result, the author considered the price of purchase, the installation, the efficiency and the reliability of smaller inverters.

I.4.3. Future of the converter technology

I.4.3.1. Modular Multilevel Converters

In [21] ABB proposes a new VSC type based on Modular Multilevel Converter (MMC) technology. It uses advanced IGCT (integrated Gate-Commutated Thyristor) with efficiency over 98.5% (all included) with a range of power between 50 MVA and 500 MVA.

I.4.3.2. Semiconductors with SiC and GaN

A lot of information can be found on the Internet about the different technologies of semiconductors. The state of the art for powerful applications with voltage source converters is to use IGBT (Insulated Gate Bipolar Transistors) with Silicon (Si).

In the future, Gallium Nitride (GaN) and Silicon Carbide (SiC) can be expected to replace Silicon. According to EPC (Efficient Power Conversion Corporation), GaN base semiconductors will be more prominent in domestic, computer applications and telecom. SiC will take over in industrial applications with the capability of higher voltages and currents.

In [22], one can learn that GaN has an electrical breakdown 10 times higher than Si. It also offers higher operating temperature and an exceptional carrier mobility.

Cree, a company cited in [22], plans to develop future MOSFETs at 3.3-kV and 6.5-kV levels. They also target to go as high as 10 kV. This is currently the market for IGBTs. SiC's low switching losses will provide significant performance advantages. According to the same company, SiC is five times better than Si in terms of frequency and is twice better in terms of current, with lower thermal losses.

Since they are extremely fast, systems based on GaN transistors or SiC MOSFETs are more sensitive to the inductances and capacitors induced by the layout. A lot of work is currently being made to improve the design of converters so as to diminish these negative effects.

I.5. Different technologies of variable speed machines

This section will dive into the different technologies of variable speed machines powerful enough for hydraulic applications (with power outputs in the range of MW at least). The machines that satisfy these criteria are generally polyphase (usually three phases) distributed radial flux machines. Most of these machines have stator designs that are extremely similar. These stator designs are well known by electrical engineers, for that reason and to shorten the main text, the description of these stator designs is laid off in APPENDIX A, p 163. Readers not familiar with the notions of three-phase winding,

distributed winding, winding layers, bars, conductors and strands, slot filling factor, parallel paths, integer slot winding and fractional slot winding, coil span and coil span reduction or finally winding factors can refer to APPENDIX A.

In the following Figure I-8, the electrical topologies of fixed speed machines and of different technologies of variable speed machines are displayed. These different technologies of variable speed will be discussed in the following section.

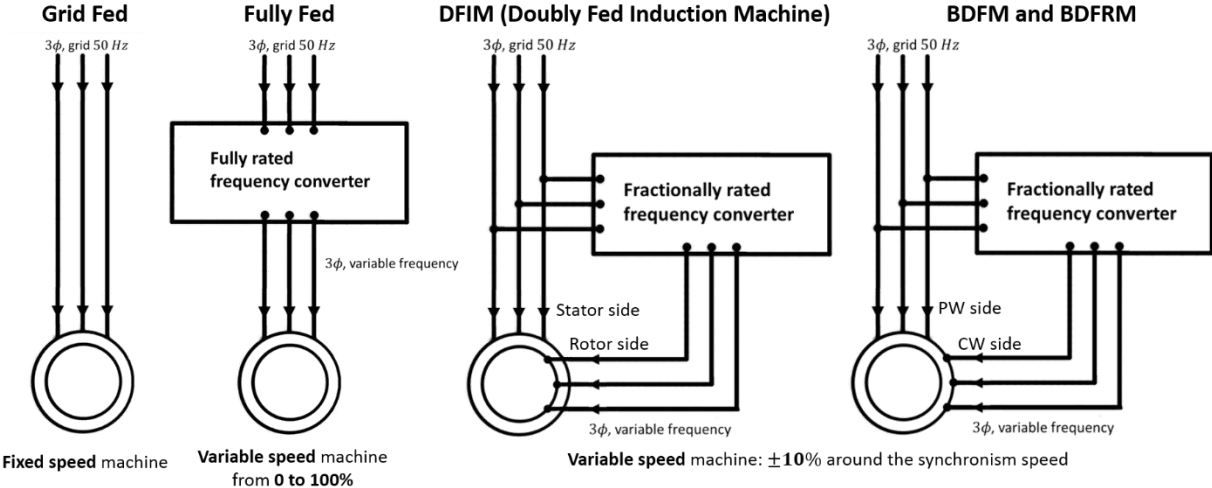


Figure I-8 : Topologies of fixed speed machines and different technologies of variable speed machines. The DFIM has one stator fed at the grid frequency and a rotor fed at variable frequency through a partial scale Power Converter. BDFM and BDFRM have two stator windings: the Power Winding (PW) fed at the grid frequency, and the Command Winding (CW) fed at variable frequency through a partial scale Power Converter.

I.5.1. Fully-Fed, full speed range that implies fully rated power converters

Fully-Fed machines can be synchronous (salient poles, turbo, permanent magnets, or reluctance) or asynchronous machines. One can refer to APPENDIX B, p 171 and APPENDIX C p 175 for more information about synchronous and asynchronous machines. Machines are referred to as fully-fed when all their power is passing through a power converter. The speed of these machines is dependent on the feeding frequency. Feeding them with a power converter will allow for variable speed operation from 0 to 100 % of the maximum speed.

To this day, the most powerful fully-fed machine ever commissioned was a 100 MW synchronous machine in Grimsel, Switzerland, refer to I.4.2.

Variable speed operation of fully-fed machines can have advantages and drawbacks. Among the advantages:

- Fully-fed machines have a complete speed range, from 0 % to 100 % of the maximal speed. This is a considerable advantage in comparison to other technologies that can only vary the speed from 80 % to 100 % of the maximal speed. Even if most of the operation occurs between 80 % and 100 % of the maximal speed, being able to operate around 0 % allows faster and easier start and stops. Thanks to this advantage it is possible to switch from generator to turbine and vice versa a lot faster.

- A full-size converter also allows for better control of the harmonics injected into the network. It is easier to meet Grid Code requirements. When not operated at maximum power, it also allows a higher compensation power to help the network balance.

The principal drawback is the price of the converter technology. As previously said in I.4.2, p 17, a price estimation of the VSC technology is around \$ 0.10 per W.

I.5.2. Doubly-Fed Induction Machine: DFIM, a variable speed machine with a small power converter but with brushes

Doubly-Fed Induction Machine: DFIM, is currently the only kind of doubly-fed machines in operation in hydropower generation. This technology has recently been developed for high power and commissioned to PSPs. For example, in Linthal, Switzerland, four 250 MW DFIM were commissioned by ALSTOM now GE in 2015.

A DFIM has the advantage of being able to operate at speed varying up to 10% around its synchronism speed (a larger speed range would lead to trouble for the rotor sizing as it is explained more at length in D.4, p 181).

A DFIM also has some disadvantages. One of them is the use of brushes. Brushes can be heavy and need to be replaced several times in the lifetime of the machine. This can be complex depending on the location of the machines which are often in the mountains for a PSP project.

Another disadvantage is the price of its rotor. The rotor is wound with a three-phase winding which is a lot more expensive than manufacturing a salient pole rotor or a squirrel cage rotor.

I.5.3. New kind of Doubly-Fed Machines: BDFM and BDFRM, the advantage of doubly-fed machines without the brushes

I.5.3.1. Origin and history of the BDFM and BDFRM

The idea of the BDFM originated in the 20th century from Siemens Brothers and Lydall in 1902 [23]. In the 1910s the principles of self-cascaded machines: two induction machines sharing the same shaft was studied by Hunt [24],[25] and Creedy [26]. Broadway *et al* researched the concept of the BDFM in the 1970s: bringing the two stators together in the same iron frame [27], [28] and [29]. They were also the first to investigate a salient pole rotor: the BDFRM.

I.5.3.2. Advantages and disadvantages in comparison to the DFIM

The Brushless Doubly-Fed Induction Machine (BDFM) and the Brushless Doubly-Fed Reluctance Machine (BDFRM), are two new types of doubly-fed machines that are very similar. Both technologies aim to have the same advantages as DFIM: variable speed with a power converter rated only for a fraction of the total power output of the machine.

The advantages of BDFM and BDFRM over DFIM are:

- They are more robust. Since there are no brushes and no slip rings, there is no risk of wear for these pieces. The maintenance of the machine is reduced.
- The rotor of BDFRM has no winding so no copper losses.
- The rotor of BDFM does not need to be wounded. It is theoretically possible to design BDFM with die-casted rotors which could lead to much cheaper rotors to manufacture. However, in this case, the bars of the rotor must be perfectly isolated from the iron stacks to avoid current flows between the nested-loops (see I.5.3.5.2 p 32, Figure I-10). In fact, these currents are extremely unfavorable as it is explained and modeled in [30]. Some steps should be taken during the manufacturing process to create a non-conductive layer around the iron stack before die-casting the nested-loops. A comparison of some of the possible processes can be found in [31].

The main disadvantage seems to be the complexity of electromagnetic interactions in these machines. They can be confusing for machinists used to have machines with interactions on the fundamental harmonic. Another uncertainty is the efficiency that could get obtained from such machines, especially for powerful generators as the one used for hydraulic power generation. So far, both technologies have been studied in laboratories. Some models have been studied for example, for the BDFM, coupled-circuit model in [31] (more information in II.3.2.1), d-q and reduced d-q models in [32] (more information in II.3.2.1), electric equivalent circuit model in [32] (more information in II.3.2.3), FEM model in [33], [34], [35], and [36], and nodal-based magnetic equivalent circuit model in [37]. Prototypes have also been designed and tested as in [32]. But most of these prototypes had modest power outputs. For that reason, and because methods for proper optimization of these machines are not yet well defined, the efficiencies and power factors of the prototypes were low.

I.5.3.3. Differences between BDFM and BDFRM, advantages - disadvantages

As it will be explained in the following parts, the BDFM and BDFRM are identical in terms of harmonic interactions. The main difference is that a reluctance rotor creates these interactions in the BDFRM while an induction rotor creates the interactions for the BDFM. Despite the striking similarities, in literature, they have generally been studied separately. Still, some comparison work has already been done in the literature, like in [38] for example.

Advantages of BDFRM over BDFM according to [38]:

- The modeling and the command of the BDFRM are simpler, there are fewer state variables.
- The efficiency could be a bit higher since there are no currents so no Joule Losses in the rotor. (It is like withdrawing the slip losses of the asynchronous machine). But this has not been proved yet and there may be more core losses.

Disadvantages of BDFRM over BDFM according to [38]:

- The BDFRM produces a current with higher harmonic content.

- The practical experience on reluctance machines is much smaller in comparison to induction machines.

The advantages and disadvantages of BDFRM in comparison to BDFM are not well studied. Some knowledge has to be accumulated on these two technologies to be able to determine which one is to be preferred depending on the desired specifications. It would be interesting to further compare both technologies, especially in the case of big power generation. In addition to the results in [38], and based on personal intuitions, I expect BDFRM to have slightly better power factor. A BDFM is probably better suited for cases where the integrity of the rotor is more at risk. In fact, a BDFM has a massive rotor while the BDFRM technology currently depends on laminated rotors. For powerful machines, the limits towards bigger machines are generally the cooling process and the mechanical limits of the rotor iron. In these cases, a BDFM seems better suited. Even if these statements seem almost evident, they have not yet been backed by proper comparison results.

The rotor's role in the BDFRM is easier to understand. For that reason, the working principle of the BDFRM will be explained first in 1.5.3.4. Then it will be explained how the BDFM achieves the same behavior in 1.5.3.5.

1.5.3.4. The Brushless Doubly-Fed Reluctance Machine: BDFRM

1.5.3.4.1. Topology

The BDFRM technology is based on two stator windings, in the same magnetic frame, that interact with each other through a reluctance rotor. The two stator windings do not interact with each other directly in the stator frame. Since they are in the same magnetic core, they need to have a different number of pole pairs to avoid magnetic couplings. One of the stator winding is fed with a fixed frequency: it is connected to the grid and is referred to as the power winding or the grid winding. The second stator winding is fed with a bidirectional voltage sourced inverter. This second winding is referred to as the control winding or command winding. Without the command winding, the power winding would impose a natural speed (expressed in equation (36), p 34). The feeding frequency of the command winding is the degree of liberty that will enable the speed variation of the generator.

This topology can be seen in Figure I-8. The topology of the BDFM is the same as the topology of the BDFRM. Only the rotor structure will change.

1.5.3.4.2. Different kind of reluctance rotors

The rotor of the BDFRM is a reluctance rotor. It can be a salient pole rotor or a laminated rotor with axial flux barriers (see Figure I-9). In [39], *Schulz et al* compare the BDFRM salient and laminated rotors. In their results, the laminated rotor with axial flux barriers could have twice the torque of the salient pole rotor.

A laminated rotor can be axially laminated or radially laminated (see Figure I-9). The axially laminated rotor will promote a higher coupling between the two stator windings. Despite this

advantage, in [39] the authors are making the case for radially laminated rotors because they will have lower magnetic losses thanks to the laminations.

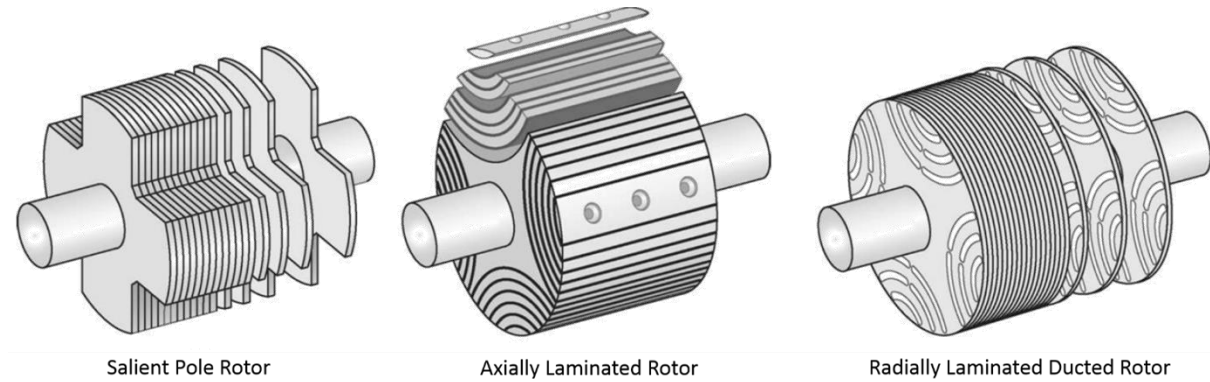


Figure I-9: Different designs of reluctance rotors, (from [40])

1.5.3.4.3. Analytical expression of the airgap flux densities from the two stator windings

The following part is adapted from [40] which took [41][42][43][44] and [45] as main references.

To develop the analytical computations of the flux density in the airgap the following assumptions will be made:

- The iron has an infinite permeability.
- The two stator windings are uniformly distributed around the airgap.
- The excitation currents are sinusoidal.
- The rotor is a salient pole rotor such that the airgap permeance takes the values of a sinusoid plus a constant.

From these assumptions, the harmonic content in the airgap of the BDFRM will be computed, the conclusions on the harmonic interactions between the two stators windings are presented in Table I-2, p 27.

The permeance of the airgap is defined as:

$$\Lambda_{ag}(\theta_{ag}, \theta_{rm}) = \frac{\mu_0}{\delta_{ag}(\theta_{ag}, \theta_{rm})} \quad (3)$$

With Λ_{ag} the permeance of the airgap.

θ_{ag} , the position in the airgap in the reference frame of the stator.

θ_{rm} , the mechanical position of the rotor in the reference frame of the stator.

δ_{ag} , the radial airgap length.

From the last assumption above the permeance of the airgap can be written:

$$\Lambda_{ag}(\theta_{ag}, \theta_{rm}) = m + n \cdot \cos[S_r(\theta_{ag} - \theta_{rm})] \quad (4)$$

m and n are two positive real numbers.

S_r is the number of saliencies of the rotor.

When the three phases of a stator winding are fed by balanced currents:

$$\begin{cases} i_a(t) = \widehat{I}_s \cos(\omega_s t + \angle I_s) \\ i_b(t) = \widehat{I}_s \cos\left(\omega_s t + \angle I_s - 2\frac{\pi}{3}\right) \\ i_c(t) = \widehat{I}_s \cos\left(\omega_s t + \angle I_s + 2\frac{\pi}{3}\right) \end{cases} \quad (5)$$

\widehat{I}_s is the amplitude of the currents of the stator winding.

$\angle I_s$ is the phase of the grid current.

ω_s is the feeding pulsation of the winding.

t is the time variable.

The magnetomotive force created by a three-phase stator winding can be expressed as [46]:

$$\Theta_{3\phi}(\theta_{ag}, t) = \widehat{\Theta}_{3\phi} \cos\left(\omega_s t - \frac{P}{2}\theta_{ag} + \phi_{winding} + \angle I_s\right) \quad (6)$$

$\Theta_{3\phi}$ is the magnetomotive force in the airgap as a function of the position and the time.

$\widehat{\Theta}_{3\phi}$ is the amplitude of the fundamental harmonic of the magnetomotive force and can be expressed as in (7).

P is the number of poles of the winding.

$\phi_{winding}$ is the position of the stator winding in the stator reference frame.

$$\widehat{\Theta}_{3\phi} = \frac{3}{2} \cdot \frac{4}{\pi} \cdot \frac{N_s k_w}{P} \cdot \widehat{I}_s \quad (7)$$

N_s is the number of turns in series per phase of the stator winding.

k_w is the winding factor.

The airgap flux density can be computed with the airgap permeance and the magnetomotive force in the airgap:

$$B_{ag}(\theta_{ag}, \theta_{rm}, t) = \Lambda_{ag}(\theta_{ag}, \theta_{rm}) \cdot \Theta_{3\phi}(\theta_{ag}, t) \quad (8)$$

From (4),(6) and (8) it is possible to express the radial airgap flux density created by the power winding in the BDFRM:

$$\begin{aligned} B_{ag,g}(\theta_{ag}, \theta_{rm}, t) &= \{m + n \cos[S_r(\theta_{ag} - \theta_{rm})]\} \\ &\cdot \widehat{\Theta}_{3\phi,g} \cos\left(\omega_g t - \frac{P_g}{2}\theta_{ag} + \phi_{grid\ winding} + \angle I_g\right) \end{aligned} \quad (9)$$

Let's define the phase of the power winding magnetomotive force:

$$\angle \Theta_{3\phi,g} = \phi_{grid\ winding} + \angle I_g \quad (10)$$

Considering (10), (8) can be developed into:

$$B_{ag,g}(\theta_{ag}, \theta_{rm}, t) = \widehat{\Theta}_{3\phi,g} \left[m \cos\left(\omega_g t - \frac{P_g}{2} \theta_{ag} + \angle\Theta_{3\phi,g}\right) + n \cos\left(\omega_g t - \frac{P_g}{2} \theta_{ag} + \angle\Theta_{3\phi,g}\right) \cos(S_r \theta_{ag} - S_r \omega_{rm} t - S_r \theta_{rm0}) \right] \quad (11)$$

With θ_{rm0} the position of the rotor at $t = 0$.

ω_{rm} the mechanical pulsation of the rotor.

(11) can be further developed into:

$$B_{ag,g}(\theta_{ag}, \theta_{rm}, t) = \widehat{\Theta}_{3\phi,g} \left[m \cos\left(\omega_g t - \frac{P_g}{2} \theta_{ag} + \angle\Theta_{3\phi,g}\right) + \frac{n}{2} \left[\cos\left((\omega_g - S_r \omega_{rm})t - \left(\frac{P_g}{2} - S_r\right) \theta_{ag} + \angle\Theta_{3\phi,g} - S_r \theta_{rm0}\right) + \cos\left((\omega_g + S_r \omega_{rm})t - \left(\frac{P_g}{2} + S_r\right) \theta_{ag} + \angle\Theta_{3\phi,g} + S_r \theta_{rm0}\right) \right] \right] \quad (12)$$

With the same method, the expression of the control winding flux density can be developed:

$$B_{ag,c}(\theta_{ag}, \theta_{rm}, t) = \widehat{\Theta}_{3\phi,c} \left[m \cos\left(\omega_c t - \frac{P_c}{2} \theta_{ag} + \angle\Theta_{3\phi,c}\right) + \frac{n}{2} \left[\cos\left((\omega_c - S_r \omega_{rm})t - \left(\frac{P_c}{2} - S_r\right) \theta_{ag} + \angle\Theta_{3\phi,c} - S_r \theta_{rm0}\right) + \cos\left((\omega_c + S_r \omega_{rm})t - \left(\frac{P_c}{2} + S_r\right) \theta_{ag} + \angle\Theta_{3\phi,c} + S_r \theta_{rm0}\right) \right] \right] \quad (13)$$

Equations (12) and (13) give the expression of the radial flux density in the airgap. From the two equations, it is important to note the presence of a fundamental harmonic and of two sidebands harmonics. The two sidebands harmonics are created by the saliency of the rotor. In the case of the grid winding, the fundamental harmonic has $\frac{P_g}{2}$ poles and is pulsating at ω_g the pulsation of the grid winding. The two sidebands harmonics have a harmonic spatial order of $\frac{P_g}{2} - S_r$ and $\frac{P_g}{2} + S_r$. They are pulsating at $\omega_g - S_r \omega_{rm}$ and $\omega_g + S_r \omega_{rm}$ respectively. The idea behind the BDFRM technology, is to create an interaction of the two stators windings fundamental harmonic with one of the sideband harmonic of the other winding.

1.5.3.4.4. Harmonic coupling in a BDFRM for torque creation

The condition for an electromagnetic interaction between two harmonics is that these two harmonics need to have the same harmonic spatial order (the same number of poles or nodes) and the same rotating speed, so the same frequencies. Since the cosine function is an even function, the harmonics can also interact if they have an opposed number of poles and opposed frequencies.

For example, let's consider the power winding fundamental and the 1st control winding sideband. The harmonic spatial order of the power winding fundamental is $\frac{P_g}{2}$, its frequency ω_g . The harmonic spatial order of the control winding 1st sideband is $\frac{P_c}{2} - S_r$, its frequency $\omega_c - S_r\omega_{rm}$. If the system of equations (14) is verified, then an interaction between these two harmonics will be possible:

$$\begin{cases} \frac{P_g}{2} = \frac{P_c}{2} - S_r \\ \omega_g = \omega_c - S_r\omega_{rm} \end{cases} \quad (14)$$

The system of equations (14) results in a condition on the number of saliencies of the rotor and a condition on the rotating speed of the BDFRM as in (15):

$$\begin{cases} S_r = \frac{P_c - P_g}{2} \\ \omega_{rm} = \frac{\omega_c - \omega_g}{S_r} \end{cases} \quad (15)$$

In (12) and (13), since cosine is an even function, it is possible to put a minus to the sign inside the cosine function of (12) or (13) without changing them. Using the same logic as in (14) and (15) would then lead to the system of equations of (16). Like the conditions of (15), the conditions of (16) would lead to an interaction between the power winding fundamental and the 1st control winding sideband harmonic:

$$\begin{cases} S_r = \frac{P_c + P_g}{2} \\ \omega_{rm} = \frac{\omega_c + \omega_g}{S_r} \end{cases} \quad (16)$$

The positive case shown in equation (16) is often preferred to the negative case in equation (15). In fact, it leads to a higher number of saliencies for the rotor which is generally preferable from a manufacturing point of view. For example, a BDFRM with 6 poles for the power winding and 4 poles for the control winding would only have one saliency with equation (15) but five saliencies with equation (16).

When the rotor verifies the conditions of equation (15) or equation (16), it ensures cross-coupling between the two stator windings.

A similar analysis as in equations (14), (15) and (16) can be done for all the different coupling between the fundamental harmonics and the sidebands harmonics. Table I-2 summarizes the four different interactions that can happen between one fundamental and one harmonic of the opposite winding. This table gives for each interaction, the conditions necessary for the interaction to happen (in term of number of poles of each winding, number of rotor saliencies, mechanical speed of the rotor, and feeding frequencies of each winding).

Table I-2: Different cases of interactions between the fundamental harmonics and the sidebands harmonics of the BDFRM with the related conditions on the number of rotor saliencies and the mechanical speed

Interaction Between: Power Fundamental And Control 1 st sideband	Interaction Between: Control Fundamental And Power 1 st sideband	Interaction Between: Power Fundamental And Control 2 nd sideband	Interaction Between: Control Fundamental And Power 2 nd sideband
If the number of poles and frequencies are the same, this results in the following conditions			
$\begin{cases} S_r = \frac{P_c - P_g}{2} \\ \omega_{rm} = \frac{\omega_c - \omega_g}{S_r} \end{cases}$	$\begin{cases} S_r = \frac{P_g - P_c}{2} \\ \omega_{rm} = \frac{\omega_g - \omega_c}{S_r} \end{cases}$	$\begin{cases} S_r = \frac{P_g - P_c}{2} \\ \omega_{rm} = \frac{\omega_g - \omega_c}{S_r} \end{cases}$	$\begin{cases} S_r = \frac{P_c - P_g}{2} \\ \omega_{rm} = \frac{\omega_c - \omega_g}{S_r} \end{cases}$
If the number of poles and frequencies are opposed (the cosine function is even)			
$\begin{cases} S_r = \frac{P_c + P_g}{2} \\ \omega_{rm} = \frac{\omega_c + \omega_g}{S_r} \end{cases}$	$\begin{cases} S_r = \frac{P_c + P_g}{2} \\ \omega_{rm} = \frac{\omega_c + \omega_g}{S_r} \end{cases}$	$\begin{cases} S_r = \frac{-P_g - P_c}{2} \\ \omega_{rm} = \frac{-\omega_g - \omega_c}{S_r} \end{cases}$	$\begin{cases} S_r = \frac{-P_g - P_c}{2} \\ \omega_{rm} = \frac{-\omega_g - \omega_c}{S_r} \end{cases}$

In Table I-2, identical conditions are highlighted with identical colors. It can be seen that one set of conditions always leads to two interactions. For each set of conditions, there will always be one harmonic from the power winding that will interact with the fundamental of the control winding and one harmonic from the control winding that will interact with the fundamental of the power winding.

In Table I-2, the pulsations can be positive or negative depending on the rotation direction; but the number of poles or saliencies that can be manufactured are necessarily positive. Even if a negative number of poles has some mathematical meaning it cannot be implemented in a design. Because of that, some of the conditions of Table I-2 cannot be achieved in a real BDFRM. For example, the two last conditions highlighted in red cannot be achieved. Depending on the number of poles of the grid and control windings, the conditions highlighted in orange and blue are sometimes possible and sometimes not. Only the conditions highlighted in green are always possible. On the contrary, the conditions highlighted in red are never possible. Moreover, the conditions highlighted in green are the ones that lead to the highest number of rotor saliencies. For that reason, the green conditions are the one chosen most of the times for a BDFRM design. In most BDFRM designs, the fundamentals of the power and control windings will interact with the first sideband of the control and power winding respectively.

1.5.3.4.5. Torque of the BDFRM

An analytical expression of the electromagnetic torque produced by the BDFRM can be found in the literature. In [43], the analytical expression in steady state is given as:

$$\Gamma_{em} = -\frac{3}{2} \left(\frac{P_g + P_c}{2} \right) L_{gc} I_g I_c \sin(\phi_\Gamma) \quad (17)$$

g is the subscript indice referring to the grid (= power) winding of the BDFRM.

c is the subscript indice referring to the command (= control) winding of the BDFRM.

P is the number of poles of the command or the grid winding depending on the indices.

I is the amplitude of the current of the command or the grid winding depending on the indices.

$L_{gc} = \frac{3}{2} L_{gcmax}$ is the mutual inductance between the two stators winding through the rotor.

ϕ_Γ is referred to as the torque angle. It depends on the position of the rotor and the position of the two windings. More information about the definition of this angle can be found in [43]. As a brief summary, the authors in [43] took the case where the two fundamentals MMF harmonic of the two stator windings had a common maximum (in this PhD, a fundamental MMF harmonic can be seen in Figure E-3, p 188). ϕ_Γ is then defined as the angle from this common maximum to the closest maximum of the airgap permeance times the number of saliencies. Depending on the rotor position ϕ_Γ can vary from 0 to 2π .

As it can be seen in [23], the torque of the machine not only depends on the rotor design to maximize L_{gc} but also on its position that impacts ϕ_Γ . For a given design, and for given currents in the stator windings, the torque of the BDFRM will vary as a sine wave depending on the rotor position.

1.5.3.5. The Brushless Doubly-Fed Induction Machine: BDFM

The stator of the BDFM is identical to the stator of the BDFRM: two balanced three-phase windings in the same magnetic frame. They have a different number of poles to avoid magnetic interactions inside the stator frame. They are fed with different frequencies. The windings will interact thanks to the rotor. The difference being that the BDFRM's rotor is a reluctance rotor and the BDFM's rotor is an inductive one. The inductive cage of the BDFM is a special one. In 1.5.3.4.3 and in Table I-2 of 1.5.3.4.4, it was shown that the number of saliencies of the reluctance rotor was fixed in order to allow the interactions between fundamental harmonics and the sidebands harmonics of the other stator winding. The same will be true for the BDFM: if the BDFM is equipped with a squirrel cage, a special number of bars will be necessary to render the interactions between harmonics and fundamental possible. This will be demonstrated in 1.5.3.5.1. A similar demonstration can be found in [47].

It is important to keep the two stators windings electrically independent in the frame of the stator: they must be linked through the rotor only. Induction machines with double stator winding which have the same number of poles for the two stators also exist. This technology, generally referred to as Double Stator Induction Machine (DSIM) or Double Stator Induction Generator (DSIG) differs from the

BDFM technology. With a DSIM it is not possible to implement variable speed without the use of two three-phase inverters connected to each stator windings. The BDFM technology gives the advantage of variable speed with only a portion of the power passing through an inverter. DSIM technology can be seen as induction generator with 6 phases. As explained in [48], the advantage of DSIM is the elimination of the $6m \pm 1$ airgap harmonics, with $m = 1,3,5 \dots$. This reduces the related copper losses and decreases the torque harmonics. Polyphase machines can also operate despite the loss of one of the stator winding. Thus, they are more reliable and are used for example for the propulsion of large ships. The DSIM technology has inherent disadvantages: it is by construction a fully-fed technology; it is not possible to connect a six-phase machine to a three-phase network without a power converter with six phases. The windings of these machines are also a bit different from the windings generally used in heavy power generation. If this technology had to compete in power generation, it would have to compete against other fully-fed technologies. The DSIM will not be studied during this PhD.

1.5.3.5.1. Analytical expression of the airgap flux densities of the two stator windings

As for the BDFRM (see equation (6)), the fundamental of the magnetomotive force (MMF) created by the two three-phase stator windings can be expressed as:

$$\Theta_{3\phi}(\theta_{ag}, t) = \widehat{\Theta}_{3\phi} \cos\left(\omega_s t - \frac{P}{2}\theta_{ag} + \phi_{winding} + \angle I_s\right) \quad (18)$$

In the case of the BDFM, the rotor and the stator will be considered smooth to avoid the harmonics related to teeth in the analytical development. The radial airgap length is constant: δ_{ag} . The fundamental magnetic flux density harmonic in the airgap due to a balanced three-phase winding fed by three-phase currents can be expressed as:

$$B_{3\phi}(\theta_{ag}, t) = \frac{\mu_0}{\delta_{ag}} \widehat{\Theta}_{3\phi} \cos\left(\omega_s t - \frac{P}{2}\theta_{ag} + \phi_{winding} + \angle I_s\right) \quad (19)$$

Let's define the amplitude of the fundamental flux density:

$$\widehat{B}_{3\phi} = \frac{\mu_0}{\delta_{ag}} \widehat{\Theta}_{3\phi} \quad (20)$$

And now, let's define the phase of the fundamental flux density related to the winding position and the current phases:

$$\angle B_{3\phi} = \phi_{winding} + \angle I_s \quad (21)$$

With the previous definitions, the fundamental of the flux density in the airgap created by the two stator windings can be written as:

$$B_g(\theta_{ag}, t) = \widehat{B}_g \cos\left(\omega_g t - \frac{P_g}{2} \theta_{ag} + \angle B_g\right) \quad (22)$$

$$B_c(\theta_{ag}, t) = \widehat{B}_c \cos\left(\omega_c t - \frac{P_c}{2} \theta_{ag} + \angle B_c\right) \quad (23)$$

\widehat{B}_g the amplitude of the fundamental of the airgap flux density created by the grid winding.

\widehat{B}_c the amplitude of the fundamental of the airgap flux density created by the control winding.

ω_g the pulsation of the currents feeding the grid winding.

ω_c the pulsation of the currents feeding the control winding.

P_g the number of poles of the grid winding.

P_c the number of poles of the control winding.

θ_{ag} position in the airgap in the reference frame of the stator.

The reader can note that in (22) and (23), if P_g and P_c are defined positive, the rotation direction of the flux density will be imposed by the sign of ω_g and ω_c that can be set positive or negative. Like the BDFRM, the power/grid and control windings do not need to create a flux density rotating in the same direction.

With ω_{rm} as the mechanical pulsation of the rotor, the two previous equations can be passed in the rotor reference frame using equation (24):

$$\theta_{ag} = \theta_{ag,r} + \omega_{rm} t + \theta_{ag,r t=0} \quad (24)$$

If the initial position of the rotor is assumed to be null: $\theta_{ag,r t=0} = 0$, then the flux density phases do not need to be changed. Using (24), (22) and (23) become:

$$B_g(\theta_{ag,r}, t) = \widehat{B}_g \cos\left(\left(\omega_g - \frac{P_g}{2} \omega_{rm}\right) t - \frac{P_g}{2} \theta_{ag,r} + \angle B_g\right) \quad (25)$$

$$B_c(\theta_{ag,r}, t) = \widehat{B}_c \cos\left(\left(\omega_c - \frac{P_c}{2} \omega_{rm}\right) t - \frac{P_c}{2} \theta_{ag,r} + \angle B_c\right) \quad (26)$$

To allow the two stator windings interaction through the rotor, the stator windings need to create compatible currents in the rotor induction cage. By compatible, we imply here that to interact, the rotor currents need to have the same frequency and the same spatial distribution.

The induced rotor currents frequencies will be equal to the frequency of flux densities in the rotor reference frame. From (25) and (26) this leads to:

$$\omega_{rg} = \omega_g - \frac{P_g}{2} \omega_{rm} = \omega_c - \frac{P_c}{2} \omega_{rm} = \omega_{rc} \quad (27)$$

ω_{rg} and ω_{rc} are the electrical pulsations of the induced rotor currents from the power winding and control winding respectively.

Equation (27) can be transformed to show the equivalent condition on the rotor mechanical speed:

$$\omega_{rm} = \frac{2(\omega_g - \omega_c)}{P_g - P_c} \quad (28)$$

Another condition arises from the spatial distribution of the currents. The current phase shift between two adjacent bars of the rotor will be the same as the flux density phase shift. For the grid winding, the phase shift of the fundamental flux density between two adjacent rotor bars can be written:

$$\angle B_{g,\theta_{ag,r}=0} - \angle B_{g,\theta_{ag,r}=\frac{2\pi}{N_r}} = \frac{P_g}{2} \frac{2\pi}{N_r} \quad (29)$$

With N_r , the number of rotor bars and, $\frac{2\pi}{N_r}$, the angle between two adjacent bars.

The same equation can be written for the control winding. To have the same spatial distribution, the rotor currents induced by the two fundamentals need to have the same phase shift between each bar (the same spatial distribution). Since $\frac{P_g}{2} \neq \frac{P_c}{2}$, this condition is only possible if the phase shifts are equal modulo 2π . The new condition on the phase shifts can be written:

$$\angle B_{g,\theta_{ag,r}=0} - \angle B_{g,\theta_{ag,r}=\frac{2\pi}{N_r}} = \angle B_{c,\theta_{ag,r}=0} - \angle B_{c,\theta_{ag,r}=\frac{2\pi}{N_r}} + 2q\pi \quad q = \pm 1, \pm 2, \pm 3, \dots \quad (30)$$

Combining equation (29) and equation (30) :

$$\frac{P_g}{2} \frac{2\pi}{N_r} = \frac{P_c}{2} \frac{2\pi}{N_r} + 2q\pi \quad q = \pm 1, \pm 2, \pm 3, \dots \quad (31)$$

Equation (31) can be rearranged to obtain the condition on the number of bars:

$$N_r = \frac{P_g - P_c}{2q} \quad q = \pm 1, \pm 2, \pm 3, \dots \quad (32)$$

The preferred value of q will be $q = 1$, since the higher q is, the less rotor bars there will be. With $q = 1$, the number of rotor bars is already very small. For example, for a machine with 8 pole pairs for the grid winding and 4 pole pairs for the control winding, the number of nests would be $N_r = \frac{16-8}{2} = 4$. A rotor cage with only 4 bars.

The conditions on the mechanical speed and the number of rotor bars that will allow an electrical interaction between the currents induced from the two stator-windings are summarized in (33):

$$\begin{cases} \omega_{rm} = \frac{\omega_g - \omega_c}{N_r} \\ N_r = \frac{P_g - P_c}{2} \end{cases} \quad (33)$$

The reader can notice that the conditions in (33) for the BDFM and the conditions in (15) for the BDFRM are identical. The notion of saliencies in the BDFRM (S_r) has been replaced by the notion of bars for the BDFM (N_r).

As for the BDFRM, since the cosine function is even, the conditions can also be written as:

$$\begin{cases} \omega_{rm} = \frac{\omega_g + \omega_c}{N_r} \\ N_r = \frac{P_g + P_c}{2} \end{cases} \quad (34)$$

For the same reason as the one given after equation (32), q is taken equal to 1. The conditions of (34) are generally preferred over the condition of (33). In fact, the conditions of (34) lead to a higher number of rotor bars. The example already taken for equation (32) would lead to: $N_r = \frac{16+8}{2} = 12$: a rotor cage with 12 bars instead of 4 bars with the conditions given by (32).

We still have to remember in equation (34) that ω_g and ω_c can be negative depending on the rotation direction of the flux density they are referring to.

The system of equation of equation (34) is the same as the system of equation highlighted in green in Table I-2, p 27 for the BDFRM. Even if it is not obvious when looking at equation (18) to equation (34), the conditions that are given in equation (34) lead to the same interactions as the green conditions in Table I-2, p 27 for the BDFRM. Under these conditions, the fundamental harmonics of the power and control windings will interact with the first sideband harmonics of the control and power winding respectively. The rotor ensures cross-coupling between the two stator windings.

1.5.3.5.2. Special Nested-Loop rotor

The number of bars imposed by the equation (34) is still small. As shown in [27], it conduces to a very high referred rotor leakage reactance. It is possible to increase the number of bars in the rotor by separating each bar and distributing it across several slots. As explained in [47], the bars are replaced by several concentric loops and referred to as “nests”. The nests are all isolated from each other. Sometimes, for manufacturing reasons, the nests are connected with each other but there should not be any induced currents between the different nests. A scheme of the nested-loop technology is presented in Figure I-10. A 3D representation of a 10 nests rotor, with 6 loops per nest is shown in Figure III-1, p 78.

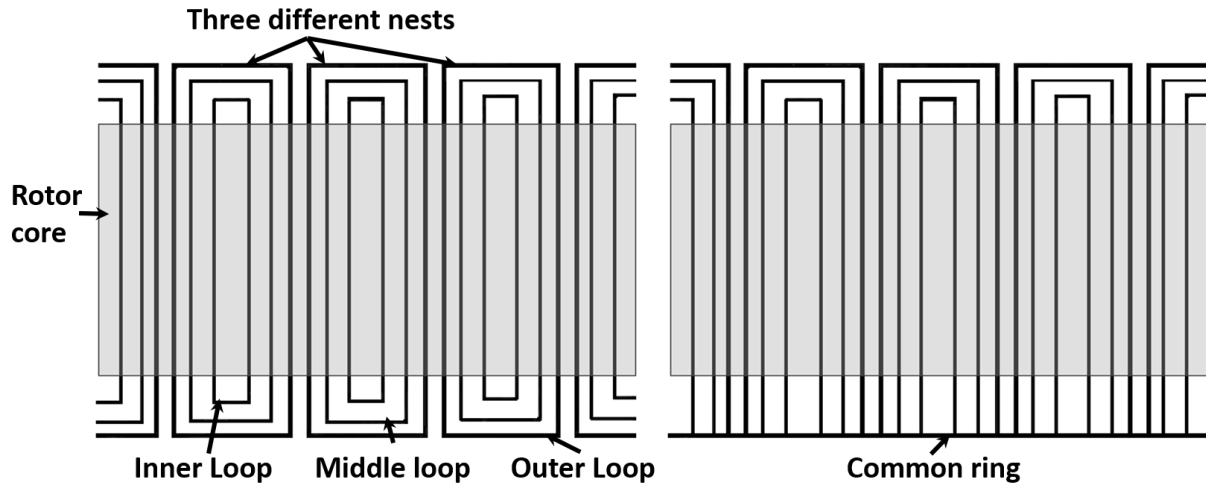


Figure I-10: Scheme of a BDFM rotor with $p_g + p_c$ nested-loops; left: isolated from each other's, right: with a common ring

In the notations, N_r will be kept to express the number of nests of the rotor of the BDFM. The number of rotor slots will be expressed as $N_{slot,r}$. It can be calculated thanks to N_r and the number of loops per nest $N_{loops/nest}$:

$$N_{slot,r} = 2N_r N_{loops/nest} \quad (35)$$

$N_{slot,r}$ the number of rotor slots.

N_r the number of nests of the rotor.

$N_{loops/nest}$ the number of loops for each nest of the rotor.

1.5.3.5.3. Comparison between nested-loop rotors and other rotor designs for BDFM

In [32], Roberts tried to design different kinds of rotors to compare them. He was able to manufacture small prototypes and to compare torque characteristics.

Roberts compared 7 different designs:

- Rotor 1: a nested-loop rotor verifying the conditions of (34).
- Rotor 2: a new rotor design for BDFM with nests and a double layer winding, trying to improve upon the nested-loop design by giving each loop the same coil span, see Figure I (definition of coil span: see A.8, p 168).
- Rotor 3: a rotor with a number of nests to couple with the two stator windings but that do not respect the second condition of (34) to prove the importance of this condition in the BDFM cascaded mode torque.
- Rotor 4: a rotor with a number of nests that verify the second condition of (34), but with nests not homogeneously distributed over the rotor.
- Rotor 5: a squirrel cage rotor that verifies the conditions given in (34): with only N_r bars.
- Rotor 6: a rotor with two wounded double-layer windings, so four layers in total, one winding with P_g poles and the other one with P_c poles. The two rotor windings are connected.
- Rotor 7: a standard squirrel cage that does not verify the conditions for cross-coupling of (34).

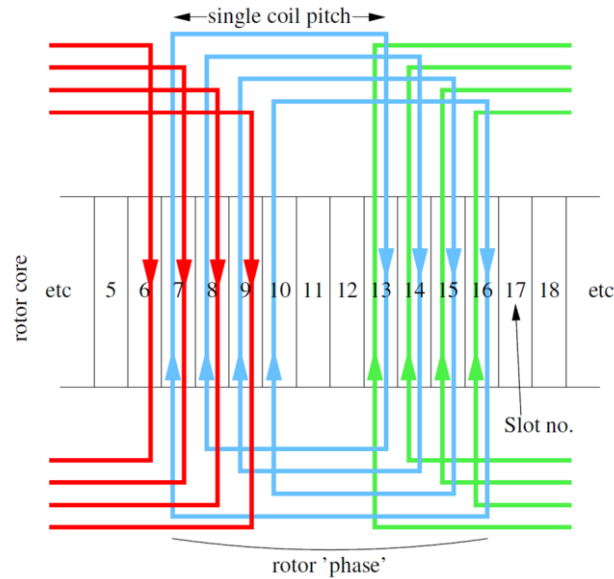


Figure 11: Prototype of a new double-layer design rotor (Rotor 2 [32])

The comparison of the different prototypes in [32] brings interesting results. It compares first all the rotors on simple induction mode: only one stator winding is fed and the second is in open-circuit. In this mode, the machine tries to operate as an induction machine. The results show that the better the rotor will be to cross couple the stator windings, the worse it will be to operate as an induction machine. To get the results in self-cascaded mode, one of the stator windings is fed while the other is short-circuited. Without any surprise, the rotors that do not meet the conditions for cross-coupling of equation (34) have a small torque in self-cascaded mode.

According to the tests results of the prototypes, the best rotor design for torque creation in self-cascaded mode is the nested-loop rotor (rotor 1). This is a bit disappointing since rotor 2 was designed as a potential improvement for torque creation over rotor 1. However, these prototypes were only designed for small machines (originally 22 kW), the results could be different with other designs. The rotors were not tested for the highest torque under operation but only in a particular case where one winding is short-circuited. Moreover, it is possible that the rotor 2 was not well optimized. The results could be different under different circumstances. For all these reasons, more investigation into comparative advantages between rotor 1 and 2 would still be needed before rejecting rotor 2 for a potential improvement.

1.5.3.5.4. Natural speed, slip, and power

The natural speed of a BDFM (or a BDFRM) is the mechanical speed of the machine when the Command Winding (CW) is fed with DC voltage:

$$\omega_n = \frac{\omega_g}{N_r} \quad (36)$$

ω_n is the natural speed.

N_r is the number of rotor nests generally defined according to the conditions of (34).

The natural speed of a BDFM is similar to the synchronous speed of a DFIM. It is the mechanical speed when there is no power passing through the power converter.

Because of (36) and (34), a BDFM will have the tendency to turn slower than the synchronous speed linked to the Power Winding (PW). Thus, the BDFM technology appears to be a good solution in the cases where the mechanical speed is low. For the renewable energy sector, this can be viewed as another advantage of BDFM and BDFRM technologies over DFIM. This is the reason why these technologies are currently highly investigated for wind farm generators. In fact, wind farm generators need variable speed technology to optimize the efficiency across a range of speed that is rather slow for an electrical machine. At the power wind turbines are dealing with, it is hard to design DFIM with enough poles for their synchronous speed to match the rotating speed of the blades.

As for an Induction Machine (IM) or DFIM, the notion of slip can be introduced for the BDFM. Since there are two windings, a slip will be defined for each winding, as in [49]:

$$s_g = \frac{\omega_g - p_g \omega_{rm}}{\omega_g} \quad (37)$$

$$s_c = \frac{\omega_c \pm p_c \omega_{rm}}{\omega_c} \quad (38)$$

Where $\pm p_c$ depends on the windings connections of the PW and CW. If the field from the CW rotates in the same direction as the one from the PW when they are both fed with 3 phases currents, then it is a $-$, if it rotates in the opposite direction it is a $+$. In other words, if the orders of connection of the phases are the same (+A, -C, +B, -A, +C, -B) for both windings, then the magnetic fields will rotate in the same direction and the CW slip will be: $s_c = \frac{\omega_c - p_c \omega_{rm}}{\omega_c}$. If the orders of phases are inverted: (+A, -C, +B, -A, +C, -B) for the PW and (+A, -B, +C, -A, +B, -C) for the CW, the magnetic fields will rotate in opposite directions and the CW slip will be: $s_c = \frac{\omega_c + p_c \omega_{rm}}{\omega_c}$. Of course, it is possible to inverse phases B and C of the CW with the power converter. The rotating direction of the CW can vary through the operation of the power converter. In this PhD, we will take the arbitrary decision that the phases orders are the same for both windings: the CW slip will be: $s_c = \frac{\omega_c - p_c \omega_{rm}}{\omega_c}$. The case where the CW will be operated by the power inverter so that the direction of its field rotates in the opposite direction to the one of the PW, will be considered in the equations by a negative CW pulsation: $\omega_c < 0$.

1.5.3.5.5. The equivalent circuit of the BDFM

Equivalent schemes for the BDFM have been defined in the literature, see Figure I-11 from [49]. All the quantities are expressed referred to the power winding. The scheme is valid for all modes of operations, including the cross-coupling mode. The equivalent scheme assumes that saturation of the iron circuit does not significantly affect the parameter values.

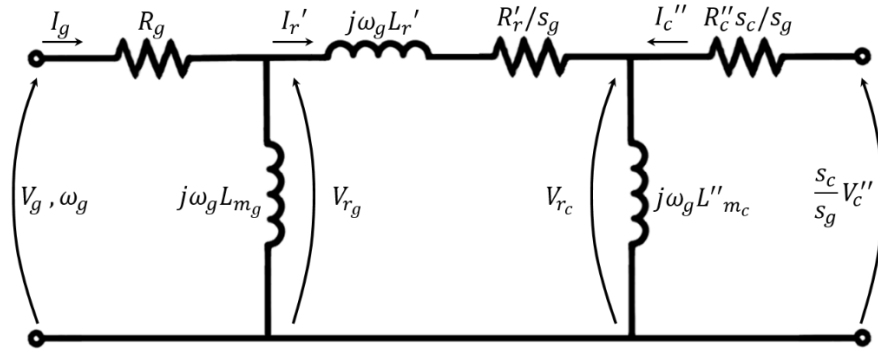


Figure I-11: Per phase equivalent circuit of a Brushless Doubly-Fed Induction Machine expressed on the side of the PW as generally found in the bibliography [49]

I_g is the current of the PW.
 I_r' is the rotor currents.
 I_c'' is the current of the CW referred to the PW.
 R_g is the PW resistance.
 R_c'' is the CW resistance.
 R_r' is the rotor winding resistance.
 $\omega_g L_{mg}$ is the magnetizing reactance for the PW.
 $\omega_g L''_{mc}$ is the magnetizing reactance for the CW.

This model of the equivalent circuit was updated in [32], see Figure II-8, p 66.

1.5.3.5.6. Torque expression derived from the equivalent circuit

As explained in [49], the torque of the BDFM can be derived from the equivalent circuit:

$$\Gamma = \frac{3|V_g V_c'' s_c|}{\omega_n |\omega_g L_r' s_g|} \sin \delta \quad (39)$$

s_g is the slip of the power winding.

s_c is the slip of the control winding.

δ the load angle.

1.5.3.5.7. Relationship between grid winding and control winding power, and sizing of the power converter

With the equivalent circuit, the power of the CW can also be approximated from the power of the PW and the speed of the machine [49]:

$$P_c = P_g \frac{\omega_{rm}}{\omega_n} \quad (40)$$

The converter rating can also be estimated, it is given for example in [50]:

$$S_{inv} \approx S_m \frac{\omega_{c \max}}{\omega_{c \max} + \omega_g} \quad (41)$$

S_{inv} is the rating of the inverter connected to the command winding.

S_m is the rated power of the machine.

$\omega_{c\ max}$ is the maximal pulsation that must be attained by the command winding to fulfill the maximal mechanical speed needed.

Equation (41) shows that the power converter for a BDFM (or BDFRM) is comparable to a power converter for a DFIM subject to the same specifications (in terms of rated power for mechanical speed variations).

1.5.3.5.8. The biggest BDFM to date

The biggest BDFM machine built to date is a 250 kW 4/8 poles generator built as a step toward bigger BDFMs for wind turbines, with the objective of reaching, one day, up to 3 MW. This machine has a speed range of 320 – 680 rpm with a natural speed of 500 rpm (see equation (36)). The PW was rated at 690 V, 178 A, at 50 Hz and the CW was designed for 620 V, 73 A, at 18 Hz. A performance analysis and testing of this machine can be found in [51]. This machine had to be built with techniques appropriate to large generators including magnetic wedges for the slots of the stator.

1.6. Conclusion

The needs for a growing energy storage capacity was highlighted in the first part of this chapter. So far, at the level of the grid, the storage energy market is composed for more than 98% of PSPs. A comparison between different storage technologies suggests that the coming years will probably see the development of new PSPs and Lithium-Ion batteries.

A few years ago, Lithium-Ion batteries were not competitive in comparison to PSPs from a financial point of view and for large energy storage. It appears that their price has gone down in the past few years and that some big projects have already been developed in 2017. The future of this technology is still uncertain, its competitiveness is still hard to evaluate: the future price of batteries, their lifespan, the capacity to scale up in this new market... In this first chapter, the point of view that currently, PSPs are still competitive was shared. In the future, Lithium-Ion batteries can be expected to be the preferred solution in isolated areas and small grids or in other locations where the landscape excludes a PSP solution. Lithium-Ion batteries might also become more competitive than new PSPs projects with a high infrastructure cost. In this scenario, Lithium-Ion will take some of the market shares of PSP for energy storage at the grid level. Yet retrofits (changing the technology of a hydroelectric dam to turn it into a PSP) can also be expected to stay competitive. In fact, when the dam is already built, the infrastructure cost of retrofits projects is a lot lower than the cost of new projects.

Concerning the PSP technology, the advantage of variable speed over fixed speed was reminded to the reader. Variable speed improves the power regulation in pump mode. It increases the quantity of energy that can be stored. It also increases the hydraulic efficiency and is faster to stabilize after a perturbation.

Variable speed machines are relying on variable frequency. The basics of power electronics that provide variable frequency were explained. The notions of rectifier, inverter, and converter were

discussed. Different technologies of converters were presented: Voltage Source Converter (VSC), Current Sourced Converter (CSC), Indirect Matrix Converter (IMC) and Conventional (Direct) Matrix Converter (CMC). VSCs are generally preferred over the CSC technology for pairing with electrical machines despite their more expensive prices. A VSC rejects fewer harmonics on the grid because it can be operated in PWM. PWM also allows reactive power control. Moreover, a VSC is generally smaller than a CSC since the capacitors DC storage take less place than the inductances DC storage. IMC and CMC are investigated in laboratories but not manufactured yet for powerful applications. Other future architectures were presented: MMC, power converters based on smaller power converters put in parallel. New semiconductor technologies were also reviewed: Gallium Nitride (GaN) and Silicon Carbide (SiC). These semiconductors can handle higher voltages, higher currents, higher frequencies, and have better efficiencies than Silicon (Si). In the future, it can be conjectured that the GaN technology will be more prominent in domestic, computer applications, and telecom. The SiC solution will probably take over in industrial applications.

Different technologies of variable speed machines were compared: fully-fed with Synchronous Machines (SM), or Induction Machines (IM); and doubly-fed with Doubly-Fed Induction Machines (DFIM), Brushless Doubly-Fed Induction Machines (BDFM), or Brushless Doubly-Fed Reluctance Machines (BDFRM).

- The fully-fed machines are designed with a power converter rated for their nominal apparent power. The speed variation can vary from 0 to 100%. The stator and rotor designs are the same as for fixed speed machines. These electrical machines are simpler to design, to manufacture, to control and operate. The main drawback being the converter price that can be more expensive than the machine itself.
- The doubly-fed machine works with a power converter sized only for a fraction of the total apparent power of the machine. One winding is connected to the grid and a second one is connected to the converter. The rotor of a DFIM must be wound with a three-phase winding. The design and construction of such a rotor are more challenging than for rotors of fully-fed machines. Moreover, the rotor needs to be fed with brushes that must be replaced over the lifespan of the machine.

Because of the disadvantages of the DFIM, new technologies of doubly-fed machines are investigated: the BDFRM and the BDFM. The working principles of these machines were explained. The two technologies have analogous stators. The stators have two windings: the Power Winding (PW or Grid Winding) and the Control Winding (CW or Command Winding). The PW is connected to the grid and the CW is connected to the converter. The two windings have different frequencies and number of poles so as to avoid interaction in the stator magnetic core. They are interacting through the rotor which creates harmonics around each fundamental. In the BDFRM, a reluctance rotor creates the harmonics and in the BDFM, an induction rotor creates the harmonics.

Both technologies were discovered and studied a long time ago: at the beginning of the 20th century. The advancement in power electronics and the new computing power allow us to investigate them further and to envisage an application in the renewable energy sector.

In this Ph.D., the BDFM will be further investigated. As stated in this first chapter, the BDFM's rotors were estimated to be structurally stronger than the BDFRM's laminated rotors. This has not yet been highlighted in the literature, probably because the only prototypes that were built were in the kW range (250 kW for the biggest [51]). For these kinds of machines, with a weight lower than a few hundred kilograms, the mechanical stress on the rotor is generally not an issue (these machines are not driven at extremely high speed). In large-hydro application, the power of a turbine can be up to a few hundred MW. The weight of these machines is in the range of a hundred tons or more. At this level, the mechanical robustness of the rotor becomes critical.

In the following chapter, simulations methods, sizing, and optimizations techniques for electrical machines will be investigated. An example will be given on an Induction Machine (IM), and the state of the art of these methods in relation to the BDFM will be discussed.

CHAPTER II. SIMULATIONS METHODS, DESIGN AND OPTIMIZATION OF ROTATING MACHINES FOR HIGH POWER GENERATION: STATE OF THE ART, EXAMPLE, AND LIMITS TOWARD A SIMILAR APPLICATION FOR THE BDFM

II.1.	Introduction.....	43
II.2.	Simulations methods, design, and optimization of rotating machines for high power generation	43
II.2.1.	Multiphysics problems imply Multiphysics models.....	43
II.2.2.	Optimization methods: with analytical and semi-analytical models or with Finite-Element Methods (FEM)	44
II.2.2.1.	Difference between Sizing and Optimizing	45
II.2.2.2.	Optimization principles and different kind of algorithms for optimization based on analytical and semi-analytical models.....	46
II.2.2.2.1.	Optimization principles	46
II.2.2.2.2.	Deterministic algorithms	47
II.2.2.2.3.	Stochastic algorithms	48
II.2.2.2.4.	Design of experiments.....	49
II.2.2.3.	Cades, a software for optimizations with analytical and semi-numerical models	49
II.2.2.4.	Magnetic model implementing reluctance network.....	50
II.2.2.5.	Reluctool: a tool to represents reluctance networks.....	50
II.2.2.6.	Finite-element methods.....	51
II.2.2.6.1.	History and principles.....	51
II.2.2.6.2.	A finite-element software for electromagnetism: Flux2D and an optimization software associated: Got-It	52
II.2.3.	Optimization example of an IM using first an analytical iterative method, followed by a semi-analytical 1 st order optimization.....	52
II.2.3.1.	The Typical Tidal Project (TTP) specifications.....	52
II.2.3.2.	Different analytical methods for Induction Machine sizing	53
II.2.3.3.	First sizing of an Induction Machine with the Typical Tidal Project specifications using an iterative method	54
II.2.3.4.	Semi-analytical method for a 1 st order optimization of Induction Machines	56
II.2.3.5.	Implementation of the semi-analytical model from APPENDIX F in Cades.....	57

II.2.3.6.	Comparison between the analytical model and finite-element simulations	58
II.2.3.6.1.	Geometry chosen for the comparison	58
II.2.3.6.2.	Magnetizing Inductance comparison between the semi-analytical model and finite-element calculations.....	59
II.2.3.7.	Results of 1 st order optimizations with Cades of an Induction Machine on Typical Tidal Project specifications.....	60
II.2.3.7.1.	Imaginary or real machines.....	61
II.2.3.7.2.	Pareto curve and parametrized optimization: maximal efficiency depending either on saturation or on the length of the design.....	61
II.3.	Limits to apply the previous methods to the new kind of doubly-fed machines.....	64
II.3.1.	Empirical knowledge for a first sizing.....	64
II.3.2.	Semi-analytical models to be paired with a 1 st order optimizations do not exist yet...	65
II.3.2.1.	Limits of the coupled-circuit model.....	65
II.3.2.2.	Limits of the d-q model	66
II.3.2.3.	The equivalent circuit	66
II.3.2.4.	Reluctance Network	67
II.3.3.	Finite-element methods: for experimental research plan. FE simulations are much more time consuming for a BDFM than for usual rotating machines because of the different frequencies of the stator windings	68
II.4.	Conclusion	70

II.1. Introduction

In the previous chapter, different technologies of variable speed machines were investigated. At the end of the chapter, a new technology: the BDFM, was chosen to be further studied because of its interesting characteristics and possible improvements over DFIM for large hydro applications. As highlighted in the previous chapter, a few BDFM prototypes were already built in the past, but these machines were never sized for powerful applications in the MW range.

In this chapter, the different methods usually used for simulating, sizing, and optimizing electrical machines will be reviewed. The goal is to identify these methods and see whether and how they can be applied to the BDFM.

The electrical machines simulation part will deal with analytical models, semi-analytical models, and numerical methods. These models and methods have different advantages and drawbacks in terms of quickness, accuracy, development, or possible pairing with optimization algorithms.

The difference between sizing and optimizing will be explained. The optimization part will show how multi-objective problems can be addressed with special objective functions or Pareto curves. Different kind of optimization algorithms will be presented: stochastic or deterministic; algorithms of order 0, or more powerful 1st order algorithms.

Following the presentation of simulations and optimization methods and software, an optimization example on an Induction Machine (IM) will be presented. A first sizing will be made with an iterative analytical model. Then a more complex and accurate semi-analytical model paired with a 1st order optimization algorithm will be used to improve the IM design. Finally, with iterative FE simulations, more accurate than the semi-analytical model, it will be possible to verify the behavior of the machine and adjust some parameters.

A comparison of the results obtained with the semi-analytical model and FE simulations will highlight which part of the semi-analytical model would benefit from being more accurate. Solutions to improve its accuracy will be proposed.

The second part of this chapter will study how the methods applied during the design of the IM could be used in the case of the BDFM. This part will specifically highlight areas where future work is needed to enable future optimizations of BDFM designs.

As it will be seen, some analytical sizing tips already exist in the literature. Some work has been done for the BDFM with wound rotors. However, a complete semi-analytical model, derivable and useful to pair with a 1st order optimization algorithm is not available in the literature yet. Moreover, the end of this chapter will show that FE simulations of a BDFM can take much longer than FE simulations of usual machines. This would seriously slow down an optimization process based on iterative FE simulations.

II.2. Simulations methods, design, and optimization of rotating machines for high power generation

II.2.1. Multiphysics problems imply Multiphysics models

Electrical machines are complex. An electrical machine design is a multiphysics problem. It includes magnetic, electrical, thermal, mechanical and fluid dynamics phenomena. Because it is a

multi-physic problem, the design of electrical machines often implies to couple several models:

- Electromagnetic models to determine electrical values like currents, voltages and resulting copper losses. Magnetic values to compute resulting torque and iron losses.
- Fluid dynamics and thermal model to determine the temperature in different parts of the machine.
- Mechanical simulations to verify the eigenfrequencies of the machine and avoid vibration problems.

Fluid dynamics and thermal models, as well as mechanical models, are impacted by the geometrical design of the machine. Since the geometrical design of the new technologies studied in this work (BDFRM and BDFM) are similar to designs of previous technologies, they will not require us to completely reconstruct these models. For that reason, in the following part, the focus is set on electromagnetic models and not the fluid dynamics, thermal, or mechanical ones.

II.2.2. Optimization methods: with analytical and semi-analytical models or with Finite-Element Methods (FEM)

As stated in II.2.1, the goal of an electromagnetic model is to obtain electrical values and magnetic values from known geometric and electrical inputs. Most of the models will fit in three categories: analytical models, semi-analytical models, and numerical models. The choice of the model will have a big impact on the complexity to set it up, its intricacy, its precision and accuracy and finally the computation time during solving. Figure II-1 gives an idea of the expectations we can have of different models in terms of computing time and intricacy depending on the category they belong. It should be noted that an increase in the intricacy of the model is generally done with the end goal of improving the model’s accuracy. However, sometimes, the added complexity of a model can deteriorate its accuracy. Especially when the added complexity adds some parameters that are not well known.

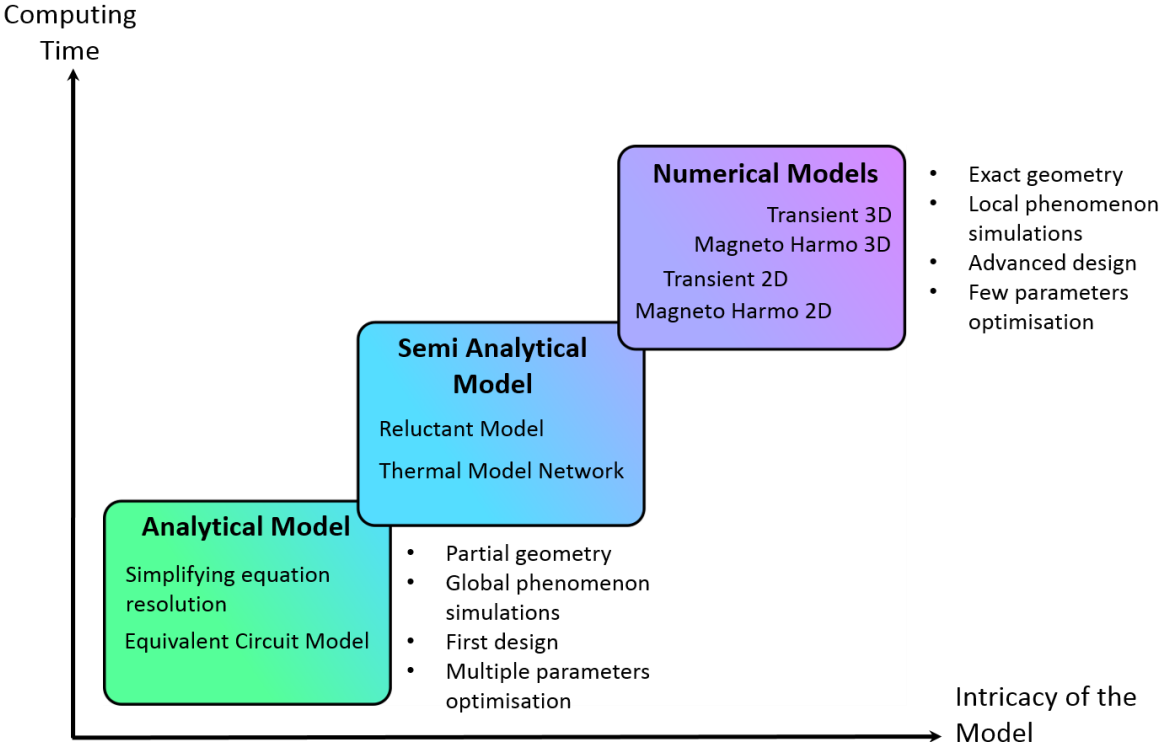


Figure II-1: Reasonable expectations from the three big categories of models in terms of speed and intricacy [52].

- Analytical models are based on simplifying assumptions. They have a huge advantage in terms of computing time. The design of such models requires experts and is time-consuming. They try to focus on macro-phenomena.
- Semi-analytical models can be both fast and accurate. They start to focus on some impactful local phenomena. The design of such models also requires experts and time.
- Numerical models are currently mostly represented by FE Methods. With FE software, it is possible to apply these models to new designs with ease. With a good definition of the geometry and the mesh, these models can bring accurate results of global and local phenomena. The computation complexity of these models puts a limit on their capacity to explore all the design possibilities and to do optimizations on multiple parameters.

All the categories presented in Figure II-1 can be useful. Depending on the phase of the design and the objectives, some models will be more relevant.

For example, at the beginning of the design, a designer might want to explore a wide range of parameters. He might want to know which parameters are the most influent and do a fast first sizing or optimization to get a broad idea of the characteristics of the machine. In this case, an analytical or semi-analytical model will be a judicious choice. These models are fast in computing time, and the inaccuracies they may have should not be a big issue during initial phases. Moreover, these models are often derivable which enables fast 1st order optimizations as presented in II.2.2.2.

Later during the design process, when most of the parameters are already defined, more intricate and accurate numerical models can become more pertinent. With numerical models, it becomes possible to fine-tune a few specific parameters with Design of Experiments (DOE). They also allow to better assess the behavior of a design: its power, voltages and currents outputs, its efficiency, etc.

The following parts will dive deeper into the analytical, semi-numerical, and FEM models. Examples of different tools will also be given to develop analytical, semi-analytical or FE models. The list given will not be exhaustive; of course, many tools doing a similar job exist. The tools examples given here were simply the ones used or studied during this work.

II.2.2.1. Difference between Sizing and Optimizing

During the first sizing of an electrical machine (see II.2.3.2, p 53 dealing about IM sizing), the idea is often to use general analytical equations to determine some parameters of the machine. It is impossible to determine from a set of analytical equations more variables than the number of independent equations. The number of variables defining an electrical machine is high. Hundreds of parameters can be defined. The number of equations used for the sizing is much lower, in many analytical models only a few dozens. Thus, to size a machine, an expert is needed. He will fix as inputs many variables needed to start the resolution of equations. Doing so, the expert will make some hypotheses, based on his knowledge. Table II-3, p 55 shows the hypotheses (inputs) that were made for the first IM sizing on the TTP simulations. Of course, it is possible to implement loops on inputs parameters to test different possibilities and to find better set of parameters. Doing so, the limits of computation power are quickly reached with a computation time that increases exponentially with the number of varying inputs. This is the point when optimization methods based on analytical expressions

become interesting. With methods of 1st order optimizations (II.2.2.2.2), the optimum can be located much more rapidly than with a method where all the possibilities are explored. The differences between these concepts of sizing and optimizing are more thoroughly discussed in [53].

The following part will explain the principles behind analytical and semi-numerical optimizations. Even if optimization methods are able to find optimums among all the possibilities, we will see that they still require the knowledge of experts to set some constraints and define what can be realistically achieved or not.

II.2.2.2. Optimization principles and different kind of algorithms for optimization based on analytical and semi-analytical models

II.2.2.2.1. Optimization principles

The general principle of an optimization is to find values of variables that minimize the objective function(s) while respecting all the sizing constraints. This can be formulated with equation (42):

$$\begin{cases} \min f_{obj}(y) \\ g(y) \leq 0 \\ h(y) = 0 \end{cases} \quad (42)$$

With y , the inputs parameters.

f_{obj} , the objective function to be minimized.

g , the inequality constraints (for example the maximum diameter, or maximum voltage).

h , the equality constraints (in some cases the frequency, or the nominal rotating speed).

For an electrical machine, the objective function could be on the efficiency or the price of the machine. If the objective function is well defined, the algorithm will generally try to reach the limits of the magnetic and the electrical loading simultaneously.

The constraints issued by the specifications of electrical machines are generally:

- The dimensions, inertia, current and voltages, etc.
- Based on geometric coherence (for example, all the geometric parameters must be positive).
- Linked to the fabrication process: the filling factor, the size of the conductors, etc.

An optimization can be mono (with only one objective) or multi-objective. A mono-objective optimization can be solved with a mono-objective optimization algorithm. For a multi-objective optimization, two different approaches are possible:

- The first method consists in decomposing the multi-objective problem into several mono-objective problems. The objective function will then be a ponderation of each mono-objective problems.

$$f_{obj}(y) = \sum B_n f_{obj,n}(y) \quad \text{With } \sum B_n = 1 \quad (43)$$

This first method will lead to rapid results, but the choice of the ponderation of each mono-objective problem will impact the results. During this choice, the designer will have to choose the influence of each objective. For example, the importance of the weight in comparison to the importance of the efficiency.

- The second method uses Pareto principles. For two given objectives, the optimization result will not be given by a point but by a line. A solution will be part of the Pareto line if an improvement on one of the two objectives will automatically result in a deterioration of the other objective. Any point of the Pareto line is not better than another point on the same line, it will be a tradeoff, improving one objective at the expense of the other. In principle, it could be possible to use Pareto methods for more than two objectives. For three objectives, the Pareto optimum would be given as a surface; for four objectives, it would be a 3D object. Pareto principles are very useful for decision support, see Figure II-2. Thus, they are generally used on two objectives or three objectives only, with more objectives they are too complicated to represent and to interpret.

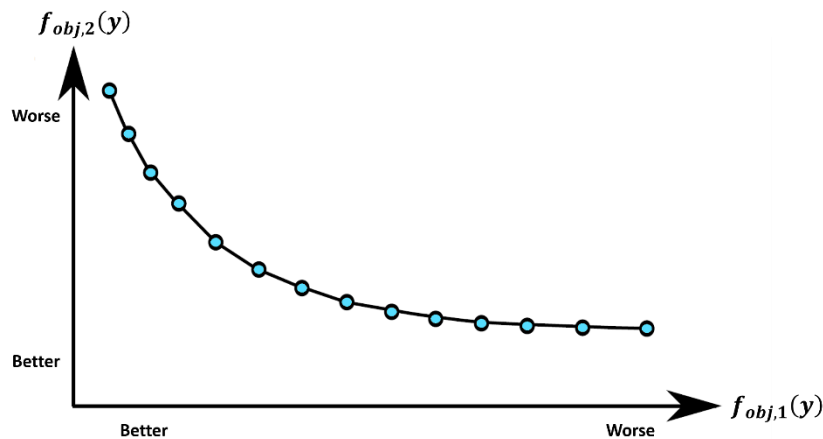


Figure II-2 Pareto curve for two objectives

Optimization problems can often be solved with optimization algorithms. Different types of algorithms exist. Understanding the advantages and disadvantages of these different groups is important for the choice of an adapted algorithm.

The following parts will present two families of optimization algorithms. Deterministic algorithms and stochastic algorithms. These varieties of algorithms can be cascaded to result in hybrid algorithms. The Design of Experiments method (DOE) will also be presented. This method could be seen as one kind of deterministic algorithm. The user chooses some parameters to be investigated and some experiments are defined to study the impact of the parameters on the objective function.

II.2.2.2.2. Deterministic algorithms

A deterministic algorithm is an algorithm that will always reach the same result from a given starting point. These algorithms can be classified into three different methods:

- Methods of order 0. These methods only need the result of the objective function. They are not precise and converge slowly. They can be used successfully on problems with limited

dimensions (depending on the complexity of the problem and the computational power). Their limits in dimensions can be reached quickly: the duration of the optimization will increase exponentially with the number of dimensions studied. Their only advantage is that they avoid to compute the gradient of the objective function that can be complex to generate.

- 1st order methods. They imply the computation of the gradient of the objective function(s) and the computation of the Jacobian of the constraints. These methods will converge much faster using the gradient information. They can only be applied to functions that are differentiable.
- 2nd order methods (example SQP: Sequential Quadratic Programming). They use the second derivative(s) of the objective function(s) and the Hessian matrix of the constraints. These methods have little advantages in terms of converging speed over 1st order methods. The big difference is between 1st order and methods of order 0. More information can be found in [54], [55], and [56].

All the methods cited above can get stuck in local minimums. In this case, different starting points will lead to different results. This is shown in Figure II-3 representing a problem with one dimension (y is the only parameter). For electrical machines designs, with dozens of dimensions, the designer needs to be aware of the potential of numerous local minimums. This can make the search for the only global minimum much harder.

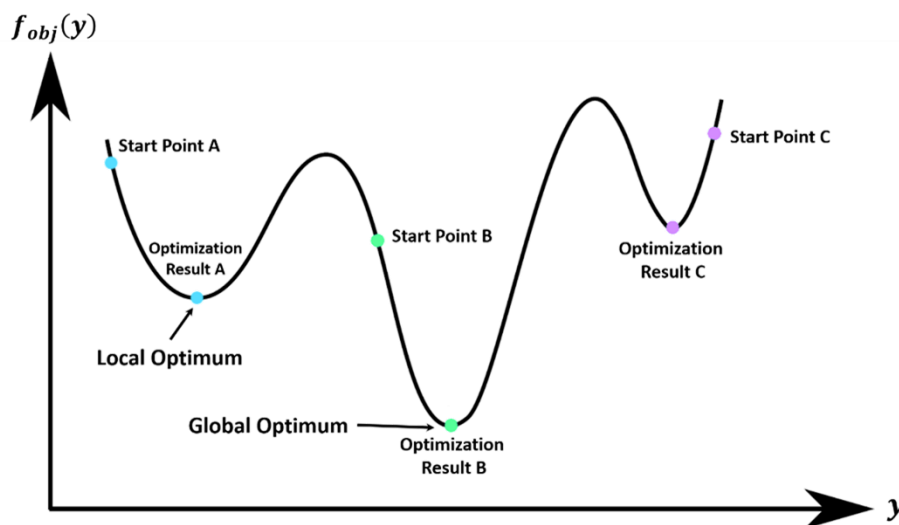


Figure II-3: Local and global optimums with the results that 1st order deterministic algorithms would probably get depending on the starting point

II.2.2.2.3. Stochastic algorithms

With stochastic algorithms, two optimizations with the same starting point will not necessarily lead to the same result. On the contrary of deterministic methods, stochastic algorithms do not need the gradient and the Jacobian matrix. Thus, stochastic algorithms are a kind of 0 order algorithms. In these methods, each new iteration is determined from the previous iterations but also from probabilities or randomness.

These algorithms will be able to explore all the dimensions of a problem in order to converge on the global minimum. Some Stochastics algorithms are even able to find all the local optimums and the global optimum. However, they converge a lot slower than 1st order deterministic algorithms.

Once again, different types of stochastic algorithms can be cited:

- Genetic algorithms. They are based on Darwin's theory of evolution by natural selection [57].
- Simulated Annealing methods: they are using thermodynamics laws of annealing of a solid [58].
- Particle Swarm Optimization Methods: they are based on social behaviors and motions in swarms [59] and [60].

Because of their slowness in comparison to deterministic algorithms, stochastic algorithms are not well suited for cases with hundreds of parameters and constraints.

Deterministic methods of 1st order can be paired with stochastic algorithms. For example, stochastic algorithms can be used to define the starting points of determinist methods. Such a pairing would be referred to as a hybrid-method and be well adapted for resolution of nonlinear systems with a high number of constraints and many local minimums.

II.2.2.2.4. Design of experiments

Design of experiments (DOE) is also a kind of 0 order optimization. In DOEs, the user will select some parameters to be investigated. A plan of consecutive experiments to study the impact of these parameters on the objective function will then be defined either by the user or the algorithm. With a clever definition of the DOE, the number of evaluations and the computation time will be contained [61]. The results of the DOE can either be used to directly optimize or to define a substitution function (for example polynomials) that will mimic the objective function response as a function of the considered parameters. This second technic is referred to as the response surface methodology. This substitution function (or response surface) can then be used for optimization (using deterministic solutions or polynomials knowledge).

II.2.2.3. Cades, a software for optimizations with analytical and semi-numerical models

CADES [54], was developed in the G2Elab, a laboratory of Electrical Engineering in Grenoble, France. It is a tool for sizing and optimizing with analytical and semi-analytical models. It is now commercialized and further developed by the company Vesta System. The system to be optimized has to be described through multiphysics equations. For electromagnetic problems, it can be described using reluctance networks (see II.2.2.4). Similar networks can be used to describe thermal problems.

The program performs a formal derivation of all the equations and semi-analytical models. The gradients of all the outputs (such as voltages, torque...) are obtained as functions of all the inputs (such

as geometric values, currents...). These gradients are stored in components. They can then be used for optimization or sensibility studies using optimization algorithms, both deterministic (see II.2.2.2.2) and stochastic (see II.2.2.2.3).

II.2.2.4. Magnetic model implementing reluctance network

Using an analogy between magnetic and electrical properties (see Table II-1), the magnetic state of a machine can be represented by an equivalent circuit similar to an electrical circuit. This circuit will be referred to as a permeance circuit or reluctance network.

Table II-1: Electric and Magnetic analogy [62] and [63]

Electric	Magnetic
Potential V	Magnetic Potential Θ
Current I	Magnetic Flux ϕ
Resistance R	Reluctance R
Electric Conductivity σ	Magnetic Permeability μ
Electric Field \vec{E}	Magnetic Field \vec{H}
Current density \vec{j}	Flux density \vec{B}

To define a permeance circuit, the magnetic circuit is divided into elements. A reluctance (analog to a resistance) or a magnetomotive force (MMF) source (analog to a voltage) is assigned to each element. For examples, see Figure II-4 for the definition of a stator tooth’s reluctance network; Figure E-2 in APPENDIX E, p 185, for the representation of the airgap; or Figure II-9, p 67, for the representation of one rotor pole of a BDFRM with a reluctance network. The definition of these elements should be done along the pathway of the flux in the machine: it requires some expertise in the technology of the machine to be represented. The analytical resolution of the permeance circuit, using Kirchhoff laws, will give the flux (analog to a current) in every branch of the circuit. From this flux, it will be possible to calculate the coenergy in the network and to derive the magnetic torque from this energy (more explanations in [63]). All the electromagnetic variables such as voltages and currents can also be computed from the flux in all the branches.

This method is economical in computation time in comparison to FE methods and can furthermore be derivable. However, the initial creation of a reluctance network specifically designed for one technology of electrical machine requires expertise and can be time-consuming.

Further information on the principles and how to implement a reluctance network are given in APPENDIX E, p 185.

II.2.2.5. Reluctool: a tool to represents reluctance networks

The tool Reluctool (used by [40] in Figure II-4, in Figure II-9, p 67, and in Figure E-2 of APPENDIX E p185) was developed in the G2Elab to simplify the definition and the resolution of reluctance networks: [63] and [64]. As for Cades, it is commercialized and has been further developed by the company Vesta System.

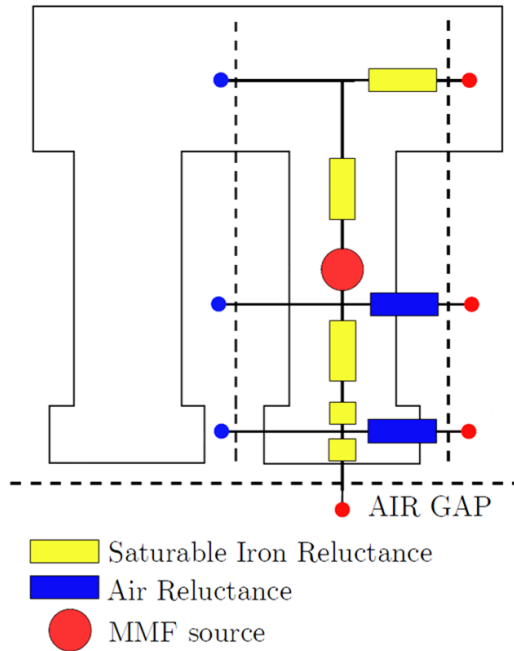


Figure II-4: Reluctance network for one stator tooth and its respective slot [40]

In Reluctool, the reluctances can be linear (for the air) or saturable (for the iron): they can depend on the flux going through them, considering the B(H) curve of a given material. This allows considering saturation in every branch. A permeance model is a semi-analytical model since it uses implicit equations because of the saturable permeances.

Reluctool has been integrated into Cades. The automatic generation of derivative calculation has been coded, so it is compatible with 1st order optimizations (see II.2.2.2.2, p 47).

II.2.2.6. Finite-element methods

II.2.2.6.1. History and principles

Methods with FE computations have already proved their effectiveness. Sufficiently accurate precision during the sizing of electromagnetic systems can be achieved. In the literature, the first publications about FE computation on electrical machines were in 1971 on a Direct Current saturated machine [65]. FE can also be applied to heat transfer, fluid flow, mass transport and structural analysis problems. The invention of the FEM can be traced back to the 1940s. It was first investigated on elasticity mechanical problems and vibrations [66] and [67].

The idea behind FE is to chunk a large problem into a large quantity of smaller problems that can be solved with algebraic equations (hence the name finite-element). FEM for magnetic problems are based on Maxwell equations under the hypothesis of almost stationary states. These equations express the relations between the electrical field \vec{E} , the magnetic field \vec{H} , the magnetic induction \vec{B} the electric induction \vec{D} , the current density \vec{j} and the electrical charge density ρ as in (44).

$$\begin{cases} \text{rot}(\vec{E}) = \frac{\partial \vec{B}}{\partial t} \\ \text{rot}(\vec{H}) = \vec{j} \\ \text{div}(\vec{B}) = 0 \\ \text{div}(\vec{D}) = \rho \end{cases} \quad (44)$$

FEM can be paired with optimization algorithms. The derivatives of the objective function as a function of the inputs cannot be computed for FEM. As a consequence, optimization algorithms that can be paired with FEM are deterministic algorithms of order 0 (refer to II.2.2.2.2, p 47) and stochastic algorithms (refer to II.2.2.2.3). As explained earlier, these algorithms are slower than 1st order deterministic algorithms. Moreover, FEM are already heavier processes than analytical and semi-analytical models. These combined drawbacks prevent to do extensive multi-parameters optimizations using FEM, especially in 3D FEM. For that reason, electrical machines are not designed from scratch with optimization algorithms running with FEM.

FEM are generally used to verify the characteristics of analytically designed electrical machines. FEM allow to check the forecasted performances of a machine, to search for harmonics that could lead to vibrations and to observe local quantities (maximum flux density, maximum currents). FEM can also be used to optimize a few parameters with a Design of Experiments method (DOE) (refer to II.2.2.2.4, p49).

II.2.2.6.2. A finite-element software for electromagnetism: Flux2D and an optimization software associated: Got-It

Many different FE software are available. They are generally designed and optimized for one kind of application: heat transfer, solid elasticity, electromagnetism... Flux2D is one example of a commercial FE software designed primarily for electromagnetism applications. Flux2D was developed in the G2Elab. It was then commercialized by CEDRAT that was bought in 2016 by ALTAIR. Most of the FE simulations in this Ph.D. were done using Flux2D.

Flux2D can be paired with Got-It which is an optimization software. With Got-It and Flux2D, it is possible to do deterministic 0 order optimizations (II.2.2.2.2, p47), stochastic optimizations (II.2.2.2.3) and DOE (II.2.2.2.4).

II.2.3. Optimization example of an IM using first an analytical iterative method, followed by a semi-analytical 1st order optimization

II.2.3.1. The Typical Tidal Project (TTP) specifications

One objective of this Ph.D. was to compare different technologies of variable speed machines. To do so, the ideal approach would be to select a few projects with different specifications and to size the different technologies for these projects. It would then be possible to do a comparison. The observation of the different advantages and drawbacks of each topology will help to extrapolate what are the more suitable technologies depending on the specifications.

First, a Typical Tidal Project (TTP) was selected to compare the technologies. The idea behind the project was to take advantage of the tide getting in and out of a bay to produce renewable electricity. To do so, 12 bulb turbines will be set up at the entrance of the bay. These turbines will produce electricity both when the tide comes in and the tide goes out. The major specifications of this project are summarized in Table II-2.

Table II-2: Major specifications of each electrical machines (12 identical) to be installed in the Typical Tidal Project (TTP)

Rated Active Power:	$P = 22 \text{ MW}$
Rated Synchronous Speed:	$n_s = 60 \text{ rpm}$
Turbine speed range:	$n = 40 \text{ to } 66 \text{ rpm}$
Bulb frame outer diameter:	$D_{frame} = 7 \text{ m}$
Stator maximal outer diameter:	$D_{out \text{ max}} = 5.2 \text{ m}$
Maximal length of the machine	$L_{max} = 2.1 \text{ m}$
Converter Voltage for fully-fed (from ABB)	$V_{max} = 3300 \text{ or } 6600 \text{ V}$

At the time of the offer, ALSTOM was still in the business of hydro-generation (this Ph.D. was started in ALSTOM Renewable). The design that had been proposed by ALSTOM was a salient pole synchronous machine, fully-fed by a Voltage Sourced Converter coming from wind turbine technology from ABB. In 2015, this project was awarded to an offer from General Electric which proposed a squirrel cage IM fully-fed by the stator. Since ALSTOM did not win this project, it was decided to take it as an example for this Ph.D. Later, in 2016, ALSTOM renewable was bought by GE to become GE Renewable. The project was kept as an example for this Ph.D. and no critical information about the design that won the project will be given in this work. Even the project name will remain undisclosed, it will only be referred as a Typical Tidal Project (TTP).

II.2.3.2. Different analytical methods for Induction Machine sizing

As explained in II.2.2.6, FEM are not adequate for the optimization of electrical machines from a blank sheet of paper. Analytical methods are used for a first sizing (using an optimization software or not) and FEM can then be used for further adjustments. There are many different analytical methods available for the first sizing of an IM. Some can be found in the literature: [68], [69] and [70]. Other methods are secrets well-kept in companies manufacturing electrical machines. In general, the analytical tools used to size machines can be classified into two different groups: the ones using general theoretical approaches, and the other ones using past experiences and databases of machines in operation. The tools used by manufacturing companies are generally a mix of these two different methods.

In GE Renewable, previously ALSTOM Renewable, the core business for hydro was Salient Pole Synchronous Machines. The goal here is not to disclose the analytical method used in GE for the SPSM, nor the one more recently developed for the DFIM. Consequently, it was decided to use an analytical sizing method using a theoretical approach, described in the literature: [70]. This method will be used to obtain the first draft of the IM sized for the TTP specifications.

In II.2.2, the difference between sizing and doing an optimization was explained. Deterministic methods based on analytical equations were then discussed. The method described in [70] would fit under the sizing appellation (it is not an optimization). In this method, the rotor diameter size increases in a loop until the specified torque is reached. Many other inputs have to be defined by an expert and will not be investigated by the sizing model.

This analytical method can be automated. During this work, it was decided to implement it in MATLAB, the authors of [70] decided to implement it in Excel using Visual Basic for Applications (VBA).

II.2.3.3. First sizing of an Induction Machine with the Typical Tidal Project specifications using an iterative method

As stated before, in the method from [70], some parameters of the IM need to be defined as inputs. In fact, there are 35 parameters that are defined as inputs. An expert will set them using his experience and the specifications of the project. Table II-3 presents the most important inputs defined at the beginning of the process. The only input that will vary during the sizing process will be the rotor diameter. At each iteration, the rotor diameter will increase until a specified torque is reached.

The model uses analytical equations to compute the outputs. The equations can be found in [70]. To summarize:

- The flux density in every part of the machine is based on the principle of flux conservation, considering the flux density as a sine wave in the airgap (B_{ag} , the airgap flux density, is an input and imposes the flux in the rest of the IM).
- For the rotor, the copper cross area of the bars is computed from the geometrical inputs and from the rotor diameter that slowly increases iterations after iterations.
- The maximal rotor current is obtained with the maximal rotor current density and the useful copper cross area of the rotor bars.
- The current distribution in each bar of the rotor is computed to respect the maximal rotor current and the sinusoidal distribution with the fixed number of poles.
- The torque is computed with the flux density in the airgap and the rotor currents without considering any phase shift between the currents and the flux density.
- The stator currents are computed from the rotor currents, a transformation ratio, and the power factor.
- The stator dimension parameters are computed to respect the maximum stator current density and the maximum flux density specified.

The model implemented in MATLAB has 37 outputs. As for the inputs, Table II-3 only presents the most important outputs computed by the sizing model.

Table II-3: Inputs and outputs of the sizing analytical model implemented in MATLAB, equations can be found in [70]

Inputs parameters	Values given to MATLAB implementation
Rated phase voltage:	$V_r = 3300 \text{ V}$
Rated Frequency:	$f_r = 16 \text{ Hz}$
Number of poles:	$N_{poles} = 32$
Rated Power:	$P_r = 22 \text{ MVA}$
Rated Torque:	$T_r = 3.501 \text{ kNm}$
Maximum airgap flux density:	$B_{ag} = 1 \text{ T}$
Maximum tooth flux density:	$B_t = 1.8 \text{ T}$
Maximum yoke flux density:	$B_y = 1.4 \text{ T}$
Maximal Current Density (RMS):	$J = 3.2 \text{ A. mm}^{-2}$
Shaft Diameter:	$D_{sh} = 2630 \text{ mm}$
Rotor Aspect ratio (L_{core}/D_r):	$\lambda = 1$
Shape of the slot, rectangular or trapezoidal:	Rectangular
Thickness of the airgap:	$\delta_{ag} = 15 \text{ mm}$
Lamination pack coefficient:	$K_{ir} = 0.94$
Filling coefficient of the stator slots:	$K_{cs} = 0.499$
Filling coefficient of the rotor slots:	$K_{cr} = 0.95$
Number of slots per pole and per phase:	$q = 3$
Winding pitch reduction (expressed in slot number):	$nr = 3$
Rotor slot number:	$N_{sr} = 192$
Rotor slot skewing ratio (τ_i/τ_p):	$R_i = 0.2$
Rated power factor:	$\cos \varphi = 0.9$
Stator drop voltage at rated load:	$\Delta V = 100 \text{ V}$
Outputs parameters	Values obtained from MATLAB
Diameter of the rotor:	$D_r = 3030 \text{ mm}$
Length of the active material:	$L_{core} = 3030 \text{ mm}$
Height of the rotor yoke:	$h_{RotorYoke} = 72 \text{ mm}$
Smallest width of a rotor tooth:	$w_{RotorTooth} = 29.4 \text{ mm}$
External diameter of the rotor yoke:	$D_{ext yr} = 2774 \text{ mm}$
Slot useful height of the rotor:	$h_{ur} = 113 \text{ mm}$
Rotor slot width:	$w_{br} = 16 \text{ mm}$
RMS current in each rotor slot:	$I_{r rms} = 5844 \text{ A}$
Number of conductors in series per phase:	$Z_{ph} = 192$
Number of conductors in series per slot:	$Z_c = 2$
RMS current in each stator slot:	$I_{s rms} = 2605 \text{ A}$
Number of stator slots:	$N_{ss} = 288$
Stator inner diameter:	$D_{is} = 3060 \text{ mm}$
Minimum width of a stator tooth:	$w_{st} = 19.7 \text{ mm}$
Stator slot width:	$w_{ts} = 14 \text{ mm}$
Slot useful height of the stator:	$h_{us} = 233.3 \text{ mm}$
Height of the stator yoke:	$h_{StatorYoke} = 72 \text{ mm}$
Inner diameter of the stator yoke:	$D_{inn ys} = 3557 \text{ mm}$
Outer diameter of the stator yoke:	$D_{ext ys} = 3700 \text{ mm}$

The method in [70] does not attempt to compute some outputs that would be interesting for an optimization (like the efficiency, the price of the machine etc.). Additional equations would be needed to define an objective function and to implement an optimization from this model.

II.2.3.4. Semi-analytical method for a 1st order optimization of Induction Machines

For the IM on the TTP specifications, it would be interesting to do an optimization on outputs such as the efficiency and the cost of the machine. Such an optimization could be tried with FE simulations, but as explained in II.2.2.6, only 0 order deterministic methods (II.2.2.2.2) or stochastic algorithms (II.2.2.2.3) would be available. With such methods exploring more than a few parameters would be too long: it is even possible to mathematically demonstrate (see the demonstration in [71]) that with more than 10 discrete parameters to explore, it is not certain that the optimum will be found in a finite computational time using a recursive function. This demonstration can be applied to continuous parameters optimization with 0 order deterministic methods: with 0 order deterministic methods, continuous parameters are explored after being discretized. For that reason, a 1st order optimization would be preferable since it could optimize much more than 10 parameters in a finite computation time.

As explained in II.2.2.2 and II.2.2.4, to do a 1st order optimization an analytical model or a semi-analytical model can be developed. There is also the possibility to pair the 1st order optimization algorithm with a reluctance network. This model needs to be more complex than in [70] to compute more accurately the objective function depending on the efficiency and price of the IM. The model should consider the flux leakage (in the airgap and through the slots). The model should also determine the flux density in the airgap, the rotor induced currents amplitudes and phases through equations and not as inputs. The new model should finally consider the saturation curve of the stator and rotor iron to design machines that reach both the magnetic and electrical limits.

Analytical models able to compute such parameters have already been developed in the past, for example in [55]. Reluctance Network representations of IMs have also been developed: [72]. Creating a reluctance network for an IM is very time-consuming. The rotor currents are induced; to be able to compute them, the temporal behavior of the machine is needed (the EMF (Electromotive Force) on the rotor loops as a function of time are needed). The rotor currents are also MMF (Magnetomotive Force) sources; they also have an impact on the flux going through the network. Therefore, the resolution of the reluctance network for an IM must be iterative. The network would have to be designed to have reluctances parametrized as a function of the rotor position (see E.2, p 187) and MMF sources parametrized as a function of the time (see E.3).

Since a Reluctance Network publicly available for the IM was not found, and since their construction is time-consuming, it was decided to develop further the analytical method from [55]. One considerable advantage of avoiding reluctance networks is that with analytical equations, the number of teeth and poles do not need to be fixed; they do not even need to be discrete. As it will be explained in II.2.3.7.1 and APPENDIX H, p 221, this will allow to explore the set of real machines much faster.

The analytical method obtained is presented in APPENDIX E.

To summarize this method, it uses as inputs the mechanical characteristics of the machine, the terminal voltage, the slip and the properties and price of its materials (like conductivity for the conductors or B(H) curves for the iron sheets). With these parameters, it computes all the outputs, with a per phase equivalent circuit, including the electromagnetic state of the machine, its efficiency, and its price.

In comparison to [55], the model of APPENDIX F was adapted for powerful IMs:

- The stator slots are now rectangular (and not trapezoidal).
- The stator winding is made of bars, with two bars per slot, a number of conductors per bars and a number of strands per conductor (explanation in A.3, p 164).
- This allows for the possibility of fractional winding and reduction of coil span (see A.7 and A.8) that are now considered by the model.
- The rotor slots are also rectangular to allow for a squirrel cage made of copper bars.
- The leakage inductances have been updated (thanks to [73] and [12]) for the new stator and rotor slots geometries and to consider the case of reduced coil span.
- Saturation is now considered with B(H) curves obtained with interpolation of measured B(H) curved on samples. The B(H) measurements were done with an Epstein Frame on samples of iron sheets used by GE.
- The iron losses are computed according to Bertotti's model [74]: as a sum of hysteresis losses, Eddy current losses, and excess losses.
- The flux in the airgap is now determined in an iterative loop. On the first iteration, the airgap flux density is computed from the feeding voltage of the stator. On the following iterations, the voltage drop due to the stator current is considered. Since the stator current depends on the machine saturation, this is done in an iterative loop until convergence. The iterative loops iterate the calculation on the "airgap voltage" until convergence.
- Objective functions were defined to compute the efficiency and the price of the IM.

II.2.3.5. Implementation of the semi-analytical model from APPENDIX F in Cades

The semi-analytical model described in APPENDIX F was coded in Cades (software presented in II.2.2.3). It has 81 inputs and 206 outputs. The loop on the "airgap voltage" (see APPENDIX F) was written as an implicit function in CADES. The harmonic leakage reactance part (see "sigmaNuSPlus" and "sigmaNuSMinus" in APPENDIX F) was written in a C++ function. Cades can deal with Java and C++ codes and still achieves 1st order optimizations by code derivation.

Thanks to Cades, several optimizations were done on different specifications.

These optimizations were mostly done with a Sequential Quadratic Programming (SQP) algorithm. This algorithm is a 2nd order algorithm (as defined in II.2.2.2.2, p 47) available in Cades. But the second derivatives are approximated for faster calculations, so it is comparable to a 1st order algorithm.

The following part and APPENDIX H (p 221) will show the results and give an analysis of an optimization that was done to maximize the efficiency of the IM. The first inputs parameters for these

optimizations were taken from the first analytical sizing given in Table II-3. Constraints were fixed by experience and to specifications of the TTP given in Table II-2.

II.2.3.6. Comparison between the analytical model and finite-element simulations

II.2.3.6.1. Geometry chosen for the comparison

In APPENDIX H, p 221, and in II.2.3.6.2, the optimization results of an IM with the semi-analytical model of APPENDIX F, p 189, will be presented. During the scope of this Ph.D., the maximal dimensions of the machine for the TTP were changed. For APPENDIX H, the maximal outer diameter was set to 5.2 m, the length of the machine to 2.1 m, and the power output to 20 MW. At the beginning, it was tried to size an IM with a maximal outer diameter of 4.5 m, a maximal length of 1.8 m, and a rated power of 22 MW. These dimension constraints were very challenging; the semi-analytical model paired with an SQP algorithm was not able to meet all the constraints. Under these conditions, the algorithm was not trying to optimize the objective function, but simply to verify all the constraints. To verify the semi-analytical model used, it was then tried to reproduce the geometry with FEM on Flux2D for a comparison purpose.

When the design was simulated on Flux2D, the stator currents were too high, and there was a lot of flux leakage. After a few iterations, using a method similar to DOE (see II.2.2.2.4, p 49), the geometrical parameters of the IM were slightly changed so as to maintain the rated power and diminish the reactive power (see APPENDIX G, p 217). As it can be seen there, the semi-analytical model was right that the constraints were not reasonable. The machine saturation was very high. This pushed the semi-analytical model to increase the teeth width. With wide teeth but still the same need for the copper cross section, the optimization led to long slots (as it can be seen in Figure G-1 and Figure G-2). Such a design had a lot of flux leakage and would not be built for mechanical reasons (long teeth could lead to mechanical issues).

Later during the sizing process, a fully-fed synchronous machine (with wounded salient poles) was designed with an outer diameter of 6.04 m and a length of 2.1 m. So, it is not surprising that the constraints of a maximal outer diameter of 4.5 m and maximal length of 1.8 m were too challenging.

Even if the design obtained after the DOE with FE simulations (see Table G-1, p 217 in APPENDIX G) did not meet the constraints initially fixed, it was a good design to compare the two models.

In the following parts, the reader should keep in mind that the comparison is made on an IM that is very saturated and has a lot of leakages. The design for the comparison was pushed beyond what would be normally acceptable to reach the 22 MW rated power. However, the Pareto curves given in II.2.3.7.2, starting p 61, show that it would be possible to design an induction machine within the specifications without such high saturation.

II.2.3.6.2. Magnetizing Inductance comparison between the semi-analytical model and finite-element calculations

In the semi-analytical model, the parameters of the equivalent scheme are determined. The equivalent scheme is then used to compute the power output, the currents, the efficiency, and other characteristics of the machine.

In the FE simulations, the currents, torque and power output of the machine are directly obtained. To compare the FE simulations to the semi-analytical model, the parameters of the equivalent scheme were determined using no-load and blocked rotor tests. These tests and the determination of the equivalent parameters are described in APPENDIX J, p 243.

The no-load and blocked-rotor tests to determine the parameters of the equivalent circuit of the IM were done with 2D FE simulations. With 2D simulations, the effect of the rotor skewing and the end-winding leakage reactance were not considered. Therefore, in the following comparison, the rotor skewing effect and end-winding leakage reactance were withdrawn from the analytical model results.

As explained in J.1, p 243, it is not possible to separate the stator leakage reactance X_S from the magnetizing reactance X_m with a no-load test. Figure II-5 shows a comparison of the sum of the magnetizing reactance and the stator leakage reactance ($X_m + X_S$) depending on the stator voltage between the FE simulations and the semi-analytical model of APPENDIX F. The parameters of the machine used for this comparison can be found in Table G-2.

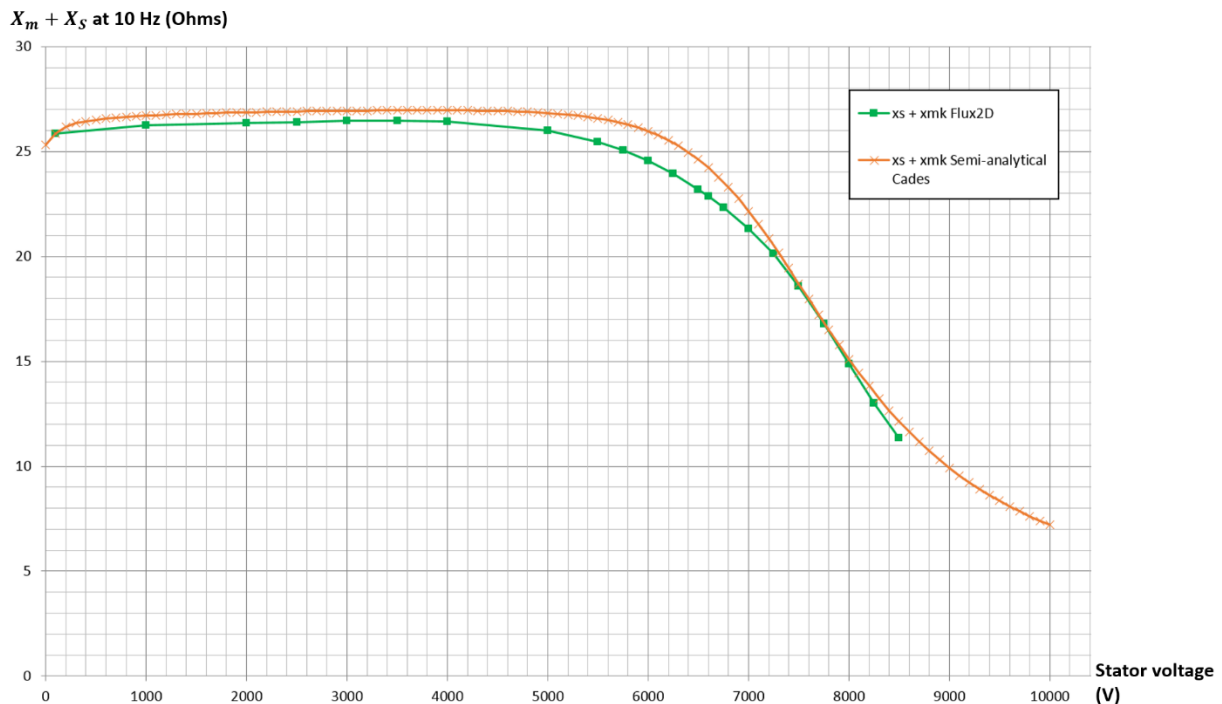


Figure II-5: Comparison of the sum of the magnetizing reactance and the stator leakage reactance $X_m + X_S$ between the semi-analytical model and FE2D simulations. The IM used for this comparison was obtained in APPENDIX G after a DOE with FE simulations. It is designed to operate at a nominal stator voltage of 6600 V

In the electrical circuit, the magnetizing inductance represents the part of the stator current that is wasted to magnetize the machine. Without saturation, it represents the stator current needed to magnetize mostly the airgap and the iron a bit. When saturation appears, more current is needed to magnetize the iron, the magnetizing current increases and the magnetizing inductance drops. The

leakage inductance is mostly unaffected by saturation (and so by the stator voltage). Figure II-5 shows that without saturation, the sum of the magnetizing reactances and stator leakage reactance of the two models are almost equal. The same can be said after the saturation knee in the saturated part. It is in the saturation knee that the difference between the two models is the most noticeable. Saturation in Flux2D appears slightly before saturation in the semi-analytical model. This can be explained by small saturation that appears locally in the teeth in the FE2D model. There is no such saturation in the analytical model where the flux density is considered uniform in the equations. If it was needed, the model could be further improved with a method more intricate on the flux paths in the machine and the leakage reactances. In this respect, reluctance networks (see APPENDIX E and II.2.2.4) seem to be adequate to keep a derivable semi-analytical model. The drawback is that a reluctance network will not be able to investigate as many machines as the semi-analytical model presented (to create a reluctance network, the number of poles and number of slots must be fixed, the set of imaginary machines to explore is reduced with reluctance networks, see II.2.3.7.1 for explanations on imaginary machines).

In both models, saturation starts around 5000 V. The machine was designed to work at 6600 V which is a bit far in the saturation knee (as stated at the beginning of this chapter, the teeth of this machine are heavily saturated in load scenarios). This machine was kept for a comparison purpose, but if a machine had to be chosen for the real project, a less saturated machine under load mode would be chosen (one shown in the Pareto curves given in II.2.3.7.2, p 61 for example).

The magnetizing inductance is a very important parameter in the equivalent scheme. With the resistances (that are far easier to obtain), the slip and the voltage imposed, it is one of the parameters that will mostly drive the torque and the efficiency of the IM (the leakage reactances are small in comparison to the magnetizing reactance). Since the machine should be operated in the saturation knee, to reach the magnetic and electrical loading simultaneously, the magnetizing reactance in the saturation knee needs to be accurate. To conclude, Figure II-5 shows that the magnetizing inductance is well approximated by the semi-analytical model, even in the saturation knee where the error is still inferior to 5 %.

With this part and Figure II-5, it has been verified that the semi-analytical model was giving correct results for one geometry. It will now be possible to use it for further optimizations of the IM on the TTP specifications.

II.2.3.7. Results of 1st order optimizations with Cades of an Induction Machine on Typical Tidal Project specifications

As a summary of the optimizations, according to the analytical model, the efficiency of the IM designed and presented in Table II-3, from the method in [70] was around $eff = 90.5\%$ with a power factor of $cos\Phi = 0.277$ and a rated power $P_u = 4.8 MW$.

The optimization on Cades using the semi-analytical model described in APPENDIX F, showed that it was possible to improve the design to reach efficiencies over 97%, with a power factor meeting the $cos\Phi = 0.8$ constraint, and a rated power meeting the $P_u = 20 MW$ constraint.

II.2.3.7.1. Imaginary or real machines

The concept of imaginary machines was introduced in [75] with the notion of imaginary Pareto fronts. It is a powerful tool for the definition of the “right formulation of the constraints” during the “optimization problem setting”.

The idea behind the concept is to use the continuity of semi-analytical models based on equations. For real machines, some input and output parameters should be discrete; for example, the number of poles, the number of slots, the number of parallel paths, etc. However, the models based on equations do not need discrete values as inputs. The semi-analytical model of APPENDIX F can compute the efficiency of an IM with for example 16.65 pole pairs and 465.22 slots. These machines will be referred to as imaginary machines: they do not have a physical meaning, they are not possible to manufacture.

Some parameters of real machines should be discrete because of their physical meaning: number of poles, number of slots, number of conductors in series, number of parallel paths. Some parameters of real machines should be discrete for technological or commercial reasons: for example, the strands size. It could be physically possible to manufacture conductors with strands of any size, but there is a limited quantity of strand sizes commercialized. The same goes for the iron sheets width. Another example for small machines would be the outer diameter that can also be imposed to discrete values for commercial reasons.

Even if imaginary machines cannot be manufactured, 1st order optimization processes based on derivatives will work on these imaginary machines. Without these imaginary machines as intermediaries, the optimization processes would need to launch optimizations on all the possible combinations of discrete parameters to be sure to find a global optimum. Depending on the number of discrete parameters and the values they can take, this could lead to a combinatorial explosion of the optimizations to be carried out.

The imaginary optimums are useful to determine whether the set of constraints accepts a solution and give an idea of what can be expected. Indeed, the set of real machines is a subset of the set of imaginary machines: the real machines are part of the set of imaginary machines. After finding an optimum with imaginary machines, it will be much easier to find an optimal real machine close to the imaginary optimum and avoid the search through all the possible discrete parameters combinations. This process is explained in APPENDIX H, p 221.

An example of the optimization process from imaginary machines to real machines for given specifications is also presented in APPENDIX H, p 221. Table H-1 gives the inputs of the optimization for the first and the last iterations of the last step. Table H-2 gives the outputs for the first and the last iterations of the same step.

II.2.3.7.2. Pareto curve and parametrized optimization: maximal efficiency depending either on saturation or on the length of the design

The concept of Pareto curve was presented in II.2.2.2.1 and shown in Figure II-2, p 47. With two objectives, the Pareto line shows all the possible combinations where the two objectives cannot be jointly improved; the improvement of one objective leads to the deterioration of the other. Another concept presented here is the parametrized optimization. It can be interesting to see the best optimum

of an objective function depending on the value of a parameter, for example, to visualize the impact of one or two constraints on the optimum that can be reached.

Figure II-5 showed that saturation in the semi-analytical model was appearing a bit later than in Flux2D. An important element in the sizing and optimization process is to reach the magnetic and electrical limits simultaneously. Since saturation in the semi-analytical model is appearing a bit too late, it is interesting to see what would be the optimal machine found by the 1st order optimization depending on the machine saturation. To do so, a parametrized optimization curve of the maximal efficiency of the machine as a function of the flux density in the teeth is plotted in Figure II-6.

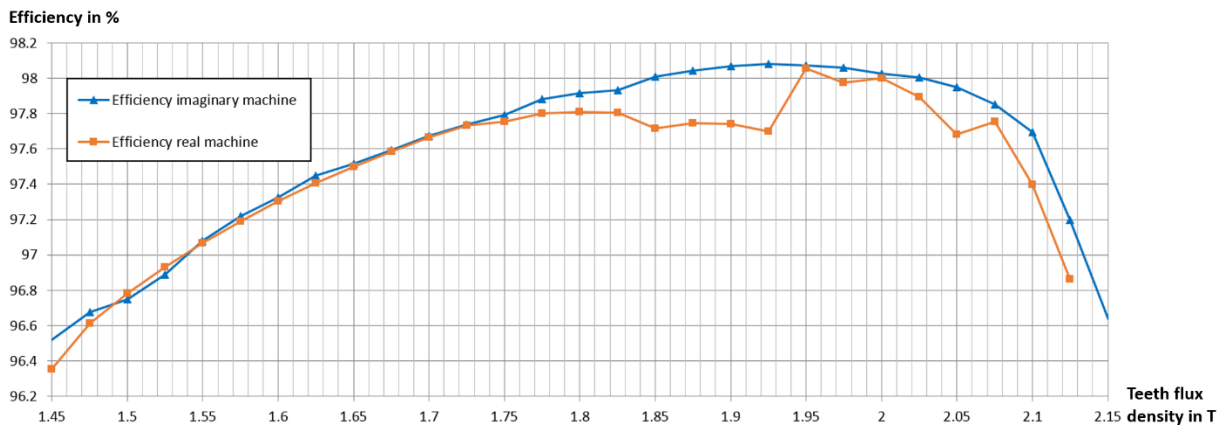


Figure II-6: Parametrized optimization: maximum efficiency reached after each optimization as a function of the imposed teeth flux density for the specifications of the TTP

The parametrized optimization in Figure II-6 was plotted for imaginary and real machines. As explained in APPENDIX H, parametrized optimizations or Pareto curves for imaginary machines are much faster to obtain than the ones for real machines. Figure II-6 shows that the parametrized optimization for imaginary machine already gives a very good idea of what can be expected for real machines. For the parametrized optimization for imaginary machines, the feeding voltage was fixed to 6600 V. For real machines, the feeding voltage was set as a degree of liberty under 6600 V to adjust for the difference in number of poles, slots, turns in series, and parallel paths.

Figure II-6 also shows that if the optimization algorithm was set without constraints on the maximum flux density, it would lead to designs with optimum efficiencies for teeth flux densities in the range of 1.9 T. This flux density would be much higher than usual designs for hydro machines that are generally in the range of 1.6 to 1.7 T in the teeth. We should also remember that, since the semi-analytical model is slightly under-estimating the beginning of the saturation knee (refer to Figure II-5), the efficiency of the parametrized optimization probably starts to decrease a bit too late. In Figure II-6, it starts to decrease after 1.95 T, and it might start to decrease after 1.85 if the saturation knee was perfectly right.

On the other hand, if the maximal teeth flux density is fixed to 1.7 T, the loss in efficiency is small (efficiency with teeth flux density fixed to 1.7 T: $\eta_{optimum1.7T} = 97.7\%$, with teeth flux density fixed to 1.9T: $\eta_{optimum1.9T} = 98.1\%$). For that reason, the design that was selected from the parametrized optimization of Figure II-6 was the design where the teeth flux density is fixed to 1.7 T. With this design, the efficiency is still high: around 97.7 %, and the local saturation in the teeth should not be too high. All the input and output parameters of this design are given in Table H-1 and Table H-2, p 226 and 227 in APPENDIX H.

Another interesting information that can be visualized with a Pareto curve is the impact of the volume or the size of the machine on the optimum that can be reached. It is clear that the bigger the machine, the higher the optimum efficiency should be. With a bigger machine, it is possible to either diminish the flux density or the current density in the machine. But the question: “to what extent does the volume of the machine impact the maximum efficiency?” is a tough question to answer without a Pareto curve. Figure II-7 shows the Pareto curve of the maximum efficiency depending on the length of the machine. This curve was done only for imaginary machines, however, such a curve with real machines would look approximately the same (but would take much longer to create).

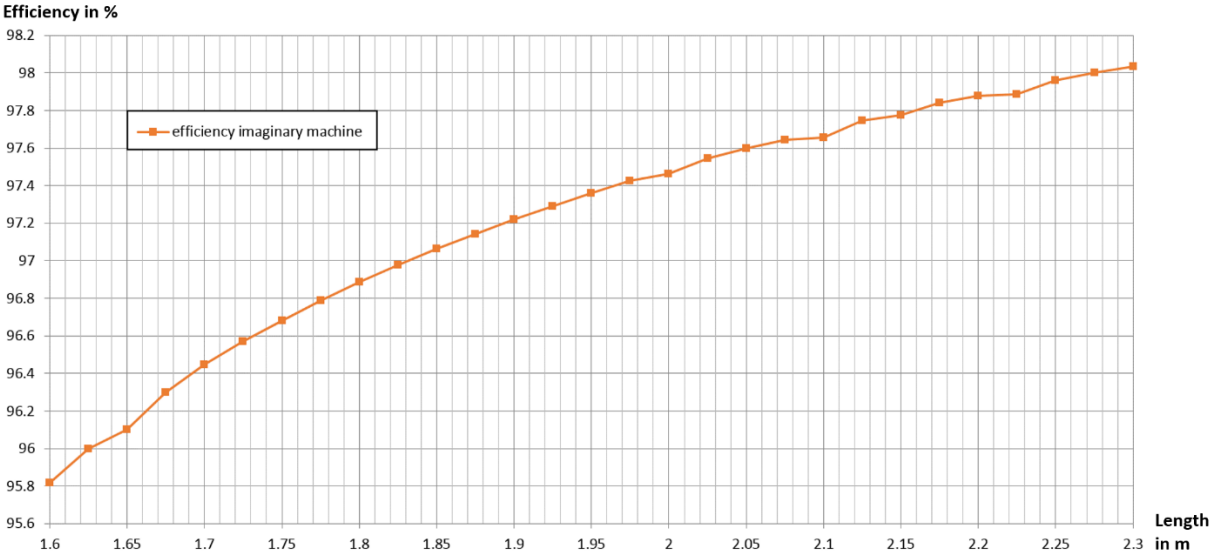


Figure II-7: Pareto curve: maximum efficiency reached after optimizations as a function of the maximum length of the machine for the specifications of the TTP and for a maximum flux density in the teeth of 1.7 T

With Figure II-7, it is possible to assess the impact of the length of the machine on the maximum efficiency to be expected. According to the specification of the TTP given in Table II-2, p 53, the maximal length of the machine should be 2.1 m. Figure II-7 shows that if it was possible to make a machine 0.2 m longer, the efficiency could be increased by about 0.4 % (from 97.6 % to 98 % with the imaginary machines). On the contrary, with a design 0.3 m shorter, the efficiency would be about 0.7 % lower. As a side note, the Pareto curve in Figure II-7 is given for lengths between 1.6 and 2.3 m. Of course, it could have been possible to explore farther on the upper side. On the contrary, it was not possible to explore much lower than 1.6 m, under this length, the optimization algorithm was hardly finding any geometry meeting all the constraints (in particular, the power factor, the rated power, the maximum current density, and the outer frame diameter).

In every efficiency optimization, the machine diameter and length (d_{Out} and l) went to their maximum constraint: $d_{Out} = 5.2 m$ and $l = 2.1 m$. This is not surprising since increasing the copper and iron sheets size diminishes the losses. To decrease the rotor resistance, the maximal width of the copper short-circuit ring was also reached in every optimization ($ban = 0.1 m$).

The algorithm also diminished the airgap radial width to the minimum width specified ($wGap = 0.01 m$). This is not surprising neither: when the airgap radial width diminishes, the magnetizing current diminishes too. The minimum airgap radial width is generally set by mechanical and production limits. Decreasing the airgap radial width also increases the iron losses due to the teeth harmonics, but the analytical model does not take these losses into account.

This work will not go deeper into the many questions that can be quickly answered by Pareto curves obtained from imaginary machines computed with a semi-analytical model with 1st order optimizations. With such a tool, the following questions should find visual and interesting answers: What is the best number of poles for a fully-fed machine? Is it better to go for a high number of poles and high frequencies or a small number of poles and low frequencies? With a good speed reducer, when the rated rotation speed is a degree of liberty, what is the optimum rotation speed? What is the impact of the power factor constraint on the efficiency or the size of the machine? What is the impact of the airgap radial length on the performance of the machine? What is the impact of the temperature on the efficiency of the machine? And this list could keep growing for many pages with the reader's imaginations.

II.3. Limits to apply the previous methods to the new kind of doubly-fed machines

II.2 presented different methods to size and optimize electrical machines. Analytical methods for sizing and semi-analytical methods using optimization algorithms for optimization were talked about. Reluctance Networks were presented as a possible improvement over semi-analytical methods used for optimization. FEM was the most accurate and the slowest of all the models presented, especially for optimization.

II.2.3 gave an example of the design of an IM for the specifications of the TTP. This example used an analytical method for the first sizing. The design was then improved with an optimization thanks to a semi-analytical model. Finally, iterative FE simulations could be used to fine-tune some of the characteristics of the IM.

The following part will investigate existing methods, like the one used in II.2.3, to design a BDFM or a BDFRM.

II.3.1. Empirical knowledge for a first sizing

After the design of prototypes in laboratories, some empirical knowledge was reported in the literature. Methods were developed to optimize some parameters of the BDFM. A lot of these developments were done for the BDFM with wound rotors. These kinds of rotors were described in [32] (see Rotor 6 in I.5.3.5.3) where it was highlighted that they are less performant (in terms of torque and efficiency) than nested-loop rotors. This was explained in [32] by the fact that in wound rotors, the resistance is higher than in nested-loops rotors. Despite its lower performance, a wound rotor is easier to manufacture for a prototype or a low power BDFM than a copper nested-loop rotor. Moreover, the wound rotor windings are analogous to the stator windings and are easier to study analytically, so easier to optimize than nested-loop.

A wound rotor for a BDFM is made of two rotor-windings that are linked electrically. Each rotor winding is made to match the number of poles of the fundamental of one stator winding. In [76], the optimum value of rotor turns ratio was analytically determined with considerations on the power output depending on the electrical and the magnetic loading. In [77], building on a rotor designed with the rotor turns ratio specified in [76], the authors proposed an iterative analytical method to optimize four stator quantities (the slots area and the number of turns per coil of two stator windings).

Some sizing tips are not bound to BDFM with wound rotors. For example, in [50], using geometrical considerations, a formula is proposed to compute the cross-coupling factor of the two stator windings depending on the number of poles of each winding and of the rotor loop span. This formula is presented in IV.3.1.3, in equation (96), p 130 during the first sizing of a BDFM on the specifications of the TTP.

For further information on how to do the first sizing of a powerful BDFM with nested-loop, the reader can refer to the dedicated CHAPTER IV.

II.3.2. Semi-analytical models to be paired with a 1st order optimizations do not exist yet

As already stated in I.5.3.2, p 20, some (semi-)analytical models of the BDFM can be found in the literature: a coupled-circuit model in [31], a d-q and reduced d-q models in [32], and an electric equivalent circuit model in [32].

II.3.2.1. Limits of the coupled-circuit model

In [31], the coupled-circuit model was developed for one BDFM prototype specifically and did not address leakage reactances. The model was improved in [32] to compute some of the leakage inductances and to be generalized to different BDFM designs. The assumptions of this model are:

- The stator and rotor iron are considered to have an infinite permeability.
- The flux lines in the airgap are radial.
- The airgap is “smooth” with a cylindrical stator and a cylindrical rotor (the tooth effect is neglected). The airgap radial length is computed with Carter’s Factor.
- The conductors have a zero depth and a finite width.
- The leakage effect is added with self-inductance terms only.

In this model, considering every coil of the two stator windings and the rotor nested-loops, all the mutual and self-inductances are computed. With all these inductances and with all the resistances, it is then possible to solve the circuit equations with the two stator voltages as inputs for example. In [32], the mutual inductances are computed with Fourier series or by direct integrations. It is important to note here that the mutual inductances depend on the rotor position. In order to solve the coupled-circuit model for a new rotor position, the inductances will have to be computed again.

This method is useful to learn more about the harmonic content in the BDFM, especially to learn about the creation of the harmonics responsible for the interaction between the two stator windings. But this method is not able to consider the magnetic saturation. This is a major drawback if the goal is to design a semi-analytical model for optimization. As already stated in II.2, during the sizing of an electrical machine, an important point is to reach the limits of the electrical loading and the magnetic loading simultaneously. If a model does not give information on the magnetic loading, it will not be able to reach these two limits at the same time.

II.3.2.2. Limits of the d-q model

The d-q model developed in [32], solves the rotor position problem of the coupled-circuit model. To do so, the coupled-circuit model is transformed into the rotor reference frame (a frame which rotates at the same speed as the rotor). All the assumptions of the coupled-circuit model presented in II.3.2.1 are kept in the d-q model.

The d-q model will be faster than the coupled-circuit model to deal with rotor rotation, but it will still have the same drawback of not considering the magnetic saturation.

As explained in II.3.2.1, a model that does not consider saturation will not be able to optimize a BDFM to reach the magnetic loading and the electrical loading simultaneously.

II.3.2.3. The equivalent circuit

The equivalent circuit model of the BDFM was already presented in Figure I-11, p 36. With this model, the steady states of the BDFM can be simulated to study power flow, currents, and voltages. In [32], the author describes how to extract the parameters of the equivalent circuit from the d-q model. This leads to an equivalent circuit slightly different from the equivalent circuit of Figure I-11, where the position of the rotor was considered (see Figure II-8).

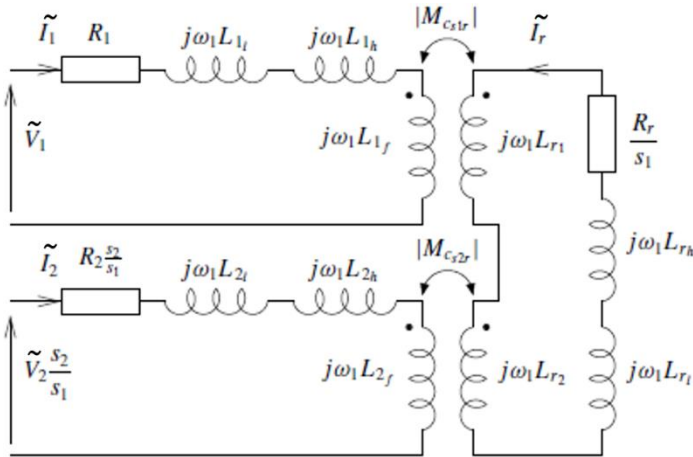


Figure II-8: Per phase equivalent circuit of the BDFM with a mutual inductance representation from [32]

With: R_1 and R_2 are the stator PW and CW resistances.

ω_1 is the stator PW pulsation.

s_1 and s_2 are the stator PW and CW slips.

L_{1l} and L_{2l} are the stator PW and CW leakage inductances.

L_{1h} and L_{2h} are the stator PW and CW harmonics inductances.

L_{1f} and L_{2f} are the stator PW and CW fundamental inductances.

L_{r1} and L_{r2} are the rotor inductances that link with the stator fundamentals.

L_{rl} and L_{rh} are the rotor leakage and harmonics inductances.

M_{cs1r} is the mutual inductance between the PW and the rotor nested-loops.

M_{cs2r} is the mutual inductance between the CW and the rotor nested-loops.

To consider the rotor position, the voltages and currents of the equivalent circuit are shifted with the phases of the mutual inductances with the rotor:

$$\begin{aligned}\tilde{V}_1 &= V_1 e^{j\angle M_{cs1r}} & \tilde{V}_2 &= V_2 e^{j\angle M_{cs2r}} \\ \tilde{I}_1 &= I_1 e^{j\angle M_{cs1r}} & \tilde{I}_2 &= I_2 e^{j\angle M_{cs2r}} \\ \tilde{I}_r &= I_r\end{aligned}$$

As for the IM with the semi-analytical model of APPENDIX F, an equivalent circuit with parameters computed by a semi-analytical model could become a powerful tool for the optimization of a BDFM.

The method to develop the equivalent circuit in [32] does not consider saturation. For the same reason already explained in II.3.2.1 and II.3.2.2, saturation needs to be considered to develop a complete optimization tool that reaches the magnetic loading and electrical loading at the same time. Saturation of the BDFM is especially difficult to consider since it is due to the addition of two magnetic fields with different numbers of poles and different frequencies.

In III.3, starting p 85, a new equivalent circuit will be developed for the BDFM. The results differences between the new equivalent circuit and the equivalent circuit from [32] presented in Figure II-8, will be shown in the figures of part III.3.6, starting p 100.

II.3.2.4. Reluctance Network

The leakage inductances of an IM play an important role in the operation of the machine. In particular, they have a major impact on the magnetic loading. Saturation in a BDFM is harder to predict than the one of an IM. Since the two stator fields have a different number of poles, in some regions of the BDFM, the flux densities of these fields will be in the same direction and add up. In other regions, they will go in opposite directions and subtract from each other. The reluctance network representation of the BDFM would probably be more accurate for the leakage and harmonic inductance determination. The reluctance network could also help to better determine saturation and to include saturation in the magnetizing inductance of each stator winding.

In [40], a reluctance network was developed for a BDFRM. Figure II-4, and Figure E-2 show how the tooth and the airgap were represented in this reluctance network. Figure II-9 shows how the rotor representation was developed.

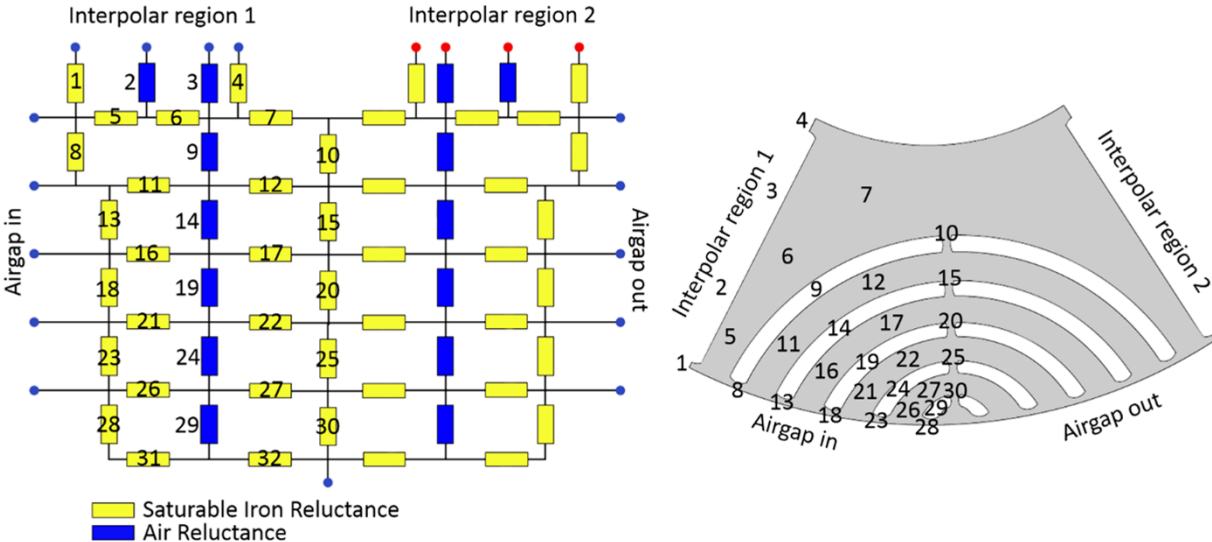


Figure II-9: Rotor representation of the BDFRM with a reluctance network, from [40].

The reluctance representation of the stator and the airgap developed in [40] does not need to be changed to develop a reluctance network for the BDFM. As explained in I.5.3.5, the stators of the BDFM

and BDFRM are similar. This is not the case for the rotors. For the BDFM, the rotor reluctance network representation would be analogous to the stator representation. The difficulty would be to impose the MMF sources of rotor nested-loops (as for the reluctance network representation of an IM, see II.2.3.4). The induced currents in the nested-loops will depend on the FEM in each loop, so they will depend on the time derivative of the flux passing through the nested-loops. To compute the time derivative, the reluctance network airgap would have to be designed to allow for the rotation of the rotor (as explained in E.2, p 187). Since the flux passing through the nested-loops is also dependent on all the MMF sources of the network, the calculation of the MMF sources will have to be an iterative process. In [37], a nodal-based magnetic equivalent network of a BDFM is presented for a simple geometry and gives promising results.

A reluctance network would probably be more accurate than the semi-analytical model adapted from APPENDIX F for the IM. The drawback would be that it is hard to design a reluctance network without fixing some parameters. For example, the reluctance network in [40] fixed the number of poles, the number of stator and rotor teeth and the number of flux barriers of the BDFRM to be optimized. This reduces the number of parameters an optimization software can explore.

In some cases, it could be interesting to have two semi-analytical models:

- A first one, like the one developed in APPENDIX F for the IM, would help to fix the ideal number of poles for the two stator windings and for the rotor. It would also fix the number of stator and rotor teeth.
- A reluctance model would then optimize the other parameters with more accuracy than the first model would have been able.

This would be especially interesting for the BDFM and BDFRM. For example, when the mechanical speed and the grid frequencies are imposed, the total number of poles ($P_g + P_c$) is known and imposed by the natural speed (see equation (36), p 34). The repartition of the total number of poles between P_g and P_c is then a much tougher question: it will impact the cross-coupling, saturation, and the iron losses. Some empirical knowledge has been gathered in the literature with prototypes of a few kW ([77], [78], and others) up to 250 kW [51] that have been built. For a larger BDFM with a higher number of poles, having an optimization software able to take this decision before using a reluctance network to optimize the other parameters with more accuracy could lead to very good results.

II.3.3. Finite-element methods: for experimental research plan. FE simulations are much more time consuming for a BDFM than for usual rotating machines because of the different frequencies of the stator windings

FE models were also investigated, for example in [33], [34], and [35]. In [36], a special magneto-static application for BDFM that was developed in [35], was used in an optimization perspective.

As explained in II.2.2.6, FEM do not allow to compute the derivatives of an objective function depending on every input. They cannot be used with 1st order optimization algorithms. FEM can be used with DOE for optimizations (see II.2.2.2.4), but as explained, with this method the number of parameters that can be investigated is limited.

FE simulations are generally implemented on special software. As told in II.2.2.6.2, for this work, FE simulations were mostly implemented on Flux2D.

Flux2D, like many other FE software, offers solutions for faster simulations. For example, it is possible to use symmetries to do the simulations on a part of the electrical machine geometry. Thanks to these symmetries, many simulations of electrical machines only need one pole representation which saves a lot of time. When doing steady-state simulations, it is also possible to use a magneto-harmonic application that only considers the fundamental harmonic. This application only takes one solving iteration. On the contrary, time-stepping application (magneto-transient in Flux2D) can take hundreds or thousands of iterations.

One particularity of the BDFM and BDFRM is their two stator windings. As presented in I.5.3.4.1, the two windings have different frequencies and numbers of poles. The number of poles of the rotor is also different.

In many cases, the different number of poles prevent from using symmetries. For example, a BDFM with 12 poles for the grid winding and 6 poles for the control winding would have $\frac{12+6}{2} = 9$ rotor nests. With such a configuration, it would not be possible to define a symmetry. Sometimes it is possible to get a symmetry over half the machine, but rarely more. The BDFM or BDFRM simulations using FE are inherently heavier than usual electrical machines simulations.

The different frequencies of the two windings prevent from using the magneto-harmonic application of Flux2D that only works with one fundamental frequency. To use the magneto-harmonic application, one winding should get short-circuited or opened. This is a huge drawback for the fast computation of the steady states of a design, to get the influence of one parameter using a DOE for example (refer to II.2.2.2.4, p 49 for more information about DOEs).

Moreover, transient simulations of a BDFM for steady states can be much heavier than transient simulations of usual machines. In fact, transient simulations are generally launched on an electrical period with a time-step defined by the highest harmonic frequency to be studied. The electrical periods of a BDFM can be much longer than the electrical periods of usual machines: with two windings with different frequencies, an electrical period will be the shortest amount of time needed for the two frequencies to accomplish an integer number of periods. For example, a usual machine is fed with 50 Hz and has a 0.02 s period. For a BDFM, if the grid winding is operated at 50 Hz and the command winding at 7.5 Hz for example, the electrical period of the BDFM will be 0.4 s. In 0.4 s, the command winding will accomplish 3 periods and the grid winding 20 periods. In mathematical terms, this would be the least common multiple of the period of each winding. Of course, some CW periods do not even lead to a least common multiple with the PW periods.

II.4. Conclusion

In this chapter, three different kinds of models or methods used for simulating and sizing electrical machines were identified:

- Analytical models: they can be fast but will suffer from inaccuracies, due to nonlinear behaviors like saturation for example. They are helpful to understand the basics behind each technology and thus are often used in university courses and are described in the literature.
- Semi-analytical models: they try to take nonlinear behaviors into account. They can result from complexification of existing analytical models, or take other forms, as reluctance networks for example. Most of these models are still considered to be fast, but they demand time and expertise to be developed. If these methods are derivable, they can become powerful tools when paired with 1st order optimization algorithms.
- Numerical methods: they are heavier from a computation point of view in comparison to the previous models, but they are generally more accurate. FE methods are examples of numerical methods. With specific software developed for these methods, they are generally easier to manipulate than the previous models for the study of electrical machines. These methods are not derivable and cannot be paired with 1st order optimization algorithms like semi-analytical models.

The difference between sizing and optimizing was explained. Analytical and semi-analytical models can be used for sizing. Sizing implies that there are still many parameters that need to be fixed by the designer as a starting point. These parameters are then used by the model to compute the outputs parameters. Optimization implies that an algorithm will try to improve some parameters (inputs or outputs) based on constraints and on the result of an objective function. With the addition of an objective function, the same analytical and semi-analytical models used for sizing can be used for optimizations. If the models are derivable, the optimization software can be a 1st order algorithm; it will then use the derivatives. 1st order optimization algorithms can be much faster and explore more parameters at once than algorithms not relying on derivatives. Numerical methods can also be used for optimizations, but these models are generally not derivable. For optimization, the gain in accuracy of FE simulations is balanced by the loss of rapidity. Moreover, FE optimizations cannot have as many degrees of liberties (less than 10) as semi-analytical optimizations (hundreds or even thousands).

The message here is not that a semi-analytical model paired with an optimization algorithm is superior to any other solutions. In the best-case scenario, different models are needed depending on the advancement of the design process. In the beginning, when a lot of parameters are undefined, having a model able to consider quickly all the possibilities is more important than having a very accurate model. Then for more advanced design, when many parameters are fixed and only a few need to vary, it becomes important to switch to a more intricate and accurate model.

As an example of how these methods and models can work together, an IM was sized according to the specifications of the TTP (Typical Tidal Project). A first sizing design was done with an automatized iterative analytical method found in the literature and coded in MATLAB. This first sizing

was then used as the starting point of a 1st order optimization. This optimization was an SQP algorithm paired with a semi-analytical model developed in Cades to be both derivable and consider saturation. Finally, using more accurate FE simulations, it was possible to verify and adjust some parameters of the design.

The semi-analytical model showed that the initial specifications of the TTP were too restrictive on the machine size. This was confirmed by FE simulations: the optimized IM, according to these specifications, was operating at too high electrical and magnetic loadings. This had led to a design that would not pass mechanical requirements with long and thin stator teeth.

Nonetheless, the semi-analytical model showed some promising abilities. The accuracy of this model was verified with a comparison with FE2D simulations on the magnetizing inductance depending on saturation (and one load test which was not presented in this chapter). The powerful concepts of imaginary machines and Pareto curves were presented. Imaginary machines are machines where the discrete parameters are linearized. They do not have a physical sense (for example a machine with 3.5 poles does not make any physical sense), but the set of imaginary machine is easier to explore with a 1st order optimization algorithm than the set of real machines. With imaginary machines, it is also possible to quickly find out whether a problem has a solution or not: is it “well-posed” or not? In some cases, the specifications are impossible to fulfill, the problem is “ill-posed”. If the set of solutions is null for imaginary machines it is not worth trying to find a solution in the set of real machines: the set of real machines is included in the set of imaginary machines. Imaginary machines can then help to quickly find which constraint should be released to define a problem with solutions. The imaginary machines also allow to plot Pareto curves and parametrized optimizations curves much faster than with real machines. These Pareto curves and parametrized optimizations curves can help to visually answer tough questions during the design and optimization process. Finally, the imaginary machines help to find the discrete parameters to launch the optimizations for real machines. It was then possible to use the semi-analytical model with a 1st order optimization algorithm to explore the set of imaginary machines and find optimums that could not be found with iterative explorations with FE2D simulations. In APPENDIX H, the method to go from imaginary machines to real machines was presented. In this chapter, it was shown with parametrized optimizations that the optimums reached by real machines were close to the optimums reached by imaginary machines.

Even if it was already giving satisfying results, the semi-analytical model that was presented could still be improved. Especially for the computations of the leakage reactances, for the flux conservation (the flux leakage is not considered), and for local saturation. For example, a reluctance network could be implemented, but this would diminish the set of imaginary machines that can be studied (the reluctance network is based on a geometry that should make physical sense).

Finally, after the sizing example of the IM machine, it was interesting to see whether and how a similar process could be applied for the BDFM.

Analytical sizing tips were found in the literature and will be used in CHAPTER IV for a first BDFM sizing on the specifications of the TTP. Some of the analytical tips that were found apply for the BDFM technology with a wound rotor. These wound rotors lead to machines that are less powerful and less

efficient but are easier to study analytically and to manufacture, especially in the power range from kilowatts to dozens of kilowatts.

Some complete analytical models were also found in the literature. In general, they did not consider saturation. Saturation in a BDFM is harder to evaluate because of the interaction of the two magnetic fields of each stator winding. A complete semi-analytical model, derivable to be paired with a 1st order optimization algorithm is not available in the literature and will be hard to create.

Finally, BDFM optimizations with FE methods were found to be more challenging than for usual machines. Indeed, the BDFM stator windings and nested-loop rotors limit the use of symmetries that generally reduce the problem size by several-folds for usual machines. Furthermore, it is not possible to study steady states of a BDFM with dedicated applications that only consider the fundamental frequency. In fact, a BDFM uses two stator windings with a different frequency for each. To further complicate matters, a BDFM has longer electrical periods because of these two different frequencies.

Because of all the factors mentioned above, steady states simulations of a BDFM using transient FE applications take much longer than usual electrical machines steady states simulations. The IM magneto-harmonic iterative simulations, done in APPENDIX G, were only taking a few minutes each. For a BDFM, transient simulations would probably take more than a day each.

To conclude, processes for rapid and accurate optimizations of a BDFM do not exist yet. Especially for a nested-loop BDFM. Some concepts were highlighted in this chapter or can be found in the literature but still need further developments. In CHAPTER III, some tools will be developed to enable the sizing and optimization of a BDFM. Such a sizing will then be presented in CHAPTER IV. It would be interesting to develop a semi-analytical model of the BDFM that would determine the parameters of the equivalent scheme (like the semi-analytical model of the IM in APPENDIX F). It would also be interesting to explore methods for faster FE simulations of the BDFM.

CHAPTER III. METHODS AND TOOLS DEVELOPED FOR THE DESIGN AND THE OPTIMIZATION OF THE BRUSHLESS DOUBLY-FED INDUCTION MACHINE

III.1. Introduction.....	75
III.2. Verification of analytical results and better understanding of the BDFM thanks to harmonic analysis with FE magneto-transient simulations.....	76
III.2.1. Geometry of the BDFM used for the FE magneto-transient harmonic analyses.....	76
III.2.2. Results of the BDFM FE magneto-transient harmonic analyses	78
III.2.2.1. The cross-coupling effect of the rotor nested-loops.....	78
III.2.2.2. Influence of the rotor position	81
III.2.2.3. Saturation impacts on the BDFM harmonics and power flow	84
III.3. New equivalent circuit model developed for the BDFM.....	85
III.3.1. Reasons to develop a new equivalent circuit model of the BDFM	85
III.3.2. From the equivalent circuit of the IM to the equivalent circuit of the BDFM	86
III.3.2.1. Starting from the equivalent circuit of an Induction Machine with a mutual inductance representation and access to the rotor terminals.....	86
III.3.2.2. Transformation from the mutual inductance representation to the transformer representation.....	88
III.3.2.3. Fusion of the per phase equivalent circuit of the two IMs representing the PW and CW to obtain the BDFM equivalent circuit. To merge the two representations, the rotor frequency must be equal in the two circuits.....	91
III.3.2.4. Mathematical tricks to get the equivalent circuit of the BDFM expressed with the pulsation ω_1	94
III.3.2.5. Expression of the equivalent circuit in the power winding reference frame: topology of the new model	96
III.3.3. Determination of the equivalent circuit parameters with electrical tests inspired by a common method used for induction machines	97
III.3.4. Implementation in a 1 st order analytical optimization software (CADES) of the method to determine the equivalent parameters.....	98
III.3.5. Taking saturation and iron losses into account in the equivalent scheme	99
III.3.6. Results comparison between the new model, previous models, and FE methods	100
III.4. Development of a fast model: FE based coupled-circuit method, using the expressions of the mutual inductances as functions of the rotor position.....	104

III.4.1.	An FE based method inspired by the analytical coupled-circuit method	104
III.4.2.	Advantages and disadvantages of the FE based coupled-circuit method over the analytical coupled-circuit method.....	105
III.4.2.1.	Advantages	105
III.4.2.2.	Disadvantages.....	105
III.4.3.	Validation of the FE based coupled-circuit method and applications in this work.....	106
III.5.	A model that considers saturation based on FE magneto-harmonic simulations	107
III.5.1.	Principles of FE magneto-harmonic simulations in Flux2D	107
III.5.2.	Computation of the equivalent permeability.....	108
III.5.3.	Idea to use FE magneto-harmonic simulations with two different frequencies.....	111
III.5.4.	Magneto-harmonic simulations for the BDFM technology, a method to compute the mutual interactions	111
III.5.4.1.	Two magneto-harmonic simulations with one frequency each to emulate a magneto-harmonic simulation with two frequencies.....	111
III.5.4.2.	Comparison of the FE magneto-harmonic method on a non-saturated load scenario with the FE based coupled-circuit method and FE magneto-transient method	112
III.5.5.	Saturation consideration in the new magneto-harmonic method with two sources at different frequencies.....	113
III.5.6.	Summary of the iterative process of the magneto-harmonic method for the BDFM with saturation	115
III.5.7.	Comparison of the magneto-harmonic method developed for the BDFM with magneto-transient simulations.....	115
III.6.	Perspectives towards a complete semi-analytical model of the BDFM to implement optimizations with a 1 st order algorithm.....	117
III.7.	Conclusion	118

III.1. Introduction

In CHAPTER I, specifically in I.5.3.4.3 and I.5.3.4.4, the interactions of the two stator windings of a BDFRM was explained with mathematical expressions of the harmonics created by the rotor saliency. In a BDFM, the rotor windings will have the purpose to create the same harmonics as the rotor saliency of a BDFRM. To do so, the rotor windings will have to verify specific conditions, as determined in I.5.3.5.1, and expressed in equations (33) or (34). To meet these conditions on different designs, a special cage rotor, referred to as nested-loops, was presented in Figure I-10. CHAPTER III will start with the verification of the working principle of such a rotor. To do so, harmonic analyses of the airgap flux density with FE transient simulations will be used to verify how the rotor winding impacts the airgap harmonic content of a BDFM.

The harmonic analyses at the beginning of CHAPTER III will show that the equivalent circuits found in the literature are not able to consider correctly the impact of the rotor mechanical position. Thus, a new equivalent circuit to overcome this drawback will be developed in III.3. With this new equivalent circuit, a new method for the determination of the equivalent circuit parameters, based on simple electrical tests will be presented (in III.3.3).

In CHAPTER II, the difference between sizing and optimization was presented. Different types of models and their advantages for the design or optimization of electrical machines were identified. The presented models can be classified in two major types: the analytical or semi-analytical models (like the coupled-circuit model, the d-q model, the equivalent circuit, the reluctance network), and the numerical models (like FE simulations). There is no one size fits all models. Depending on the design phase, some models will be preferable than others. For example, during the definition of the specifications, or for an optimization, semi-analytical models paired with 1st order algorithms are powerful tools. For the verification of the behavior of the machine or of local variables in the machine, or for transient responses, numerical models are the way to go. A semi-analytical model example, paired with a 1st order optimization algorithm, was given for the Induction Machine. It demonstrated the power of this alliance during the definition of the specifications or optimization phases. This diversity of models for usual electrical machines was exposed to illustrate the shortfall of models available for the BDFM. There is no semi-analytical model available to be paired with 1st order optimization algorithms for the BDFM. FE simulations of the BDFM are limited by the lack of symmetries and the two frequency sources; they take much longer than FE simulations of usual electrical machines. Consequently, in the last parts of CHAPTER III, several new methods and models will be developed and presented.

In III.4, the first new method will be an FE based coupled-circuit method. In this method, the mutual inductances will be determined as functions of the rotor position through multiple magneto-static FE simulations. The main drawback of this method will be its inability to consider saturation. However, it will be much faster than magneto-transient simulations.

In III.5, a second new method will build upon magneto-harmonic simulations for usual electrical machines. A magneto-harmonic method for the BDFM will be designed, taking the two sources with different frequencies into account. This method will consider saturation and will enable load case simulations faster than magneto-transient applications but slower than the FE based coupled-circuit method.

Finally, in III.6, perspectives will be given toward implementing a complete semi-analytical model of the BDFM. This model will be closely related to the Induction Machine model presented in APPENDIX F.

III.2. Verification of analytical results and better understanding of the BDFM thanks to harmonic analysis with FE magneto-transient simulations

The following part will help to understand the complex interactions between the two stators windings and the rotor in a BDFM. To do so, time and space harmonics analyses of the flux density in the airgap of the BDFM will be carried out with FE simulations.

Some harmonic analyses of BDFM airgap magnetic fields can already be found in the literature. For example, in [79], a comparison of BDFRM and BDFM designs is done through airgap harmonic analyses. Four rotors are compared: a salient pole reluctance rotor, a reluctance rotor with magnetic barriers, a rotor with nested-loops, and a salient pole reluctance rotor with nested-loops. The harmonic analyses are done for a power winding with 2 poles and a control winding with 6 poles (so 4 nests or rotor saliencies as seen in equations (16) and (34)). They show that, for these geometries, the reluctance rotors with magnetic barriers generate the best cross-coupling between the two stator windings. The nested-loop rotor is the one that generates the highest harmonic content in the airgap.

A computation of the flux density in the airgap of a BDFM from FE simulations can also be found in [81]. In [81], the airgap flux density computed by an analytical method developed in [80] is compared to FE simulations results. The flux density computation is done for a BDFM with a power winding with 4 pole pairs and a control winding with 6 pole pairs (so 10 rotor nests). The analytical method of [80] is analogous to the coupled-circuit method found in [32] and presented in II.3.2.1. This analytical method does not consider saturation and so, the FE simulations results presented in [81] do not consider saturation either.

With the harmonic analyses performed in the following part, the impacts of the nested-loops, the rotor position, and saturation, will be shown for a given geometry. Thus, it will be possible to study simultaneously the rotor position and saturation impacts on the magnetic state of the machine.

This is different than what exists in the literature previously quoted. In fact, the harmonic analyses presented in the literature are sometimes space-harmonic analysis only, without consideration of time (as in [79]). Some analyses do not investigate saturation (as in [81]), and most do not examine the impact of the rotor position (as in [79] and [81]).

III.2.1. Geometry of the BDFM used for the FE magneto-transient harmonic analyses

As explained in II.3.3, the study of a BDFM with FE simulations can be much more time consuming than other technologies of electrical machines. There are fewer symmetries in a BDFM than in usual machines. Indeed, a BDFM has two stator windings and one rotor nested-loops with a different number

of poles for each. The two different main frequencies of the two stator windings prevent from using FE magneto-harmonic applications imposing one fundamental frequency.

For that reason, it was decided not to use the specification of the TTP (Table II-2, p 53). In fact, a natural speed (as defined in equation (36), p 34) close to 60 rpm would imply the sum of the power and control windings pole pairs to be around 50 (see equation (36)). To diminish the size of the simulation, it was decided to do the study for a power winding with only 6 pole pairs and a control winding with only 4 pole pairs. The main parameters of the BDFM that will be used in CHAPTER III are presented in Table III-1.

Table III-1: Characteristics of the BDFM used for CHAPTER III FE and analytical studies

Stator Parameters	
Length of the machine	1795 mm
Outer Stator diameter	2600 mm
Inner Stator diameter	1600 mm
Number of slots	144
Stator slot width	16 mm
Stator slot height	180 mm
Stator core stacking factor	0.93
Grid Winding pole pairs	6
Control Winding pole pairs	4
Rotor Parameters	
Rotor Outer Diameter	1580 mm
Rotor Inner Diameter	800 mm
Number of slots	120
Rotor Slot Width	16.08 mm
Rotor Slot Height	110 mm
Rotor Core Stacking Factor	0.93
Number of Nests	10
Number of Loops per Nest	6

Two 3D representations of the rotor with the 10 nests and 6 loops per nest are given in Figure III-1. In this figure, the design on the right has been proposed to reduce the centrifugal stress on the base section area of the end-windings. For a rotational speed of 350 rpm (this BDFM has a natural speed of 300 rpm on a 50 Hz network), the stress on the base section copper area of the outermost loop would be 72 N/mm² for the left design and 16 N/mm² for the right one. Design guidelines generally recommend not to go over 50 N/mm² for copper. Thus, for mechanical reasons, the right design of Figure III-1 would be preferred over the left design for a real machine. The 3D representations of Figure III-1 and the centrifugal stress computation were performed by the mechanical R&D team of GE renewable hydro.

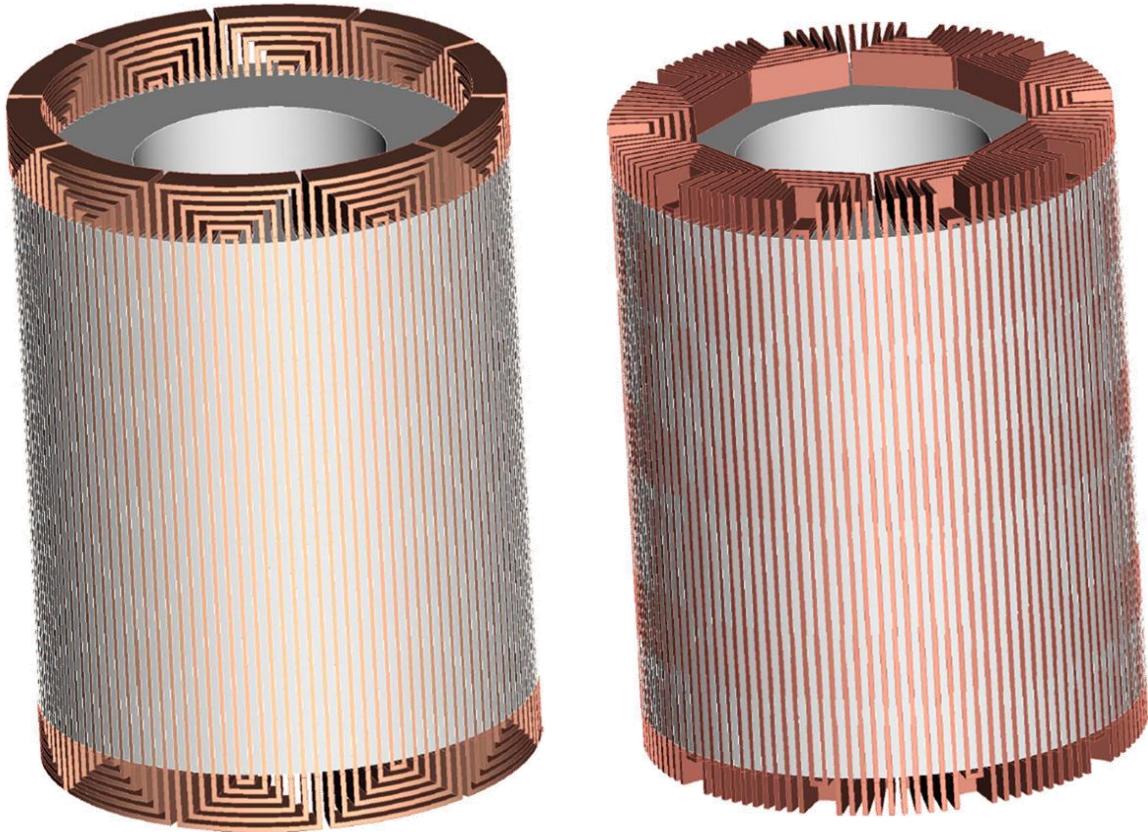


Figure III-1: Nested loops rotor of a BDFM with 10 nests and 6 loops per nest. The rotor on the left is the usual nested-loops design. The rotor on the right was designed to diminish the centrifugal forces on the end windings, especially for the outermost loops. These 3D representations and the centrifugal stress computation were performed by the mechanical R&D team of GE renewable hydro.

III.2.2. Results of the BDFM FE magneto-transient harmonic analyses

The following sections will present the results of FE simulations to show the cross-coupling effect of the rotor, the impact of its position, and the consequences of saturation. To limit the length of this part and to simplify it, only the harmonic-analyses of the two fundamentals and the main harmonics will be presented. Readers who would prefer exhaustive harmonic analyses results can refer to the linked tables from APPENDIX I, p 235.

III.2.2.1. The cross-coupling effect of the rotor nested-loops

To begin, the rotor impact on the harmonics of a BDFM will be studied. To do so, seven simulations will be presented.

The first two simulations will show the harmonic analyses of the airgap flux density created by each stator: Table III-2 for the Power Winding (PW) and Table III-3 for the Command Winding (CW). The rotor nested-loops were not considered in the corresponding FE simulations: the rotor was in “open circuit”.

The following two simulations will show the rotor nested-loop interactions with the flux density created by each stator: Table III-4 for the PW and Table III-5 for the CW. For each simulation, one stator will be fed, the nested-loops will be considered, and the second stator will be in “open circuit”.

The 5th and 6th simulations will show the cascaded mode of a BDFM: Table III-6 for the PW and Table III-7 for the CW. For each simulation, one stator will be fed, the nested-loops will be considered, and the second stator will be “short-circuited”.

Finally, the 7th simulation will show the cross-coupled operation of the two stator windings: Table III-8. Both stator windings will be fed and the nested-loops will be considered.

The simulations will be launched for a power winding fed by a 100 V, 100 Hz voltage and a control winding fed by a 40 V, 25 Hz voltage. The rotor will turn at the speed for cross-coupling to happen: $\frac{100+25}{10}60 = 750 \text{ rpm}$ (from equation (34), p 32). This rotation speed would be too high for such a rotor in real conditions, but this is not a problem for FE simulations. With these frequencies, the saturation effect starts to appear for a power winding voltage around 15000 V and a control winding voltage around 6000 V. With the voltages chosen in this part, the BDFM is far from saturation.

Table III-2 and Table III-3 present the airgap flux density generated by the PW and CW.

Table III-2: Harmonic analysis of the flux density in the airgap due to the PW (more harmonics in Table I-1, p 235)

PW voltage: 100 V, frequency: 100 Hz, rotor nested-loops in open-circuit, rotor speed: 750 rpm				
Harmonic Spatial Order	Amplitude (T) / (pu): Table III-2 reference		Phase (Rad)	Frequency (Hz)
6	0.00307 T	1.000 pu	2.585 rad	100 Hz

Table III-3: Harmonic analysis of the flux density in the airgap due to the CW (more harmonics in Table I-2, p 235)

CW voltage: 40 V, frequency: 25 Hz, rotor nested-loops in open-circuit, rotor speed: 750 rpm				
Harmonic Spatial Order	Amplitude (T) / (pu): Table III-2 reference		Phase (Rad)	Frequency (Hz)
4	0.00386	1.257	-2.106	25

In Table III-2 and Table III-3, the PW and CW create fundamental that have the same spatial order as their number of pole pairs.

Table III-4 and Table III-5 present the impact of the nested-loops on the flux density generated by the PW and CW. Table III-4 is the simple-induction mode with the PW fed, and Table III-5 is the simple-induction mode with the CW fed. As it can be seen in Table III-4, interacting with the flux density of the PW, the nested-loops will create a new harmonic with a spatial order matching the number of poles of the CW and a 25 Hz frequency. If the mechanical speed of the rotor or the pulsation of the PW harmonic was different, the pulsation of the induced harmonic would also be different than 25 Hz. The fundamental of the PW is impacted and its amplitude is lower than in the case without the nested-loops (comparison between Table III-4 and Table III-2). This is not surprising: the currents in the rotor nested-loops are opposing the flux density that is inducing them. In Table III-5, the contrary happens: interacting with the fundamental of the CW, the nested-loops will create a new harmonic with a spatial order matching the number of poles of the PW and pulsating at 100 Hz.

Table III-4: Harmonic analysis of the flux density in the airgap due to the PW and nested-loop interactions (more harmonics in Table I-3, p 235)

PW voltage: 100 V, frequency: 100 Hz, CW in open-circuit, rotor speed: 750 rpm				
Harmonic Spatial Order	Amplitude (T) / (pu): Table III-2 reference		Phase (Rad)	Frequency (Hz)
4	0.001994	0.650	-2.543	25
6	0.002755	0.898	2.589	100
14	0.000325	0.106	0.699	150

Table III-5: Harmonic analysis of the flux density in the airgap due to the CW and nested-loop interactions (more harmonics in Table I-4, p 236)

CW voltage: 40 V, frequency: 25 Hz, PW in open-circuit, rotor speed: 750 rpm				
Harmonic Spatial Order	Amplitude (T) / (pu): Table III-2 reference		Phase (Rad)	Frequency (Hz)
4	0.00369	1.202	-2.114	25
6	0.00378	1.233	2.049	100
16	0.00051	0.165	1.962	225

Table III-6 and Table III-7 present the impact of the opposite winding when it becomes short-circuited. Table III-6 is the self-cascaded mode with the PW fed, and Table III-7 is the self-cascaded mode with the CW fed. It is interesting to note that in the self-cascaded modes, the amplitudes of the harmonics are lower than in the simple-induction modes (comparison between Table III-6, Table III-7, and Table III-4, Table III-5). The currents induced in the opposite winding, are also opposing the flux densities that induced them.

Table III-6: Harmonic analysis of the flux density in the airgap due to the PW with the CW in cascaded mode through the nested-loops (more harmonics in Table I-5, p 236)

PW voltage: 100 V, frequency: 100 Hz, CW in short-circuit, rotor speed: 750 rpm				
Harmonic Spatial Order	Amplitude (T) / (pu): Table III-2 reference		Phase (Rad)	Frequency (Hz)
4	0.000319	0.104	-2.306	25
6	0.001793	0.585	2.703	100
14	0.000531	0.173	0.704	150
16	0.000290	0.095	-0.767	225

Table III-7: Harmonic analysis of the flux density in the airgap due to the CW with the PW in cascaded mode through the nested-loops (more harmonics in Table I-6, p 237)

CW voltage: 40 V, frequency: 25 Hz, PW in short-circuit, rotor speed: 750 rpm				
Harmonic Spatial Order	Amplitude (T) / (pu): Table III-2 reference		Phase (Rad)	Frequency (Hz)
4	0.00339	1.104	-2.146	25
6	0.00200	0.652	1.945	100
14	0.00041	0.135	-1.989	150
16	0.00080	0.260	1.917	225

Table III-8 presents the final load mode: the cross-coupling mode. It is kind of a superimposition of the two self-cascaded modes presented in Table III-6 and Table III-7.

Table III-8: Harmonic analysis of the flux density in the airgap during a load case without saturation of the BDFM (more harmonics in Table I-7, p 237)

PW voltage: 100 V, frequency: 100 Hz, CW voltage: 40 V, frequency: 25 Hz, rotor speed: 750 rpm				
Harmonic Spatial Order	Amplitude (T) / (pu): Table III-2 reference		Phase (Rad)	Frequency (Hz)
4	0.00370	1.207	-2.160	25
6	0.00352	1.149	2.302	100
14	0.00024	0.078	-0.143	150
16	0.00055	0.180	1.682	225

The tables, from Table III-2 to Table III-8, help us to apprehend how the nested-loops are interacting with the flux densities of the two stator windings, and how the cross-coupling mode is happening. To better understand the influence of the rotor position (at $t = 0$), new harmonics tables will be presented in the following part with only the rotor position varying.

III.2.2.2. Influence of the rotor position

In this part, the same simulations as the simulations made from Table III-2 to Table III-8 will be done; the only difference will be the rotor position that will be increased by 13° in the positive direction at $t = 0$ (the value of this angle was chosen randomly).

Table III-9 and Table III-10 present the airgap flux density generated by the PW and CW. They can be compared to Table III-2 and Table III-3. As it can be seen in this comparison, the fundamental harmonics created by the PW and CW are identical in amplitudes, phases, and frequencies after a rotor rotation. However, differences can be seen in the other harmonics (for example in the comparison of Table I-8, p 238, and Table I-1, p 235). In fact, with the rotor rotation, the harmonics related to the rotor teeth are impacted.

Table III-9: Harmonic analysis of the flux density in the airgap due to the PW. Rotor position at $t = 0$ is rotated by $+13^\circ$ (more harmonics in Table I-8, p 238)

PW voltage: 100 V, frequency: 100 Hz, rotor nested-loops in open-circuit, rotor speed: 750 rpm. Rotor position at $t = 0$ is rotated by $+13^\circ$.				
Harmonic Spatial Order	Amplitude (T) / (pu): Table III-2 reference		Phase (Rad)	Frequency (Hz)
6	0.00307 T	1.000 pu	2.585 rad	100 Hz

Table III-10: Harmonic analysis of the flux density in the airgap due to the CW. Rotor position at $t = 0$ is rotated by $+13^\circ$

CW voltage: 40 V, frequency: 25 Hz, rotor nested-loops in open-circuit, rotor speed: 750 rpm. Rotor position at $t = 0$ is rotated by $+13^\circ$.				
Spatial Order	Amplitude (T) / (pu): Table III-2 reference		Phase (Rad)	Frequency (Hz)
4	0.00386	1.257	-2.106	25

Table III-11 and Table III-12 present the simple-induction modes for the PW and CW respectively. They can be compared to Table III-4 and Table III-5. These comparisons show that the amplitudes of the flux density harmonics are not impacted by a rotor rotation in simple-induction modes. The phases of the fed windings are not impacted either. However, the phases of the harmonics created by the rotor have changed. For example, in the simple-induction mode with the PW fed, the phase of the harmonic induced by the nested-loops (with a special order of 4) goes from -2.543 rad in Table III-4, to 1.4711 rad in Table III-11. In the simple-induction mode with the CW fed, the phase of the harmonic induced by the nested-loops (with a special order of 6) goes from 2.049 rad in Table III-5 to -0.220 rad in Table III-12. Without any explanations (they will come with the introduction of the new equivalent circuit in III.3), the reader can still notice the following interesting equations.

$$-0.220 - 2.049 = -2.269 = (6 + 4) \cdot 13 \cdot \frac{\pi}{180} \quad (45)$$

so

$$\Delta \text{phases}_{\text{harmonics}} = -0.220 - 2.049 = -(p_g + p_c) \cdot \Delta \theta_0$$

With p_g and p_c , the number of pole pairs of the PW and CW respectively.
 $\Delta \theta_0$, the difference in rotor position in radian at $t = 0$ between the two simulations.

Similarly:

$$1.4711 - (-2.543) - 2\pi = -2.269 = -(6 + 4) \cdot 13 \cdot \frac{\pi}{180} \quad (46)$$

so

$$\Delta \text{phases}_{\text{harmonics}} = 1.4711 - (-2.543) - 2\pi = -(p_g + p_c) \cdot \Delta \theta_0$$

These impacts of the rotor position on the behavior of the BDFM are interesting. In most of the equivalent circuits present in the literature, the position of the rotor has no effect on the equivalent circuit. In [32] and in other publications by the same authors: [82], [49], [76], and [77], the rotor position is considered in the equivalent circuit. Nevertheless, the equivalent circuit from these publications does not verify the results in equations (45) and (46) (this can clearly be seen in Figure III-15, p 103 for example).

Table III-11: Harmonic analysis of the flux density in the airgap due to the PW and nested-loops interaction. Rotor position at $t = 0$ is rotated by $+13^\circ$ (more harmonics in Table I-9, p 238)

PW voltage: 100 V, frequency: 100 Hz; CW in open-circuit; rotor speed: 750 rpm. Rotor position at $t = 0$ is rotated by $+13^\circ$.				
Harmonic Spatial Order	Amplitude (T) / (pu): Table III-2 reference		Phase (Rad)	Frequency (Hz)
4	0.00199	0.650	1.4711	25
6	0.00276	0.898	2.589	100
14	0.00033	0.106	2.4438	150

Table III-12: Harmonic analysis of the flux density in the airgap due to the CW and nested-loops interaction. Rotor position at $t = 0$ is rotated by $+13^\circ$ (more harmonics in Table I-10, p 238)

CW voltage: 40 V, frequency: 25 Hz; PW in open-circuit; rotor speed: 750 rpm. Rotor position at $t = 0$ is rotated by $+13^\circ$.				
Harmonic Spatial Order	Amplitude (T) / (pu): Table III-2 reference		Phase (Rad)	Frequency (Hz)
4	0.00369	1.202	-2.114	25
6	0.00378	1.233	-0.220	100
16	0.00051	0.165	-2.576	225

Table III-13 and Table III-14 present the self-cascaded mode for the PW and CW respectively. They can be compared to Table III-6 and Table III-7. These comparisons show that the amplitudes of the flux density harmonics are not impacted by a rotor rotation in self-cascaded modes. The phases of the fed windings are not impacted either. However, the phases of the harmonics created by the rotor have changed. The same phase shift can be observed in the self-cascaded modes and in the simple-induction modes: the phase shift properties observed in equations (45) and (46). For example, in the self-cascaded mode with the PW fed, the phase of the harmonic induced by the nested-loops (with a special order of 4) goes from -2.306 rad in Table III-6, to 1.708 rad in Table III-13. As in (46): $1.708 - (-2.306) - 2\pi = -(p_g + p_c) \cdot \Delta\theta_0$.

Table III-13: Harmonic analysis of the flux density in the airgap due to the PW with the CW in cascaded mode through the nested-loops. Rotor position at $t = 0$ is rotated by $+13^\circ$ (more harmonics in, Table I-11 p 239)

PW voltage: 100 V, frequency: 100 Hz, CW in short-circuit, rotor speed: 750 rpm. Rotor position at $t = 0$ is rotated by $+13^\circ$.				
Harmonic Spatial Order	Amplitude (T) / (pu): Table III-2 reference		Phase (Rad)	Frequency (Hz)
4	0.00032	0.104	1.708	25
6	0.00179	0.585	2.703	100
14	0.00053	0.173	2.449	150
16	0.00029	0.095	-3.036	225

Table III-14: Harmonic analysis of the flux density in the airgap due to the CW with the PW in cascaded mode through the nested-loops. Rotor position at $t = 0$ is rotated by $+13^\circ$ (more harmonics in, Table I-12, p 239)

CW voltage: 40 V, frequency: 25 Hz, PW in short-circuit, rotor speed: 750 rpm. Rotor position at $t = 0$ is rotated by $+13^\circ$.				
Harmonic Spatial Order	Amplitude (T) / (pu): Table III-2 reference		Phase (Rad)	Frequency (Hz)
4	0.00339	1.104	-2.146	25
6	0.00200	0.652	-0.324	100
14	0.00041	0.135	2.025	150
16	0.00080	0.260	-2.621	225

Finally, Table III-15 presents the cross-coupling mode that can be compared to Table III-8. Unlike for the simple induction-modes and self-cascaded modes, both the amplitudes and the phases of every flux density harmonics are impacted by the rotor position.

Table III-15: Harmonic analysis of the flux density in the airgap during a load case without saturation of the BDFM. Rotor position at $t = 0$ is rotated by $+13^\circ$ (more harmonics in Table I-13, p 240)

PW voltage: 100 V, frequency: 100 Hz, CW voltage: 40 V, frequency: 25 Hz, rotor speed: 750 rpm. Rotor position at $t = 0$ is rotated by $+13^\circ$.				
Harmonic Spatial Order	Amplitude (T) / (pu): Table III-2 reference		Phase (Rad)	Frequency (Hz)
4	0.00315	1.027	-2.213	25
6	0.00030	0.098	0.433	100
14	0.00092	0.301	2.264	150
16	0.00107	0.348	-2.731	225

To understand the impact of saturation, new harmonics tables will be presented in III.2.2.3 with only the feeding voltages varying.

III.2.2.3. Saturation impacts on the BDFM harmonics and power flow

To finish the airgap flux density harmonic analyses, the impact of the magnetic saturation will be presented in Table III-16 and Table III-17. These tables will introduce cross-coupling cases where only the feeding voltages of the PW and CW will vary in comparison to Table III-8 (rotor position at $t = 0$ is the same as in the cross-coupling case of Table III-8). The PW and CW voltages will vary proportionally such that Table III-16 and Table III-17 can be compared to Table III-8. The per unit values of Table III-16 and Table III-17 were also made such that they are comparable to the per unit values of Table III-8.

Without saturation, the amplitudes of the flux density harmonics should be proportional to the voltages. The cross-coupling simulation in Table III-16 was made at voltages to be in the saturation “knee”. The cross-coupling simulation in Table III-17 was made at voltages to go very far in saturation.

As it can be seen, comparing the results in Table III-16 and Table III-17 to the one of Table III-8, the main effect of saturation can be seen in the apparition of new harmonics. In Table III-16, the apparition of the harmonics 2 and 8, and in Table III-17, 2, 8, and 10. The amplitudes of the harmonics of the PW and CW (harmonics 6 and 4) are slightly diminished in comparison to the linear case. In Table III-16, the amplitudes are in pu: 1.184 (for the CW) and 1.097 (for the PW) whereas in Table III-8 they were 1.207 (for the CW) and 1.149 (for the PW). The phases of the PW and CW harmonics are also impacted by saturation, especially in very high saturation. In Table III-17, the phases are -2.180 for the CW harmonic and 2.287 for the PW harmonic; in Table III-8, they were -2.160 for the CW harmonic and 2.299 for the PW harmonic.

Table III-16: Harmonic analysis of the flux density in the airgap during a BDFM load case without saturation (more harmonics in Table I-14, p 241)

PW voltage: 17 500 V, frequency: 100 Hz, CW voltage: 7 000 V, frequency: 25 Hz, rotor speed: 750 rpm				
Spatial Order	Amplitude (T) / (pu): Table III-2 reference extrapolation if linear		Phase (Rad)	Frequency (Hz)
2	0.0506	0.094	2.898	-50
4	0.636	1.184	-2.161	25
6	0.589	1.097	2.299	100
8	0.0830	0.155	-2.724	175
14	0.1157	0.216	0.832	150
16	0.0548	0.102	0.174	225

Table III-17: Harmonic analysis of the flux density in the airgap during a BDFM load case without saturation (more harmonics in Table I-15, p 241)

PW voltage: 30 000 V, frequency: 100 Hz; CW voltage: 12 000 V, frequency: 25 Hz; rotor speed: 750 rpm				
Harmonic Spatial Order	Amplitude (T) / (pu): Table III-2 reference extrapolation if linear		Phase (Rad)	Frequency (Hz)
2	0.121	0.225	2.606	-50
4	1.034	1.926	-2.180	25
6	0.807	1.504	2.287	100
8	0.2095	0.390	-2.511	175
10	0.0918	0.171	-0.967	250
14	0.2275	0.424	0.984	150
16	0.0977	0.182	-0.534	225

To conclude, several harmonic analyses were done on multiple magneto-transient simulations. These harmonic analyses showed how the nested-loops of the rotor enable the cross-coupling of the PW and CW at the right rotor speed. The analyses also highlighted the importance and the impact of the rotor mechanical speed and position. Finally, the impact of saturation, from an airgap flux density was presented in the last tables.

III.3. New equivalent circuit model developed for the BDFM

III.3.1. Reasons to develop a new equivalent circuit model of the BDFM

Some equivalent circuit models developed for the BDFM can be found in the literature. In [83] for example, the reader can find the analytical development of an equivalent circuit starting from the coupled-circuit model (coupled-circuit models are introduced in II.3.2.1, p 65), transformed into a d-q model (introduced in II.3.2.2, p 66), and finally transformed into an equivalent circuit model. As already stated, the major drawback of the equivalent circuit obtained through d-q model is the unaccounted effect of saturation.

Equivalent circuit results have been compared to FE simulation and to prototype results in the cases of self-cascaded tests and induction tests (one stator winding is either open or short-circuited) for example in [32] or [83]. For the determination of the equivalent scheme parameters, a method implying measurements of torque-speed characteristics, for self-cascaded (one stator winding is short-circuited) and simple induction (one stator winding is in open-circuit), paired with an optimization for the extraction of the parameters, has been developed and presented in [82]. Previous methods were based on multi-frequency measurements of voltages and currents; these methods are described in [84] and [85].

At the beginning of the tools development, it was found that the equivalent circuits from the literature were giving a good correlation to FE results in the cases where one stator winding was short-circuited or opened (self-cascaded or simple induction tests). However, the power flow was wrong during normal load operation (both stator windings fed at the same time). These inaccuracies will be shown in greater details in III.3.6, p 100. Therefore, a new equivalent circuit is presented in this work. This new equivalent circuit exploits what was already presented in the work of Roberts [32]. The explanation leading to this new equivalent circuit was done quite differently from what was described in [32] or [83]. Instead of starting from the coupled-circuit model (as in [32] and [83]), it was decided to start directly from the analogy with the well-known equivalent circuit of the induction machine. Thanks to this shortcut, the explanations given here are much shorter than the demonstrations found in the literature. It makes physical sense and can be well understood by people used to work with induction machines despite not being an appropriate full demonstration. In the end, it leads to an equivalent circuit identical to the previous equivalent circuits in the special self-cascaded and simple induction modes. Thus, the results will not change in the cases where the previous equivalent circuits were already giving good correlations with FE simulations.

As it will be seen, the new equivalent circuit and the previous ones will differ in how the phases of the two stator windings are taken into account. In the coupled-circuit mode (two stator windings are simultaneously fed), this will lead to more accurate results as it will be shown in III.3.6, p 100.

A new method for the determination of the parameters of the equivalent circuit will also be shown in this work. This new method will be based on simple electrical tests in simple induction and self-cascaded modes. The extractions of the parameters will be made with an optimization algorithm. This will be presented in III.3.3, p 97.

III.3.2. From the equivalent circuit of the IM to the equivalent circuit of the BDFM

III.3.2.1. Starting from the equivalent circuit of an Induction Machine with a mutual inductance representation and access to the rotor terminals

To establish the equivalent circuit of the BDFM, we will start from the equivalent circuit of the Induction Machine. The equivalent circuit of the Induction Machine is well known. Since the equivalent circuits of the two stators will be added together through the rotor, the representation will be pictured

with rotor terminals accessible. The equivalent circuit can be represented with either a mutual inductance or with a turns ratio. We must start from the representation with a mutual inductance so as to consider the phase shift between the rotor and the stator. For general squirrel cage machines, this phase shift does not have an impact on the torque and on the power generated by the machine. Therefore, it is not considered in most representations. For the BDFM, the phase shift between the two stator windings will be a parameter influencing the power generated. The phase shift between the two stators and the rotor cannot be ignored.

In order not to over complicate the development of the equivalent circuit, the iron losses in the stator and rotor cores will not be represented. These iron losses can be represented by a resistance in parallel with the magnetizing inductance.

Under these conditions, the per phase equivalent circuit of the IM with the mutual inductance representation is reminded in Figure III-2.

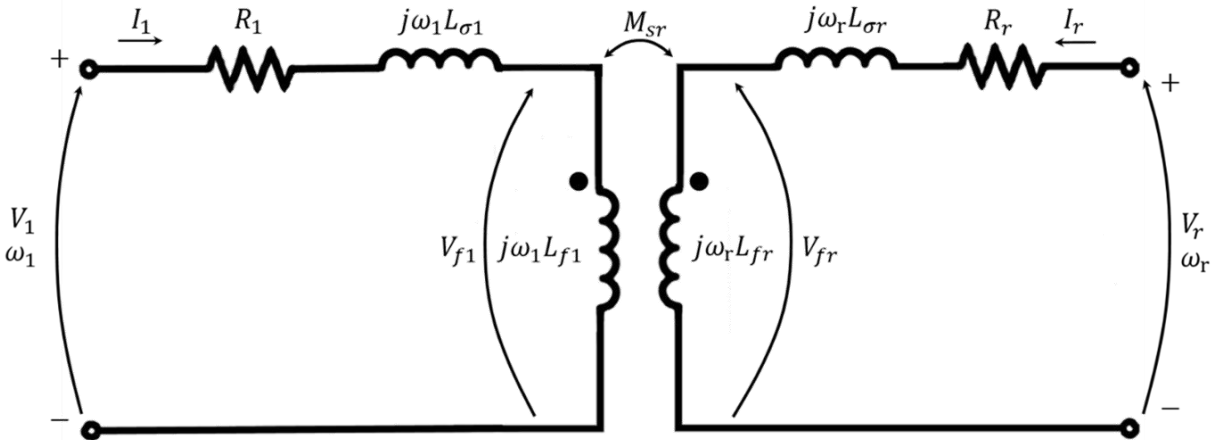


Figure III-2: Per phase equivalent scheme of the Induction Machine with rotor terminals accessible

- R_1 represents the Joules losses incurring in the stator.
- L_{f1} is the inductance representing the fundamental harmonic flux seen by the stator winding.
- $L_{\sigma 1}$ is the inductance representing the leakage and the harmonics fluxes of the stator.
- $L_{\sigma 1} = L_{l1} + L_{h1}$, with L_{l1} the inductance of the leakage flux: the flux not passing through the airgap to the rotor, and L_{h1} the inductance of the harmonics created by the stator.
- L_{fr} is the inductance representing the fundamental harmonic flux seen by the rotor winding.
- $L_{\sigma r}$ is the inductance representing the leakage and the harmonics fluxes of the rotor.
- $L_{\sigma r} = L_{lr} + L_{hr}$, with L_{lr} the inductance of the leakage flux: the flux not passing through the airgap to the stator, and L_{hr} the inductance of the harmonics created by the rotor.
- M_{sr} is the mutual inductance between the stator and the rotor.

In Figure III-2, the leakage and harmonic fluxes are separated from the fundamental fluxes for both the stator and the rotor. Under these conditions, the flux of the fundamental is the same in the stator and in the rotor.

$$L_{f1}I_1 = L_{fr}I_r \tag{47}$$

Thus, this is the ideal case where the magnitude of the mutual inductance can be expressed such as:

$$|M_{sr}| = \sqrt{L_{f1}L_{fr}} \quad (48)$$

The phase of the mutual inductance will depend on the rotor position. The mutual inductance is pulsating at the mechanical speed times the number of poles of the harmonic it is related to.

Like for the voltages and currents, the mutual inductance will be written as a complex with the phase taken for $t = 0$. The mutual inductance can be written

$$M_{sr} = |M_{sr}|e^{i\angle M_{sr}} \quad (49)$$

III.3.2.2. Transformation from the mutual inductance representation to the transformer representation

An IM has one stator winding, a BDFM has two stator windings. From an equivalent circuit point of view, a BDFM looks like two inductions machines sharing the same rotor. To prepare for the BDFM equivalent circuit, in the IM equivalent circuit, the subscript 1 and 2 will be used. For the IM equivalent circuit, 1 and 2 will represent the stators of two different machines. In the BDFM equivalent circuit 1 will be used for the PW and 2 for the CW.

To convert the equivalent circuit from the mutual inductance representation to the transformer representation, it is easier to have a mutual inductance that is real. For induction machines, it is not a problem to get rid of the phase of the mutual inductance and to just keep its amplitude. In fact, for squirrel cage machines, the phase of the rotor current is not important. For a BDFM, the phases of the rotor induced currents are important. Thus, in the IM equivalent circuit, this angle will be kept and passed to the phase of the stator voltage and current. It can be done thanks to a simple mathematical trick: notice that equations (50) and (52) are equivalent and that equations (51) and (53) are also equivalent. Consequently, the two representations of the Figure III-3 are equivalent.

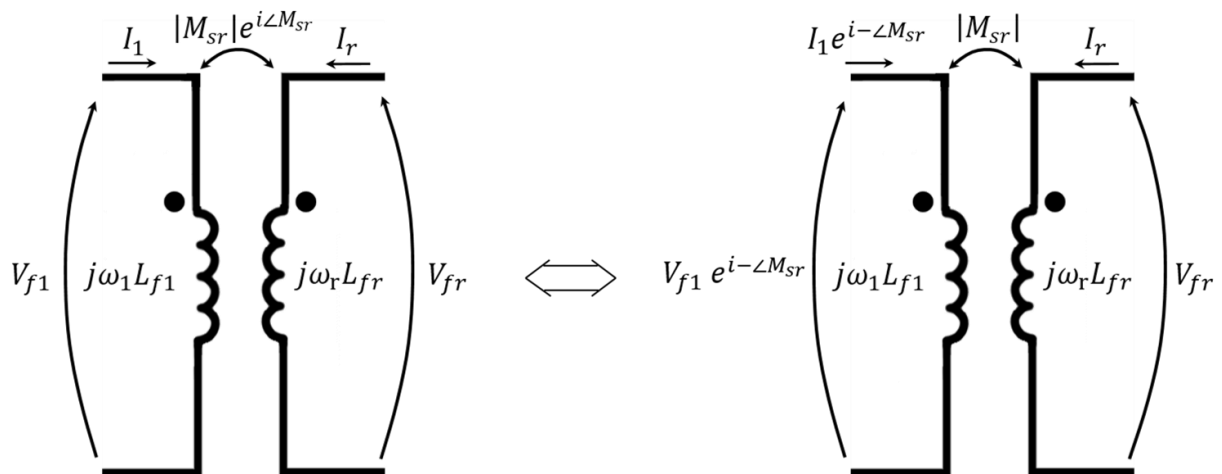


Figure III-3: Mutual inductance. Notice that the right and left representations are equivalent and yield the same equations.

The left representation in Figure III-3 yields the following two equations:

$$V_{f1} = j\omega_1 I_1 L_{f1} + j\omega_r I_r |M_{sr}| e^{i\angle M_{sr}} \quad (50)$$

$$V_{fr} = j\omega_r I_r L_{fr} + j\omega_1 I_1 |M_{sr}| e^{-i\angle M_{sr}} \quad (51)$$

The right representation in Figure III-3 yields the following two equations:

$$e^{i\angle M_{sr}} \cdot (V_{f1} e^{-i\angle M_{sr}} = j\omega_1 I_1 e^{-i\angle M_{sr}} L_{f1} + j\omega_r I_r |M_{sr}|) \quad (52)$$

$$V_{fr} = j\omega_r I_r L_{fr} + j\omega_1 I_1 e^{-i\angle M_{sr}} |M_{sr}| \quad (53)$$

With the assumption: $\omega_r L_{fr} \gg R_r$, it is possible to introduce the transformer representation equivalent to the mutual inductance representation. Figure III-4 shows these two equivalent representations.

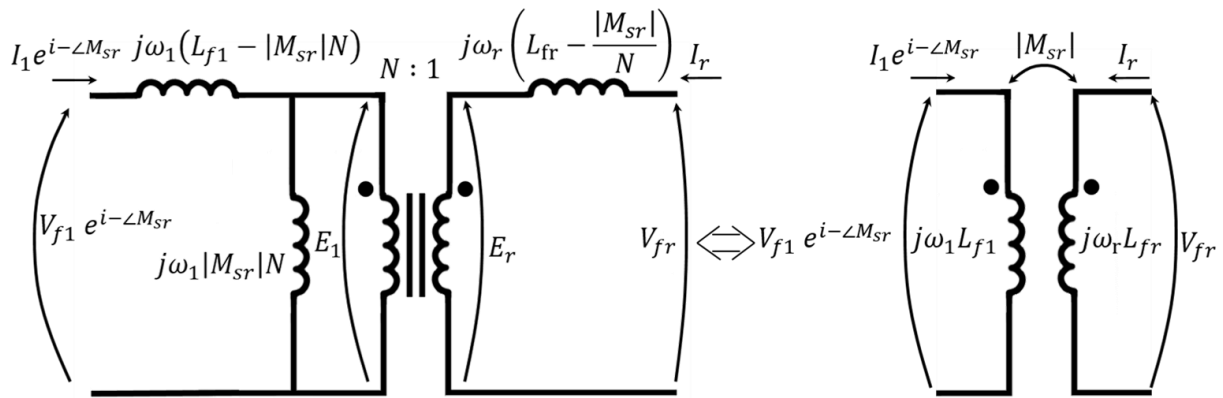


Figure III-4: Equivalence between the transformer representation and the mutual inductance representation

The ideal coupling case between the rotor and the stator was taken (with the separation of the fundamental from the leakage and harmonic reactances) as explained and shown in equations (47) and (48). Under these conditions, the effective turns ratio between the stator and the rotor in the transformer representation can be expressed as:

$$N = \sqrt{\frac{L_{f1}}{L_{fr}}} \quad (54)$$

From equations (48) and (54), the two following equations can be written:

$$|M_{sr}|N = L_{m1} = L_{f1} \quad (55)$$

$$\frac{|M_{sr}|}{N} = L_{mr} = L_{fr} \quad (56)$$

With L_{m1} , the magnetizing inductance of the stator.

L_{f1} , the inductance representing the fundamental harmonic of the stator winding.

L_{mr} , the magnetizing inductance seen on the rotor side.

L_{fr} , the inductance representing the fundamental harmonic of the stator winding on the rotor side.

With (55) and (56), the left part of the scheme in Figure III-4 can be simplified. This simplification arises from the fact that the mutual inductance was defined between two inductances that were both fully linking to the fundamental harmonic flux and only the fundamental harmonic flux. This is the reason why $L_{m1} = L_{f1}$ and $L_{mr} = L_{fr}$.

Considering the simplifications of equations (55) and (56) and the equivalences in Figure III-3 and Figure III-4, the per phase equivalent circuit of an induction machine can now be drawn, with rotor terminals accessible, and with a transformer representation.

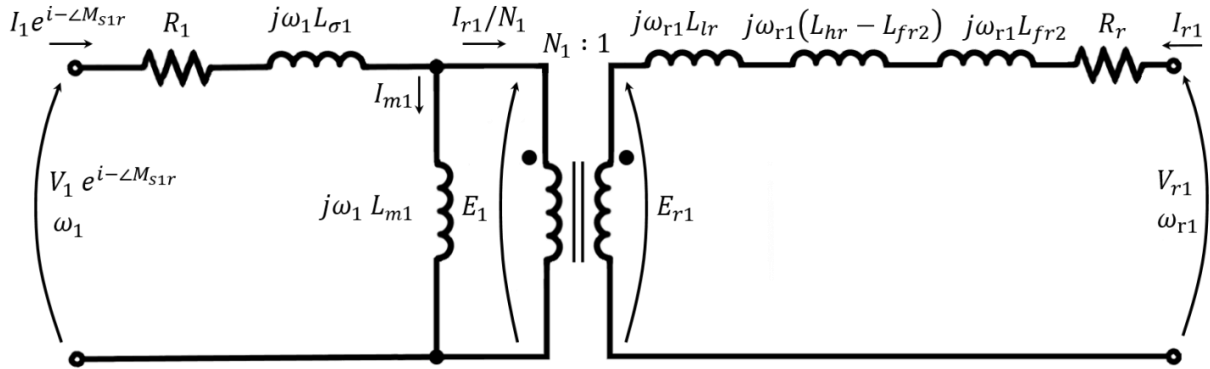


Figure III-5: Per phase equivalent circuit of the Induction Machine with a transformer representation and rotor terminals accessible

L_{lr} is the leakage inductance of the rotor (representing the rotor flux that does not pass through the airgap).

L_{hr} is the harmonic inductance of the rotor (representing the rotor flux that passes through the airgap, but that does not match the fundamental harmonic of the stator of the IM).

L_{fr2} is introduced as a mathematical trick (since $j\omega_{r1}(L_{hr} - L_{fr2}) + j\omega_{r1}L_{fr2} = j\omega_{r1}L_{hr}$). For an induction machine, L_{fr2} is part of the harmonic inductance, but for the BDFM representation coming in the following figures, L_{fr2} represents the flux created from the rotor induced current, that will match the spatial distribution of the fundamental of the opposite stator winding. If subscript 1 represents the PW then subscript 2 represents the CW.

That is the reason why in Figure III-5, $L_{\sigma r1}$ was separated into L_{lr} (the leakage inductance of the rotor that does not pass through the airgap), $L_{hr} - L_{fr2}$ (the harmonic inductance of the rotor minus the CW fundamental harmonic inductance on the rotor side), and L_{fr2} (the CW fundamental harmonic inductance on the rotor side). This was to stress the fact that the magnetizing inductance for the CW: L_{fr2} is part of $L_{\sigma r1}$. Similarly, the fundamental inductance of the rotor that will link to the PW: L_{fr1} is part of $L_{\sigma r2}$.

III.3.2.3. Fusion of the per phase equivalent circuit of the two IMs representing the PW and CW to obtain the BDFM equivalent circuit. To merge the two representations, the rotor frequency must be equal in the two circuits

In a BDFM, there are two stator windings and nested-loops for the rotor. As previously explained, magnetic interactions between the two stator windings in the stator iron must be avoided (through the stator such an interaction would not create torque). To avoid such interactions the two stator windings will have different pole numbers. If there were two different rotor windings with a matching number of poles for each stator winding, the BDFM equivalent circuit would be represented as two equivalent circuits of Induction Machines.

For the interaction of the two stator windings through the rotor, there is only one rotor winding. For an interaction to occur in the rotor, the induced rotor currents need to have the same frequency. The same frequency is obtained at special conditions, at the cross-coupling speed as it is reminded from equation (57) to equation (61).

To be in the cross-coupling conditions, the rotating speed of the rotor is defined as (refer to equations (33) and (34)):

$$\omega_{rm} = \frac{\omega_1 \pm \omega_2}{p_1 \pm p_2} \quad (57)$$

ω_{rm} is the mechanical pulsation of the rotor.

ω_1 and ω_2 are the pulsation of the currents feeding the power and control windings respectively.

p_1 and p_2 are the numbers of pole pairs of the power and control windings respectively.

As explained in I.5.3.5.1, p 32, to develop the equivalent circuit of the BDFM, only the case where the number of rotor nests is the highest will be considered. Equation (57) becomes:

$$\omega_{rm} = \frac{\omega_1 + \omega_2}{p_1 + p_2} \quad (58)$$

Under the condition that the PW and CW have the same phase order (see explanations in I.5.3.5.4, p 34), the slips s_1 and s_2 are defined as:

$$s_1 = \frac{\omega_1 - p_1 \omega_r}{\omega_1} \quad (59)$$

$$s_2 = \frac{\omega_2 - p_2 \omega_r}{\omega_2}$$

With these notations, the pulsations of the induced currents in the rotor can be written

$$\omega_{r1} = s_1 \omega_1 = \omega_1 - p_1 \omega_r \quad (60)$$

$$\omega_{r2} = s_2 \omega_2 = \omega_2 - p_2 \omega_r$$

The combination of equations (58), (59), and (60) gives:

$$\begin{aligned}\omega_{r1} &= s_1\omega_1 = \omega_1 - p_1\omega_{rm} = \omega_1 \frac{p_1 + p_2}{p_1 + p_2} - p_1 \frac{\omega_1 + \omega_2}{p_1 + p_2} = \frac{p_2\omega_1 - p_1\omega_2}{p_1 + p_2} \\ \omega_{r2} &= s_2\omega_2 = \omega_2 - p_2\omega_{rm} = \omega_2 \frac{p_1 + p_2}{p_1 + p_2} - p_2 \frac{\omega_1 + \omega_2}{p_1 + p_2} = \frac{p_1\omega_2 - p_2\omega_1}{p_1 + p_2}\end{aligned}\quad (61)$$

So finally, in (61) the expression of ω_{r1} and ω_{r2} are opposed. In cross-coupling conditions the following equation is true:

$$\omega_{r1} = -\omega_{r2}\quad (62)$$

Here, the reader should note that the result in equation (62) is independent of the rotation direction of the magnetic fields of the PW and CW. They can rotate in the same or opposite directions, the pulsations of the rotor currents induced by the PW and CW will always verify $\omega_{r1} = -\omega_{r2}$.

However, if instead of choosing $\omega_{rm} = \frac{\omega_1 + \omega_2}{p_1 + p_2}$ and $N_r = p_1 + p_2$ as in (58) and (34), p32, we had chosen $\omega_{rm} = \frac{\omega_1 - \omega_2}{p_1 - p_2}$ and $N_r = p_1 - p_2$ as in (33), the rotor pulsations would then verify: $\omega_{r1} = \omega_{r2}$.

From equation (62), $\omega_{r1} = -\omega_{r2}$. To merge the two equivalent circuits, they need to have the same rotor pulsation. To do so, the equivalent circuit of the stator 2 should have a rotor pulsation of $-\omega_{r2}$ instead of ω_{r2} . Since the equivalent circuit must represent the same equations and keep the same slip, a mathematical trick will be to impose the stator 2 pulsation to $-\omega_2$ instead of ω_2 .

In the equivalent circuit, the expression of the voltage imposed to the stator 2 in the time domain is:

$$\begin{aligned}v_2(t) &= \Re(V_2 e^{-i\angle M_{s2r}}) \cos(\omega_2 t) \\ v_2(t) &= |V_2| \cos(\omega_2 t + \angle V_2 - \angle M_{s2r}) \\ v_2(t) &= |V_2| \cos(-\omega_2 t - \angle V_2 + \angle M_{s2r}) \\ v_2(t) &= \Re(V_2^* e^{i\angle M_{s2r}}) \cos(-\omega_2 t)\end{aligned}\quad (63)$$

The same can be done for the voltage at the rotor terminals (64), for the stator 2 current (65), and for the rotor current (66):

$$\begin{aligned}v_{r2}(t) &= \Re(V_{r2}) \cos(\omega_{r2} t) \\ v_{r2}(t) &= |V_{r2}| \cos(\omega_{r2} t + \angle V_{r2}) \\ v_{r2}(t) &= \Re(V_{r2}^*) \cos(-\omega_{r2} t)\end{aligned}\quad (64)$$

$$\begin{aligned}i_2(t) &= \Re(I_2 e^{-i\angle M_{sr2}}) \cos(\omega_2 t) \\ i_2(t) &= |I_2| \cos(\omega_2 t + \angle I_2 - \angle M_{sr2}) \\ i_2(t) &= |I_2| \cos(-\omega_2 t - \angle I_2 + \angle M_{sr2}) \\ i_2(t) &= \Re(I_2^* e^{i\angle M_{sr2}}) \cos(-\omega_2 t)\end{aligned}\quad (65)$$

$$\begin{aligned}i_{r2}(t) &= \Re(I_{r2}) \cos(\omega_{r2} t) \\ i_{r2}(t) &= |I_{r2}| \cos(\omega_{r2} t + \angle I_{r2}) \\ i_{r2}(t) &= \Re(I_{r2}^*) \cos(-\omega_{r2} t)\end{aligned}\quad (66)$$

With equations (63), (64), (65), and (66), it can be noticed that the equivalent circuit can be expressed with a pulsation of $-\omega_2$ for the stator and $-\omega_{r2}$ for the rotor if the conjugate of the rotor and stator voltages and currents are taken.

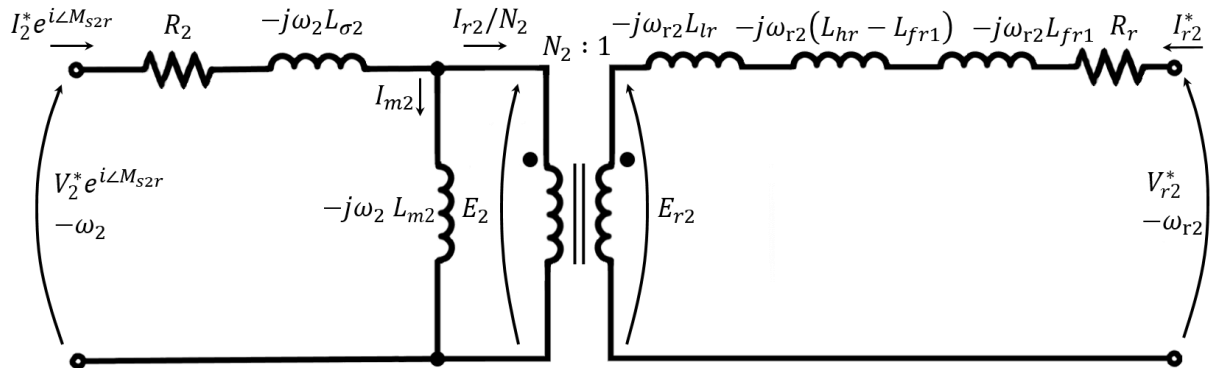


Figure III-6: Per phase equivalent circuit of the Command Winding Induction Machine with a transformer representation and rotor terminals accessible. The pulsations have been inverted because $-\omega_{r2} = \omega_{r1}$.

With the same rotor pulsations, the two per phase equivalents circuit shown in Figure III-5 and Figure III-6 can now be merged. In the BDFM, the rotor is in short circuit so $V_{r1} = 0$ and $V_{r2}^* = 0$. The rotor pulsation will be noted $\omega_r = \omega_{r1} = -\omega_{r2}$. The currents I_{r1} and I_{r2}^* will be added in the rotor without forgetting that they are in opposite directions. $I_r = I_{r1} - I_{r2}^*$ will be introduced.

When combining the two representations, L_{fr1} and L_{fr2} will be included in the magnetizing inductance of the PW an CW respectively. L_{hr} will be the harmonic inductance that do not consider the fundamentals of the PW and the CW.

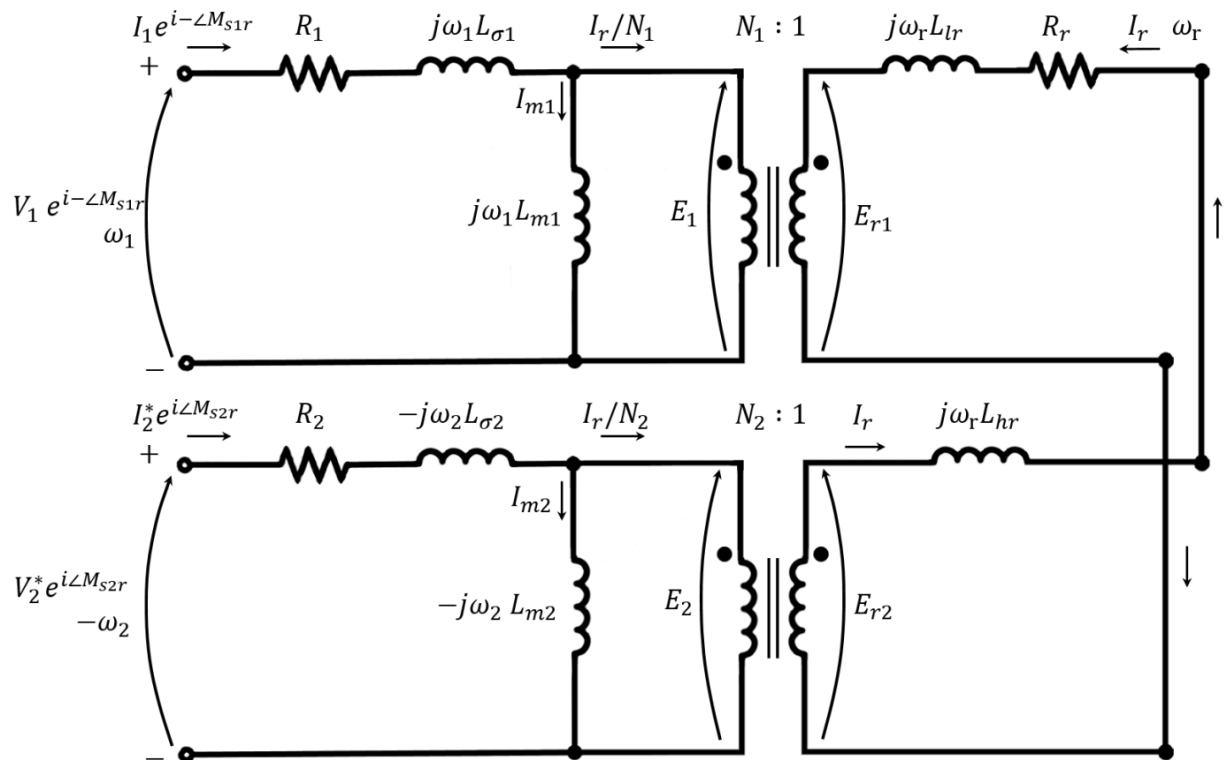


Figure III-7: Per phase equivalent circuit of a BDFM using a transformer representation

III.3.2.4. Mathematical tricks to get the equivalent circuit of the BDFM expressed with the pulsation ω_1

A mathematical trick can now be used to express the equivalent circuit at the pulsation of the PW.

The equivalent scheme is arbitrarily chosen to be expressed on the PW side; it could also be done on the CW side.

First, the CW equations will be expressed with the pulsation ω_1 . From Kirchhoff laws in Figure III-7 on the CW, the CW voltage can be expressed as:

$$V_2^* e^{i\angle M_{s2r}} = R_2 I_2^* e^{i\angle M_{s2r}} - j\omega_2 L_{2\sigma} I_2^* e^{i\angle M_{s2r}} + E_2 \quad (67)$$

From (67), the current going into the equivalent circuit on the CW side is:

$$I_2^* e^{i\angle M_{s2r}} = \frac{V_2^* e^{i\angle M_{s2r}} - E_2}{R_2 - j\omega_2 L_{2\sigma}} \quad (68)$$

The mathematical trick here is that if the numerator and the denominator of the right side of (68) are multiplied by $\frac{s_2}{s_1}$, the current will not change. So, (68) becomes:

$$I_2^* e^{i\angle M_{s2r}} = \frac{\frac{s_2}{s_1} V_2^* e^{i\angle M_{s2r2}} - \frac{s_2}{s_1} E_2}{\frac{s_2}{s_1} R_2 - j \frac{s_2}{s_1} \omega_2 L_{2\sigma}} \quad (69)$$

As the reader may remember $s_1 \omega_1 = \omega_{r1} = -\omega_{r2} = -s_2 \omega_2$. So, $\frac{s_2}{s_1} \omega_2 = -\omega_1$.

Equation (69) becomes:

$$I_2^* e^{i\angle M_{s2r}} = \frac{\frac{s_2}{s_1} V_2^* e^{i\angle M_{s2r}} - \frac{s_2}{s_1} E_2}{\frac{s_2}{s_1} R_2 + j\omega_1 L_{2\sigma}} \quad (70)$$

Equation (70) would be equivalent to a circuit fed with a voltage $\frac{s_2}{s_1} V_2^* e^{i\angle M_{sr2}}$, at the pulsation ω_1 , with a resistance $\frac{s_2}{s_1} R_2$, an inductance $L_{2\sigma}$, and an emf $\frac{s_2}{s_1} E_2$. This trick will allow to express $I_2^* e^{i\angle M_{sr2}}$ in the PW reference frame and then allow to compute $I_2^* e^{i\angle M_{sr2}}$. An important point to remember with this trick is that it conserves the current but it changes the power of the equivalent circuit since it changes the voltage.

The same trick can be applied to the rotor. From Kirchhoff laws in the rotor:

$$E_{r2} - E_{r1} = R_r I_r + j\omega_r (L_{lr} + L_{hr}) I_r \quad (71)$$

From equation (71), the expression of I_r can be expressed as:

$$I_r = \frac{E_{r2} - E_{r1}}{R_r + j\omega_r(L_{lr} + L_{hr})} \quad (72)$$

The mathematical trick here is that if the numerator and the denominator of the right side of (72) are multiplied by $\frac{1}{s_1}$, the current will not change. Equation (72) becomes:

$$I_r = \frac{\frac{E_{r2}}{s_1} - \frac{E_{r1}}{s_1}}{\frac{R_r}{s_1} + j\frac{\omega_r}{s_1}(L_{lr} + L_{hr})} \quad (73)$$

As the reader may remember: $s_1\omega_1 = \omega_r$ so $\frac{\omega_r}{s_1} = \omega_1$.

The relations between the voltages of the two transformers can be written. For the transformer representation between the PW and the rotor, the following can be written:

$$\begin{aligned} \text{So } E_{r1} &= s_1 N_1 E_1 \\ \frac{E_{r1}}{s_1} &= N_1 E_1 \end{aligned} \quad (74)$$

And for the transformer representation between the CW and the rotor:

$$\begin{aligned} \text{So } E_{r2} &= s_2 N_2 E_2 \\ \frac{E_{r2}}{s_1} &= N_2 \frac{s_2}{s_1} E_2 \end{aligned} \quad (75)$$

Equation (73) can be transformed into:

$$I_r = \frac{N_2 \frac{s_2}{s_1} E_2 - N_1 E_1}{\frac{R_r}{s_1} + j\omega_1(L_{lr} + L_{hr})} \quad (76)$$

Equation (76) would be the equation obtained if the rotor had two emf $N_2 \frac{s_2}{s_1} E_2$ and $N_1 E_1$, pulsating at ω_1 , with one resistance $\frac{R_r}{s_1}$, and an inductance $(L_{lr} + L_{hr})$. Once again, the reader must remember that with this trick, the current is conserved which will help to compute it, however, the power in the equivalent circuit is changed! It should not be forgot during the power state computation of the BDFM with the equivalent circuit (this is done in APPENDIX L, p 255). With the mathematical tricks presented in equations (69), (73), and (76), Figure III-7 can now be updated with the introduction in Figure III-8 of the equivalent circuit of the BDFM at the pulsation of the PW. The rotor and the CW pulsations are ω_1 .

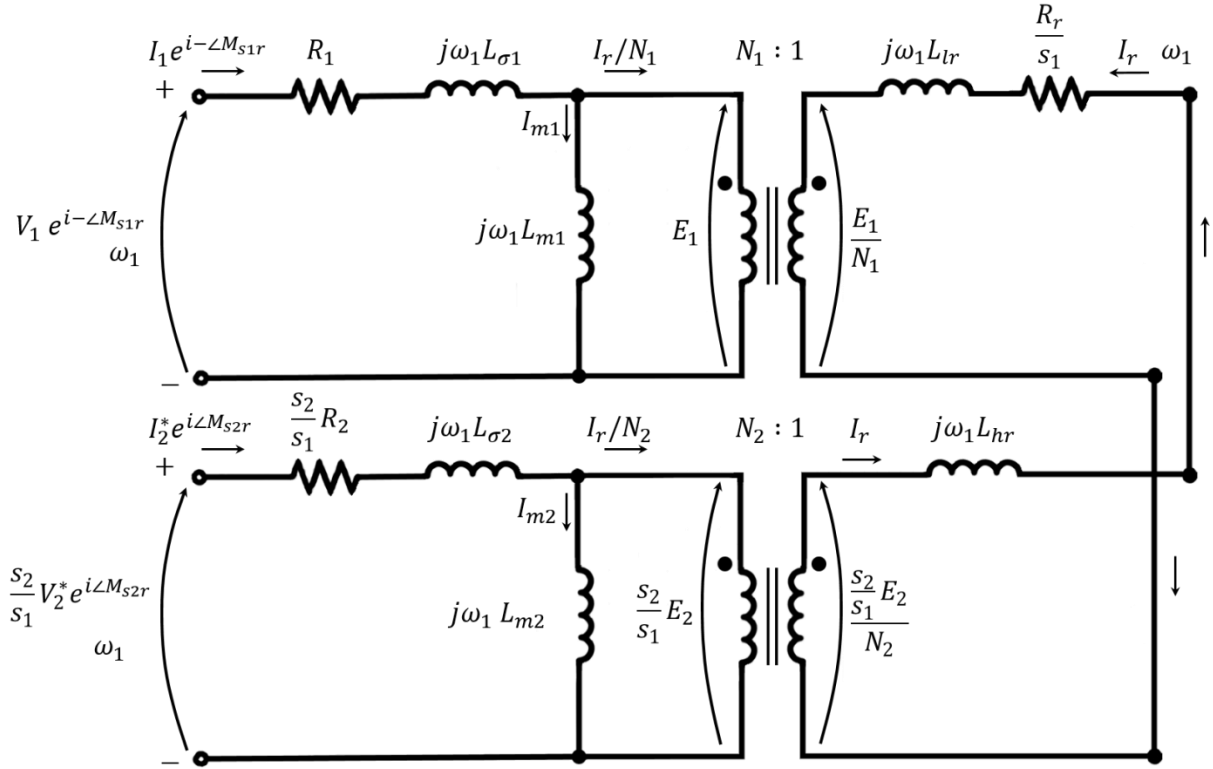


Figure III-8: Per phase equivalent circuit of a BDFM using a transformer representation and with a pulsation ω_1

III.3.2.5. Expression of the equivalent circuit in the power winding reference frame: topology of the new model

The last step to obtain the equivalent circuit of the BDFM that will be used in the rest of this work will be to express the equivalent circuit in the PW reference frame. To do so, new variables will be defined:

$$\begin{aligned}
 V_{1eq} &= V_1 e^{i\angle -M_{s1r}} \\
 I_{1eq} &= I_1 e^{i\angle -M_{s1r}} \\
 I_r' &= \frac{I_r}{N_1} \\
 R_r' &= N_1^2 R_r \\
 L_{lr}' &= N_1^2 L_{lr} \\
 L_{hr}' &= N_1^2 L_{hr} \\
 L_{\sigma r}' &= L_{lr}' + L_{hr}' \\
 V_{2eq}'' &= \frac{N_1}{N_2} V_2^* e^{i\angle M_{s2r}} \\
 I_{2eq}'' &= \frac{N_2}{N_1} I_2^* e^{i\angle M_{s2r}} \\
 I_{m2}'' &= \frac{N_2}{N_1} I_{m2}
 \end{aligned}$$

$$R_2'' = \frac{N_1^2}{N_2^2} R_2$$

$$L_{\sigma 2}'' = \frac{N_1^2}{N_2^2} L_{\sigma 2}$$

$$L_{m 2}'' = \frac{N_1^2}{N_2^2} L_{m 2}$$

With these definitions, the equivalent circuit of the BDFM expressed on the stator side can be drawn.

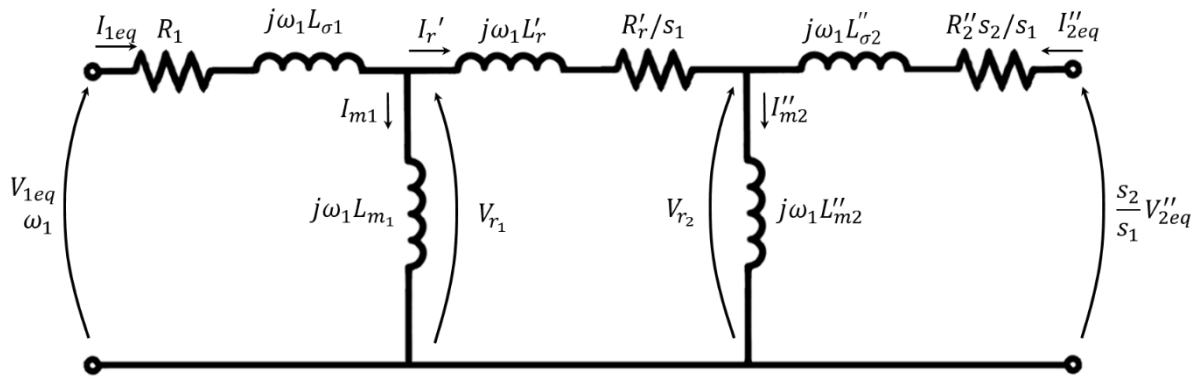


Figure III-9: Equivalent circuit of the BDFM in the PW reference frame. Watch out, as explained with equation (70) and (76), the power that goes into the equivalent circuit is not the power that goes into the BDFM. The power that goes into the BDFM is calculated with $Re(V_{2eq}'' I_{2eq}''^*)$ as demonstrated in APPENDIX L, p 255.

The new equivalent circuit of Figure III-9 can be compared to the equivalent circuit of [32], [38], or [83]. The equivalent circuit used in [32] was already presented in Figure I-11, p 36. The main differences are that the imposed voltage of the command winding and the related current need to be the conjugate complex from the one in [32]. If the conjugate complex is not taken, then there will be different induced pulsations in the equivalent scheme rotor part. It can be noted that the equivalent schemes of [38] and [83] did not consider the phase of the mutual inductance between the stator windings and the rotor. This phase is considered in [32], but the complex conjugate of the CW voltages and current is not taken in [32]. The results difference between the equivalent circuit presented in [32] and the equivalent circuit presented in Figure III-9 will be shown in the figures in III.3.6, p 100.

III.3.3. Determination of the equivalent circuit parameters with electrical tests inspired by a common method used for induction machines

A new method for the extraction of the parameters of the equivalent circuit of the BDFM (presented in Figure III-9) was developed. Previous methods were found in the bibliography, one uses torque-speed characteristics obtained with self-cascaded tests (one stator winding in short-circuit), and simple induction tests (one stator winding in open-circuit). This method found in [82] is paired with a Monte Carlo optimization algorithm. Monte Carlo algorithms do not use the 1st derivative of problems to find optimums: they are not 1st order optimization algorithms. Other former methods

were based on multi-frequencies measurements of voltages and currents, these methods are described in [84] and [85].

The idea behind the method developed during this work was to make a method comparable to the method to extract the parameters from Induction Machines. For Induction Machines, it is possible with a few simple electrical tests, only measuring the voltages and currents, to extract the parameters of the equivalent circuit. The simple electrical tests used for the Induction Machines are the blocked rotor test (to extract the rotor resistance and the leakage reactances) and the no-load test (the rotor rotates at the synchronism speed to extract the magnetizing reactance). For more information about the extraction of parameters for Induction Machines, one can refer to APPENDIX J, p 243. For a BDFM, it is also possible to implement a no-load test and blocked rotor tests. With the equations resulting from these tests, there are more independent equations than parameters to extract. Thus, it is possible to extract the parameters of the equivalent circuit of the BDFM with the voltages and currents measurements from these tests. The full method is described in APPENDIX K, p 247.

III.3.4. Implementation in a 1st order analytical optimization software (CADES) of the method to determine the equivalent parameters

To extract the equivalent circuit parameters an optimization problem with a 1st order algorithm was implemented based on the equations from (192), p 253, presented in APPENDIX K. The extraction implied 6 electrical tests: 2 no-load tests, 2 blocked rotor tests in self-cascaded mode (one stator winding is short-circuited) and 2 blocked rotor tests in induction mode (one stator winding is in open-circuit). More details can be found in APPENDIX K.

The objective function to be minimized was the sum of squared errors of equations in (192). At the first iteration, random parameters are given to the algorithm. The objective function computes how far from the electrical results these random parameters are, and then changes the parameters in subsequent iterations to decrease the error. Since the problem has many local optimums, 50 optimizations with different random starts were launched for each extraction (the extractions made for the validation of the method and the extraction for the machine presented in Table III-1 with results given in Table III-18). Each optimization was only taking seconds, the whole process was only a few minutes long.

For the validation of this parameter extraction method, imaginary electrical tests were created from imaginary equivalent circuits. Equivalent circuits were created with random values assigned to the parameters. With equations from (192), p 253 it was then possible to compute the voltages and currents the 6 electrical tests would have given for a machine with such parameters. Finally, using the extraction method previously described, it was verified that it was able to find the parameters initially assigned to the equivalent scheme.

Once validated, the extraction method was used to extract the parameters of the BDFM presented, in Table III-1, p 77. The results are presented in Table III-18. These parameters will be used for the comparison of the new equivalent scheme with FE methods in III.3.6.

Table III-18: Results of the equivalent circuit parameter extraction of the BDFM presented in Table III-1. The results are presented in Ohms, at the frequency of 50 Hz for the equivalent scheme in Figure III-8 without saturation.

Average Error (in %) on the currents of the electrical tests	0.29%
Parameters	
$R1$ (Ohm)	0.1206
$X1_{50} = 2\pi 50 \cdot L_{\sigma 1}$ (Ohm)	4.673
$Xm1_{50} = 2\pi 50 \cdot L_{m1}$ (Ohm)	18.001
Rr (Ohm)	0.9727
$Xr_{50} = 2\pi 50 \cdot L_{\sigma r}$ (Ohm)	1.406
$Xm2_{50} = 2\pi 50 \cdot L_{m2}$ (Ohm)	39.345
$R2$ (Ohm)	0.15142
$X2_{50} = 2\pi 50 \cdot L_{\sigma 2}$ (Ohm)	4.484
transformationRatio1R	1.249
transformationRatio2R	1.069

III.3.5. Taking saturation and iron losses into account in the equivalent scheme

As for the induction machine, saturation could be considered through a decrease of the magnetizing reactances depending on the saturation level. For the induction machine, a saturation factor was introduced and computed semi-analytically (see the determination of the saturation factor for the induction machine in APPENDIX F, p 189). This saturation factor was used to correct the magnetizing reactance which gave sufficiently accurate results to account for the saturation effect on the machine behavior (as shown in Figure II-5, p 59).

For the BDFM it is much harder to define a saturation factor as it was done for the induction machine. The addition of the two magnetic fields which have a different number of poles creates an intricate saturation pattern.

One idea during this work that could not be investigate was to use additional load-tests under saturation. The voltages and currents of these load tests would then have been used to determine the evolution of the magnetizing inductances parameters of the equivalent scheme. Knowing the evolution of these parameters as a function of the input voltage and frequencies (as for the Figure II-5, p 59, but this time, the inputs are in 3 dimensions since both the voltages of the PW and CW can vary and the pulsation of the CW can also vary). Knowing the evolution of both the PW and CW magnetizing reactances in function of the PW and CW voltages and CW frequency, it would then be possible to develop and adjust an analytical model to emulate the saturation impact.

The iron losses of a BDFM can be represented in the equivalent circuit by a resistance in parallel with each magnetizing inductance as shown in Figure III-10. As for the magnetizing inductances, these two resistances would vary as a function of saturation (as a function of the PW and CW voltages).

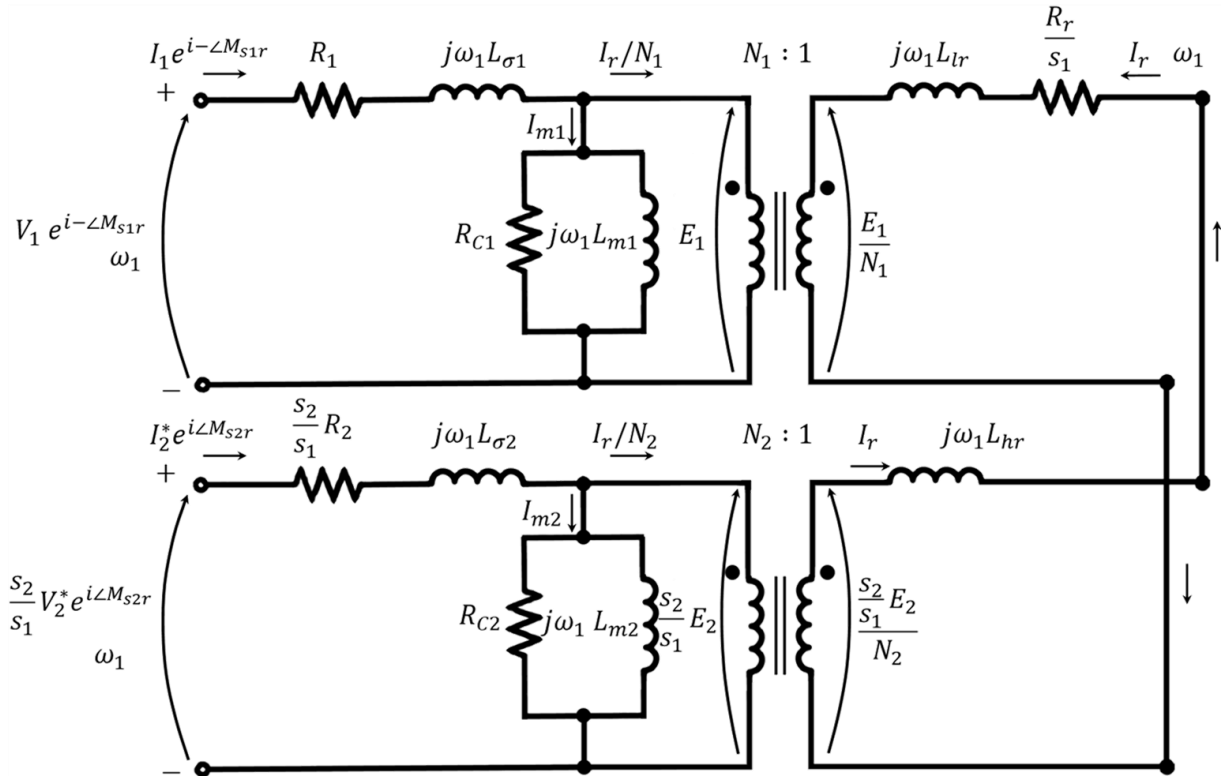


Figure III-10: Adaption of Figure III-8 with the addition of the resistances of the iron losses, in parallel to the magnetizing inductances

III.3.6. Results comparison between the new model, previous models, and FE methods

In this part, a few figures will be shown to help the reader to understand how the changes made in the equivalent circuit model (in comparison to the equivalent circuit model of [32] for example) impacts the results. It will be explained why the previous models were able to do accurate predictions on self-cascaded and induction modes but were not able to do the same for load points. The figures will always show the result from the new equivalent circuit in green, the results from the FE simulations in blue, and the result from the previous equivalent circuit in red (equivalent circuit presented in [32]).

The two equivalent circuit parameters are set from the parameters extracted through self-cascaded, simple induction, and no-load test (presented in III.3.3 and III.3.4, the parameters can be found in Table III-18, p 99).

Each figure presented in this part has hundreds of points for the FE results. It would not have been possible to compute all these results with Flux2D magneto-transient applications. They were computed without saturation with the “fast model” developed and presented in III.4.

In the first following Figure III-11 and Figure III-12, cases where the previous and new equivalent circuit lead to the exact same result are presented.

As already explained, the difference between the equivalent circuit representation of [32] and the new representation impacts the phases of the PW and CW voltages and currents. It is interesting to note that, from electrical considerations on the equivalent circuit, if the PW and CW are fed by voltage sources, it is the phase shift between the PW and CW that will influence the exchange of power in the BDFM. If the phases of the PW and CW change but their phase shift remains unchanged in the

equivalent circuit, the power exchange of the BDFM will remain constant. This explains why the difference between the previous equivalent circuit representation and the new one will only appear when the phase shift between the PW and CW is imposed (in load cases) or observed (if it is observed in self-cascaded or simple induction mode). In the cases of self-cascaded mode or simple induction mode (one winding is either short-circuited or in open-circuit), the measurements are all made on one winding only. The phase shift is neither imposed nor observed, thus the two representations will give the exact same results. Such an example is given in Figure III-11 for example. Figure III-11 shows the evolution of the amplitude of the PW current, during a load test, depending on the phase of the PW voltage. This figure was done in the special case where the rotor is not offset at “ $t = 0$ ” and the control winding not offset neither. A load test was more interesting than a self-cascaded case since for a self-cascaded test, the current amplitude would remain constant when the PW voltage phase varies.

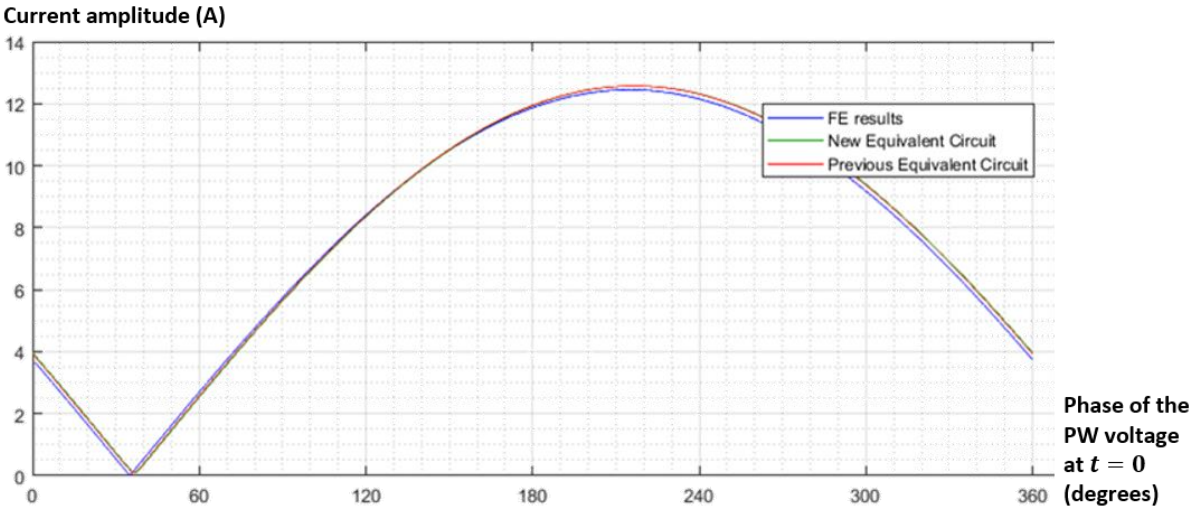


Figure III-11: Amplitude of the PW current, for load tests, depending on the phase of the PW feeding voltage at $t = 0$

For the same load tests, as in Figure III-11, it is possible to compare the amplitude of the CW current depending on the variation of the phase of the PW feeding voltage. Since only the phase of the CW is inverted in the new equivalent circuit, the phase shift between the two windings will be the same for the two equivalent circuits. As in Figure III-11, the previous equivalent circuit and the new equivalent circuit will give the indistinguishable results in Figure III-12.

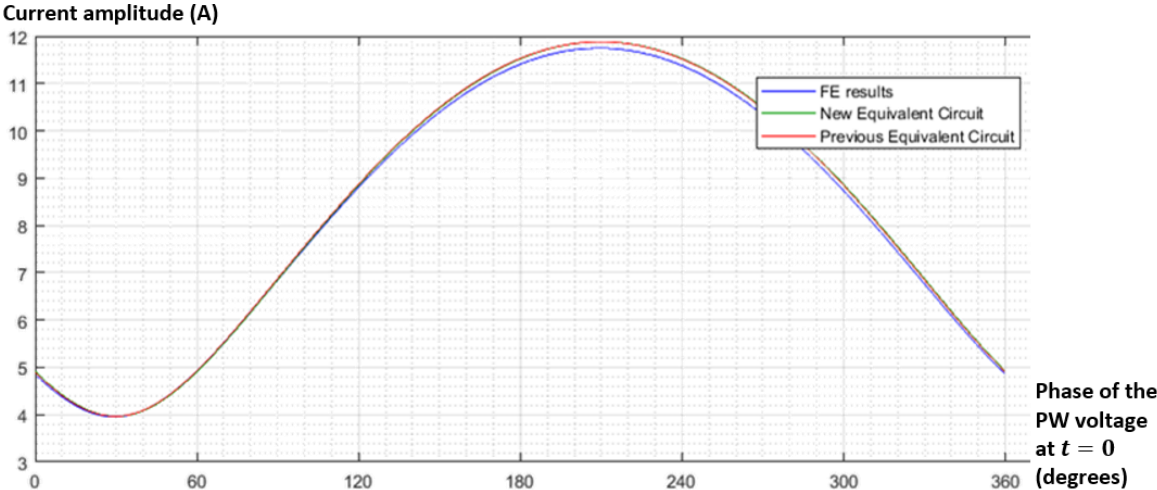


Figure III-12: Amplitude of the CW current, for load tests, depending on the phase of the PW feeding voltage at $t = 0$

The same logic cannot be applied if it is the phase of the CW feeding voltage at $t = 0$ that varies. In fact, in the new equivalent circuit, the phase applied on the CW side is minus the phase applied in the previous equivalent circuit. This will have an impact on the amplitude of the PW current (as shown in Figure III-13) and CW current (as shown in Figure III-14).

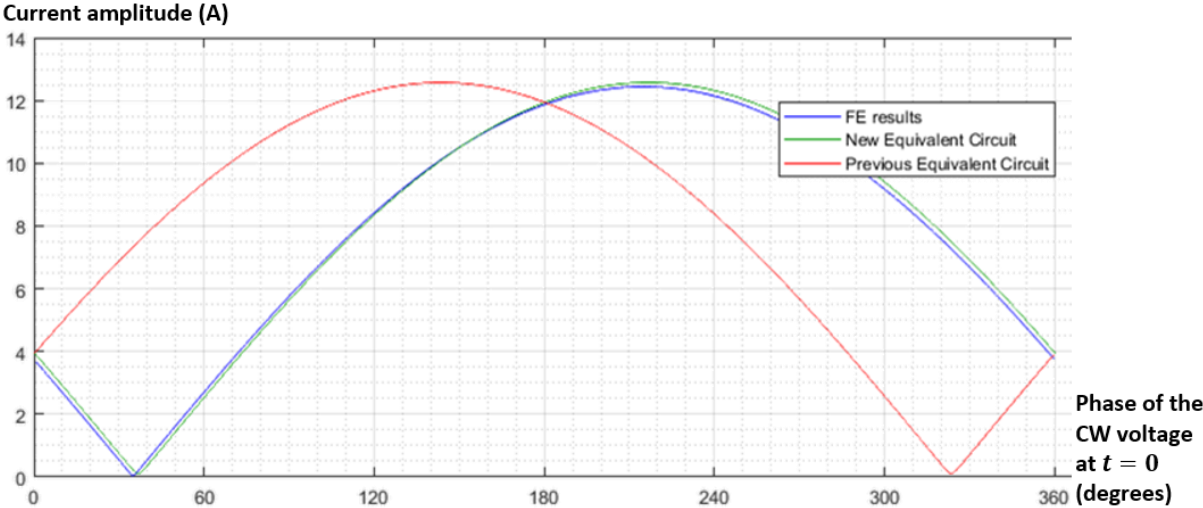


Figure III-13: Amplitude of the PW current, for load tests, depending on the phase of the CW feeding voltage at $t = 0$

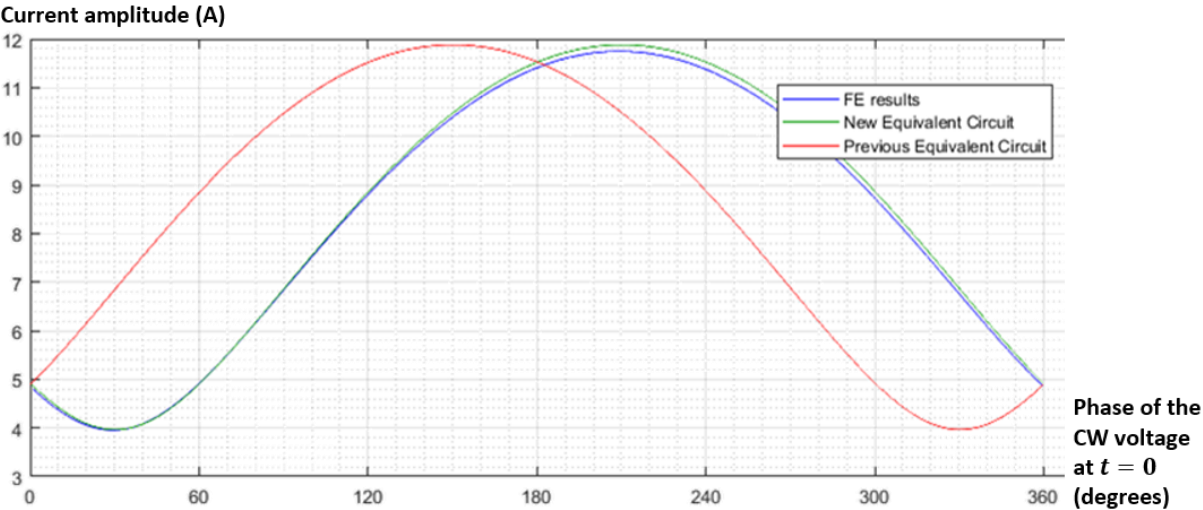


Figure III-14: Amplitude of the CW current, for load tests, depending on the phase of the CW feeding voltage at $t = 0$

In the equivalent circuit, a rotation of the rotor at $t = 0$ has an impact on the two mutual inductances between each stator winding and the rotor. Since these mutual inductances are considered differently in the two equivalent circuits, the impact of the rotor rotation will be different. This is shown in Figure III-15 and Figure III-16.

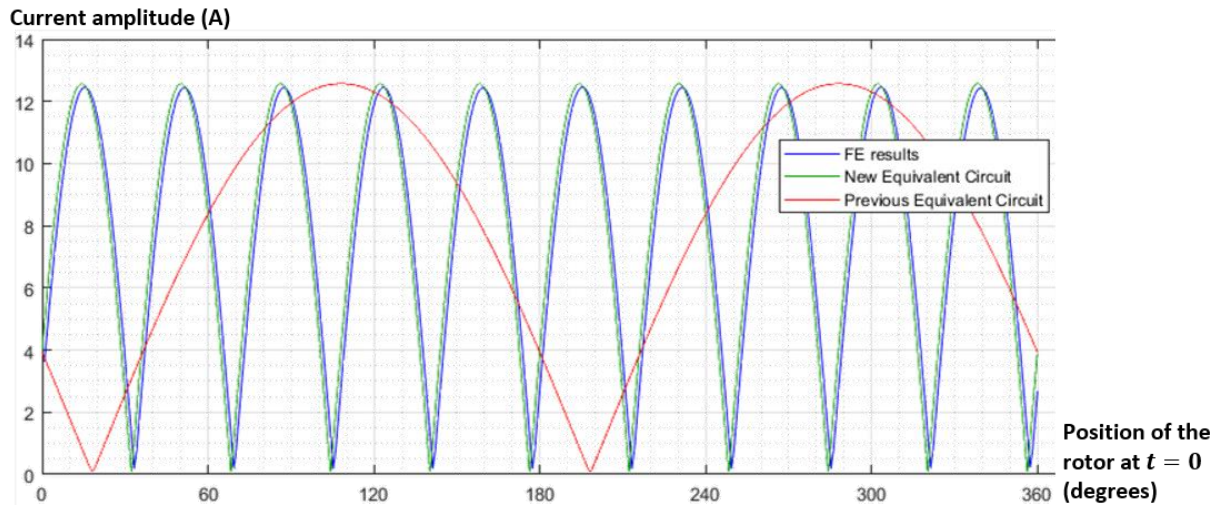


Figure III-15: Amplitude of the PW current, for load tests, depending on the position of the rotor at $t = 0$

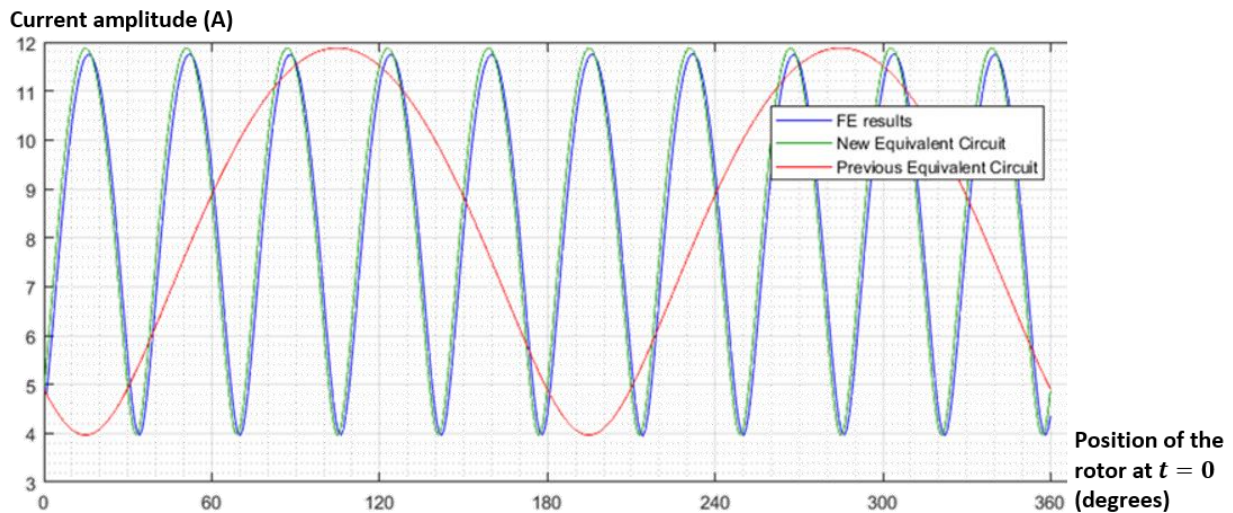


Figure III-16: Amplitude of the CW current, for load tests, depending on the position of the rotor at $t = 0$

In Figure III-15 and Figure III-16, it can be noted that the new equivalent circuit representation results have once again a good correlation with the FE results. It is not the case of the previous equivalent circuit. To understand Figure III-15 and Figure III-16, it is helping to remind here that the BDFM being simulated has for the PW: $p_g = 6$ pole pairs, and for the CW: $p_c = 4$ pole pairs. In the two figures, the new equivalent circuit behave as expected; the number of nests: $N_r = p_g + p_c = 6 + 4 = 10$ can be counted on the electrical response for a 360° rotor rotation. The previous equivalent circuit behave as if the number of nests was only: $N_r = 6 - 4 = 2$ which is wrong (the number of sine wave periods in Figure III-16 is 10 for the blue and green curves and 2 for the red curve).

Instead of looking at the amplitude of the currents of the stator windings as in Figure III-15 and Figure III-16, the phase of one stator winding current depending on the position of the rotor at $t = 0$ (as shown in Figure III-17) can be directly observed.

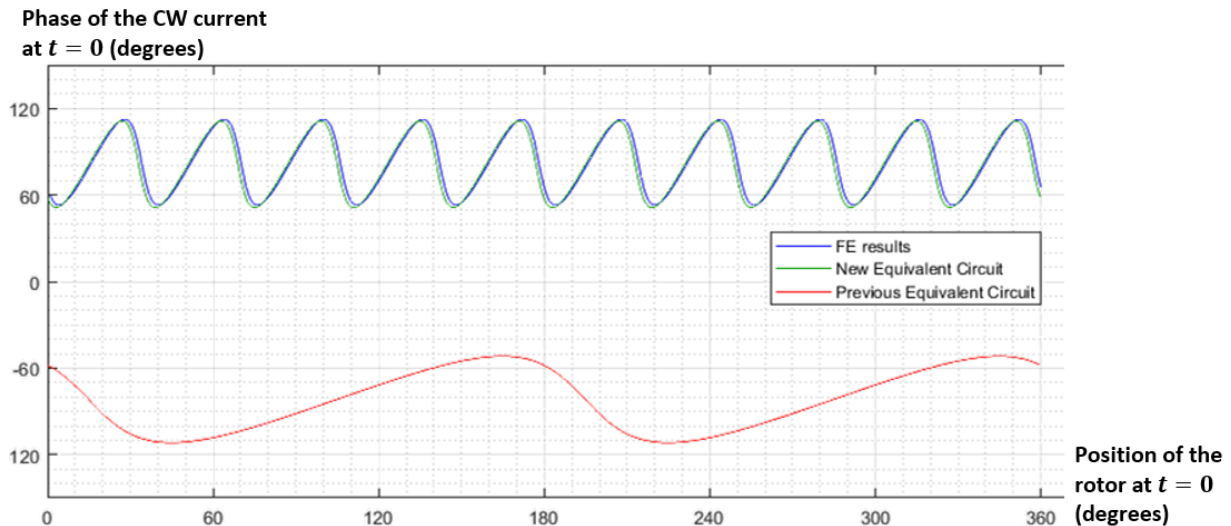


Figure III-17: Phase of the CW current, for load tests, depending on the position of the rotor at $t = 0$

Figure III-17 shows once again that the previous equivalent circuit behave as if the BDFM had a number of nests $N_r = 2$, instead of $N_r = 10$.

III.4. Development of a fast model: FE based coupled-circuit method, using the expressions of the mutual inductances as functions of the rotor position

III.4.1. An FE based method inspired by the analytical coupled-circuit method

In II.3.2.1, p 65, the analytical coupled-circuit method was presented. In the analytical coupled-circuit method, all the mutual and self-inductances of the two stator windings and the rotor nested-loops are analytically computed. With all these inductances and with all the resistances, it is then possible to solve the circuit equations with the two stator voltages as inputs for example.

Being analytical, the analytical coupled-circuit method is long to implement. Descriptions of this method applied to BDFM can be found in the literature (for example in [31], and [32]), but it is not publicly available directly coded in a program. To use this method for computation, one still has to understand it and code it in a software; this requires months of work and expertise.

As already explained in II.3.3, p 68, one of the bottlenecks for the study of a BDFM is that it is much more time consuming to simulate with FE methods than usual electrical machines. A BDFM requires transient simulations over long electrical periods (refer to extended explanations in II.3.3).

The first idea, to create faster FE simulations, was to create a method analogous to the analytical coupled-circuit method but with FE computations instead of analytical calculations. All the mutual and self-inductances between the two stator windings and the rotor nested-loops can be computed with FE simulations as functions of the rotor position. With FE simulations, it is possible to compute mutual inductances between windings with magneto-static applications. These applications are much faster to compute than magneto-transient applications. Then, as for the analytical coupled-circuit method, these mutual inductances can be used to solve the circuit equations depending on the stator voltages

and the rotor position. The solving process is analogous to the solving process of a magneto-transient application: for each step, the circuit equations are solved.

For the BDFM with the specifications presented in Table III-1, p 77, it took around 10 minutes to extract the mutual inductances for the 1440 different rotor positions (10 positions per stator slot) with an FE software developed in GE. Then once adapted into MATLAB, the solving of electrical circuit equations, to simulate hundreds of load cases with thousands of steps for each load case (to plot Figure III-11 to Figure III-17 and other figures) only took a few minutes. If magneto-transient FE simulations had been used to plot these figures, each simulation would have taken over a day, each figure would have taken months of computation.

III.4.2. Advantages and disadvantages of the FE based coupled-circuit method over the analytical coupled-circuit method

III.4.2.1. Advantages

As just explained in III.4.1, the FE based coupled-circuit method is faster to implement than the analytical coupled-circuit method. The analytical coupled-circuit method requires more work and expertise. The FE based method requires an FE software and the knowledge on how to use it. Many user-friendly FE software are available and commonly used by the scientific community.

Another advantage of the FE based method is that it remains simple to implement without requiring as many simplifying hypotheses as for the analytical coupled-circuit method. For example, the most developed analytical coupled-circuit method for the BDFM to the best of the author's knowledge (in [32]) made the following simplifying hypotheses:

- The stator and rotor iron are considered to have an infinite permeability.
- The flux lines in the airgap are radial.
- The airgap is "smooth" with a cylindrical stator and a cylindrical rotor (the tooth effect is neglected). The airgap radial length is computed with Carter's Factor.
- The conductors have a zero depth and a finite width.
- The leakage effect is added with self-inductance terms only.

With the FE based method, the iron permeability can be considered (without saturation). The flux lines in the airgap are not imposed to be radial. The real airgap is considered, with the stator and rotor teeth. The conductors are considered with their real shape and the leakage inductance is, of course, accounted for in the auto and mutual inductances measured.

III.4.2.2. Disadvantages

One of the disadvantages of the FE based method is that, since it is not an analytical method, it cannot be paired with a 1st order optimization algorithm. Thus, optimization will need to be performed with an algorithm that does not use derivatives.

On the contrary, the analytical coupled-circuit method could theoretically be paired with a 1st order optimization algorithm. This has never been done in the case of the BDFM to the best of the author's knowledge. As already explained in II.3.2.1, p 65, there would still be limitations for the optimizations of a BDFM with the analytical coupled-circuit method, since this method does not account for saturation. Moreover, it is not possible to explore the set of imaginary machines with the analytical coupled-circuit method since the equations are based on a geometry that must have a physical representation (the concepts of imaginary and real machines were presented in II.2.3.7.1, p 61). Unlike the semi-analytical model for the Induction Machine presented in APPENDIX F, the discrete parameters cannot be linearized in the coupled-circuit method. So, optimizations on the number of poles and other discrete parameters are not possible with analytical coupled-circuit methods paired with 1st order optimization algorithms.

III.4.3. Validation of the FE based coupled-circuit method and applications in this work

For the validation of the FE based coupled-circuit methods, several load tests of the BDFM with the specifications presented in Table III-1, p 77 were computed with Flux2D magneto-transient applications. The results of one load test without saturation are presented in Table III-19.

Table III-19: Validation of the FE based coupled-circuit method. Comparison, for a linear load case of the phase-neutral voltages, currents amplitudes, and phase of the currents for the phase A of the PW and CW

	Power Winding			Control Winding		
	$V: [V]$	$I: [A]$	$\angle I: [Rad]$	$V: [V]$	$I: [A]$	$\angle I: [Rad]$
Flux2D 1-night simulation	99,97	3,27	0,401	40,00	4,577	1,09
Flux2D 1-day simulation	99,99	3,39	0,395	40,00	4,635	1,07
Flux2D 5-day simulation	100,00	3,49	0,390	40,00	4,685	1,06
FE based coupled-circuit	100,00	3,65	0,388	40,00	4,795	1,05

In Table III-19, the results of three different Flux2D magneto-transient simulations are presented. These three simulations were done for the exact same load test and for the same geometry. The only difference was the number of time-steps. In the 3rd simulation, the number of time-steps was 10 times higher than in the 1st simulation (1st simulation: period simulated: 0.12 s, time step: 0.0001 s, 1 200 iterations; 3rd simulation: period simulated: 0.12 s, time step: 0.00001 s, 12 000 iterations). As it can be seen, the results between the 1st and the 3rd simulation are different by almost 10 % for the PW current. This is due to a convergence problem: from Table III-19, it is certain that the 1st simulation did not converge. It is not certain that the 3rd simulation obtained after 5 days of computation has a time-stepping small enough to be converged (to be certain a new simulation with a smaller time-stepping

would need to be carried out and give the same results). So, the results obtained with FE magneto-transient simulations should be taken with caution. Still, it can be noted that the results of the FE based coupled-circuit method and the results of the most intricate FE magneto-transient simulation are closely correlated (difference lower than 5 %).

To summarize the advantages and disadvantages of the FE based coupled-circuit method, for a BDFM this method is much faster than FE magneto-transient applications to compute load-tests. The difference in speed can be of several orders of magnitude. The major drawback is that it does not take saturation into consideration.

During this work, the method was used in the cases where hundreds of load tests had to be simulated. For example, for the comparison between FE results and the equivalent scheme from Figure III-11 to Figure III-17, p 101 to 104.

This FE based method has also been used for the iterative improvement of the BDFM design in IV.4, starting p 154.

In order to consider saturation and be faster than magneto-transient application, a new FE method will be developed in III.5.

III.5. A model that considers saturation based on FE magneto-harmonic simulations

The FE based coupled-circuit method, that was presented in III.4 proved to be very fast in comparison to the FE magneto-transient method for computing load tests of a BDFM. The major drawback of this method was its inability to consider saturation. Saturation is a very important phenomenon that should be considered during the design phase of an electrical machine (as already explained in II.2.3, p 52). This is the reason why another FE approach is investigated in this paragraph. This time, the idea was to adapt FE magneto-harmonic simulations, a magneto-harmonic simulation method for the BDFM will be developed.

III.5.1. Principles of FE magneto-harmonic simulations in Flux2D

The knowledge presented here, the fundamental principles behind magneto-harmonic applications and the calculation of the equivalent permeability for each element of the mesh, is based on Flux2D help documentation. In the equivalent permeability explanations, some bibliography is shared by the help documentation for complementary information and is reported in this Ph.D.: see [86], [87], and [88].

Magneto-harmonic simulations are designed to compute steady states. Instead of solving a problem time step by time step, as in magneto-transient simulations, the problem is solved in one step. The sources are considered sinusoidal all at the same frequency. Doing so, the solving can be much faster than a magneto-transient simulation; instead of hundreds or thousands time steps, only one is needed.

Since a magneto-harmonic simulation is solved in one step for a whole period, the permeability of each element of the mesh is fixed to a given value for the solving. In the case without saturation, this does not pose any challenge, since the permeability is the same for each mesh element of the same material and is equal to the permeability of the material without saturation. In the case of saturation, an equivalent permeability is computed iteratively for each mesh element.

The process to iteratively compute the equivalent permeability for each mesh element will have to be adapted for the BDFM case. First, the following part will explain how it works when all the sources have the same frequency. Then, the method will be adapted to cases with two different frequencies.

III.5.2. Computation of the equivalent permeability

As already explained, a magneto-harmonic simulation is solved in one step with several iterations for the computation of the equivalent permeability of each mesh element. On the first iteration, the equivalent permeability of each mesh element is set to the non-saturated equivalent permeability as shown in Figure III-18 (in green).

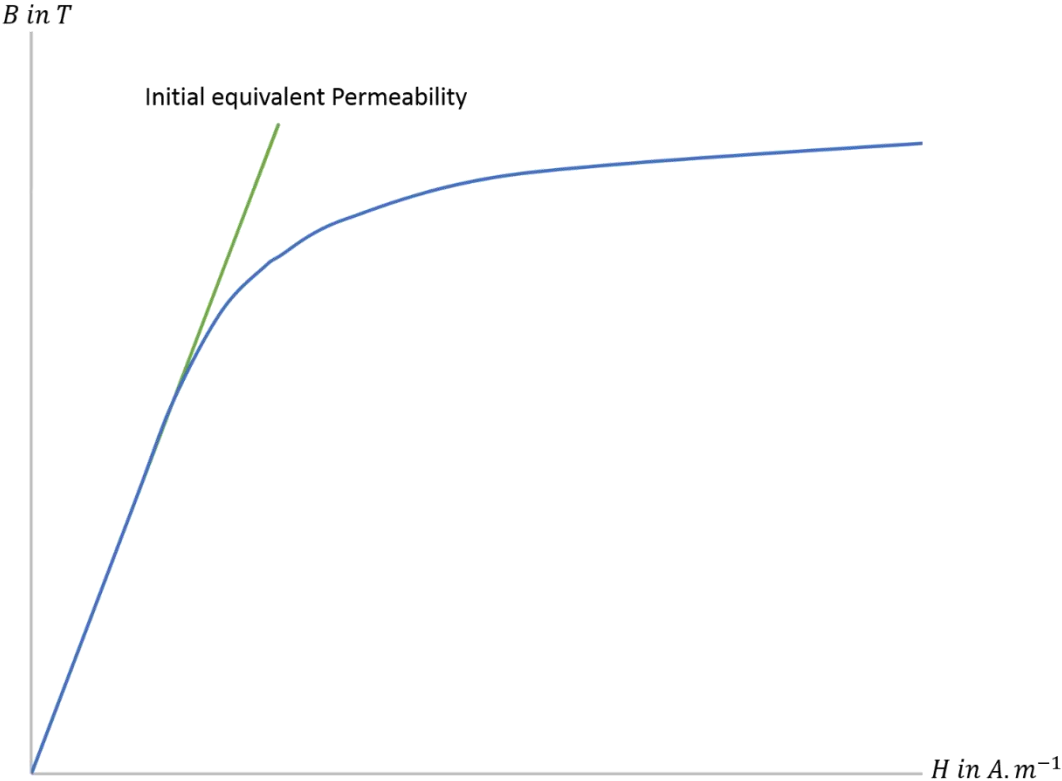


Figure III-18: Saturation B(H) curve of a material and equivalent permeability of each mesh element for the first iteration during the solving of a magneto-harmonic simulation

In each iteration, the equivalent permeabilities of each mesh element are set to a given value. The magnetic state of the machine is then computed in each element for an electrical period.

During an electrical period, the absolute value of the flux density in each element has the shape of a rectified sine wave. This is shown in Figure III-19. What matters for our understanding is the shape of the curve in Figure III-19 (not the actual values on the example of Figure III-19). During an electrical period, the absolute flux density of each element reaches a maximum noted B_{max} in Figure III-19. This

maximum flux density is used to compute the equivalent permeability of the considered mesh element in the following iteration. The minimum value is ignored, as if it was equal to 0.

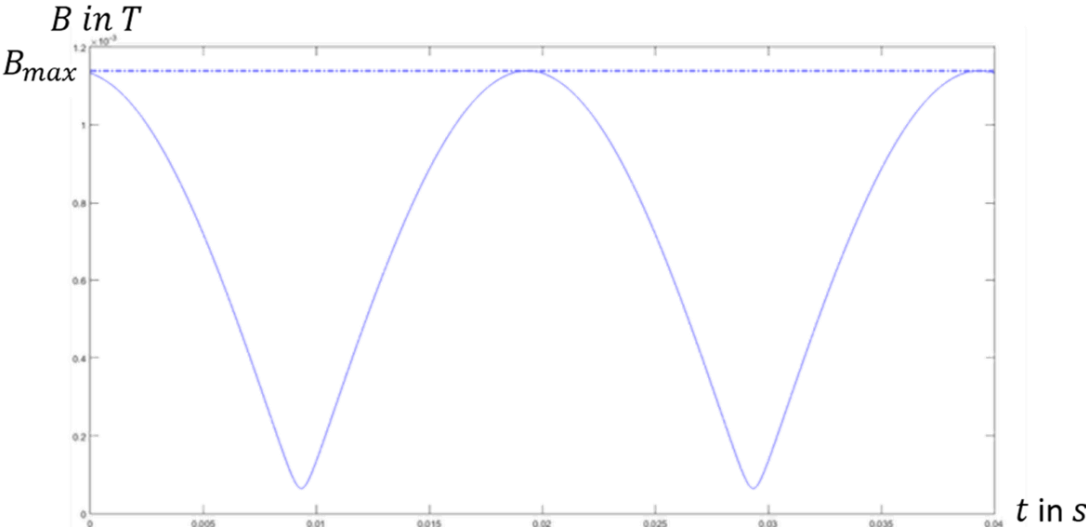


Figure III-19: Absolute flux density in one mesh element of a rotating machine during an electrical period

The value of B_{max} is reported on the $B(H)$ saturation curve. The coenergy (the magnetic energy covered per cycle) if the material was not linear can then be computed with the formula:

$$E'_{cycle\ nonlinear} = \int_0^{B_{max}} H(B)dB \tag{77}$$

$E'_{cycle\ nonlinear}$ is the magnetic energy per cycle and per volume for the nonlinear material. This coenergy can be observed in Figure III-20.

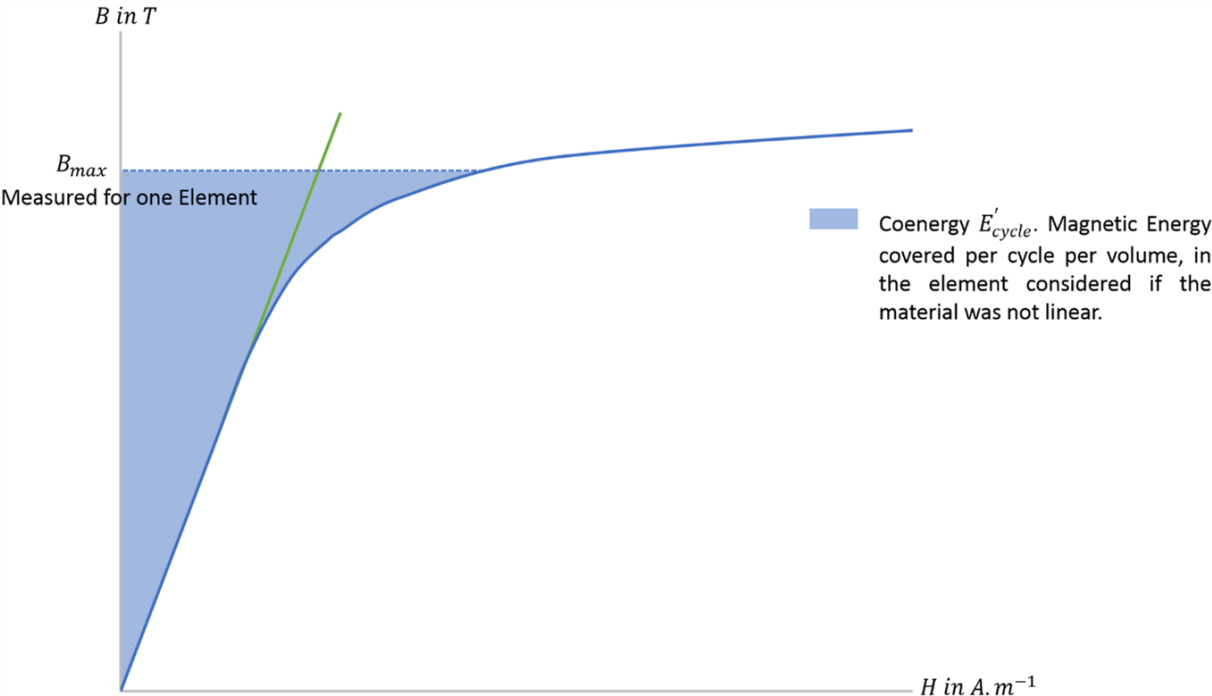


Figure III-20: The coenergy (area in blue): the magnetic energy covered per cycle, per volume, for the mesh element being considered if the material was not linear, from the maximal absolute flux density computed

A new equivalent permeability is computed such that the coenergy of the linear material is equal to the coenergy of the nonlinear material: the yellow area from Figure III-21 is equal to the blue area from Figure III-20. The coenergy for the linear material is easy to compute since the permeability is a constant:

$$E'_{cycle\ linear} = \frac{1}{2} \cdot H_{max} \cdot B_{max} = \frac{1}{2} \cdot \mu_{eq_{n+1}} \cdot H_{max}^2 = \frac{1}{2\mu_{eq_{n+1}}} \cdot B_{max}^2 \quad (78)$$

$E'_{cycle\ linear}$ is the magnetic energy per cycle and per volume for the linear material.

H_{max} is the maximum magnetic field for which the maximum flux density is reached.

$\mu_{eq_{n+1}}$ is the equivalent permeability of the mesh element considered for the next iteration of the magneto-harmonic solving.

The combination of equations (77) and (78) leads to:

$$\mu_{eq_{n+1}} = \frac{1}{2} \cdot \frac{B_{max}^2}{\int_0^{B_{max}} H(B) dB} \quad (79)$$

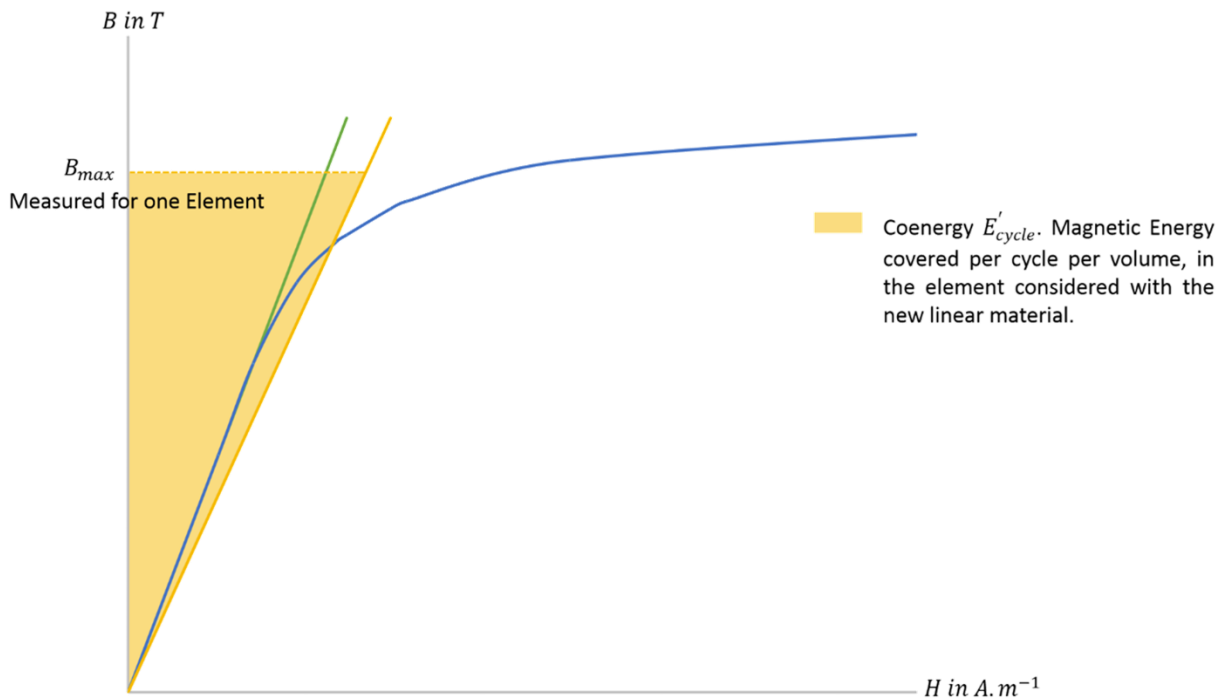


Figure III-21: The coenergy of the linear material (area in yellow): The magnetic energy covered per cycle, per volume, for the mesh element being considered if the material was not linear, from the maximal absolute flux density computed

After a few iterations, the equivalent permeability converges for each mesh-element and the final magneto-harmonic results are obtained.

III.5.3. Idea to use FE magneto-harmonic simulations with two different frequencies

The fundamental principles behind the magneto-harmonic simulations were exposed in III.5.1. Magneto-harmonic simulations are done with sources at one frequency only. The main reason is that the process of determining the iterative equivalent permeability of each mesh elements (explained in III.5.2) only work for one frequency. This is the reason why it cannot be applied as such to the BDFM. In fact, a BDFM has two stator windings, each fed at a different frequency.

In the following part, the process that was implemented in this work to carry out magneto-harmonic simulations for load tests of a BDFM will be presented. First, it will be implemented without taking saturation into account (III.5.4). Then, the iterative method to compute the equivalent permeability will be adapted in the case of sources with two different frequencies (III.5.5).

III.5.4. Magneto-harmonic simulations for the BDFM technology, a method to compute the mutual interactions

In the case without saturation, it would theoretically be possible to create a magneto-harmonic application which could deal directly with several frequencies for the sources. It would solve the same equations but deal directly with several frequencies.

The FE software used to apply the magneto-harmonic method here, Flux2D, cannot consider multiple frequencies for a magneto-harmonic simulation. In this part, it will be explained how it is possible to emulate a magneto-harmonic simulation with two different frequencies from two magneto-harmonic simulations with only one frequency each.

III.5.4.1. Two magneto-harmonic simulations with one frequency each to emulate a magneto-harmonic simulation with two frequencies

To launch a load test of a BDFM without saturation, two magneto-harmonic simulations are used. In the first magneto-harmonic simulation, only the PW is fed with voltages at his own frequency. In this simulation, the CW is in open-circuit. Saturation is not yet considered: the simulation is done with the equivalent permeability without saturation. The induced voltages of the CW are taken as outputs. The amplitudes of the CW voltages are wrong since they are given as if they were induced at the PW frequency; they must be corrected since they are induced at the CW frequency:

$$V_{c_{induced}} = V_{c_{magneto\ harmonic\ 1}} \cdot \frac{\omega_c}{\omega_g} \quad (80)$$

$V_{c_{induced}}$ are the CW corrected induced voltages.

$V_{c_{magneto\ harmonic\ 1}}$ are the CW induced voltages outputs of the 1st magneto-harmonic simulation.

ω_c and ω_g are the electrical pulsations of the CW and PW respectively.

During the second magneto-harmonic simulation, only the CW is fed with voltages at his own frequency. The PW is in open-circuit. Saturation is not yet considered: the simulation is done with the equivalent permeability without saturation. The induced voltages of the PW are taken as outputs. The amplitudes of the PW voltages are wrong since they are given as if they were induced at the CW frequency; they must be corrected since they are induced at the PW frequency. So as in (80), the corrected PW induced voltages can be expressed:

$$V_{g_{induced}} = V_{g_{magneto\ harmonic\ 2}} \cdot \frac{\omega_g}{\omega_c} \quad (81)$$

$V_{g_{induced}}$ are the PW corrected induced voltages.

$V_{g_{magneto\ harmonic\ 2}}$ are the PW induced voltages outputs of the 2nd magneto-harmonic simulation.

Finally, in the linear case without saturation, it is possible to calculate the real voltages of the PW and CW iteratively. In our application on Flux2D, this was done by a Python script. In the first iteration, the CW induced voltages are added to the feeding voltages of the CW. The PW induced voltages are calculated from the total CW voltages. The PW total voltages are then computed as the sum of the feeding voltages and induced voltages. The second iteration starts with these new PW total voltages: the CW induced voltages are computed again. This process can be iterated until convergence. In our experience, in the linear case, the convergence is very fast: less than 10 iterations which take less than a second with a Python script.

III.5.4.2. Comparison of the FE magneto-harmonic method on a non-saturated load scenario with the FE based coupled-circuit method and FE magneto-transient method

In III.4.3, the comparison between the FE based coupled-circuit method and FE magneto-transient method was given in Table III-19. The comparison between the three methods will be summarized here, in Table III-20 for the same load scenario as in Table III-19.

Table III-20: Comparison, for a linear load case of a BDFM, between the FE magneto-harmonic method, the FE based coupled-circuit method, and the FE magneto-transient method. Voltage and currents amplitudes per phase, and phase of the currents for the phase A of the PW and CW.

	Power Winding			Control Winding		
	$V: [V]$	$I: [A]$	$\angle I: [Rad]$	$V: [V]$	$I: [A]$	$\angle I: [Rad]$
Flux2D magneto-transient, simulation time: 5 days	100,00	3,49	0,390	40,00	4,685	1,06
FE based coupled-circuit, simulation time: a few seconds	100,00	3,65	0,388	40,00	4,795	1,05
Flux2D magneto-harmonic, simulation time: 5 minutes	100,00	3,52	0,386	40,00	4,712	1,06

As it can be seen in Table III-20, the magneto-harmonic method developed for sources with two frequencies gives results that are closely matching the results with the magneto-transient method. The discrepancies between the magneto-harmonic and magneto-transient results are less than 1%. As stated in Table III-20, the magneto-harmonic method takes 5 minutes from start to finish while the magneto-transient method takes 5 days and the FE based coupled-circuit method only takes seconds once the model is built. Now that the magneto-harmonic method for the BDFM works in the linear case, saturation consideration will be added.

III.5.5. Saturation consideration in the new magneto-harmonic method with two sources at different frequencies

To consider saturation for the BDFM, in the magneto-harmonic method presented in III.5.4, the iterative method for the calculation of the equivalent permeability presented in III.5.2 needs to be adapted. The problem is that for a BDFM, the absolute flux density in a mesh element as a function of the time does not have the shape of a rectified sine wave as in Figure III-19. In Figure III-22, there is an example of the shape of the absolute flux density in a random mesh-element for a BDFM without saturation. In this figure, one winding was fed at 100 Hz and the other one at 25 Hz; that is why a complete electrical period is a short 0.04 s.

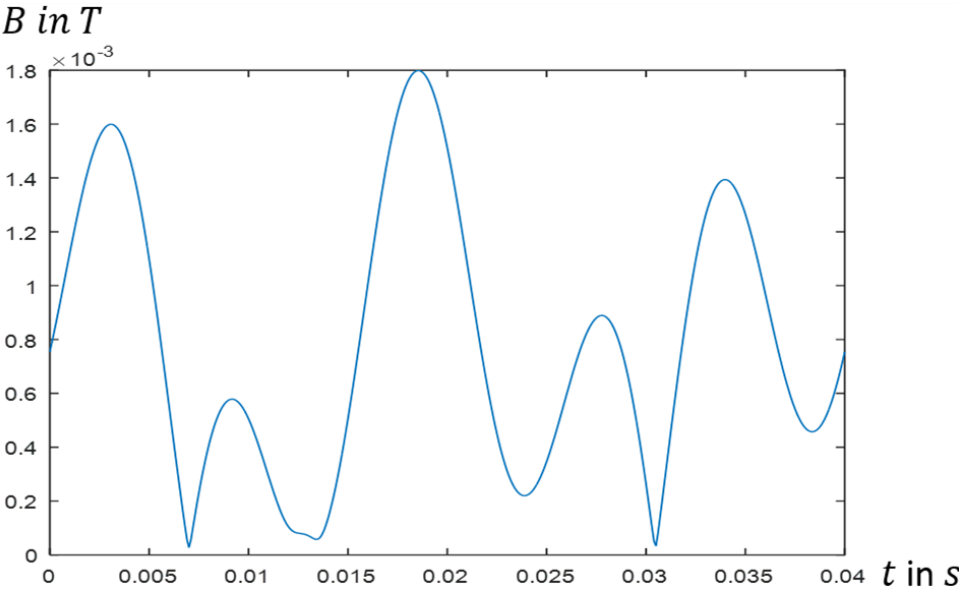


Figure III-22: Absolute flux density in one mesh element of a BDFM during an electrical period, PW at 100 Hz, CW at 25 Hz

As shown in Figure III-22, the absolute flux density in a mesh element of a BDFM is far from having the shape of a rectified sine wave. It is hard to quickly analytically determine for each mesh element the magnetic coenergy per cycle. The absolute flux density for a mesh element in a BDFM is a sum of squared cosine and sine waves. The electrical period varies depending on the frequency of the PW and CW and can, in some cases, be theoretically “infinite”. Over the electrical period, the number of local

minimums and maximums reached are not easy to analytically determine. In Figure III-22 for example, there are 5 minimums and maximums, but this number might be different for each mesh-element. The “zeroes” of the derivative of a random sum of squared cosine and sine do not have a general analytical expression.

The consideration of saturation in a magneto-harmonic simulation is an approximation. It is not imperative to find for each mesh element the exact analytical expression of the coenergy over an electrical period. A good approximation can already lead to accurate results.

The absolute flux density of each mesh element of a BDFM can be decomposed in the sum of two curves of the shape of rectified sine waves: the curve of Figure III-22 can be decomposed in two curves like in Figure III-19 (one due to the CW and one due to the PW). The maximum flux density found in Figure III-22 will be close to the sum of the two maximums found in the decomposed curves. With the method proposed in III.5.4, it is easy to have access to this decomposition since each winding is simulated in its own magneto-harmonic application.

A similar calculation method of the equivalent permeability as presented in III.5.2 will be applied, the method will differ for the determination of the maximum flux density B_{max} . For one mesh element, let's define: $B_{12_{max}}$, the maximum flux density due to the sum of the two windings; $B_{1_{max}}$, the maximum flux density due to the PW; and $B_{2_{max}}$, the maximum flux density due to the CW. Since the flux densities of the two windings do not have the same frequencies, and since the flux densities of the two windings are generally along the same direction in one mesh element (in the areas where saturation is important (the teeth), the flux is guided by the direction of each tooth) there will most probably be one moment in the total electrical period where they add up: $B_{12_{max}} \approx B_{1_{max}} + B_{2_{max}}$. If the steps of the calculation of the equivalent permeability (shown in Figure III-20 and Figure III-21) were applied with $B_{12_{max}}$, the coenergy to compute the new equivalent permeability would be overestimated (most of the local maximums in Figure III-22 are lower than the global maximum). On the contrary, if the computation was applied with either $B_{1_{max}}$ or $B_{2_{max}}$, the coenergy during each period would be underestimated (most of the local maximums in Figure III-22 are higher than $B_{1_{max}}$ or $B_{2_{max}}$).

For an approximation, a pertinent flux density to apply the steps of the calculation of the equivalent permeability (shown in Figure III-20 and Figure III-21), should be between $\max(B_{1_{max}}, B_{2_{max}})$ and $B_{1_{max}} + B_{2_{max}}$.

In [76], the magnetic loading for a BDFM is approximated by using the square root of the maximum flux density in the airgap due to each winding. This approximation of the magnetic loading would match the conditions enumerated above to define the maximum flux density for the determination of the equivalent permeability. Finally, the flux density for the computation of the equivalent permeability is defined as:

$$B_{max_{\mu eq}} = \sqrt{B_{1_{max}}^2 + B_{2_{max}}^2} \quad (82)$$

With this definition of $B_{max_{\mu eq}}$, and the steps presented in Figure III-20 and Figure III-21, it is possible to compute the equivalent permeability for each mesh-element and each iteration.

III.5.6. Summary of the iterative process of the magneto-harmonic method for the BDFM with saturation

The process of the magneto-harmonic method applied to the BDFM without saturation was described in III.5.4. The method to compute the equivalent permeability in each mesh element was described in III.5.2 for usual machines. In III.5.5, the method to determine the flux density for the determination of the coenergy per cycle ($B_{max_{\mu_{eq}}}$) was described for the BDFM. These are the elements to implement a magneto-harmonic method to be applied on the BDFM with saturation. The steps of the whole method applied with Flux2D are summarized as follows:

- 1) Magneto-harmonic simulation of the BDFM with the PW fed and the CW in open circuit. The equivalent permeability of each mesh element is imposed from the precedent iteration calculation. For the 1st step, the equivalent permeability of each mesh element is the no saturation permeability. The induced voltages of the CW are taken as outputs and corrected as in equation (80).
- 2) Magneto-harmonic simulation of the BDFM with the CW fed and the PW in open circuit. The equivalent permeability of each mesh element is the same as for the precedent magneto-harmonic simulation of the PW. The induced voltages of the PW are taken as outputs and corrected as in equation (81).
Steps 1) and 2) can be reversed.
- 3) An analytical iterative process computes the voltages of the PW and CW from the feeding voltages and the induced voltages (as explained in III.5.3).
- 4) If the voltages of the PW and CW computed in 3) are very different from the imposed voltages in 1) and 2), the magneto-harmonic simulations of 1) and 2) are done once again (this is important to get an accurate flux density in each mesh element for the computation of the equivalent permeability).
- 5) The flux density of each mesh element is extracted from the magneto-harmonic simulations of 1) and 2). For each mesh element, equation (82) is applied, followed by the steps shown in Figure III-20 and Figure III-21 to determine the new equivalent permeabilities.
- 6) Start again from 1) and 2) with the new equivalent permeabilities. Here, a relaxation can be added: start again from 1) and 2) with a proportion between the new and old equivalent permeabilities. For cases with high saturation, the relaxation was needed to avoid divergence. This process is repeated until convergence: when the voltages computed in 3) are the same as for the preceding iteration.

III.5.7. Comparison of the magneto-harmonic method developed for the BDFM with magneto-transient simulations

To validate the magneto-harmonic method for the BDFM under saturation, some load comparisons were done for the BDFM presented in Table III-1, p 77. From one load test without saturation, the voltages of the PW and CW were increased proportionally in several steps. In Table III-21, one can find the voltages of the five load scenarios that were simulated.

Table III-21: Different voltage scenarios used for the comparison between the magneto-harmonic method and the magneto-transient method

	Scenario 1	Scenario 2	Scenario 3	Scenario 4	Scenario 5
PW voltage (V)	100	7 500	15 000	17 500	20 000
CW voltage (V)	40	3 000	6 000	7 000	8 000

Each load scenario presented in Table III-21 took 4 days to be simulated with a magneto-transient Flux2D simulation. Depending on the scenario, the magneto-harmonic simulations took between 5 minutes (scenario 1) and 8 hours (scenario 5). It could be noted here that it should be possible to gain a factor of 4 at least in computing time on the magneto-harmonic method. In fact, it was not tried in this example to parallelize the simulations (each CW simulation could be computed in parallel to the same iteration PW simulation). Furthermore, a lot of time was lost in the opening, saving and closing of Flux2D simulations. This time could be saved with a more thoughtful programming; the program was not coded to be fast, but to be easy to debug if the method was not working...

Figure III-23 and Figure III-24 give the comparison results between the magneto-harmonic with saturation method, the magneto-harmonic linear method, and the magneto-transient application. In each figure, the magneto-transient results are in blue dots, the magneto-harmonic with saturation results are in green triangles, and the linear magneto-harmonic results are in red squares.

Figure III-23 gives the evolution of the total reactive power (PW + CW) depending on the scenario. The minus sign is due to the “generator” convention: the reactive power is consumed by the BDFM. The reactive power is an accurate way to verify how saturation is accounted for. If the material was linear, the reactive power should be a quadratic curve. This can be verified with the red curve of Figure III-23. Under saturation, more current is needed from the two windings to magnetize the BDFM, this translates into increased reactive power. This can be seen in Figure III-23: the reactive power of the methods considering saturation becomes higher (in absolute values) than the linear reactive power. Figure III-23 gives the impression that the magneto-harmonic method slightly over-estimates the consequences of saturation. However, the results are still in good correlation with the magneto-transient application.

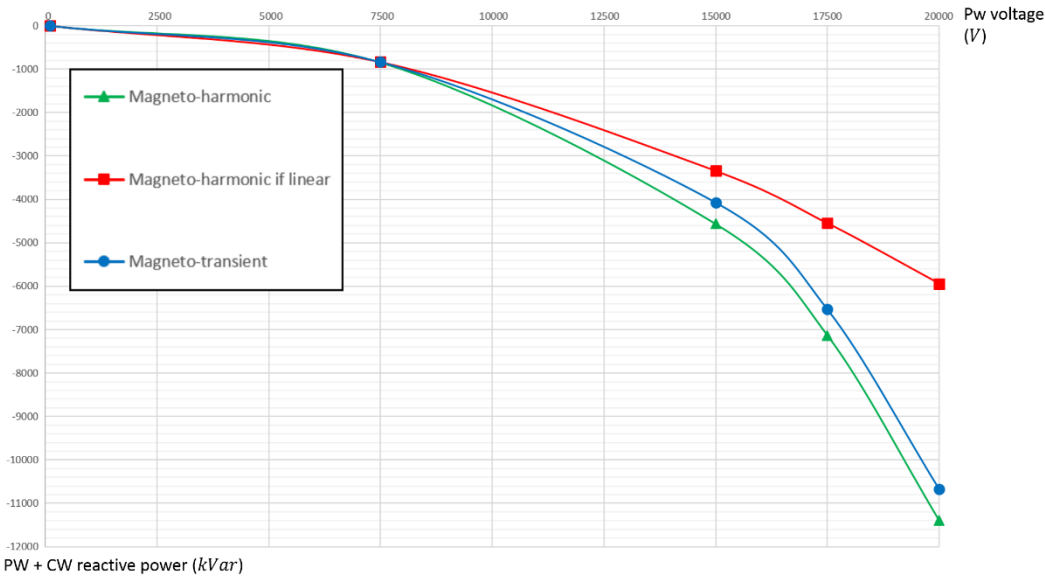


Figure III-23: Comparison of the sum of the PW and CW reactive powers for the magneto-harmonic method with saturation, the magneto-harmonic method without saturation, and the magneto-transient application.

Figure III-24 gives the evolution of the total active power (PW + CW) depending on the scenario. Unlike Figure III-23 for the reactive power, Figure III-24 shows that the active power is only slightly affected by the saturation level (the linear magneto-harmonic results in red are close to the results considering saturation in green and blue).

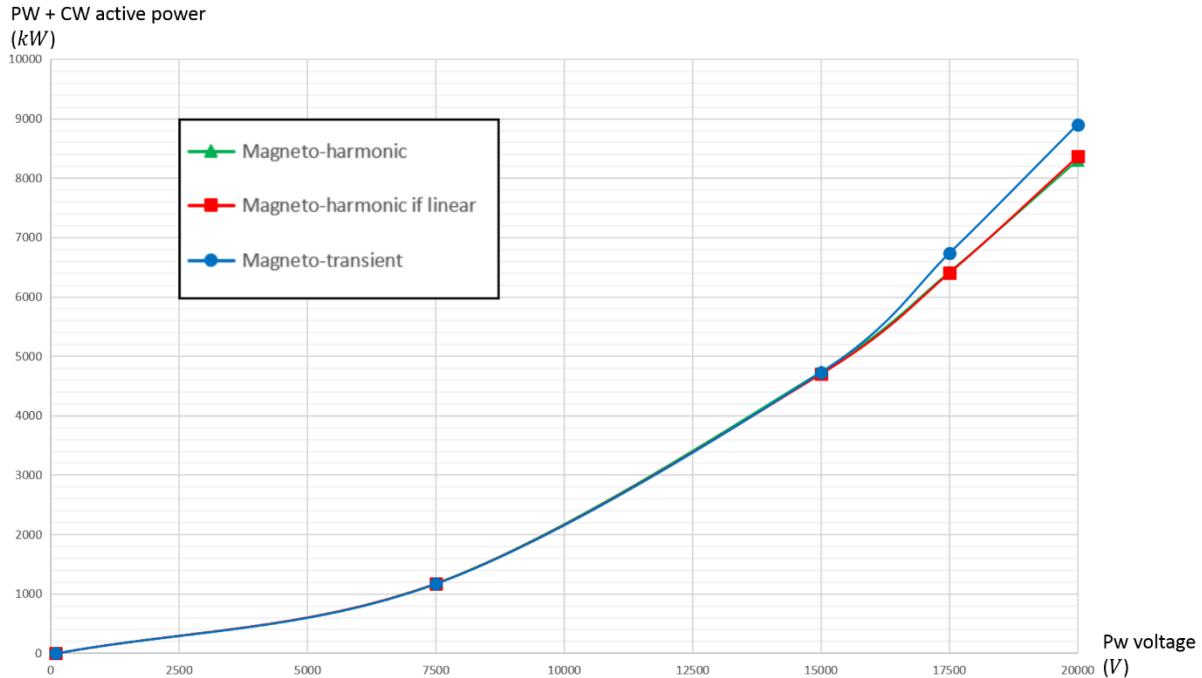


Figure III-24: Comparison of the sum of the PW and CW active powers for the magneto-harmonic method with saturation, the magneto-harmonic method without saturation, and the magneto-transient application.

To conclude, the magneto-harmonic method for the BDFM with saturation gives results that have a good correlation with the magneto-transient simulations (the green curve of Figure III-23 and Figure III-24 is always close enough to the blue curve). Since the magneto-harmonic method is faster than the magneto-transient method (hours in comparison to days), it appears as a good candidate to replace the magneto-transient method for steady-state load tests computations. In Figure III-24 it came as a surprise that saturation did not have much of an impact on the active power (red curve close to the blue and green curve). We would have expected saturation to change the amplitude of the airgap flux density harmonics, and maybe to induce a shift of the phases of these harmonics. This could have changed the active power, however, it does not appear to be the case.

III.6. Perspectives towards a complete semi-analytical model of the BDFM to implement optimizations with a 1st order algorithm

After the development of an analytical model for the Induction Machine (presented in APPENDIX F, p 189), one of the objectives of this work was to develop a similar model for the BDFM. Several issues prevented this goal to be reached before the end of the Ph.D. However, this endeavor still seems reachable. Furthermore, as it has already been shown with the Induction Machine, an analytical model of the BDFM could be a very powerful tool when paired with a 1st order optimization algorithm (refer to the optimizations of the Induction Machine in II.2.3.7.2, p 61). This part will list the major

modifications that should be made on the Induction Machine model to transform it into a BDFM model.

The stator part of the model presented in APPENDIX F can almost be taken as such for the BDFM. There is only one stator winding in the Induction Machine; all the electrical parameters should be defined for each winding in the case of the BDFM. The only equation that should be adapted would be the equation computing the stator slot leakage reactance. Indeed, for the Induction Machine, the slot leakage reactance considers the coil-span reduction. For the BDFM, the slot leakage reactance of each winding should consider the other winding.

The main difficulty is the computation of the two transformation ratios between the two stator windings and the rotor with the determination of the phase of the mutual inductances. For the Induction Machine, the number of turns in series of the rotor was taken as $1/2$ (since it was a squirrel cage rotor). The equivalent number of turns in series of a rotor with nested-loops is not easy to estimate. In this regard, some ideas could come from [32], where the coupled-circuit representation is used to derive the equivalent circuit representation (watch out, the final equivalent circuit obtained in [32] does not work for the load scenarios as shown from Figure III-11 to Figure III-17, starting p 101).

For the rotor, the number of turns in series of the nested-loops would also impact the calculation of the rotor resistance.

For the saturation factor, the magnetic loading should be approximated using the square root of the maximum flux density in the airgap due to each winding (as it was done in the magneto-harmonic method: equation (82), p 114). In fact, the results obtained for the magneto-harmonic method had a good correlation with the magneto-transient results.

III.7. Conclusion

The nested-loop rotor capacity to cross-couple the two stator windings was verified through harmonic analyses at the beginning of this chapter. As already shown analytically in I.5.3.4.3 and I.5.3.4.4 for the BDFRM, the rotor will create two harmonics around each fundamental. Under the right conditions, with the appropriate mechanical speed, number of nests, and frequencies of the PW and CW, the stator windings will cross-couple. In cross-coupling mode, one harmonic of each fundamental will have the same harmonic spatial order and same frequency as the other fundamental. As stated in CHAPTER I, in Table I-2, the cross-coupling effect always happens for two couples of one harmonic and one fundamental at the same time. If the conditions lead to an interaction between the fundamental of the PW and one harmonic of the CW, then the same conditions also lead to an interaction of the fundamental of the CW and one harmonic of the PW. This was verified in the harmonic analyses in III.2. The harmonic analyses also showed the impact of the mechanical position of the rotor on the airgap flux density harmonics and saturation.

With the harmonic analyses, it was clear that the equivalent circuits found in the literature did not consider correctly the impact of the rotor's mechanical position. This is important since without considering correctly this impact, without the correct equations, it was hard to identify correctly the parameters of the equivalent circuit (hence the complicated methods for the parameter extraction found in the literature, with frequency variations and without load tests verifications). A new

equivalent circuit was presented in III.3. It was intuited from considerations of the Induction Machine equivalent circuit. The results of this equivalent circuit were consistent with the FE simulations results. A new method for the parameters extraction with simple electrical tests and an optimization algorithm was developed III.3.3.

After the equivalent circuit, new FE methods were presented to enable faster computation for the BDFM. In fact, the magneto-transient applications launched for the load cases were taking days (4 days for the magneto-transient simulations used for the airgap flux density harmonic analyses of III.2) due to the low number of symmetries and long simulation periods.

The first method, presented in III.4, was inspired by the coupled-circuit method (which is an analytical method); thus, it was named the “FE based coupled-circuit method”. In this method, all the mutual inductances and self-inductances of the stator windings and the nested-loops are determined with magneto-static FE simulations. This process took, for the BDFM studied in this chapter, around 10 minutes. It was then possible to simulate simple-induction, self-cascaded, and load tests in a matter of seconds. The drawback of this method is that it is not possible to correctly consider the BDFM’s saturation in a magneto-static simulation. This method was only used to simulate tests without saturation. After being validated, thousands of simple-inductions, self-cascaded, and load tests were solved with this method, in less time than a workday, to verify the results of the new equivalent circuit. Without saturation, the results of the new equivalent circuit and the FE coupled-circuit method were strongly correlated as it was shown from Figure III-11 to Figure III-17.

The second FE method, presented in III.5, was a magneto-harmonic application adapted to the cases with two sources of different frequencies on Flux2D. In comparison to the previous method, it considers saturation. However, it takes much longer to compute: between 5 minutes, for the unsaturated cases, to 8 hours, for the heavily saturated cases. It was estimated that several factors could be gained in the speed of this method with optimization of the process and the Python code being used in Flux2D for the FE software. The same method was developed on an internal FE software in General Electric. In this internal FE software, some symmetries were used in the mesh construction and the matrix inversion during the solving process. Saturation was not considered, and the computation time for a load test was less than 5 seconds.

At the end of this chapter, in III.6, perspectives were given toward a complete semi-analytical model of the BDFM. One remaining challenge to develop an analytical model based on the new equivalent circuit for the BDFM (like the model presented in APPENDIX F for the IM) is the analytical determination of the transformation ratio between the stator windings and the rotor.

Semi-analytical models are extremely powerful when they are paired with 1st order optimization algorithms (as shown in II.2.3.7). It was tried at the beginning of this work to reach this goal. However, many errors were added on top of each other (equivalent circuit was taken from [32], errors in the code), such that it was hard to debug. With the new equivalent circuit and a close understanding of the analytical coupled-circuit method presented in [32], this goal may become reachable. Doing so, the elaboration of the specifications, and the early optimizations of a BDFM would become much easier. For now, the BDFM designs are necessarily done with analytical designs, followed by FE iterations in an attempt to optimize a few parameters. This process will be described in CHAPTER IV.

CHAPTER IV. EXAMPLE OF A BDFM SIZING FOR A GIVEN SET OF CHARACTERISTICS USING THE KNOWLEDGE AND METHODS OF THE PREVIOUS CHAPTERS AND FOUND IN THE LITERATURE.

IV.1.	Introduction.....	123
IV.2.	The Typical Tidal Project (TTP) specifications.....	123
IV.3.	An analytical method for a first design of the BDFM	124
IV.3.1.	Step 1: Choice of the number of poles.....	124
IV.3.1.1.	Impossible number of poles	125
IV.3.1.2.	Number of poles and rating of the power converter	127
IV.3.1.3.	Cross-coupling capability depending on the number of poles.....	130
IV.3.1.4.	Mechanical speeds to avoid: synchronism speeds and natural speed	132
IV.3.1.5.	Choice of the pole number for the specifications of the Typical Tidal Project (TTP).....	135
IV.3.2.	Step 2: Choice of the bore diameter	135
IV.3.2.1.	Choice based on the Esson factor or Electrical utilization factor	135
IV.3.2.2.	Considerations on the moment of inertia and acceleration of the rotor at rated torque.....	137
IV.3.3.	Step 3: Choice of the number of stator and rotor slots	138
IV.3.3.1.	Limits on the number of slots based on the limits of the slot pitch dimensions	138
IV.3.3.2.	Impacts of the number of layers per slot and the number of slots per pole and per phase.....	139
IV.3.3.3.	Choice of the number of stator slots.....	140
IV.3.3.4.	The number of slots of the rotor	140
IV.3.4.	Step 4: Magnetic loading and number of turns in series for each stator winding.....	141
IV.3.4.1.	Magnetic loading of a BDFM and choice of the maximum flux density.....	141
IV.3.4.2.	Theoretical number of turns in series	143
IV.3.4.3.	Choice of the number of parallel paths, conductors per slot, and the voltages of the power and control windings.....	144
IV.3.5.	Step 5: The stator currents, and the size and proportion of the slots	145
IV.3.5.1.	The stator currents	145
IV.3.5.2.	Size and proportion of the slots	146

IV.3.5.3.	Computation of the resistance of the stator windings and rotor loops.....	148
IV.3.6.	Step 6: Determination of the airgap radial length	149
IV.3.7.	Step 7: Determination of the rotor and stator yoke heights followed by the external diameter of the machine.....	150
IV.3.8.	Step 8: Determination of the stacking factor, and the number and width of ventilation ducts.....	151
IV.3.8.1.	Stacking factor in hydro machines	151
IV.3.8.2.	Ventilations ducts.....	151
IV.3.9.	Summary of the first analytical sizing of the BDFM on the specifications of the Typical Tidal Project (TTP)	152
IV.4.	FE simulation of the analytical design, and improvement of the design through an iterative process	154
IV.4.1.	FE load simulation of the analytical design with a magneto-transient application	154
IV.4.2.	Iterative process to improve the BDFM design with an FE magneto-harmonic model.....	154
IV.5.	Conclusion	156

IV.1. Introduction

In CHAPTER IV, a BDFM will be designed on the specifications of the Typical Tidal Project (TTP) (the same project that was used for the optimization of the fully-fed Induction Machine in II.2.3). The design of the BDFM will be performed in two parts. The first part will be an analytical design based on literature knowledge and experience from other hydro machines. In the second part, the magneto-harmonic method presented in III.5 and adapted to an FE software internal to General Electric will be used in an iterative process to improve the analytical design.

The analytical design will be presented in IV.3. Before going through it, the reader should be warned that some sizing equations taken in the literature were based on hypotheses that ended up being wrong. For example, some sizing equations were written in the literature with the hypothesis of a unity power factor for both the PW and CW. The dimensions limits of the TTP led to a design with low power factors for both windings. In the end, the BDFM analytically designed in IV.3 did not work as expected, as it will be shown in FE simulations in IV.4.1. The active and reactive power required by the specifications could not be achieved with the analytical design.

The iterative process to improve the BDFM design will be presented in IV.4. This iterative process will be based on the magneto-harmonic simulation method for the BDFM presented in III.5. Contrarily to what was presented in III.5, the method will not be applied to Flux2D magneto-harmonic applications. It will be applied with an FE software internal to General Electric, specifically developed for rotating machines. In fact, this method was giving the same results on the two different FE software but had faster computation time with the internal software (seconds in comparison to minutes). The only drawback is that the method developed in III.5 to consider saturation with two different frequencies has not yet been applied to this internal software. This iterative process will show that the tools developed during this work can have powerful applications during the design of a BDFM, especially for a BDFM with specifications never tried in the literature.

IV.2. The Typical Tidal Project (TTP) specifications

The TTP was already presented in II.2.3.1 starting from p 52. The specifications of this project were used to demonstrate the design and optimization process on an IM. The same specifications will be used to design a BDFM. It will then be possible to compare the two different technologies depending on different factors.

The major specifications of the TTP were presented in Table II-2 and are reminded in Table IV-1. It could be noted that the rated power changed from 22 MW in Table II-2 to 20 MW in Table IV-1, because different specification iterations were taken.

Table IV-1: Major specifications of each electrical machine (among 12) to be installed in the TTP

Rated Active Power:	$P_{rated} = 20 \text{ MW}$
Rated Synchronous Speed:	$n_s = 60 \text{ rpm}$
Turbine speed range:	$n_m = 40 \text{ to } 66 \text{ rpm}$
Bulb frame outer diameter:	$D_{frame} = 7 \text{ m}$
Stator maximal outer diameter:	$D_{out,max} = 5.2 \text{ m}$
Maximal length of the machine	$L_{max} = 2.1 \text{ m}$
Converter Voltage for fully-fed (from ABB)	$V_{max} = 3300 \text{ or } 6600 \text{ V}$

As additional information to the specifications given in Table IV-1, in the speed range $n_m = 40$ to 60 rpm the machine is operated at constant torque. At 60 rpm the machine reaches its maximum power and is operated from $n_m = 60$ to 66 rpm at constant power.

IV.3. An analytical method for a first design of the BDFM

In this part, a method to design a BDFM step by step will be presented. This method will lead to a solution that cannot be considered as an optimal design. It will rather be a first design: a good starting point for further optimizations with FE simulations or with a 1st order optimization based on an analytical model.

Some of the following steps will be based on analytical equations describing the BDFM working principles. Other steps will be adapted from sizing guidelines coming from SM and DFIM for hydro-generators. Finally, some will be based on empirical knowledge gained during the design of prototypes reported in the literature [51]. Some of the prototypes found in the literature as in [77] and [78] are based on BDFM with wound rotor. These rotors are well described in [32] (see Rotor 6 in I.5.3.5.3). The literature has shown (for example [78] or [32]) that these rotors are less performant than nested-loops rotors. However, they are easier to manufacture and easier to optimize since they have wound rotor windings. We will also try to transfer some of the optimization rules found for wound rotors to nested-loops rotors.

IV.3.1. Step 1: Choice of the number of poles

For fixed speed projects, the turbine manufacturers estimate the optimum rotational speed: the synchronous speed. For variable speed project, they estimate a range of speed $[n_{rmin}; n_{rmax}]$ at which the turbine will be operated. For a fixed speed project, the synchronous speed and the grid frequency would impose the number of poles of the machine (see equation (160) p 171 in APPENDIX B). For a variable speed project using a DFIM, the synchronous speed of the DFIM would be fixed close to the middle of the speed range $n_{sDFIM} = \frac{n_{rmin} + n_{rmax}}{2}$. This synchronous speed would minimize the maximum slip of the DFIM and the power converter rated power (see equation (160), p 171 in APPENDIX C).

The process to define the optimal number of poles for the BDFM is not yet well established. The choice of the number of pole pairs of the power winding p_g and the number of pole pairs of the control winding p_c for the BDFM depends on several factors:

- The power winding and control winding need to have a different number of poles to avoid interaction in the stator frame.
- These numbers of poles will also affect the rating of the power converter linked to the control winding.
- The cross-coupling capability of the BDFM will depend on p_g and p_c .
- The BDFM cannot operate at certain mechanical speeds: to induce currents in the rotor, there must be a slip between the mechanical speed and the rotating speed of the magnetic fields created by the power and control windings.

IV.3.1.1. Impossible number of poles

First, the number of poles of the two stator windings must be different to avoid cross-coupling through the stator iron. Therefore, the poles number must respect the following equation:

$$p_g \neq p_c \quad (83)$$

p_g and p_c are the numbers of pole pairs of the power and control windings respectively.

As noted in [26], some combinations of number of poles can lead to an unbalanced magnetic pull. The unbalanced magnetic pull happens when the forces pulling the rotor towards the stator do not cancel each other out around the machine. For example, if the forces on the right of the rotor are higher than on the left, then there will be an unbalanced magnetic pull pulling the rotor on the right. To understand, the magnetic pull can be written from the flux density of the two fundamentals in the airgap. As already expressed in I.5.3.5.1, in equations (22) and (23), p 30, the flux density in the airgap can be written:

$$B(\theta_{ag}, t) = \widehat{B}_g \cos(\omega_g t - p_g \theta_{ag} + \angle B_g) + \widehat{B}_c \cos(\omega_c t - p_c \theta_{ag} + \angle B_c) \quad (84)$$

\widehat{B}_g and \widehat{B}_c are the amplitudes of flux density fundamentals of the power winding and control winding respectively.

ω_g and ω_c are the electrical pulsations of the power winding and control winding respectively.

$\angle B_g$ and $\angle B_c$ are the phases of the flux density fundamentals.

θ_{ag} is the position in the airgap in the stator reference frame.

t is the time.

The magnetic pull can be found through the integration of the Maxwell stress tensor over the perimeter of the airgap. The Maxwell stress tensor expression is:

$$\vec{\sigma} = \frac{B_n^2}{2 \mu_0} \vec{u}_n \quad (85)$$

$\vec{\sigma}$ is the Maxwell stress tensor.

B_n is the radial flux density in the airgap.

μ_0 is the vacuum permeability.

\vec{u}_n is a radial unit vector.

Combining equations (84) and (85), the Maxwell stress tensor in the BDFM can be written:

$$\vec{\sigma}(\theta_{ag}, t) = \frac{1}{2 \mu_0} \left[\widehat{B}_g^2 \cos^2(\omega_g t - p_g \theta_{ag} + \angle B_g) + \widehat{B}_c^2 \cos^2(\omega_c t - p_c \theta_{ag} + \angle B_c) + 2 \widehat{B}_g \widehat{B}_c \cos(\omega_g t - p_g \theta_{ag} + \angle B_g) \cos(\omega_c t - p_c \theta_{ag} + \angle B_c) \right] \vec{u}_n(\theta_{ag}) \quad (86)$$

The projection of $\vec{u}_n(\theta_{ag})$ on an axis can be written $\cos(\theta_{ag} + \varphi) \vec{u}_{axis}$ where φ depends on the direction of the projection. So, the force of the magnetic pull projected on an axis can be written:

$$\vec{F}_{mp}(t) = \int_0^{2\pi} \frac{1}{2 \mu_0} \left[\widehat{B}_g^2 \cos^2(\omega_g t - p_g \theta_{ag} + \angle B_g) + \widehat{B}_c^2 \cos^2(\omega_c t - p_c \theta_{ag} + \angle B_c) + 2 \widehat{B}_g \widehat{B}_c \cos(\omega_g t - p_g \theta_{ag} + \angle B_g) \cos(\omega_c t - p_c \theta_{ag} + \angle B_c) \right] \cos(\theta_{ag} + \varphi) d\theta_{ag} \vec{u}_{axis} \quad (87)$$

\vec{F}_{mp} is the total magnetic pull force.

$$\text{Since } \cos^2(A) = \frac{1}{2} + \frac{\cos(2A)}{2} \quad \text{and} \quad \cos(A)\cos(B) = \frac{1}{2} (\cos(A+B) + \cos(A-B)).$$

$$\vec{F}_{mp}(t) = \frac{1}{2 \mu_0} \int_0^{2\pi} \left[\widehat{B}_g^2 \left(\frac{1}{2} + \cos(2\omega_g t - 2p_g \theta_{ag} + 2\angle B_g) \right) + \widehat{B}_c^2 \left(\frac{1}{2} + \cos(2\omega_c t - 2p_c \theta_{ag} + 2\angle B_c) \right) + \widehat{B}_g \widehat{B}_c \left(\cos((\omega_g + \omega_c)t - (p_g + p_c) \theta_{ag} + \angle B_g + \angle B_c) + \cos((\omega_g - \omega_c)t - (p_g - p_c) \theta_{ag} + \angle B_g - \angle B_c) \right) \right] \cos(\theta_{ag} + \varphi) d\theta_{ag} \vec{u}_{axis} \quad (88)$$

The integral $\int_0^{2\pi} [\cos(p\theta_{ag})] d\theta_{ag}$ will be null if p is an integer not equal to 0 : $\int_0^{2\pi} [\cos(p\theta_{ag})] d\theta_{ag} = 0$ if $p \in \mathbb{N}^*$. So, with $\cos(A)\cos(B) = \frac{1}{2} (\cos(A+B) + \cos(A-B))$ it can be deduced that the integral $\int_0^{2\pi} [\cos(p\theta_{ag})] \cos \theta_{ag} d\theta_{ag}$ will be null if p is an integer not equal to 1.

Equation (88) shows that the total magnetic pull force will be equal to zero if: $|2p_g| \neq 1$, $|2p_c| \neq 1$, $|p_g + p_c| \neq 1$, and $|p_g - p_c| \neq 1$. Since p_g and p_c are both positive integer, the only combination that can create an unbalanced magnetic pull from the fundamental harmonics are the combination when $p_g = p_c \pm 1$.

Finally, for an appropriate BDFM design, p_g and p_c must be chosen such as:

$$\begin{cases} p_g \neq p_c \\ p_g \neq p_c \pm 1 \end{cases} \quad (89)$$

IV.3.1.2. Number of poles and rating of the power converter

As for a DFIM, the choice of the total number of poles of a BDFM will impact the minimum rating of the power converter.

The power converter is linked to the control winding, so its rating can be defined from the maximum power and related power factor of this winding:

$$S_{power\ converter} = \frac{P_{c\ max}}{\cos \varphi_{c\ max}} \quad (90)$$

$S_{power\ converter}$ is the apparent rated power of the power converter.

$P_{c\ max}$ is the maximum active power of the control winding.

$\cos \varphi_c$ is the power factor of the control winding when the maximum active power is reached.

From the equivalent circuit, it is possible, with hypotheses, to simplify the expressions of the active and reactive powers of the grid and control windings. With these simplifications, the active power of the control winding can be expressed from the active power of the grid winding and the ratio of pulsations. Such developments can be found in p 92 of [38]:

$$P_c \approx P_g \frac{\omega_c}{\omega_g} \quad (91)$$

P_c and P_g are the active powers of the control winding and power winding respectively.

ω_c and ω_g are the electrical pulsations of the control winding and power winding respectively.

The rated active power of the BDFM is the sum of the rated powers of the grid and control windings. It is expressed as:

$$P_{rated} = P_{c\ rated} + P_{g\ rated} \quad (92)$$

P_{rated} is the rated active power of the BDFM.

$P_{c\ rated}$ is the rated active power of the control winding.

$P_{g\ rated}$ is the rated active power of the grid winding.

Replacing $P_{g\ rated}$ in equation (92) by its expression from (91) leads to:

$$P_{C_{rated}} = \frac{P_{rated}}{1 + \frac{\omega_g}{\omega_c}} \quad (93)$$

To minimize the sizing of the power converter connected to the control winding, it is important to limit the rated power of the control winding: $P_{C_{rated}}$. Equation (93) shows that the active power of the control winding depends on the total active power of the machine, and on the ratio of electrical pulsations of the two stator windings. Of course, the electrical pulsation of the power winding is fixed to the pulsation of the grid (50 Hz or 60 Hz). So, with equation (93), it is easy to see that a design that minimizes the rated power of the control winding ($P_{C_{rated}}$) will be a design that also minimizes its pulsation ω_c . It is also preferable for the control winding pulsation to be positive: the two magnetic fields of the two stator windings will then have the same rotation direction, their power will add up and not subtract from each other.

In cross-coupling mode, the electrical pulsation of the control winding depends on the mechanical speed of the rotor and the number of pole pairs (refer to the demonstration in 1.5.3.5.1, in particular, equation (34), p 32).

$$\omega_{rm} = \frac{\omega_g + \omega_c}{p_g + p_c} \quad (94)$$

ω_{rm} is the mechanical pulsation of the rotor.

p_g and p_c are the numbers of pole pairs of the power and control windings respectively.

From equation (94), and to keep ω_c as low as possible, the sum of pole pairs $p_g + p_c$ should be set so that the natural speed (mechanical speed with $\omega_c=0$) of the BDFM will be as close as possible to its operating speed. Furthermore, as it will be seen in IV.3.1.4, the natural speed should not be within the operating range of the BDFM. A logic combination of the two previous sentences leads to: the natural speed must be slightly lower than the minimal mechanical speed or slightly higher than the maximum mechanical speed.

With the example of the TTP, the rotor speed range will vary between the two following values: $n_{m_{min}} = 40 \text{ rpm}$ and $n_{m_{max}} = 66 \text{ rpm}$. Since the pulsation of the grid is 50 Hz, to meet the precedent criteria, p_g and p_c must be set such that:

$$\frac{50 \cdot 2\pi}{p_g + p_c} < \frac{40}{60} \cdot 2\pi \quad \text{or} \quad \frac{50 \cdot 2\pi}{p_g + p_c} > \frac{66}{60} \cdot 2\pi$$

Equivalent to (95)

$$p_g + p_c > \frac{50 \cdot 60}{40} = 75 \quad \text{or} \quad p_g + p_c < \frac{50 \cdot 60}{66} = 45$$

In the characteristics of the TTP, the total power of the machine is not constant over the range of speed. It is interesting to plot the total power of the machine and the approximative power of each

winding using the characteristics from Table IV-1, and equations (91), (92), and (94), for different number of poles. This is done in Figure IV-1.

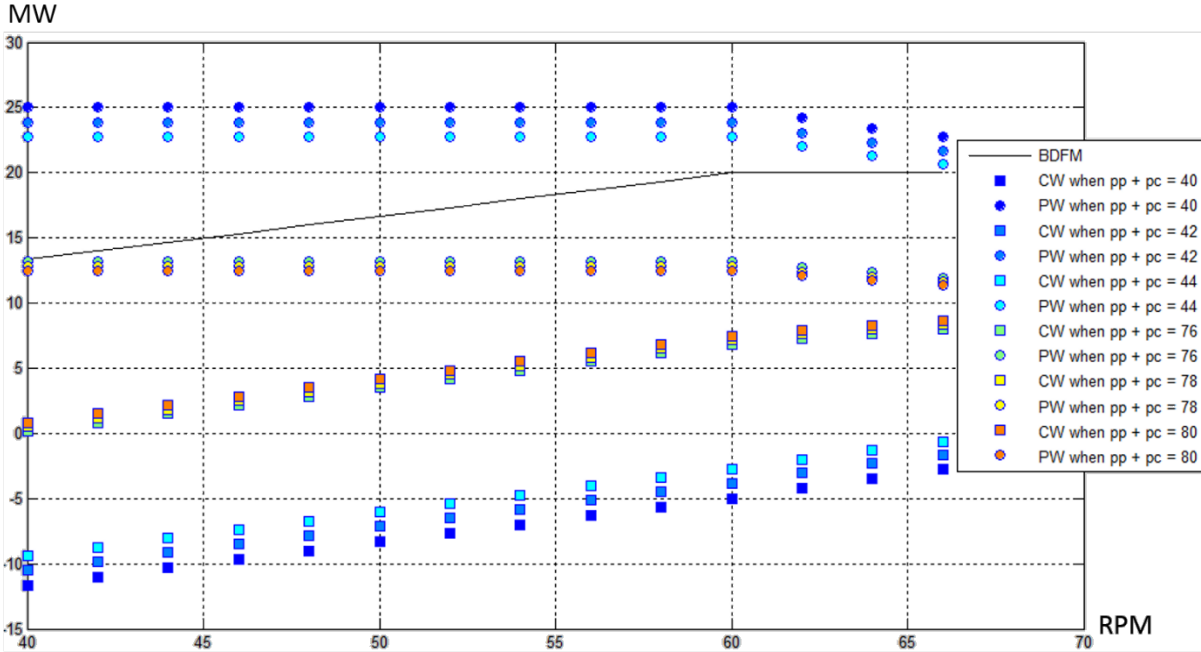


Figure IV-1: Active Power of the Power Winding (PW: discs), Control Winding (CW: squares), and BDFM (PW+CW: black curve) depending on the total number of pole pairs ($p_p + p_c$) and the mechanical speed of the rotor.

Figure IV-1 shows that when the sum of the number of pole pairs is lower than forty-five, $p_g + p_c < 45$, the control winding is always working against the power winding. One winding will generate power and the other will consume power. In this case, the natural speed will be faster than the range of speed during the BDFM operation. To decrease the speed of the BDFM, the magnetic field of the control winding will always rotate in opposite direction to the magnetic field of the power winding. In the equations, this will be translated by a “negative” control winding pulsation: $\omega_c < 0$.

When the number of pole pairs is higher than seventy-five, $p_g + p_c > 75$, the two windings will work in the same direction: the stator windings will generate power simultaneously and consume power simultaneously.

This behavior is comparable to the behavior in hypo-synchronous mode or hyper-synchronous mode of a DFIM. The noticeable difference is that for a DFIM, the synchronous speed is chosen in the middle of the speed range of the machine. With the BDFM, the natural speed must be chosen above or under the range of speed of the machine since the natural speed is a forbidden speed (see IV.3.1.4).

With Figure IV-1, it is easy to see that to minimize the sizing of the power winding, the control winding, and the power converter, the natural speed of the BDFM should be set below the lowest speed of the machine. This results in a sum of number of poles a bit above seventy-five. In the following part of the design of the TTP, we will remember from Figure IV-1, that the possible sum of pole pairs to choose from are $p_g + p_c = 76$, $p_g + p_c = 78$, or $p_g + p_c = 80$.

IV.3.1.3. Cross-coupling capability depending on the number of poles

The choices of p_g and p_c can then be determined by trying to maximize the cross-coupling factor of the stator windings through the rotor. According to geometry considerations (in [50]), this cross-coupling factor is proportional to:

$$k_{gc} \propto \sin\left(\frac{p_g s_{loop}/s_{loop_max}}{2}\right) \sin\left(\frac{p_c s_{loop}/s_{loop_max}}{2}\right) \quad (96)$$

k_{gc} is the cross-coupling factor.

s_{loop} is the rotor loop span angle.

s_{loop_max} is the maximum rotor loop span angle.

The rotor loop span angle: s_{loop} is the angle between the two bars of the external loop of each nest. The maximum value the rotor loop span angle can take can be expressed as:

$$s_{loop_max} = \frac{360}{N_r} = \frac{360}{p_g + p_c} \quad (97)$$

N_r , the number of nests, is equal to the sum of pole pairs of the power and control windings, as seen in I.5.3.5.1, equation (34), p 32.

The higher the cross-coupling factor between the two stator windings is, the better the BDFM will work. Because of the expression of the cross-coupling factor in equation (96), for a given total number of pole pairs $p_g + p_c$, different choices on p_g and p_c will not all lead to a good working BDFM.

It is possible to print the function of equation (96) for different values of p_g and p_c as a function of the ratio s_{loop}/s_{loop_max} and shown in Figure IV-2.

The best total number of pole pairs $p_g + p_c$ for the specification of the TTP was estimated to be 76, 78, or 80 in Figure IV-1. Thus, it is interesting to compare the potential cross-coupling factors of all the possible combinations of p_g and p_c according to equation (96). The results for $p_g + p_c = 76$ can be seen in Figure IV-2. As the reader should notice, equation (96) is symmetrical for p_g and p_c . If p_g and p_c are exchanged, the cross-coupling factor is not impacted.

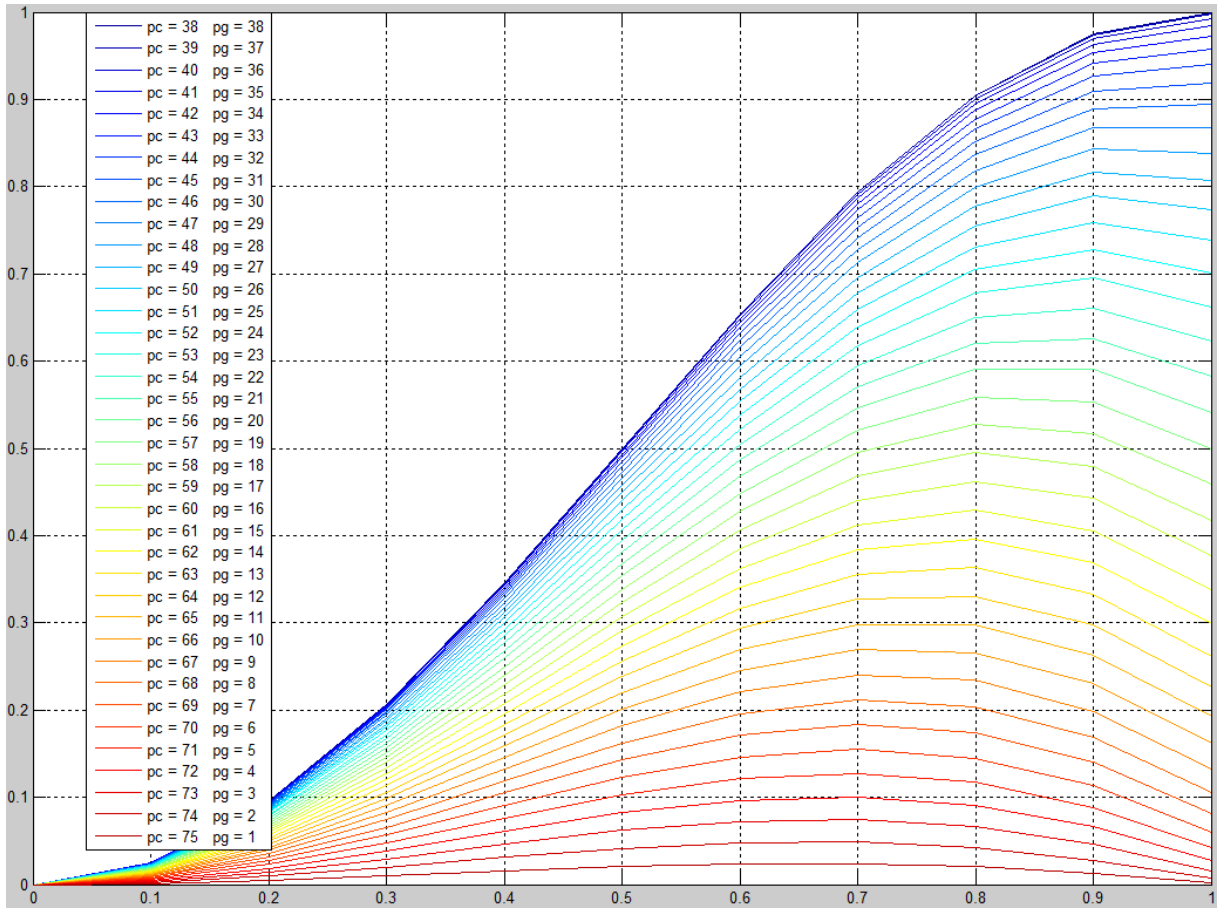


Figure IV-2: Comparison of the potential cross-coupling factors of all the possible combinations of p_g and p_c for a total sum $p_g + p_c = 76$

As it can be seen in Figure IV-2, the high cross-coupling factors are achieved when the values of p_g and p_c are close. Of course, $p_g = p_c$ gives the highest potential cross-coupling factor. But, $p_g = p_c$ is forbidden to avoid cross-coupling in the stator reference frame as reminded in equation (89). Then, the combinations of p_g and p_c where $p_c = p_g \pm 1$ are also giving very good cross-coupling capabilities. However, these combinations will create unbalanced magnetic pull as it was explained in IV.3.1.1, there are also forbidden combinations (see equation (89)).

With Figure IV-2, it is possible to select the combinations of p_g and p_c giving a high potential cross-coupling factor. If the threshold is set at 90% of the highest potential cross-coupling factor, for $p_g + p_c = 76$, there are 7 possible combinations are: $p_g = 37$ and $p_c = 39$, $p_g = 36$ and $p_c = 40$, $p_g = 35$ and $p_c = 41$, $p_g = 34$ and $p_c = 42$, $p_g = 33$ and $p_c = 43$, $p_g = 32$ and $p_c = 44$, and finally $p_g = 31$ and $p_c = 45$. Of course, as already stated, the theoretical maximum cross-coupling factor is identical if the number of pole pairs of the control and power winding are exchanged. Thus, the 7 previous combinations can be extended to 14 combinations.

To minimize the number of stator teeth (refer to IV.3.3.2), it is important to select a combination with a high Greatest Common Divisor (GCD) between the pole pairs of the two stator windings. This eliminates many combinations.

The same logic can be applied to $p_g + p_c = 78$, and to $p_g + p_c = 80$. The results of all potential pole configurations and the related GCD to the pole pairs of their two windings is given in Table IV-2.

Table IV-2: Different possible configurations of pole pairs with the greatest common divisor between the pole pairs of the two stator windings. All these configurations meet the criteria of a judicious sum of pole pairs $p_g + p_c > 75$, and a good potential cross-coupling factor.

$p_g + p_c = 76$		$p_g + p_c = 78$		$p_g + p_c = 80$	
Pole Configuration	GCD	Pole Configuration	GCD	Pole Configuration	GCD
$p_g = 37, p_c = 39$	1	$p_g = 38, p_c = 40$	2	$p_g = 39, p_c = 41$	1
$p_g = 36, p_c = 40$	4	$p_g = 37, p_c = 41$	1	$p_g = 38, p_c = 42$	2
$p_g = 35, p_c = 41$	1	$p_g = 36, p_c = 42$	6	$p_g = 37, p_c = 43$	1
$p_g = 34, p_c = 42$	2	$p_g = 35, p_c = 43$	1	$p_g = 36, p_c = 44$	4
$p_g = 33, p_c = 43$	1	$p_g = 34, p_c = 44$	2	$p_g = 35, p_c = 45$	5
$p_g = 32, p_c = 44$	4	$p_g = 33, p_c = 45$	3	$p_g = 34, p_c = 46$	2
$p_g = 31, p_c = 45$	1	$p_g = 32, p_c = 46$	2	$p_g = 33, p_c = 47$	1
		$p_g = 31, p_c = 47$	1	$p_g = 32, p_c = 48$	16

From Table IV-2, one pole configuration leads to a much higher Great Common Divisor than all the other configurations. It is the couple: $p_g = 32 = 2 \cdot 2 \cdot 2 \cdot 2 \cdot 2$ and $p_c = 48 = 2 \cdot 2 \cdot 2 \cdot 2 \cdot 3$, so $GCD(32,48) = 16$. Once again, the same result would be obtained if the number of poles of the two stator windings were exchanged. In the following part of the analytical sizing on the characteristics of the TTP, the two poles configurations: $p_g = 32$ and $p_c = 48$, and $p_g = 48$ and $p_c = 32$, will be further investigated.

IV.3.1.4. Mechanical speeds to avoid: synchronism speeds and natural speed

As seen in I.5.3.5.4, p 34, a slip can be defined for each winding. The slips definitions are reminded in equation (98):

$$s_g = \frac{\omega_g - p_g \omega_{rm}}{\omega_g} \quad (98)$$

$$s_c = \frac{\omega_c \pm p_c \omega_{rm}}{\omega_c}$$

s_g and s_c are the slips of the power and control windings respectively.

The sign of $\pm p_c$ considers the phase orders of the power and control windings, see explanations in I.5.3.5.4, after equation (38), p 35. In the following part, it will be considered that the two windings are connected with the same pattern of phases, so $s_c = \frac{\omega_c - p_c \omega_{rm}}{\omega_c}$.

If the order of the control phases is changed by the power converter (phases B and C are switched), ω_c becomes negative.

When one of the slips becomes null, the induced rotor currents from the related stator winding becomes null too. Without these induced rotor currents, the stator windings are not interacting with each other through the rotor: there is no more cross-coupling.

From equation (98), it is possible to deduce the synchronism speeds at which the cross-coupling effect of the BDFM disappears:

$$\begin{aligned} n_{sg} &= \frac{60\omega_g}{2\pi \cdot p_g} \\ n_{sc} &= \frac{60\omega_c}{2\pi \cdot p_c} \end{aligned} \quad (99)$$

n_{sg} and n_{sc} are the synchronism speeds of the grid and control windings respectively (in rpm).
 ω_g and ω_c are the electrical pulsations of the grid and control windings respectively (in $rad.s^{-1}$).
 p_g and p_c are the number of pole pairs of the grid and control windings respectively.

Under cross-coupling, the mechanical speeds and pulsations of the windings are linked by equation (34), p 32, reminded in equation (94), p 128. The pulsation of the control winding to reach the minimal and maximal speed of the interval can be computed with:

$$2\pi f_c = \omega_c = \frac{2\pi}{60} n_r (p_g + p_c) - \omega_g \quad (100)$$

ω_c is the electrical pulsation in $rad.s^{-1}$ of the control winding.

ω_g is the pulsation of the grid in $rad.s^{-1}$.

n_r is the rotating speed of the rotor given in *rpm*; it varies between the minimum and maximum speed given in the specifications.

In Table IV-3, the feeding frequency of the control winding is computed for the minimum and maximum mechanical speeds of the rotor according to equation (100).

Table IV-3: Maximum, minimum and rated feeding frequency of the control winding corresponding to the different speed of the BDFM

Pole Configuration	f_{cmin} ($n_r = 40$ rpm)	f_{cmax} ($n_r = 66$ rpm)	f_{crated} ($n_r = 60$ rpm)
$p_g = 32, p_c = 48$	3.33 Hz	38 Hz	30 Hz
$p_g = 48, p_c = 32$	3.33 Hz	38 Hz	30 Hz

Combining equations (99) and (100), it is possible to write the forbidden speeds at which there is no more cross-coupling because one of the winding does not induce current anymore in the rotor of the BDFM.

Note: the natural speed is also forbidden because, at the natural speed, the pulsation of the current induced by the rotor in the control winding is null.

The forbidden mechanical speeds can be written:

$$\left\{ \begin{aligned} n_{sg} &= \frac{60\omega_g}{2\pi \cdot p_g} \\ n_{sc} &= \frac{60 \left(\frac{2\pi}{60} n_r (p_g + p_c) - \omega_g \right)}{2\pi \cdot p_c} \\ n_n &= \frac{60\omega_g}{2\pi \cdot (p_g + p_c)} \end{aligned} \right. \quad (101)$$

n_{sg} is the synchronism speed of the power winding in *rpm*.

n_{sc} is the synchronism speed of the control winding expressed in *rpm*, it depends of the rotating speed of the rotor.

n_n is the natural speed of the BDFM in *rpm*. The natural speed corresponds to the mechanical speed that lead to a pulsation equal to zero for the control winding induced currents.

In equation (101), the synchronism speed of the power winding and the natural speed do not depend on the mechanical speed of the rotor. In Table IV-4, the synchronism speed of the power winding and the natural speed of the BDFM are computed for the two poles configurations selected.

Table IV-4: Comparison of the forbidden speeds due to the natural speed and the synchronism speed of the power winding for two different pole configurations

Pole Configuration	n_{sg}	n_n
$p_g = 32, p_c = 48$	93.75 <i>rpm</i>	37.5 <i>rpm</i>
$p_g = 48, p_c = 32$	62.5 <i>rpm</i>	37.5 <i>rpm</i>

With Table IV-4, it is possible to eliminate the pole configuration $p_g = 48, p_c = 32$ as a potential solution for the design of the TTP. Indeed, with this pole configuration, the forbidden synchronous speed of the power winding is at 62.5 *rpm*, in the middle of the range of speed in the specifications of the TTP from 40 to 66 *rpm*(specifications given in Table IV-1).

Table IV-4 does not give any information about the forbidden synchronous speed of the control winding. According to equation (101), the synchronous speed varies with the mechanical speed. Using equation (101), it is possible to plot the forbidden speeds of the BDFM as a function of the mechanical speed of the rotor.

When the rotor speed will vary between n_{rmin} and n_{rmax} (40 to 66 *rpm*), the synchronism speed of the control winding varies linearly between n_{scmin} and n_{scmax} . The case of a loss of the cross-coupling due to a forbidden speed will arise if one of the forbidden speed curves (red, blue, or green curves in Figure IV-3) crosses the mechanical speed (black curve in Figure IV-3).

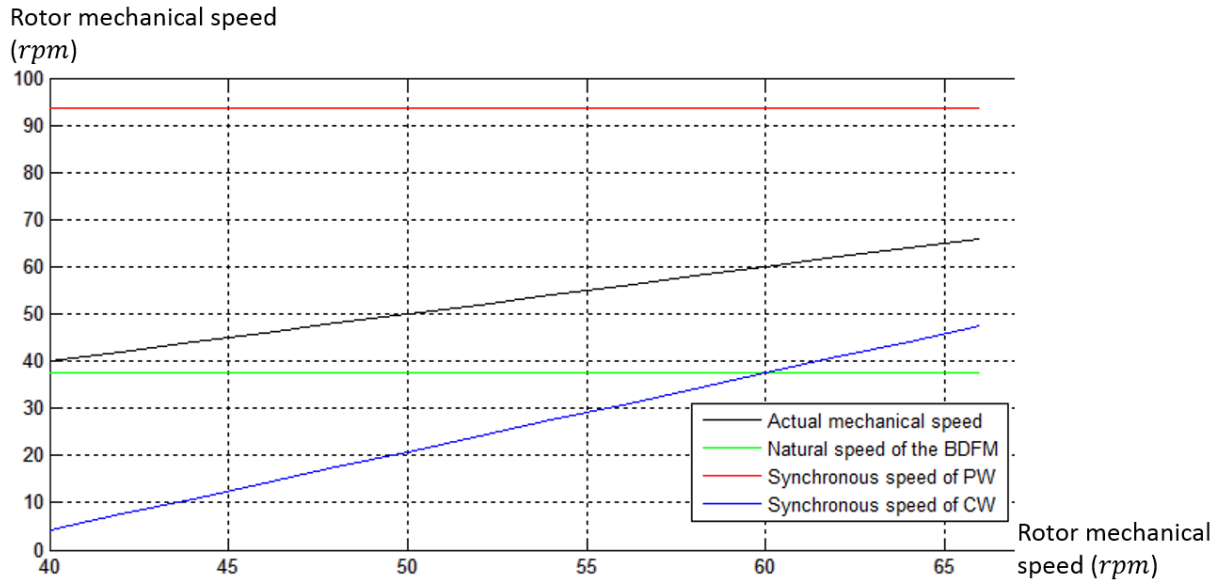


Figure IV-3: Mechanical speed of the rotor and forbidden speeds as a function of the mechanical speed for the combination with $p_g = 32$, $p_c = 48$. From equations (101) and (94).

As it can be seen in Table IV-3 and Figure IV-3, in the range of operation between 40 rpm and 66 rpm, the BDFM with $p_g = 32$ and $p_c = 48$ does not have any problem with a loss of the cross-coupling due to a forbidden speed.

IV.3.1.5. Choice of the pole number for the specifications of the Typical Tidal Project (TTP)

After considerations on the active power of the control winding, on the cross-coupling factor, on the symmetries, and on the forbidden speeds that prevent the cross-coupling, only one pole configuration was selected: $p_g = 32$ and $p_c = 48$. For projects with other specifications, especially projects rotating a bit faster, there might be more pole configurations that meet all the criteria. In this case, one additional criterion can further the selection. In the literature, to our knowledge, most of the studied BDFM have a higher number of control winding poles in comparison to the power winding. $p_g = 1$ and $p_c = 3$ in [36], or $p_g = 4$ and $p_c = 6$ in [36] and [89], $p_g = 2$ and $p_c = 4$ in [37], [78], [89] and in [51] for the 250 kW BDFM.

IV.3.2. Step 2: Choice of the bore diameter

IV.3.2.1. Choice based on the Esson factor or Electrical utilization factor

The bore diameter is the internal diameter of the stator core. For usual machine designs, the bore diameter is chosen with consideration of the electrical and mechanical utilization.

The Esson factor can be used for the electrical utilization. In synchronous machines, this factor is proportional to the product of the airgap flux density B by the stator current density A . During the

sizing of a machine, the Esson factor will thus be used to limit the current density in the conductors and saturation in the iron. The optimal Esson factor is given by curves depending on the rated power per pole and on the cooling method. These curves are internal to companies and are based on experience. The Esson factor can be expressed from the apparent power, the rotation speed of the rotor and the volume of the machine.

$$C = \frac{S_{rated}}{D_{b,s}^2 L_{core} n_r} \quad (102)$$

C the Esson factor or utilization factor in $[MVA \cdot m^{-3} \cdot s]$

S_{rated} is the apparent power of the machine at rated load in $[MVA]$.

$D_{b,s}$ is the bore diameter in $[m]$.

L_{core} is the length of the active material of the machine in $[m]$.

n_r is the rotation speed of the rotor of the machine in $[s^{-1}]$.

In equation (102), the Esson factor is expressed in $MVA \cdot m^{-3} \cdot s$. Most of the time, the Esson factor is used in $kVA \cdot m^{-3} \cdot min$. In that case, the apparent power is expressed in kVA and the maximal speed in rpm . With such units, the choice of the Esson factor is then done with cross curve that are proprietary to each company. For hydro-generators and with such units, the Esson factor will rarely be under 5 and over 15. For the specifications of the TTP, the BDFM will be designed with a utilization factor of 9.

Once the utilization factor is defined, equation (102) will give an indication on the volume of the rotor of the BDFM. The choice of the bore diameter and the length of the machine will then depend on the constraints of the project and the experience of the designer.

Using the example of the TTP, equation (102) will lead to:

$$D_{b,s}^2 L_{core} = \frac{S_{rated}}{C n_{rated}} = \frac{20000/0.8}{9 \cdot 60} = 46.30 \text{ m}^3 \quad (103)$$

For equation (103), an arbitrary power factor of 0.8 was taken.

As stated above, the Esson factor for this design was taken to 9. With this utilization factor, the BDFM might be slightly bigger than the specifications given in Table IV-1. This will be a first design, and the BDFM is expected to have a slightly lower power density than its Synchronous or Induction machines alternatives.

The speed of the BDFM was taken as the rated speed: 60 rpm . Under this speed, the BDFM will not be sized for the rated power, but for the rated torque.

Given the maximal constraints of the machine: $L_{max} = 2.1 \text{ m}$ and $D_{out,max} = 5.2 \text{ m}$, the bore diameter will be set to $D_{b,s} = 4.7 \text{ m}$ and the length of the core of the machine to $L_{core} = 2.1 \text{ m}$. This will give a product: $D_{b,s}^2 L_{core} = 4.7^2 \cdot 2.1 = 46.39 \text{ m}^3$: close to the product computed in equation (103).

IV.3.2.2. Considerations on the moment of inertia and acceleration of the rotor at rated torque

For machines designed in PSP projects, there might be other conditions on the moment of inertia of the rotor. During a faulty situation, when the machine stops to transfer its power to the network, the rotor will accelerate until the valves close to stop the flow of water. The valves are heavy mechanical components and cannot be closed instantly. Their closing speed will depend on each project, but as an indication and to give an order of magnitude to the reader, they operate in roughly half a minute. In the case of a bulb machine, there is not any valve to protect the machine, but the inclination of the blades can vary. The time constant of the blades is smaller than the time constant of heavy valves, the blades can be expected to stop producing power in a matter of a few seconds. To prevent the machine to accelerate too fast and to increase stability, a minimum moment of inertia can be imposed.

In the case of the BDFM, the rotor can be assimilated to a cylinder of iron with a constant density $\rho = 7600 \text{ kg.m}^{-3}$. Under these assumptions, the rotor moment of inertia can be expressed as:

$$\Theta_j = \frac{\pi\rho L_{core}}{32} D_{rot}^4 = \frac{m_{rot}}{8} D_{rot}^2 \quad (104)$$

Θ_j is the rotor moment of inertia (kg.m).

D_{rot} is the rotor external diameter.

m_{rot} is the rotor mass.

The moment of inertia of the rotor can be used to find how fast the machine accelerates under the rated torque.

From Newton's second law, the angular acceleration can be expressed from the rated torque and the moment of inertia:

$$\Gamma_{rated} = \Theta_j \alpha_{rated} \quad (105)$$

Γ_{rated} is the rated torque of the machine in Nm .

α_{rot} is the acceleration of the rotor in rad.s^{-2} .

The rated torque of the machine can be calculated from the rated power and speed of the machine. Considering that the machine can achieve the rated power from its rated speed n_{rated} , the rated torque can be expressed as:

$$\Gamma_{rated} = \frac{P_{rated}}{2\pi \cdot n_{rated} / 60} \quad (106)$$

τ_{rated} , the time constant to go from zero to the rated speed of the machine, can be expressed as follows:

$$\tau_{rated} = \frac{2\pi \cdot n_{rated}/60}{\alpha_{rated}} \quad (107)$$

τ_{rated} , the time constant to accelerate from zero to the rated speed of the machine in *s*. τ_{rated} , is an important time constant for the stability of a machine.

α_{rated} is the rated acceleration of the rotor in *rad. s⁻²*.

n_{rated} is the rated speed of the rotor in *rpm*.

Equations (107), (106), (105), and (104) can be combined to express the time constant τ_{rated} as:

$$\tau_{rated} = \frac{4\pi^2 n_{rated}^2 / 3600}{P_{rated}} \frac{\pi \rho L_{core}}{32} D_{rot}^4 \quad (108)$$

For some projects, equation (108) could be used as a design equation, to impose on τ_{rated} a given value. With the assumption that the rotor external diameter is equal to the bore diameter: (the airgap is small in comparison to the machine diameter): $D_{rot} = D_{b,s}$, equations (102) and (108) would give a unique solution for $D_{b,s}$ and L_{core} . In the case of a bulb turbine, the stability problems are not as important as in PSPs project; for the TTP, the time constant, τ_{rated} , will be computed, but the design will not be adapted to match the time constant to a given value:

$$\tau_{rated} = \frac{4\pi^2 \cdot 60^2 / 3600}{20 \cdot 10^6} \frac{\pi \cdot 7600 \cdot 2.1}{32} \cdot 4.7^4 = 1.51 \text{ s} \quad (109)$$

IV.3.3. Step 3: Choice of the number of stator and rotor slots

In usual machines, the number of slots is selected according to several considerations:

- The winding obtained is a three-phase balanced winding.
- The winding can contain parallel paths (see A.4, p 165).
- The winding can be a full pitch integer slot winding or a fractional slot winding with coil span reduction (see A.6, A.7, and A.8 p 167).
- The number of turns in series per stator phase must be adapted to the stator voltage and the flux density of the machine.
- The slot pitch has a minimal due to the minimum insulation distance between two bars of different phases.

IV.3.3.1. Limits on the number of slots based on the limits of the slot pitch dimensions

With normal machines, a minimum slot pitch is set depending on the voltage of the two stator windings. The minimum slot pitch will fix the maximum number of slots of the stator:

$$N_{slot,s\ max} = \frac{\pi D_{b,s}}{\tau_{slot,s\ min}} \quad (110)$$

$N_{slot,s\ max}$ is the maximum number of slots of the stator.

$\tau_{slot,s\ min}$ is the minimum slot pitch in m .

The minimum number of slots can be set by the maximum slot pitch:

$$N_{slot,s\ min} = \frac{\pi D_{b,s}}{\tau_{slot,s\ max}} \quad (111)$$

From experience, the slot pitch of a hydro machine varies between $\tau_{slot,s\ min} = 40\ mm$ and $\tau_{slot,s\ max} = 80\ mm$.

For the example on the specification of the TTP, that would give:

$$\begin{cases} N_{slot,s\ min} = \frac{\pi 4.7}{0.08} = 184\ slots \\ N_{slot,s\ max} = \frac{\pi 4.7}{0.04} = 369\ slots \end{cases} \quad (112)$$

IV.3.3.2. Impacts of the number of layers per slot and the number of slots per pole and per phase

The BDFM has two stator windings (grid and control); each stator slot will have at least two layers: one layer for the grid winding and one layer for the control winding. If the stator slots only have two layers, then the PW and CW will both be a single-layer winding. In this case, the stator windings will have to be full pitch windings with an integer number of slots per pole and per phase (see A.6, p 167). It is also possible for the stator slots to have four layers: two layers for the grid winding and two layers for the control winding. In this case scenario, it will be possible to reduce the coil span of each winding (refer to Figure A-5 and Figure A-6 in A.6, p 168 and to A.8, p 168). With four layers per slot, it will also be possible to have a fractional slot winding (refer to A.7 p 168).

The number of stator slots can be expressed as:

$$N_{slot,s} = 3q_g 2p_g = 3q_c 2p_c \quad (113)$$

p_g and p_c are the number of pole pairs of the grid and control windings respectively.

q_g and q_c are the number of slots per pole and per phase of the grid and control windings respectively.

$N_{slot,s}$ is the total number of stator slots.

With only two layers per slot, q_g and q_c will have to be integers to have full pitch winding.

For example, for the pole configuration defined in IV.3.1, with $p_g = 32$ and $p_c = 48$, the potential number of stator slots to obtain two integer slot full pitch windings would verify $q_g = \frac{48}{GCD(32,48)} k$ and

$q_c = \frac{32}{\text{GCD}(32,48)}k$, where k is an integer. For $k = 1$, this would give $N_{slot,s} = 3 \cdot \frac{48}{16} \cdot 2 \cdot 32 = 576 = 3 \cdot \frac{32}{16} \cdot 2 \cdot 48$. The minimum number of slots for a full pitch BDFM with a pole configuration $p_g = 32$ and $p_c = 48$ would be $N_{slot,s} = 576$ slots, with $q_g = 3$ and $q_c = 2$.

With two double-layer windings per slot (so four layers per slot), it would be possible to have a different number of slots with a fractional slot winding. The potential number of stator slots would verify $q_g = \frac{48}{2 \cdot \text{GCD}(32,48)}k$ and $q_c = \frac{32}{2 \cdot \text{GCD}(32,48)}k$ where k is an integer. For $k = 1$ this would lead to $N_{slot,s} = 288$ slots, with $q_g = 1.5$ and $q_c = 1$.

IV.3.3.3. Choice of the number of stator slots

As seen in IV.3.3.2, with the pole configuration $p_g = 32$ and $p_c = 48$, the number of stator slots can be $N_{slot,s} = 288$ slots, with $q_g = 1.5$ and $q_c = 1$ or $N_{slot,s} = 576$ slots, with $q_g = 3$ and $q_c = 2$. These numbers of slots per pole and per phase are low. For usual hydro machines, the number of slots per pole and per phase generally vary between $q = 2$ or 3 and $q = 8$.

For that reason, for the design using the TTP specifications, the number of stator slots will be set to $N_{slot,s} = 576$, even if it leads to a tooth width smaller than usual designs (in regard of equations (110), (111), and (112)). With this number of slots, it is still possible to choose between 2 layers and 4 layers per slot. In the first design, we will focus on a design with 2 layers per slot.

IV.3.3.4. The number of slots of the rotor

Once the number of slots of the stator is defined, it is possible to define the number of slots of the rotor. To do a nested-loop rotor, the number of rotor slots needs to be a multiple of the number of nests and the number of loops per nest:

$$N_{slot,r} = 2N_r N_{loops/nest} \quad (114)$$

$N_{slot,r}$ is the number of rotor slots.

N_r is the number of nests with $N_r = p_g + p_c$ (as explained in I.5.3.4.4, equation (16), p 26).

$N_{loops/nest}$ is the number of loops per nest.

From experience, some numbers of rotor slots must be avoided to avoid creating resonances and parasitic forces between the stator slots and the rotor slots. For example, the following should be avoided $N_{slot,r} = N_{slot,s}$ or $N_{slot,r} = N_{slot,s} \pm 2$. In fact, the slots will create harmonics in the airgap. When the number of slots of the stator and the rotor are equals or close, the harmonics will interact and create vibrations and torque oscillations generating noise and decreasing the life-cycle of the machine.

In the example of the design for the TTP, the number of nests is equal to: $N_r = 32 + 48 = 80$. It is possible to choose between $N_{loops/nest} = 2$ or $N_{loops/nest} = 3$ for example. This would lead to $N_{slot,r} = 2 \cdot 80 \cdot 2 = 320$ or $N_{slot,r} = 3 \cdot 80 \cdot 2 = 480$.

The design for the specifications of the TTP should have a rated power of $20MW$. Most of the BDFM prototypes built in the past were less powerful by several factors, the biggest built prototype being a 250 kW (reported in [51]). The pole configuration of this machine was $p_g = 2$ and $p_c = 4$. With such a pole configuration, it was easier to do a design with a reasonable number of slots. For example, $N_{loops/nest} = 3$ for the 250 kW machine of [51] according to its number of rotor slots $N_{slot,r} = 36$ and pictures reported in [90].

IV.3.4. Step 4: Magnetic loading and number of turns in series for each stator winding

IV.3.4.1. Magnetic loading of a BDFM and choice of the maximum flux density

A number of turns in series per pole and per phase has to be chosen for each winding. This number of turns in series is a function of the amplitude and frequency of the fundamental of the magnetic flux density in the airgap and the voltages in each winding. For a usual machine, the amplitude of the fundamental magnetic flux density in the airgap is chosen between 0.9 and 1.

For the BDFM, there are two fundamentals. The magnetic loading will be defined according to the equation proposed in [76] and [32]:

$$\bar{B} = \sqrt{\bar{B}_g^2 + \bar{B}_c^2} \quad (115)$$

\bar{B} is the total magnetic loading.

\bar{B}_g^2 and \bar{B}_c^2 are the magnetic loadings of the power winding and control winding respectively.

Where the magnetic loading is defined as:

$$\bar{B} = \frac{2\sqrt{2}}{\pi} B_{rms} \quad (116)$$

B_{rms} is the root mean square of the flux density.

For a BDFM, the two fundamental flux densities will be chosen such that $\sqrt{\hat{B}_g^2 + \hat{B}_c^2}$ is in the range of 0.9 to 1. \hat{B}_g and \hat{B}_c are the fundamental flux density amplitudes of the power and control windings respectively.

In the literature dealing with the optimization of the BDFM with a wound rotor, it is possible to find equations relating the rotor turns ratios and the flux density ratios. The equation giving the optimum value for the rotor turns ratio is reported to be (for example in [76] and [78]):

$$n_r = \left(\frac{p_g \cos(\phi + \delta)}{p_c \cos \phi} \right)^{\frac{2}{3}} \quad (117)$$

n_r is the rotor turns ratio.

δ is the load angle.

ϕ is the power factor of the power winding.

The rotor turns ratio can be adjusted by changing the number of turns in series for a BDFM with a wound rotor. In the case of a BDFM with nested-loops, the cross-coupling factor can be influenced by ratio of number of poles, as seen in Figure IV-2, and by the number of loops per nest and the opening of the outer loop (refer to nested-loop rotor schemes in Figure I-10, p 33, or Figure I, p 34, or the nested-loop rotor 3D representation in Figure III-1, p 78).

The flux density ratio between the two fundamentals is linked to the rotor turns ratio by:

$$\frac{\widehat{B}_c}{\widehat{B}_g} = \frac{n_r \cos \phi}{\cos(\phi + \delta)} \frac{p_c}{p_g} \quad (118)$$

To use these equations, the authors in the bibliography generally assume that $\frac{\cos(\phi + \delta)}{\cos \phi}$ is close to unity (small load factor and power factor close to 1). Once again, these assumptions can be found in [76] and [78] for example. These are quite bold assumptions that will be false if the design has too much reactive power. Under these conditions, the ratio between the two flux density fundamentals becomes:

$$\frac{\widehat{B}_c}{\widehat{B}_g} \approx \left(\frac{p_c}{p_g} \right)^{\frac{1}{3}} \quad (119)$$

As it was seen in Figure IV-2, to maximize the cross-coupling factor for a BDFM with nested-loops, p_c and p_g had to be as close as possible without being equal. According to equation (119), under the assumption of small load angle and unity power factor, the ratio of the fundamental flux densities $\frac{\widehat{B}_c}{\widehat{B}_g}$ will be close to 1.

For example, for the pole configuration defined in IV.3.1, with $p_g = 32$ and $p_c = 48$, the flux density ratio would be $\frac{\widehat{B}_c}{\widehat{B}_g} \approx \left(\frac{48}{32} \right)^{\frac{1}{3}} \approx 1.14$.

With the condition that $\sqrt{\widehat{B}_g^2 + \widehat{B}_c^2} = 1$ for exemple, this would lead to:

$$\widehat{B}_c = 1.14 \cdot \widehat{B}_g = 1.14 \sqrt{\frac{1^2}{1+1.14^2}}$$

Equivalent to:

$$\begin{cases} \widehat{B}_g = 0.66 T \\ \widehat{B}_c = 0.75 T \end{cases} \quad (120)$$

IV.3.4.2. Theoretical number of turns in series

For a normal synchronous machine, the number of turns in series per stator phase is given by the following equation:

$$N_s = \sqrt{\frac{2}{3}} \frac{U_{s,RMS}}{k_w 4 f_s \widehat{B}_{ag,f} \tau_{p,s} L_{core}} \quad (121)$$

$U_{s,RMS}$ is the RMS stator rated line to line voltage.

k_w is the winding factor, it can be computed with equations (156) and (159) see A.9 p 169.

f_s is the stator feeding frequency (for the BDFM it will be the grid frequency for the power winding and the power inverter frequency for the control winding).

$\widehat{B}_{ag,f}$ is the amplitude of the fundamental flux density in the airgap.

$\tau_{p,s}$ is the pole pitch: $\tau_{p,s} = \frac{\pi D_{b,s}}{p}$ with $D_{b,s}$ the bore diameter and p the pole pair number.

For the BDFM on the specifications of the TTP, the windings are full pitch windings after the decision taken in IV.3.3.3. If the stator slots are not skewed, the winding factors should only consider the distribution factors (see (159) in A.9 p 170). Thus, it is easy to compute the winding factors of the stator windings of the BDFM once the numbers of poles and the numbers of slots have been chosen.

For the BDFM, the number of turns in series per phase are computed for the two windings: $N_{s,g}$ and $N_{s,c}$ are the number of turns in series of the grid winding and control winding respectively.

For each winding, the number of parallel circuits and the number of conductors in series per winding and per slot can be adjusted in order to try to match the number of turns in series and the number of slots (refer to A.3 and A.4 p 164). These parameters are linked with the following equation:

$$N_{slot,s} = \frac{6N_s N_{pp}}{N_{cond}} \quad (122)$$

$N_{slot,s}$ is the number of slots of the stator which is common for both the grid and control windings.

N_s is the number of turns in series per phase of the winding.

N_{pp} is the number of parallel paths of the winding.

N_{cond} is the number of conductors per slot of the winding.

IV.3.4.3. Choice of the number of parallel paths, conductors per slot, and the voltages of the power and control windings

For the control winding, three degrees of freedom remain to set the number of turns in series per slot and per phase $N_{s,c}$. They are: the number of parallel paths $N_{pp,c}$, the number of conductors per slots $N_{cond,c}$, and the voltage of the winding $U_{c,RMS}$. The RMS stator rated line to line voltage $U_{c,RMS}$ is imposed by the power converter: 3300 V or 6600 V.

Combining equations (121) and (122), the following equation can be written for the CW:

$$\frac{6N_{pp,c}U_{c,RMS}}{N_{cond,c}} = \sqrt{\frac{3}{2}}k_{wc}4f_c\widehat{B}_c\tau_{p,c}L_{core}N_{slot,s} \quad (123)$$

k_{wc} can be computed with A.9, equation (159), p 170.

$\tau_{p,c}$ can be computed with $\tau_{p,c} = \frac{\pi D_{bs}}{2p_c}$.

f_c can be computed by $f_c = \frac{n_{rm}}{60}(p_g + p_c) - f_g$ as already shown in equation (100).

Applying equation (123) to the design with the specifications of the TTP, the following equation is obtained:

$$\frac{6N_{pp,c}U_{c,RMS}}{N_{cond,c}} = \sqrt{\frac{3}{2}}0.966 \cdot 4 \cdot \left| \frac{60}{60}80 - 50 \right| \cdot 0.75 \cdot \frac{\pi \cdot 4.7}{2 \cdot 48} \cdot 2.1 \cdot 576 = 19\,800\,V \quad (124)$$

Equation (124) shows that $N_{pp,c}$, $U_{c,RMS}$, and $N_{cond,c}$ must be found such that $\frac{6N_{pp,c}U_{c,RMS}}{N_{cond,c}} = 19\,800\,V$. With $U_{c,RMS} = 6600$ or $3300\,V$, $N_{cond,c}$ an integer, and $N_{pp,c}$ an integer. Each parallel path must pass through the same number of slots and have the same number of turns in series, so $N_{pp,c}$ must be a divisor of $\frac{N_{slot,s}}{2 \cdot 3}$. It is possible to find all the values that $N_{pp,c}$ can take with an integer factorization of $\frac{N_{slot,s}}{2 \cdot 3}$. In the first analytical design of the TTP: $\frac{576}{2 \cdot 3} = 96 = 2 \cdot 2 \cdot 2 \cdot 2 \cdot 2 \cdot 3$. This integer factorization indicates that $N_{pp,c}$ can take the following values: $N_{pp,c} = 2$, $N_{pp,c} = 3$, $N_{pp,c} = 2 \cdot 2$, $N_{pp,c} = 2 \cdot 3$, $N_{pp,c} = 2 \cdot 2 \cdot 2$, $N_{pp,c} = 2 \cdot 2 \cdot 3$, $N_{pp,c} = 2 \cdot 2 \cdot 2 \cdot 2$, $N_{pp,c} = 2 \cdot 2 \cdot 2 \cdot 3$, $N_{pp,c} = 2 \cdot 2 \cdot 2 \cdot 2 \cdot 2$, and finally $N_{pp,c} = 2 \cdot 2 \cdot 2 \cdot 2 \cdot 3$.

All the possibilities for $N_{pp,c}$, $U_{c,RMS}$, and $N_{cond,c}$ can be tried. The best result to be kept is the one where $\frac{6N_{pp,c}U_{c,RMS}}{N_{cond,c}}$ is as close to $\sqrt{\frac{3}{2}}k_{wc}4f_c\widehat{B}_c\tau_{p,c}L_{core}N_{slot,s}$ as possible. In the case of the first analytical design on the specifications of the TTP, a few simple combinations work as it can be seen in Table IV-5.

Table IV-5: Some possibilities of the choice of parallel paths, conductors in series and voltages for the control winding of the BDFM based on a first sizing on the specification of a Typical Tidal Project (TTP).

$N_{pp,c}$	$N_{cond,c}$	$N_{s,c}$	$U_{c,RMS}$ [V]	$\frac{6N_{pp,c}U_{c,RMS}}{N_{cond,c}}$ [V]
1	1	96	3 300	19 800
1	1	96	6 600	39 600
1	2	192	6 600	19 800

Table IV-5 shows that some choices are equivalent. To keep the end winding connection simple, the winding with $N_{pp,c} = 1$, $N_{cond,c} = 2$, and $U_{c,RMS} = 6600$ V will be selected.

The same logic can be applied to the power winding of the BDFM. The difference is that the voltage is not imposed by a power converter. The power winding will be connected to the grid through a transformer with a ratio that can be chosen. The voltage of the power winding is a degree of freedom.

For the power winding and the design for the TTP, $N_{pp,c} = 2$, $N_{cond,c} = 2$, and $U_{c,RMS} = 7200$ V are chosen.

IV.3.5. Step 5: The stator currents, and the size and proportion of the slots

IV.3.5.1. The stator currents

With a few hypotheses, the stator currents can now be estimated. For the control winding, the highest active power will be reached at the maximum rotor rotating speed (refer to equation (93) and the visualization in Figure IV-1). For the grid winding, the highest active power will be reached at the minimum speed under rated power (once again refer to visualization in Figure IV-1).

The stator currents per slot can be determined by the following equation:

$$i_{slot,RMS} = \frac{N_{cond}}{N_{pp}} \frac{P}{\sqrt{3}U_{s,RMS} \cos \varphi} \quad (125)$$

$i_{slot,RMS}$ is the RMS current per parallel path in A.

P is the active power of the winding in W.

$U_{s,RMS}$ is the RMS stator rated line to line voltage in V.

$\cos \varphi$ is the power factor of the winding.

Equation (125) can be applied to both the power winding and the control winding. The rated powers of the grid and control windings can be expressed as functions of the rotating speed from equation (93): as shown in Figure IV-1, p 129. Since the control winding active power increases with speed, from equation (93), it is possible to write:

$$P_{c,max} = \frac{P_{rated}}{1 + \frac{\omega_g}{\omega_{c,max}}} \quad (126)$$

$P_{c,max}$ is the maximum active power of the control winding under the rated operation in W .

$\omega_{c,max}$ is the maximum electrical pulsation of the control winding when the BDFM is operated at maximum speed. The mechanical speed and control winding pulsation are linked by equation (94), p 128.

The maximum active power of the grid winding will be reached at rated power when the control active power is minimum:

$$P_{g,max} = P_{rated} - P_{c,min} = P_{rated} - \frac{P_{rated}}{1 + \frac{\omega_g}{\omega_{c,rated}}} \quad (127)$$

The electrical pulsation of the control winding at the maximum operating speed and at the rated speed was already given in Table IV-3. Application of equations (126) and (127) to the design of the TTP will give:

$$P_{c,max} = \frac{20 \cdot 10^6}{1 + \frac{50}{38}} = 8.64 \text{ MW} \quad (128)$$

$$P_{g,max} = 20 \cdot 10^6 - \frac{20 \cdot 10^6}{1 + \frac{50}{30}} = 12.5 \text{ MW}$$

With a power factor estimation of $\cos \varphi_g = 0.8$ for the grid winding and $\cos \varphi_c = 0.8$ for the control winding, the current per parallel path can now be computed for the two windings. Application of equation (125) gives:

$$i_{slot,c,RMS} = \frac{N_{cond,c} P_{c,max}}{\sqrt{3} N_{pp,c} U_{c,RMS} \cos \varphi} = \frac{2 \cdot 8.64 \cdot 10^6}{\sqrt{3} \cdot 1 \cdot 6600 \cdot 0.8} = 1252.9 \text{ A} \quad (129)$$

$$i_{slot,g,RMS} = \frac{N_{cond,g} P_{g,max}}{\sqrt{3} N_{pp,g} U_{g,RMS} \cos \varphi} = \frac{2 \cdot 12.5 \cdot 10^6}{\sqrt{3} \cdot 2 \cdot 7200 \cdot 0.8} = 1889.5 \text{ A}$$

IV.3.5.2. Size and proportion of the slots

To limit the Joule losses and the temperature of the machine, it is usual to define a maximum current density for the stator and for the rotor. With the current per slot and the maximum current density, the slot area for each winding can be calculated:

$$A_{slot} = \frac{i_{slot,RMS}}{J_{max} k_{fill}} \quad (130)$$

A_{slot} is the surface area in mm^2 .

J_{max} is the maximum current density in the copper in $A \cdot mm^{-2}$.

k_{fill} is the filling factor of the slot (see A.3, p 164).

With equation (131), it is possible to find the slot surface area for each winding of the stator for the first analytical sizing of the TTP. From experience, the filling factor will be taken as: $k_{fill} = 60\%$ and a maximum current density $J_{max} = 2.5 A \cdot mm^{-2}$:

$$\begin{aligned} A_{slot,g} &= \frac{1\,252.9}{2.5 \cdot 0.6} = 835.3 \text{ mm}^2 \\ A_{slot,c} &= \frac{1\,889.5}{2.5 \cdot 0.6} = 1259.7 \text{ mm}^2 \end{aligned} \quad (131)$$

From the number of slots of the stator, it is possible to evaluate the width of a slot. For hydro-generators, the ratio between the width of a tooth and the width of a slot is generally around $\frac{w_{tooth}}{w_{slot}} = 1.5$ to 2. With this ratio, the bore diameter of the machine, and the number of slots it is possible to express the width of a tooth:

$$w_{slot} = \frac{\pi \cdot D_{b,s}}{N_{slot,s} \cdot \left(1 + \frac{w_{tooth}}{w_{slot}}\right)} \quad (132)$$

w_{slot} is the width of a slot in mm .

w_{tooth} is the width of a tooth in mm .

With equation (132), the width of the slots of the stator and the rotor for the first analytical design of the TTP can be computed. The ratio of the tooth width will be taken as $\frac{w_{tooth}}{w_{slot}} = 1.6$:

$$\begin{aligned} w_{slot,s} &= \frac{\pi \cdot 4.7}{576 \cdot (1 + 1.7)} = 9.86 \text{ mm} \\ w_{slot,r} &= \frac{\pi \cdot 4.7}{480 \cdot (1 + 1.7)} = 11.83 \text{ mm} \end{aligned} \quad (133)$$

$w_{slot,s}$ and $w_{slot,r}$ are the widths of the stator and rotor slots respectively.

With both the width of the slots and their surface area, it is possible to calculate the height of the slots:

$$h_{slot,s} = \frac{A_{slot,g} + A_{slot,c}}{w_{slot,s}} + h_{wedge} + h_{spacer} \quad (134)$$

$h_{slot,s}$ is the height of the stator slots, in mm .

h_{wedge} is the height of the wedges (refer to A.3, p 164), in mm .

h_{spacer} is the height of the spacers (refer to A.3, p 164), in mm .

In the first analytical design of the TTP, the sum of the heights of the wedges and the spacers can be estimated to be $h_{wedge} + h_{spacer} = 20 \text{ mm}$. The height of the stator slots is then:

$$h_{slot,s} = \frac{835.3 + 1259.7}{9.86} + 20 = 232.5 \text{ mm} \quad (135)$$

This height gives a ratio between the height and the width of the stator slots: $\frac{h_{slot,s}}{w_{slot,s}} = \frac{232.5}{9.86} = 23.6$. This ratio is a bit higher than usual ratios for hydro-machines: they are rarely out of the 10 to 20 range. It is not very surprising considering the choice of the high number of slots that was made: the more slots there are, the thinner they are...

The proportions of the slot areas taken by the power winding and control winding are also interesting. For the first design with the specifications of the TTP, these ratios will be:

$$k_{prop,g} = \frac{A_{slot,g}}{A_{slot,g} + A_{slot,c}} = 39.9 \% \quad (136)$$

$$k_{prop,c} = \frac{A_{slot,c}}{A_{slot,g} + A_{slot,c}} = 60.1 \%$$

For the rotor, it is harder to evaluate the currents per slot analytically. In a first analytical design, the area of the slots will be defined identically to the stator slots:

$$h_{slot,r} \cdot w_{slot,r} = h_{slot,s} \cdot w_{slot,s} \quad (137)$$

Equation (137) leads to the computation of the height of the rotor slots:

$$h_{slot,r} = h_{slot,s} \cdot \frac{w_{slot,s}}{w_{slot,r}} = 232.5 \cdot \frac{9.86}{11.83} = 194 \text{ mm} \quad (138)$$

IV.3.5.3. Computation of the resistance of the stator windings and rotor loops

With the number of slots, the number of parallel paths and turns in series, and the surface area per slot, it is now possible to compute the resistance per phase of each winding. For the stator windings, the resistance can be determined with:

$$R_s = \rho(T) \frac{N_s L_{turn}}{A_{slot} k_{fill} N_{pp}} \quad (139)$$

R_s is the resistance per phase of the winding in Ω ,

$\rho(T)$ is the resistivity of Copper that depends on the temperature as expressed in:

$$\rho(T) = 1.7 \cdot 10^{-8} (1 + 3.8 \cdot 10^{-3} (T - 20)) \quad \Omega \cdot \text{m}^{-1}.$$

N_s is the number of turns in series per phase.

L_{turn} is the length of a turn: $L_{turn} = 2L_{core} + 2L_{endW}$.

L_{endW} is the length of the end winding. In the case of a full pitch winding the end winding can be approximated to: $L_{endW} = \frac{\pi D_{bs}}{2p} \frac{1}{\cos(\alpha_{endW})}$.

α_{endW} is an estimation of the inclination of the end winding.

To apply equation (139) in the example of the TTP, the machine will be assumed to operate at a temperature of 100 °C and an inclination of the end winding of 20°, so $\cos(\alpha_{endW}) = 0.94$.

$$R_c = 1.7 \cdot 10^{-8} (1 + 3.8 \cdot 10^{-3} (100 - 20)) \frac{192 \left(2 \cdot 2.1 + \frac{\pi 4.7}{2 \cdot 48} \frac{1}{0.94} \right)}{1259.7 \cdot 10^{-6} \cdot 0.6} = 0.0246 \quad \Omega \quad (140)$$

Similarly, the resistance per phase of the power winding is:

$$R_g = 1.7 \cdot 10^{-8} (1 + 3.8 \cdot 10^{-3} (100 - 20)) \frac{96 \left(2 \cdot 2.1 + \frac{\pi 4.7}{2 \cdot 32} \frac{1}{0.94} \right)}{853.3 \cdot 10^{-6} \cdot 0.6} = 0.0189 \quad \Omega \quad (141)$$

Finally, the resistance of each rotor loop can be computed. To simplify the computation and obtain the same resistance for each loop, it will be assumed that they have the same end winding length: the outer loop end winding length.

$$R_r = 1.7 \cdot 10^{-8} (1 + 3.8 \cdot 10^{-3} (100 - 20)) \frac{\left(2 \cdot 2.1 + \frac{\pi 4.7}{80} \right)}{11.83 \cdot 194 \cdot 10^{-6} \cdot 0.6} = 0.0068 \quad \Omega \quad (142)$$

IV.3.6. Step 6: Determination of the airgap radial length

From a magnetic point of view, the smaller the airgap is, the less the current needed to magnetize the machine will be. A smaller airgap will thus lead to smaller Joule losses in the stator windings. However, a smaller airgap might lead to higher iron losses at the tip of the stator and rotor teeth.

Another factor to consider is the thermal expansion of the rotor under load which can reduce the airgap radial length. Furthermore, the smaller the airgap is, the higher will be the impact of a potential small eccentricity.

For the reasons cited above, the airgap radial length is generally set to a minimal constraint that considers the risk of eccentricity and the thermal expansion. These constraints are issued from experience.

In the case of the BDFM, the airgap radial length will be set to: $\delta_{ag} = 10 \text{ mm}$.

IV.3.7. Step 7: Determination of the rotor and stator yoke heights followed by the external diameter of the machine

The rotor and stator yokes height are both compromises between the yoke flux density and the weight and price of the yokes. More iron will lead to lower flux densities and iron losses, but higher cost for the machine.

To define the yoke height for usual machines, the first step is to determine the total flux per pole from the fundamental of the flux density in the airgap.

$$\widehat{\Phi}_p = \frac{2}{\pi} L_{core} \tau_p \widehat{B} \quad (143)$$

$\widehat{\Phi}_p$ is the maximum flux per pole in Wb .

\widehat{B}_f is the amplitude of the fundamental flux density in the airgap, in T .

τ_p is the pole pitch in m .

It is also possible to express the maximal flux passing through the yoke with the yoke height and the maximal flux density of the yoke for the fundamental:

$$\widehat{\Phi}_y = \widehat{B}_{y,s} h_{y,s} L_{core} \quad (144)$$

$\widehat{\Phi}_y$ is the maximum flux through a radial section of the yoke in Wb .

$h_{y,s}$ is the radial height of the yoke in m .

$\widehat{B}_{y,s}$ is the maximum flux density for the fundamental harmonic in the yoke.

The maximum flux in the stator yoke will be half of the maximum flux per pole: $\widehat{\Phi}_y = \frac{1}{2} \widehat{\Phi}_p$. With equations (143) and (144), the designer can calculate the yoke height after choosing the maximum flux density in the yoke. In general hydro design, the maximum flux density in the yoke is generally between 1.1 to 1.4 T .

$$h_{y,s} = \frac{1}{\pi} \tau_p \frac{\widehat{B}}{\widehat{B}_{y,s}} \quad (145)$$

It is possible to apply equation (145) to the two stator windings of the first analytical design on the TTP specifications. $\widehat{B}_{y,s} = 1.1 T$ can be used for both windings.

$$\begin{aligned} h_{y,g} &= \frac{1}{\pi} \cdot \frac{4.7}{32} \cdot \frac{0.66}{1.1} = 88.1 \text{ mm} \\ h_{y,c} &= \frac{1}{\pi} \cdot \frac{4.7}{48} \cdot \frac{0.75}{1.1} = 67.8 \text{ mm} \end{aligned} \quad (146)$$

$h_{y,g}$ and $h_{y,c}$ would be the theoretical radial yoke heights of the grid and control windings respectively if there was only one stator winding.

For the first analytical design of the BDFM, the yoke height will be defined as:

$$h_{y,s} = \sqrt{h_{y,g}^2 + h_{y,c}^2} \quad (147)$$

Finally, the outer diameter of the stator can be calculated by:

$$D_{out,s} = D_{b,s} + \delta_{ag} + 2h_{slot,s} + 2h_{y,s} \quad (148)$$

The inner diameter of the rotor can be calculated with:

$$D_{in,r} = D_{b,s} - \delta_{ag} - 2h_{slot,r} + 2h_{y,r} \quad (149)$$

On the first analytical example of the TTP, we find:

$$D_{out,s} = 4.7 + 10 \cdot 10^{-3} + 2 \cdot 232.5 \cdot 10^{-3} + 2\sqrt{88.1^2 + 67.8^2} 10^{-3} = 5.4 \text{ m} \quad (150)$$

$$D_{in,r} = 4.7 - 10 \cdot 10^{-3} - 2 \cdot 194 \cdot 10^{-3} - 2\sqrt{88.1^2 + 67.8^2} 10^{-3} = 4.0 \text{ m} \quad (151)$$

IV.3.8. Step 8: Determination of the stacking factor, and the number and width of ventilation ducts

Before testing the analytical design with FE simulations, the stacking factor (see A.2, p 163) and the number of ventilation ducts for the rotor and the stator need to be determined.

IV.3.8.1. Stacking factor in hydro machines

The stacking factor depends on the staking process during the manufacturing of the machines. For hydro-machines, the manufacturing process leads to a stacking factor around $k_{stacking} = 0.90 - 0.95$. For the rotor and the stator of the BDFM designed on the TTP specifications, the stacking factor will be imposed to $k_{stacking} = 0.93$.

IV.3.8.2. Ventilations ducts

Ventilations ducts in the stator and the rotor are important to evacuate the heat generated during the operation of the machine. The number of ventilation ducts can be determined from the length of the machine, the width of each ventilation duct and the width of each stack of iron between two ventilation ducts:

$$N_{ducts} = \frac{L_{core}}{w_{duct} + w_{stack}} \quad (152)$$

N_{ducts} is the number of ventilation ducts.

w_{duct} is the width of each ventilation duct, this width depends on the cooling method.

w_{stack} is the width of the stack of iron between each ventilation duct, it also depends on the cooling method.

For the analytical design on the TTP, the width of stator ducts will be set to $w_{duct,s} = 7 \text{ mm}$, the width of rotor ducts will be set to $w_{duct,r} = 8 \text{ mm}$, and the width of each stack of iron will be set close to $w_{stack} = 60 \text{ mm}$. Applying equation (152) with these parameters leads to:

$$N_{ducts,s} = \frac{2100}{7 + 60} = 31.3 \approx 31 \quad (153)$$

$$N_{ducts,r} = \frac{2100}{8 + 60} = 30.9 \approx 31 \quad (154)$$

IV.3.9. Summary of the first analytical sizing of the BDFM on the specifications of the Typical Tidal Project (TTP)

In the previous parts, a BDFM was analytically sized for the specification of the TTP. Table IV-6 summarizes all the parameters determined during the analytical design. To obtain these parameters, some hypotheses and choices were made during the analytical design. Some equations used the assumption of a unity power factor (like equations (91), (117), (118), and (119)). In equation (103), the Esson factor was chosen to be equal to 9. In equation (120), to choose the amplitudes of the fundamental of the airgap flux densities, the condition $\sqrt{\hat{B}_g^2 + \hat{B}_c^2} = 1$ was set. In equation (129), the stator currents were determined with an arbitrary power factor of 0.8. In equation (138), the rotor currents were not determined to fix the rotor slot area and rotor slot height. To compute the resistances of the windings, the temperature of the machine during operation was estimated at 100°C in (140), (141), and (142).

All these hypotheses and choices were motivated by experience or taken in the literature. However further simulations are needed to confirm whether the design of Table IV-6 meets the specifications of the TTP.

Table IV-6: Characteristics of the analytical design of the BDFM on the specifications of the TTP

Stator Geometric Parameters			Related equation
Length of the machine	2100 mm		(103)
Stator outer diameter	5 400 mm		(150)
Stator inner diameter	4 710 mm		(103)
Number of slots	576		(112) and (113)
Stator slot width	9.86 mm		(133)
Stator slot height	232.5 mm		(135)
Stator wedge height	20 mm		(135)
Stator core stacking factor	0.93		
Number of ventilation ducts	31		(153)
Width of a ventilation duct	7 mm		(153)
Rotor Geometric Parameters			
Rotor outer Diameter	4 690 mm		(103)
Rotor inner Diameter	4 000 mm		(151)
Number of nests	80		(114) or (16)
Number of loops per nest	3		(114)
Number of slots	480		(114)
Rotor slot width	11.8 mm		(133)
Rotor slot height	194 mm		(135)
Rotor wedge height	20 mm		(135)
Number of ventilation ducts	31		(153)
Width of a ventilation duct	8 mm		(153)
Rotor current frequency at 40 rpm	28.66 Hz		(27)
Rotor current frequency at 60 rpm	18 Hz		(27)
Rotor current frequency at 66 rpm	14.8 Hz		(27)
Resistance per loop	0.0068 Ω		(142)
Stator Winding Characteristics			
	Grid Winding	Control Winding	
Number of pole pairs	32	48	(93) and (96)
Number of slots per pole and per phase	3	2	(113)
Number of parallel paths	2	1	(124)
Number of conductors per slot	2	2	(124)
Proportion of conductor area in the slot	39.9 %	60.1 %	(136)
Line to line RMS Load Voltage	7200 V	6600 V	Table IV-5
Feeding Frequency at 40 rpm	50 Hz	3.33 Hz	(100)
Feeding Frequency at 60 rpm	50 Hz	30 Hz	(100)
Feeding Frequency at 66 rpm	50 Hz	38 Hz	(100)
Resistance per phase	0.0189 Ω	0.0246 Ω	(140) and (141)

IV.4. FE simulation of the analytical design, and improvement of the design through an iterative process

IV.4.1. FE load simulation of the analytical design with a magneto-transient application

The analytical design presented in Table IV-6 was simulated in an FE software: Flux2D magneto-transient application, for verifications of the machine characteristics under load. The results can be seen in Table IV-7.

Table IV-7: Results of a load test of the analytical BDFM design with FE magneto-transient simulations. Verifications of the phase-neutral voltage amplitudes, current amplitudes, and phase of the currents for the phase A of the PW and CW. Verification of the active power per phase, reactive power per phase and power factor.

PW voltage: 5878.7 V, frequency: 50 Hz. CW voltage: 5388.8 V, frequency: 30 Hz. Rotor speed: 60 rpm.						
	V: [V]	I: [A]	$\angle I$: [Rad]	P: [MW]	Q: [MVar]	Power Factor
PW	5878.7	1910.78	1.641	0.395	5.602	0.070
CW	5388.8	1552.96	1.393	-0.709	4.124	-0.190

As it can be seen in Table IV-7, the magneto-transient results show that the analytical design does not meet the specifications it was based on. The total power of the BDFM is far from the 20 MW (less than 1 MW per phase for both the PW and CW). However, the BDFM is almost consuming 30 MVar of reactive power: $3 \cdot 5.602 + 3 \cdot 4.124 = 29.178$ MVar. The reactive power consumption of this design is far greater than the active power in a load scenario. It can also be seen that the power factors of the PW and CW are far below 0.8 (0.07 for the PW and 0.19 for the CW). This was completely unexpected; such a problem was not encountered on the first random BDFM designed in this work and presented in Table III-1, p 77. With these low power factors, the hypotheses made for the analytical design in equations (91), (117), (118), and (119) are false: power factors are not close to unity for the stator windings.

It is not obvious which design step led to a bad BDFM design. To improve it, an FE magneto-harmonic model, analogous to the idea developed in III.5 was used. This method cannot consider saturation, but it can at least improve the design for the linear characteristics. If the design works in the linear characteristics, it will be a first step toward making it happen with saturation.

IV.4.2. Iterative process to improve the BDFM design with an FE magneto-harmonic model

The analytical design of the BDFM, summarized in Table IV-6, was not working as expected. It was first simulated on Flux2D magneto-transient with saturation and then on the FE magneto-harmonic model based on the FE software internal to General Electric. With this FE software, each load scenario

computation was taking less than 5 seconds without considering saturation. It could be possible to pair this FE magneto-harmonic model with a Design Of Experiment (DOE) method, as presented in II.2.2.2.4, p 49. However, the iterative process presented in this part was directly done by the author of this work. Extensive results are given in Table M-1, p 261, in APPENDIX M. Figure IV-4 gives the evolution of the power factor of the PW and CW depending on the iteration.

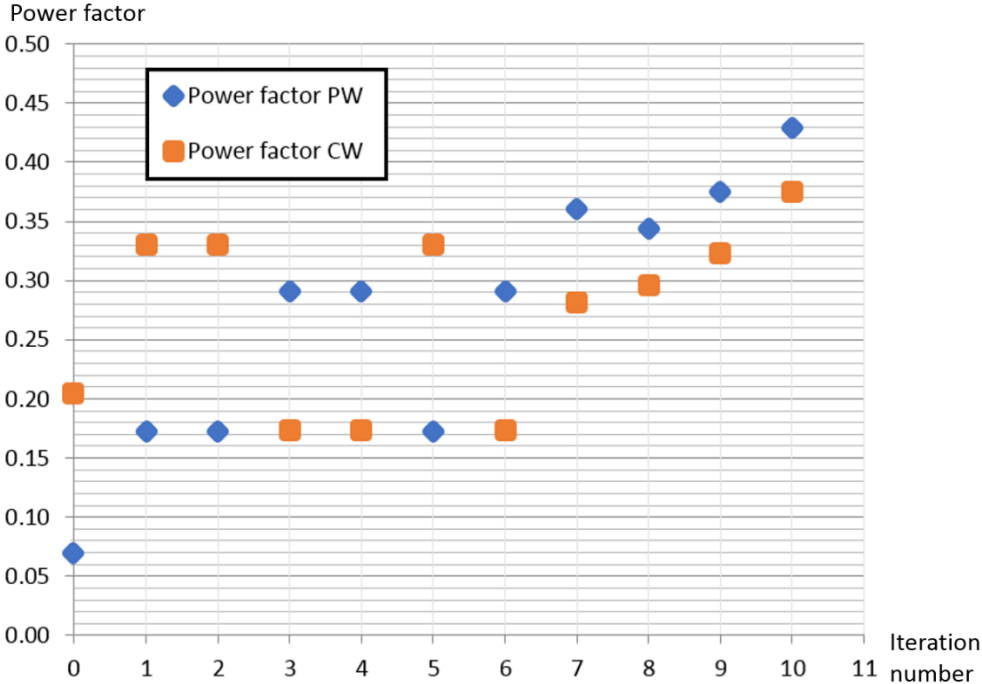


Figure IV-4: Evolution of the power factor of the BDFM designs during the iterative process starting from the analytical design at iteration 0

As it can be seen in Figure IV-4, in 10 iterations, the power factor of the PW and CW were greatly improved. For the PW, the power factor went from 0.07 for the analytical design, up to 0.43 for the last iteration. For the CW, it went from 0.20 to 0.38. Table M-1, p 261, shows that the total power of the BDFM was also improved from 2.87 MW to 12.6 MW. These are very good improvements in just a few iterations that took approximately one day of work. However, they are not yet enough to meet the power factor and total power requirements for the TTP. Moreover, during these iterations, the maximum outer diameter of the specifications has been exceeded, going from 5.4 m in the analytical design, to 6.4 m for the last iteration (the maximum outer diameter was 5.2 m according to the specifications in Table IV-1).

More iterations could lead to a BDFM meeting the requirements from a rated power point of view. However, it was clear while playing with the magneto-harmonic simulations, that the dimensions specifications given in Table IV-1 would not be achieved.

The BDFM need a high number of poles to operate at such speed ($p_g + p_c = 80$ in the designs of CHAPTER IV to operate from 40 rpm to 66 rpm). This high number of poles translates into a high number of teeth. If the teeth are too thin, this leads to a high tooth flux leakage which translate into very low power factors. To increase the widths of the teeth, the bore diameter and outer diameter of the BDFM has to be increased. This does not imperatively translate into heavy machines since the

stator and rotor yokes are also very thin (still due to the high number of poles). However, this is a bottleneck when the footprint of the machine is limited in the requirements.

From this conclusion, the BDFM seems more suitable for higher speed. At very low speeds, as in the specifications of the TTP, they could become interesting in cases where the turbine could be fitted inside the rotor, at the usual position of the shaft. In this configuration, the bore diameter could be large enough to fit all the teeth needed for the high number of poles.

IV.5. Conclusion

The objective of this chapter was to size a BDFM for the specifications of the Typical Tidal Project (TTP). A first design was obtained with an analytical design method in IV.3. The sizing equations were taken either from literature or from experience based on other hydro machines. The low speed in the specifications and the dimensions limits for the TTP led to a design with low power factors for the PW and CW. With such power factors, some of the hypotheses used for the analytical design ended up being wrong. FE simulations showed that the active and reactive power required by the specifications could not be achieved with the analytical design.

In IV.4, the analytical design was improved by an FE iterative process. This process was based on the FE magneto-harmonic method for the BDFM developed and presented in III.5. However, unlike in III.5, this method was not applied with Flux2D magneto-harmonic applications. An FE software developed in General Electric specifically for rotating machines was preferred for computation time reasons. This internal software was not adapted to consider saturation; however, it was able to compute load cases without saturation in less than 5 seconds (in comparison to 5 minutes when based on Flux2D as presented in III.5). This iterative process illustrated the effectiveness of the methods developed in CHAPTER III. In just a day of work, 10 iterations were done to improve the BDFM design, with as much as 20 FE load tests per scenario. As a reminder, at the beginning of this work, the FE load tests scenario performed with magneto-transient applications were taking days. During the iterations, the design went from a rated power of 2.87 MW to 12.6 MW. To explore further, it could have been possible to pair the magneto-harmonic developed with a Design of Experiment method (as presented in II.2.2.2.4). However, this iterative process presented in IV.4 already seemed to indicate that the specifications of the TTP were not well indicated for a BDFM. The mechanical speed of the specifications (40 to 66 rpm) was very slow for a machine fed at 50 Hz by the grid. To operate at this speed, the number of pole pairs was very high ($p_g = 32$ and $p_c = 48$ for the designs in CHAPTER IV). With these number of poles, the minimal number of slots to design the three phases windings of the PW and CW was very high: $N_{slot,s} = 576$ slots. With the outer diameter dimensions limits given by the specifications, this led to very thin slots and low power factors. The BDFM technology seems more adequate for higher speeds. For very low speed, they could become interesting in cases where the turbine could be fitted inside the rotor in place of the shaft. In this configuration, the bore diameter could be large enough to fit all the teeth needed for high number of poles.

GENERAL CONCLUSION

With the renewable energy boom, energy storage will have a bigger and bigger role to play in the stability of future Grids. In CHAPTER I, Pumped-hydro Storage Plants (PSPs) were compared to other energy storage systems. It was noted that, due to their advantages over other energy storage solutions, PSPs already play a considerable stabilization role in developed countries. There is still some place for new installations in emerging countries and for retro-fitting the fixed speed aging infrastructures already installed by variable speed technologies. In CHAPTER I, it was also shown that variable speed technologies can improve the cycle efficiency and the power adjustability of PSPs compared to fix speed technologies. A state of the art assessment of variable speed machines was done. Current technologies such as fully-fed machines or Doubly-Fed Induction Machines (DFIM) were presented. These machines have the advantages of variable speed machines, but they are limited in their operation by some drawbacks (replacement of brushes and slip rings for the DFIM, price of power converters for fully-fed machines). At the end of CHAPTER I, two new doubly-fed technologies were introduced: the Brushless Doubly-Fed Reluctance Machine (BDFRM) and the Brushless Doubly-Fed Induction Machine (BDFM). These technologies have advantages and disadvantages over the current technologies of variable speed machines. On the plus side, they do not have slip rings, and their power converters do not need to be rated at the machine rated power. However, these advantages and the drawbacks need further investigations before planning to introduce the BDFM and BDFRM in future PSP projects. Finally, it was decided in CHAPTER I to study further the BDFM because its rotor seems easier to manufacture and appears to have better mechanical characteristics than the rotor of the BDFRM.

In CHAPTER II, methods to simulate, design and optimize rotating machines were presented. Three groups of methods were identified: the analytical methods, the semi-analytical methods, and the numerical methods. The advantages, disadvantages, and uses of these methods were discussed. The analytical methods are useful to understand the machines behavior and for 1st sizings. The semi-analytical methods can be more accurate and very useful for the determination of the specifications or for optimizations. Finally, numerical methods are generally the most intricate and accurate ones, they are often easier to implement than semi-analytical methods (since there are already existing software for numerical methods), however, they take much more computation time and cannot be used for optimizations on more than a few parameters. The example of the Induction Machine (IM) was taken to illustrate these methods. A fully-fed IM was optimized for the specifications of the TTP. The first design of the Induction Machine was obtained with an analytical method. Then it was optimized with a 1st order optimization algorithm paired with a semi-analytical method. This optimization proved to be a powerful tool and gave the opportunity to introduce the concepts of real and imaginary machines. Imaginary machines cannot be built: some of their parameters that should be discrete (like pole number, tooth number, etc.) are linearized. An optimization in the set of imaginary machines is much faster, for a 1st order optimization algorithm, than an optimization in the set of real machines. The set of real machines is included in the set of imaginary machines. Thus, imaginary machines are extremely useful to determine if a solution to a problem exists, to get an estimation of the best optimum, and even to help finding the optimum in the set of real machines. At

the end of CHAPTER II, the limits to apply the illustrated methods to the BDFM were shown. In particular, the fact that FE simulations took much longer for a BDFM than for other rotating machines. Because of the different frequencies of the PW and CW, normal magneto-harmonic applications cannot be used to solve steady-state scenarios of a BDFM. Magneto-transient applications also take longer for the BDFM simulations since a BDFM does not have as many symmetries as usual machines and has longer electrical periods. In the light of the powerful optimizations done for the IM, the need to create new semi-analytical methods for the BDFM was also highlighted.

0 was dedicated to the development and improvement of existing methods for faster simulations and optimizations of the BDFM. A careful harmonic analysis combined with a comparison of cross-coupling tests between FE simulations and results of equivalent circuit found in the literature led to a new equivalent circuit for the BDFM. A new method to determine the parameters of this equivalent circuit from electrical tests was also presented. Then two FE methods, much faster than the FE magneto-transient application were presented to simulate load tests of the BDFM in steady-state. The first method, the coupled-circuit FE based method was the fastest but did not consider saturation. With this method, after a few minutes to build the model, it was possible to simulate in seconds, load tests that would have taken days on magneto-transient simulations. This method was used to compare the new equivalent circuit model with FE results: thousands of load cases were simulated in minutes. The second FE method presented was an adaptation of the magneto-harmonic application for the BDFM. It considered saturation and was much faster than FE magneto-transient applications when applied on Flux2D. However, it was slower than the coupled-circuit based FE method. This second method was taking 5 minutes for linear cases and up to a few hours for heavily saturated cases (when the magneto-transient method on Flux2D was taking around 5 days independently of saturation). The difficulty for this magneto-harmonic method was to adapt the computation of the equivalent permeability of every mesh element in the case of two sources with different frequencies. This method was also adapted in another FE software internal to GE, but without saturation consideration. In this new software, it was taking only a few seconds to simulate load cases. Finally, at the end of CHAPTER III, the analytical determination of the parameters from the geometry was also considered. Some difficulties towards that goal were identified. Nevertheless, it seems to be an achievable goal which would lead to the elaboration of a derivable semi-analytical model. Such a model, paired with a 1st order optimization algorithm could be extremely powerful during the sizing of a BDFM (as shown for the IM in CHAPTER II).

Finally, in CHAPTER IV, a BDFM was designed and optimized for the same specifications as the IM of CHAPTER II. This design showed the limits of the current analytical design method for the BDFM. It also displayed the power of the new FE methods developed in CHAPTER III. CHAPTER IV also showed that for specifications with very slow mechanical speed (the mechanical speed for the TTP was from 40 rpm to 66 rpm), a BDFM needs a much bigger outer diameter than a fully-fed machine (in comparison to the IM in CHAPTER II for example). With a fully-fed machine, the feeding frequency can be diminished to limit the number of poles. For a BDFM, the PW frequency is imposed by the grid at 50 Hz. This leads to a high number of poles for the PW and CW. The high number of poles leads to high number of stator teeth. To accommodate all these teeth (if they are too thin, the power factors of the PW and CW drop) a minimal bore diameter is required. This minimal bore diameter was inconsistent

with the specifications of the TTP. The large bore diameter would not necessarily lead to a machine much heavier than usual. In fact, with the large bore diameter, the teeth would not need to be as deep as for usual machines. Similarly, the stator and rotor rims would not need to be as thick as usual because of the high number of poles. The BDFM technology seems to be more indicated for projects with speed between 200 to 600 rpm. In a project with a mechanical speed close to the TTP speed, a BDFM could be interesting if the project allows the turbine to be fitted inside the rotor, in the usual position of the shaft.

APPENDICES

APPENDIX A.	Stator of Radial Machines with Three-Phase Distributed Winding Design	163
A.1	Three phase winding	163
A.2	Stacking factor	163
A.3	Number of winding layers, number of conductors per slot and slot filling factor	164
A.4	Number of parallel paths.....	165
A.5	Number of slots per pole and per phase.....	167
A.6	Integer-Slot winding	167
A.7	Fractional-Slot winding.....	168
A.8	Coil Span and reduction of Coil Span	168
A.9	Winding Factor	169
APPENDIX B.	Synchronous Machines.....	171
B.1	Synchronous Machines with salient poles	171
B.2	Synchronous Machine with non-salient poles and wound rotor	172
B.3	Synchronous Machine with permanent magnets	172
APPENDIX C.	Induction Machines	175
C.1	General principles.....	175
C.2	Equivalent scheme	176
C.3	Torque characteristic of an asynchronous machine	177
C.4	Impact of the rotor resistance on the torque	177
C.5	Diminishing the rotor current during starting operation	178
C.6	Efficiency	179
APPENDIX D.	Speed Control with Induction Machines: Wound Rotors, Rheostat, and Doubly-Fed Induction Machines	181
D.1	Induction Machine with wound rotor	181
D.2	Starting with a rheostat connected to the rotor winding	181
D.3	Speed control with a rheostat	181
D.4	Speed control with the slip power recovery (SPR): sub-synchronous cascade and Doubly-Fed Induction Machine (DFIM)	181
D.5	DFIM with a rotary transformer to avoid the brushes and the slip rings.....	184
APPENDIX E.	Principles and Determination of a Reluctance Network	185

E.1	Reluctance calculation.....	185
E.2	Airgap representation in Reluctance Networks:	187
E.3	Modeling of Magnetomotive Force	187
APPENDIX F.	Semi-Analytical Model of an Asynchronous Machine Used for Sizing with a First Order Optimization Method in Cades	189
APPENDIX G.	Example of Improvements Using FEM and a Method Comparable to Design of Experiment for an Induction Machine Design.....	217
APPENDIX H.	From imaginary to real machines using the Semi-Analytical model presented in APPENDIX F and a 1 st order optimization.....	221
H.1	Methodology.....	221
H.1.1	Close attention needs to be paid to avoid mistaking local optimums for global optimums.....	221
H.1.2	From imaginary machines to real machines for optimizations and Pareto curves.....	222
H.2	Analyses of the results and interpretations	225
H.3	Results of the optimizations for one set of constraints	226
H.4	Evolution of a few interesting parameters during the optimization.....	232
APPENDIX I.	Harmonic analyses of a BDFM.....	235
APPENDIX J.	Determination of the Parameters of the Equivalent Circuit of an Induction Machine Using No-Load and Blocked Rotor Tests.	243
J.1	Determination of the magnetizing inductance and stator leakage reactance: no-load test.....	243
J.2	Determination of the sum of stator and rotor leakage reactance: blocked-rotor test	244
APPENDIX K.	Determination of the equivalent circuit parameters of the BDFM from electrical tests.....	247
K.1	No load tests.....	248
K.2	Blocked Rotor test:	250
APPENDIX L.	Computation of the power state of the BDFM through the electrical state of the equivalent scheme.	255
L.1	Resolution of the equivalent scheme electrical state	255
L.2	The power state of the BDFM	258
APPENDIX M.	An iterative process for the improvement of the BDFM design with FE magneto-harmonic simulations	261

APPENDIX A.

Stator of Radial Machines with Three-Phase Distributed Winding Design

A.1 Three phase winding

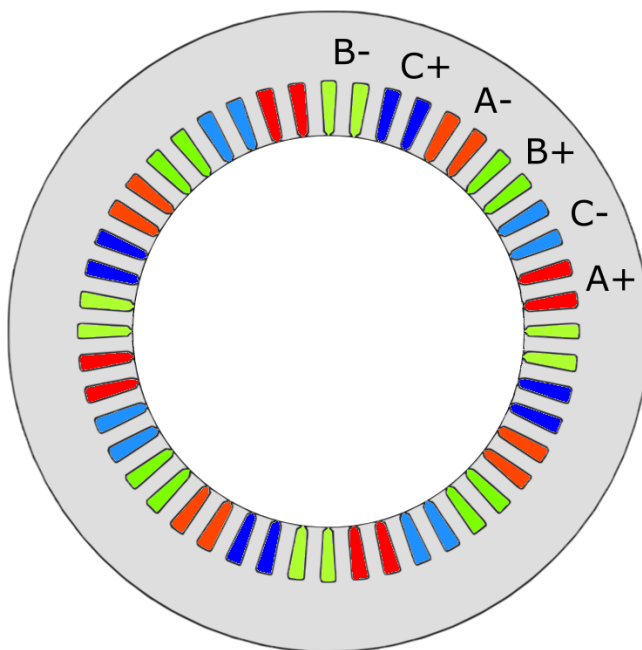


Figure A-1: Section view of the stator of an 8 poles 48 slots three-phase machine

The stators of radial machines with three-phase distributed windings are almost identical. These stators are generally made of FeSi electrical sheets to diminish the Eddy currents. The windings are placed into the slots of the stator. The succession of the A+, C-, B+, A-, C+, B- phases will create a rotating magnetic field when fed with balanced three-phase currents and voltages.

Figure A-1 shows the stator of an 8 poles 48 slots stator with a distributed integer slot winding with 2 slots per pole and per phase.

A.2 Stacking factor

Figure A-1 is a cross-section of a stator of a three-phase radial machine. Concerning the magnetic steel, we could also say that it is a top view of the magnetic steel sheet. The stator of the machine can consist of a pile of thousands of such magnetic steel sheets that are each a few *mm* thick. The sheets are stacked together to diminish the Eddy currents: they are in parallel of the magnetic flux. The small insulation between each sheet will prevent the apparition of induced currents. These thin insulations and the fact that the processing cannot be perfect will increase the volume of the core of the machine. The stacking factor is the ratio of the sum of the magnetic still thickness of each sheet divided by the core length of the machine. The stacking factor will vary between 0 and 1. If the insulations are small in comparison to the thickness of the sheets, the stacking factor will be close to unity.

A.3 Number of winding layers, number of conductors per slot and slot filling factor

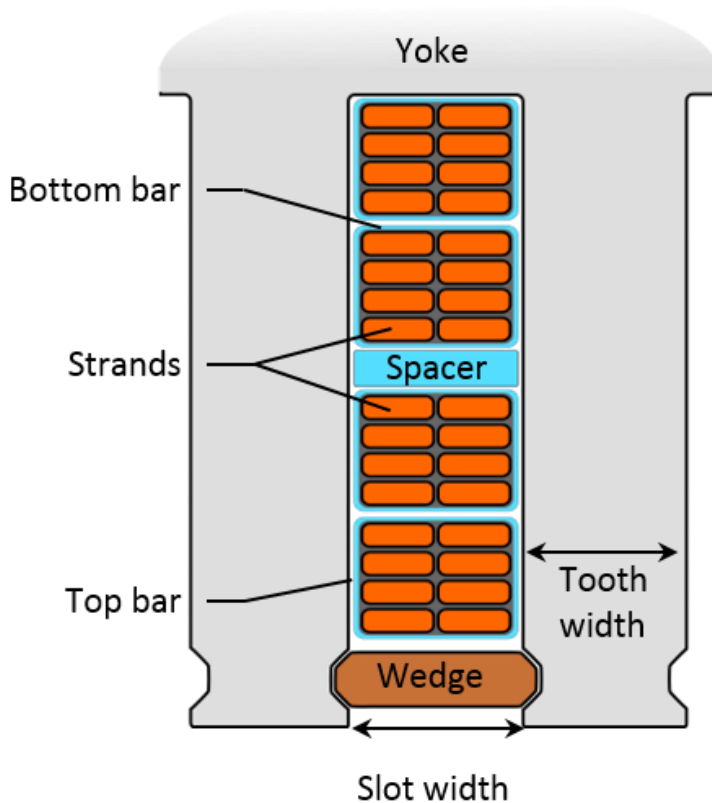


Figure A-2: Slot with 2 winding layers (2 bars), 4 conductors per slot (so 2 conductors per bar) and 32 strands per slot (which gives 8 strands per conductor)

The **number of winding layers per slot** impacts how many coils there is per slot. To shorten the coil span (refer to A.9, p 169), some slots will accommodate two different phases which require at least a double-layer winding.

When there are two layers per slot they are generally separated by an insulator (see the spacer in Figure A-2). We refer at the bar the closest to the airgap as the top bar. The bar the furthest to the airgap is the bottom bar.

For concentrated winding with only one layer per slot, there is a winding every other tooth. With two layers per slots, it is possible to have a winding around each tooth.

The **number of conductors per slot** is an integer. For slots with two winding layers, this number is greater than two. The bars can thus be subdivided into conductors. In Figure A-2 there are two conductors per bar so four conductors per slot. For a given bar, the conductors can either be in series or in parallel depending on the voltage output and current per phase.

The **number of strands per slot** must also be an integer. Conductors are divided into strands to get rid of the skin effect and to increase the cross-section of the conducting area. Figure A-2 shows eight strands per conductors or thirty-two strands per slot. For the strands to see exactly the same flux linkage, we can use Roebel bars. As explained in [91], in Roebel bars, the position of each strand is rotating in the conductor along the axis of the conductor.

The **slot-filling factor** is the proportion of the cross-section of copper (or conductor area) with the cross-section of the slot. If the slot filling factor was 0.6 that would mean that 60 % of the slot is filled by conductors. The rest would be insulation and void. The slot-filling factor depends on the thickness of the insulations around each conductor, around each bar, the number of conductors per slot and the thickness of the spacer between the bars. To increase the slot filling factor, one can use conductors

that have rectangular cross sections (as in Figure A-2). These kinds of conductors are used in the big machines we are dealing with for this Ph.D. Another option if possible is to use a better insulator, the insulation thickness can then be reduced. A normal filling factor in machines for hydro purposes would be in the range of 40 to 60%.

The larger is the **tooth width**, the more flux can be carried in the magnetic steel without saturating it. To increase the tooth width, the **slot width** must be decreased or the airgap diameter must increase. For a given filling factor and slot height, the slot width is the only way to adjust the conductor cross-section which directly impacts the Joule losses.

The **wedges** are inserted after the bars to maintain them in position. Their dimensions are imposed by mechanical considerations. From a magnetic point of view, they have disadvantages. They have an impact on the slot leakage, the torque ripple, and the maximum flux density in the teeth. The wedges are inserted in the teeth; thus, they will increase the iron saturation in the related part of the teeth. This can also have an impact on the flux density in the airgap and impact the torque ripple due to the teeth harmonics. An increase of the wedges' width will also increase the slot flux leakage.

There are ways to diminish the torque ripple, for example skewing the rotor or the stator. Skew refers to the fact that the slots of the rotor and of the stator are not facing each other in a parallel pattern. To do so, the slot of the stator or of the rotor are inclined.

The **spacer** is an electric insulation between the top bar and the bottom bar. Its main purpose is to insulate these two bars when they belong to different phases.

A.4 Number of parallel paths

To be able to adjust the currents and the voltages in the phases of the machine it is possible to implement parallel paths. The more parallel paths there are, the bigger the phases currents and the smaller the phases voltages. When designing a winding layout with parallel paths, it is important to make sure that all the parallel paths of one phase will always see the same flux in normal conditions (without faults). If this is not achieved the parallel paths will not have the same induced FEM and circulating currents will occur resulting in heating from Joule losses.

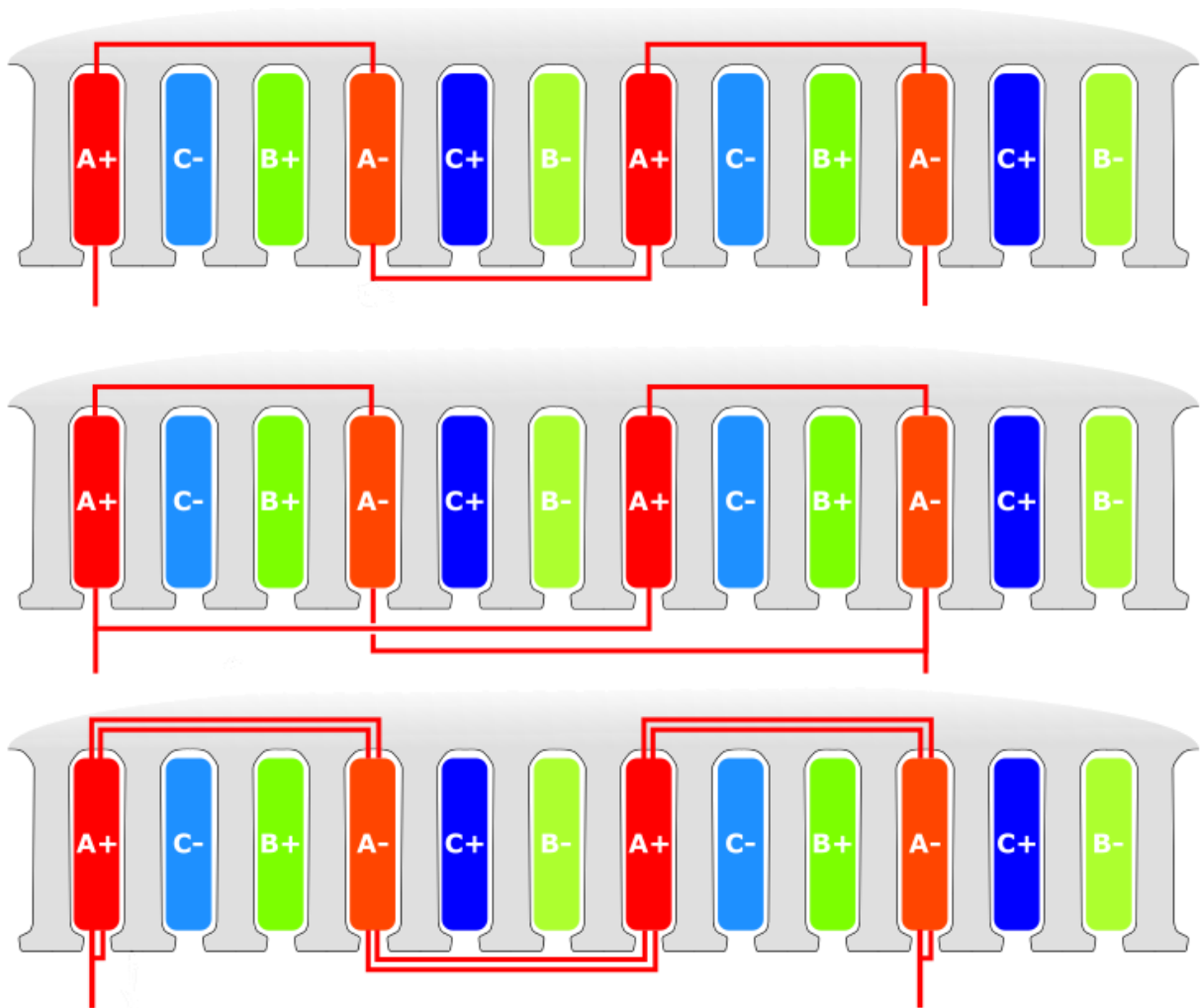


Figure A-3: Three different configurations of windings layout. The top one has one parallel path and the two others two parallel paths.

In Figure A-3, the parallel paths of the second and third cases should always see the same flux linkage. In the case of a fault (for example a short circuit) or in the case of an eccentricity, the parallel paths of the third case should still see the same flux passing through them. That would not be the case for the second winding layout, indeed in the case of an eccentricity circulating currents will occur between the parallel paths. In [92] a study on the impact of the circulating current between parallel paths of a DFIM was done for static and dynamic eccentricities. In this study, the parallel paths were distributed as in the second case shown in Figure A-3. There were 4 parallel paths for the stator. During an eccentricity, the circulating currents occurring between these parallel paths had the positive effect of decreasing the unbalanced magnetic pull.

From the side of the grid, the cases with two parallel paths will have twice the current, half the voltage and the same power output as the case with one parallel path.

With the third case shown in Figure A-3, it would be possible to have many more parallel paths if needed. During a fault, the parallel paths in this configuration will still see the same flux linkage so they will not have an impact.

A.5 Number of slots per pole and per phase

The number of slots per pole and per phase is often referred to as q . It gives an indication on the distribution of the windings. It can be computed by the equation:

$$q = \frac{N_s}{2 p \cdot m} \quad (155)$$

p is the number of pole pairs.

N_s is the number of slots of the stator.

m is the number of phases.

When q is an integer, the winding is an integer-slot winding (Refer to A.6, p 167).

When q is fractional and superior to 1, the winding is a fractional-slot winding (refer to A.7, p 168).

When q is fractional and inferior to 1, the winding is a concentrated winding.

When q is superior to 1, the bigger it is, the more sinusoidal the magnetic field in the airgap gets. In fact, since the coils are distributed over several slots for a given phase in each pole, there will be small steps in the EMF.

The fundamental winding factor will decrease with bigger q but the harmonics winding factor will decrease faster. Refer to A.9, p 169.

A.6 Integer-Slot winding

Integer slot winding can either be a single-layer winding like in Figure A-4, or a double-layer winding like in Figure A-5 and Figure A-6. In the case of single-layer, the winding will be a full pitch winding. With a double-layer winding, it will be possible to diminish the coil span see Figure A-5 and Figure A-6.

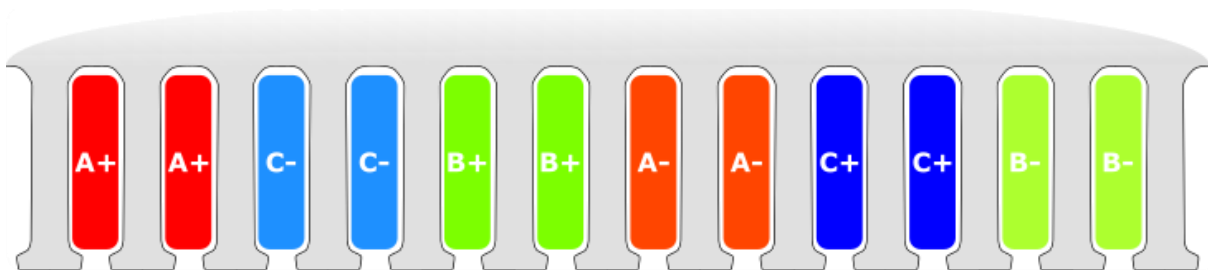


Figure A-4: Winding of a 2-pole 12-slot 3-phase machine with a single layer per slot. $q=2$ and the coil span is full pitch (6 slots)



Figure A-5: Winding of a 2-pole 12-slot 3-phase machine with two layers per slot (double-layer winding). The coil span is reduced by one slot pitch ($coil\ span = 5\ slots$ instead of $oil\ span = 6\ slots$).

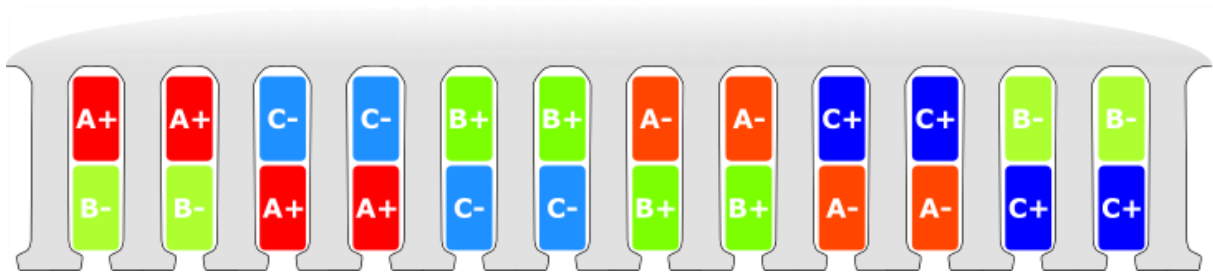


Figure A-6: Winding of a 2-pole 12-slot 3-phase machine with double-layer winding. The coil span is reduced by two slots pitch ($coil\ span = 4\ slots$ instead of $oil\ span = 6\ slots$).

A.7 Fractional-Slot winding

To have three balanced phases the fractional slot windings have two layers (double-layer winding).

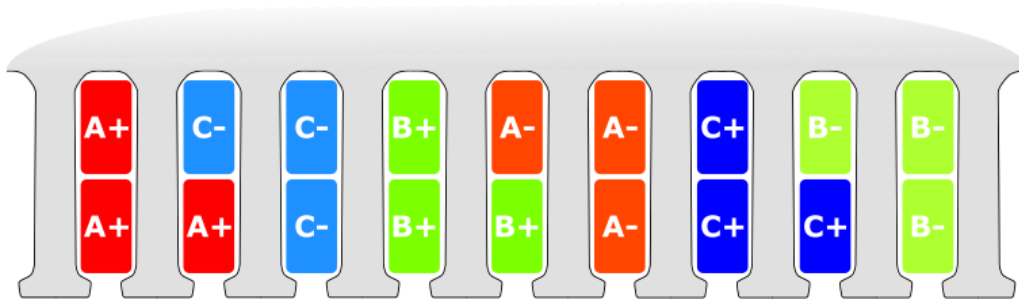


Figure A-7: Fractional slot winding of a 2-pole 9-slot 3-phase machine with a double-layer winding

A.8 Coil Span and reduction of Coil Span

The coil span of a winding is the distance between one conductor and its corresponding return conductor.

It can be expressed as a length, as an angle, or as a number of slot pitches.

The coil span will influence the length of the end winding. Thus, it will influence the Joule Losses and the leakage reactance. This is the reason why it is extremely interesting to reduce it. The downside of reducing the coil span is that it reduces the winding factor (refer to (157), p 169).

As long as there is a double-layer winding, it is possible to reduce the coil span with integer and fractional slot winding (refer to Figure A-5, Figure A-6 and Figure A-7).

A.9 Winding Factor

The **winding factor** is a ratio between the flux linked by the winding and the flux that would have been linked if it was a single layer full pitch integer slot winding without skewing with only one slot per pole and per phase and with the same number of turns.

The winding factor can be computed for each harmonic. If not specified, the winding factor is related to the fundamental.

The winding factor expression is as follow:

$$k_w = k_p \cdot k_d \cdot k_s \quad (156)$$

k_p is the pitch factor (or coil span factor).

k_d is the distribution factor.

k_s is the skew factor.

The pitch factor k_p considers the reduction of the coil span. When the coil span is not full pitch the length of the individual turns is reduced and they do not embrace the same flux.

$$k_p = \sin\left(\nu \cdot \frac{s_{coil}}{\tau_p} \cdot \frac{\pi}{2}\right) \quad (157)$$

s_{coil} is the coil span.

ν is the harmonic number.

τ_p the pole pitch.

The following formula of the skew factor is applicable when the rotor bars are inclined. If it was the stator bars, one would need to replace the number of rotor slots by the number of stator slots.

$$k_s = \frac{\sin\left(\nu \cdot P \cdot \frac{\pi}{2} \cdot \frac{N_{skew}}{N_{sr}}\right)}{\nu \cdot P \cdot \frac{\pi}{2} \cdot \frac{N_{skew}}{N_{sr}}} \quad (158)$$

ν is the harmonic number.

P the number of poles.

N_{skew} the number of slots of the skew.

N_{sr} the number of rotor slots.

The distribution factor k_d can be expressed as follows.

$$k_d = \frac{\sin\left(\frac{\nu \cdot \pi}{2 \cdot m}\right)}{q \cdot \sin\left(\frac{\nu \cdot \pi}{2 \cdot m \cdot q}\right)} \quad (159)$$

ν is the harmonic number.

m is the number of phases, most of the time $m = 3$ for hydro-generators.

q is the number of slots per pole and per phase.

APPENDIX B.

Synchronous Machines

B.1 Synchronous Machines with salient poles

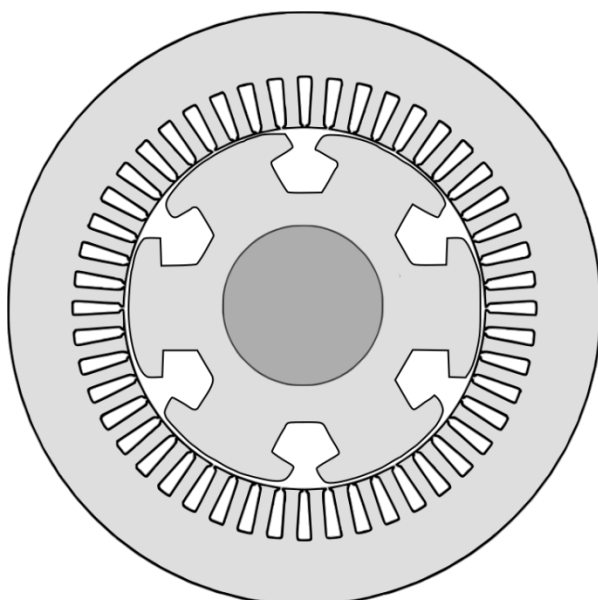


Figure B-1: Section view of a salient pole synchronous machine

The stator of the synchronous machine (as shown in Figure B-1) is a three-phase winding stator as described in APPENDIX A. Sine wave currents are passing through the three-phase winding and are creating a rotating magnetic field. This field has an even number of poles and is rotating at the frequency of the currents divided by the number of pole pairs.

The term synchronous machine refers to electrical machines which magnetic field is not rotating in the reference frame of the rotor. For a constant torque to be created the magnetic field of the stator and of the rotor must have the same number of poles and must be rotating at the same speed. Since the magnetic field does not rotate in the reference frame of the rotor, the rotor must rotate at the same speed as the magnetic field created by the stator. This rotational speed is referred to as the synchronism speed: n_s .

The synchronism speed n_s can be expressed as:

$$n_s = \frac{\omega_s}{p} \times \frac{60}{2\pi} \quad (160)$$

n_s is the rotating speed of the rotor at synchronism speed in revolution per minute.

ω_s is the feeding pulsation of the stator.

p is the number of pole pairs.

Rotor conductors are surrounding the salient poles. The excitation current flowing through the rotor conductors is direct. As stated above, the magnetic field created by the rotor is static in the reference frame of the rotor.

The stator frame is made of thin sheet of soft magnetic materials (generally FeSi). The electrical sheets will diminish the eddy currents and improve the efficiency of the machine.

The rotor does not need to be made of electrical sheets since the magnetic field is not rotating in the reference frame of the rotor and will not create eddy currents. However, some small eddy currents may arise from the harmonics due to the slotting effect or in starting mode.

Damping bars, playing the role of a squirrel cage can be added to the rotor. They may help in starting mode to reach the synchronism speed. They can also absorb some of the transient state and unbalanced condition of the machine.

Because of the synchronism speed, the speed at which this machine works is fixed by the feeding frequency and the number of poles. Thus, if variable speed is needed, the only way is to change the feeding frequency. To do so, a power inverter will generally be used. This power inverter will see all the power produced or consumed by the machine. It will have to be sized at least to the rated power of the machine. If lagging or leading reactive power is to be supplied to the grid the power inverter will have to be sized accordingly. For big machines, the price of such power inverter may be prohibitive.

B.2 Synchronous Machine with non-salient poles and wound rotor

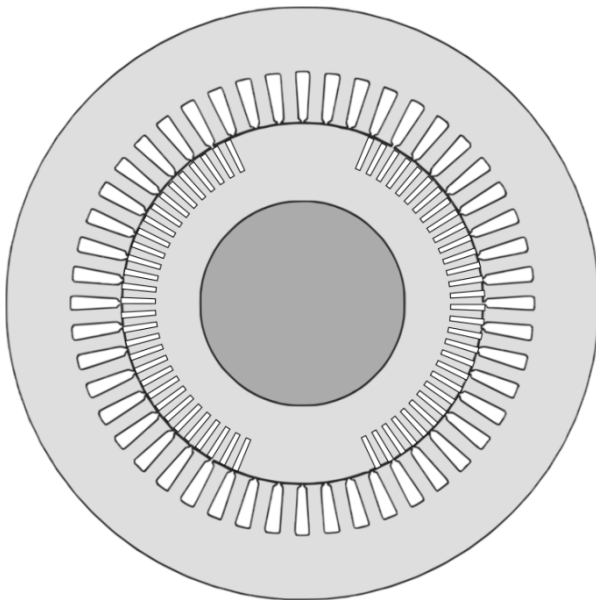


Figure B-2: Section view of a turbomachine: a synchronous machine with a wound rotor

Non-salient synchronous machines are sometimes called turbomachines. Their advantage over salient pole machines is that they can turn faster. Their rotor is mechanically stronger. This is a big advantage. Indeed, it is approximately true that when well-designed the torque produced by a machine is proportional to the radius of the airgap and the length of the machine. Thus, for a given size the faster a machine turns the more powerful it can be (the torque being constant). As long as the speed of the machine is not an issue it is always interesting to make it turn fast. To turn fast these kinds of machines have generally 2 to 4 poles. Fed with the same frequency: 50Hz or 60Hz they have a faster synchronism speed than salient pole machines.

These machines are generally used for large power plants, for example as generators in steam power plants or nuclear power plant. The drawback of this kind of design is that the magnetic field in the airgap is less sinusoidal when compared to salient pole machines.

The rotors of big turbo generators are sometimes cooled by hydrogen and not air since hydrogen is 7 to 10 times better at cooling than air. The stators are then cooled with water [93].

B.3 Synchronous Machine with permanent magnets

The field of the rotor can be created with permanent magnets instead of coils and electrical currents. With these topologies, the Joule Losses at the rotor can be avoided which is beneficial for the

global efficiency of the machine. The disadvantage being that the field created by the magnets cannot be controlled. The magnets magnetic field it is mostly constant and depends on the properties of the magnets and the design of the machine. In some mode operation, this is a disadvantage, for example in traction, when reaching high speed, rotor flux weakening to limit the stator voltage cannot be done as easily as with wound rotor synchronous machines. It is still possible to operate permanent magnet synchronous machine in flux weakening operation as it is described in [94] for example.

In renewable energy, Synchronous Permanent Magnets Machines are sometimes used for wind turbines, in power up to a few Megawatts. They are not used for bigger machines like the ones used for PSPs. One of the reasons being the high price and the instability of the price of permanent magnets.

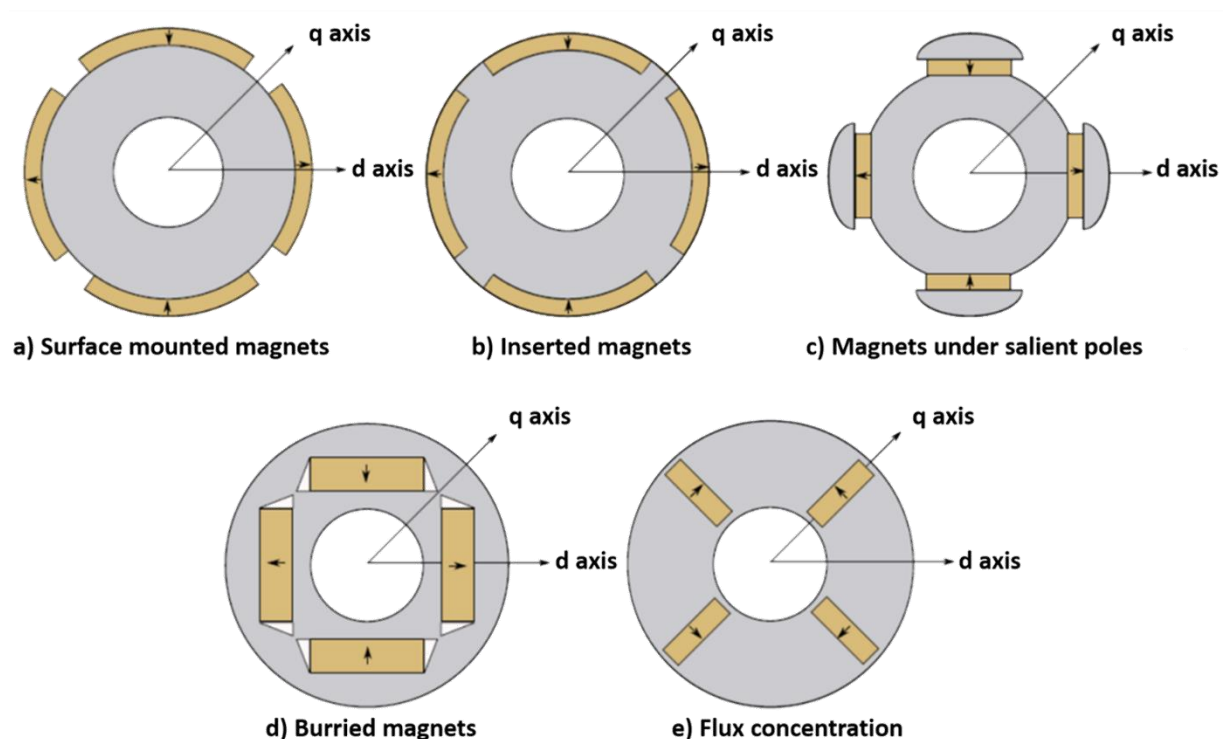


Figure B-3: Different kind of radial flux rotors with permanent magnets [95]

In Figure B-3 different topologies of rotors for radial flux permanent magnets machine are shown. Some characteristics of each topology are quickly summarized in the following list:

- Important airgap radial length because of the width of the magnets, the quadrature impedance L_q is close to the direct impedance L_d .
- Bigger flux leakage in comparison to a). Some of the flux of the permanent magnet is lost as it does not cross the airgap.
- Induction in the airgap closer to a sinusoid.
- Inversed saliency ($L_d < L_q$).
- Best torque density thanks to flux concentration.

APPENDIX C. Induction Machines

C.1 General principles

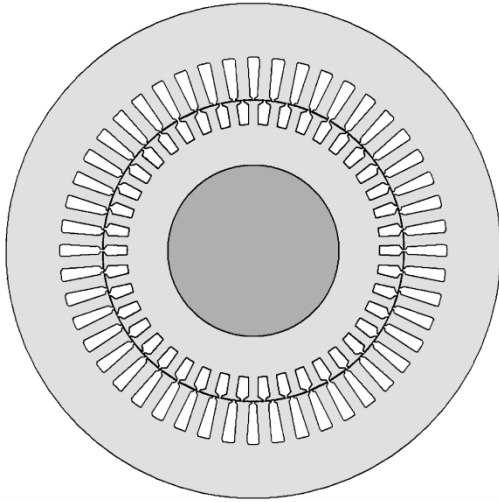


Figure C-1: Section view of a squirrel cage asynchronous machine

For asynchronous machines, the rotor is not anymore the magnetic inductor.

The stator is the same as in synchronous machines (as shown in Figure C-1): it is composed of a three-phase winding as described in APPENDIX A. Sine wave currents are passing through the three-phase winding and are creating a rotating magnetic field. This field has an even number of poles and is rotating at the frequency of the currents divided by the number of pole pairs.

The rotor conductors often take the shape of a squirrel cage for small machines. When the rotor is not rotating at the same speed as the stator magnetic field, an emf is induced between the rotor bars. This emf is at the origin of rotor currents: the induced currents. The interactions between the magnetic field of the stator and the magnetic field of the rotor create the torque.

The slip is defined as the difference between the magnetic field rotational speed or synchronism speed and the rotor rotational speed:

$$s = \frac{n_s - n_{rm}}{n_s} = \frac{\omega_s - p \omega_{rm}}{\omega_s} \quad (161)$$

$\omega_s = 2\pi f$ where f is the electrical frequency of the stator.

ω_{rm} is the mechanical pulsation of the rotor.

$\omega_r = g\omega_s$ is the electrical pulsation of the rotor.

Generally, the rotor bars are skewed (see Figure C-2). The skew allows diminishing the electromagnetic vibrations.

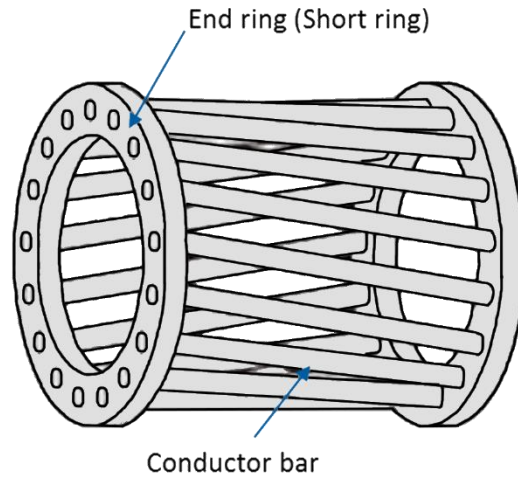


Figure C-2: Squirrel cage of an induction machine. The conductor bars are inclined or skewed

C.2 Equivalent scheme

The asynchronous machines can be assimilated to a transformer with a secondary winding closed on a $\frac{R_2}{s}$ resistance.

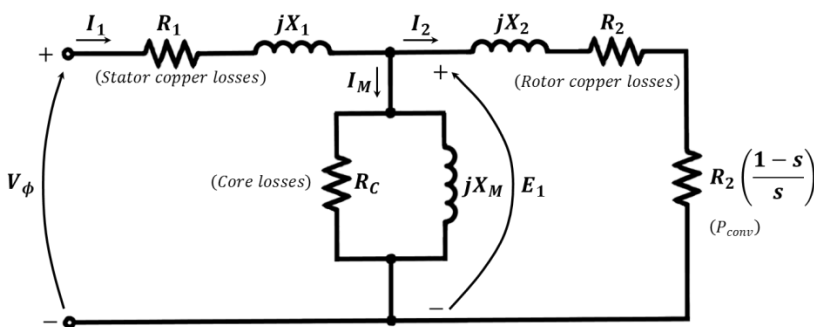


Figure C-3: Per phase equivalent circuit of an asynchronous machine with rotor losses resistance and rotor conversion resistance separated

I_1 is the primary current
 I_2 is the rotor currents
 R_1 Stator winding resistance
 X_1 Stator leakage reactance
 R_2 Rotor winding resistance
 X_2 Rotor leakage reactance
 I_M Magnetizing current
 X_m Magnetizing reactance
 R_c Iron loss resistance. It represents the core losses so it is slightly slip dependant.
 V_ϕ The phase voltage
 E_1 The airgap voltage

The total power absorbed by the asynchronous machine can be expressed as:

$$P_{tot} = 3 V_\phi I_1 \cos \varphi \quad (162)$$

The total stator Joule losses are expressed as

$$P_{Js} = 3R_1 I_1^2 \quad (163)$$

The total rotor Joule losses are expressed as

$$P_{Jr} = 3R_2 I_2^2 \quad (164)$$

The total power transmitted to the rotor can be expressed as:

$$P_e = P_{tot} - P_{Js} - P_{iron\ losses} = 3 \frac{R_2}{s} I_2^2 \quad (165)$$

Equations (164) and (165) show that $P_{jr} = sP_e$. This translates the fact that for an asynchronous machine, the rotor efficiency cannot be greater than $\eta_{rotor} = 1 - s$ (if the iron losses of the rotor are considered equal to zero then $\eta_{rotor} = 1 - s$). The overall efficiency of an asynchronous is always smaller than $1 - s$.

$$\eta_{asynchronous} < 1 - s \quad (166)$$

C.3 Torque characteristic of an asynchronous machine

The torque of an asynchronous machine is proportional to the slip close to the synchronism speed. When the slip increases, the torque increases up to a certain point where it reaches a maximum. The asynchronous motor is in a stable operation between the point of maximum torque and the point of minimum torque. In Figure C-4, the torque is positive, the machine is in motor mode. The generator mode would arise if the rotor rotates faster than the synchronism speed.

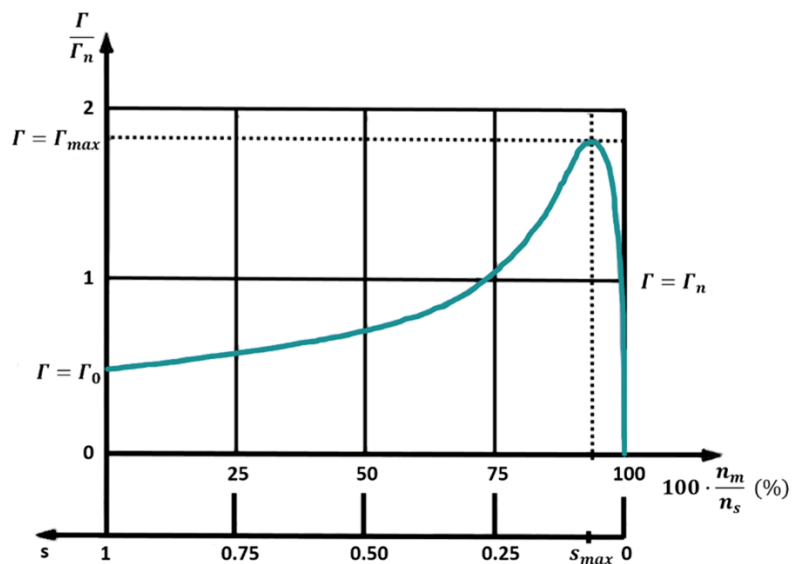


Figure C-4: Torque of an asynchronous machine in function of the slip [96]

The torque of an induction machine can be expressed as a function of the slip, the rotor current and the rotor resistance from the equation (165):

$$\Gamma = \frac{3 R_2}{\omega_s s} I_2^2 \quad (167)$$

C.4 Impact of the rotor resistance on the torque

Equation (167) shows that when the rotor resistance of an induction machine varies, all the other characteristics of the machine being fixed, the torque of the machine is impacted. The torque is also

dependent on the current of the rotor which is also linked to the rotor resistance. From the equivalent scheme consideration we can write:

$$I_2 = \frac{V_\phi}{\left(\frac{R_2}{s}\right) + sX_2} \quad (168)$$

In the end, the impact of the variation of the rotor resistance for a given induction machine can be plotted. Figure C-5 shows the impact of the resistance on the torque of an induction machine as a function of the slip.

As it can be seen, a lower resistance does not improve the maximal torque that can be obtained but this torque can be obtained for a lower slip thus at a better efficiency. In all the stable operation points a lower resistance allows a higher efficiency. For the starting operation, a lower resistance reduces the torque and also increases the current flowing through the rotor and thus the generated heat.

For big machines, it is common to use copper for the squirrel cage of the rotor instead of aluminum in order to reduce the rotor resistance [97].

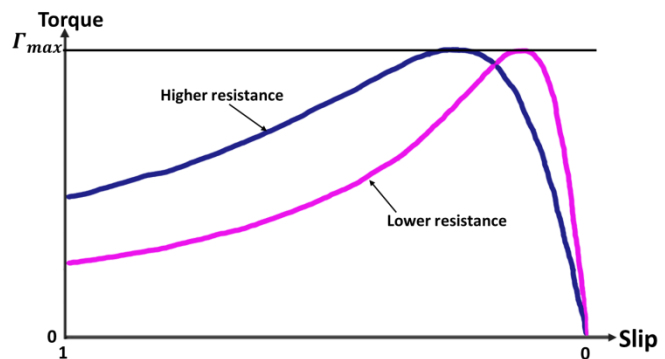


Figure C-5: Impact of rotor resistance on the torque of an asynchronous machine

C.5 Diminishing the rotor current during starting operation

The torque for a start is a lot lower than the torque that can be obtained during operation and the current passing through the rotor is 5 to 10 times higher than the rated current. The starting operation is creating a lot of heat. Thus many asynchronous machines cannot stop and start more than a few times an hour.

There exist several solutions to this problem [98]:

- First, the stator voltage could be diminished during the starting operation if possible. This can be made by an autotransformer for example. For a machine in operation with the stator with a Delta configuration, the connection of the stator can be changed to a Y configuration during the start.
- Second, to obtain greater starting torque and smaller starting current, some machine with double cage have been produced (see Figure C-6). The rotor squirrel cage is then composed of two cages, one deeper than the other. When the rotor current frequency is low, the current is subdivided into the two cages and so the rotor resistance is low. When the rotor current has a high frequency, during starting operation, the current is flowing mostly in the closest cage to the airgap due to eddy currents. The resistance of the rotor is increased during the starting operation, this resistance becomes relative to

the section of the cage the closest to the airgap and not to the section of the two cages. As seen in Figure C-5, a higher resistance during starting operation translates into a bigger torque and smaller rotor currents.

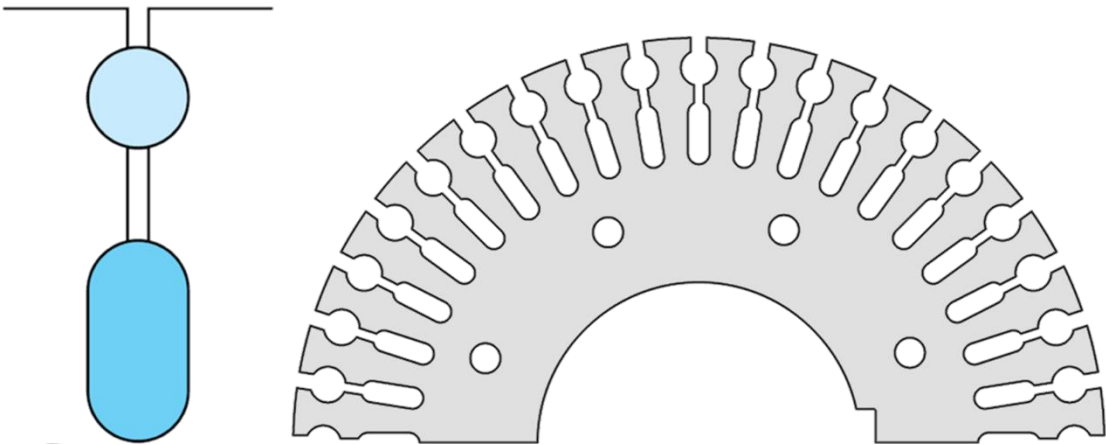


Figure C-6: Rotor shape and slot shape of a squirrel cage machine with a double cage to increase the torque starting current [98]

Note: In the case where the stator of the induction machine is connected to an inverter, the problems of the starting torque and starting current disappear. In fact, if the inverter is able to go to very low frequencies, it will be possible to start the machine and to increase slowly the rotating speed of the shaft by increasing slowly the feeding frequency of the stator. In such starting scenarios, the slip will be small and the Joules losses due to the slip will remain limited.

C.6 Efficiency

The efficiency of asynchronous machines can be high for machines with big power. For example, according to [96], for machines with power over 5 MW, the efficiency of is over 97% .

APPENDIX D. Speed Control with Induction Machines: Wound Rotors, Rheostat, and Doubly-Fed Induction Machines

D.1 Induction Machine with wound rotor

Induction machines with wound rotor allow designing induction machine with copper for the conductors of the rotor without the need of casting a copper squirrel cage which is a lot harder than for an aluminum one. In fact, the melting point of aluminum is 660.3°C whereas the melting point of copper is 1085°C .

Wounded induction machines are more expensive than induction machine with squirrel cages, but they can have many advantages.

D.2 Starting with a rheostat connected to the rotor winding

As seen in C.5, double cage rotors have been developed for the rotor to have a low resistance under normal operation and to increase the resistance while starting the machine. With a wound rotor, it is simple to connect the winding to a rheostat to increase the resistance while starting, and thus increase the torque and diminish the rotor current. Under normal operation, the rheostat is disconnected to benefit from the low resistivity of copper [98].

As explained in C.5, in the case of a machine fed by an inverter the problem of the starting torque and current vanishes.

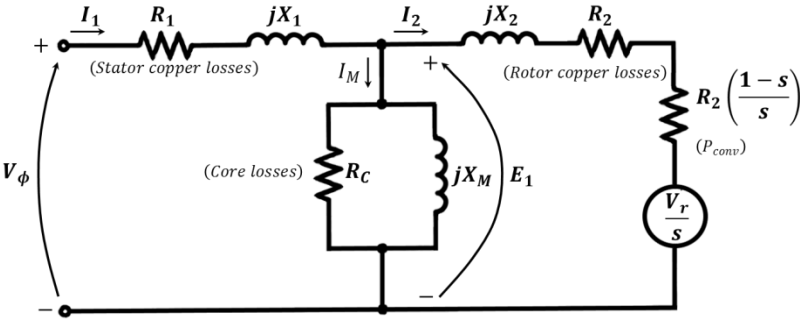
D.3 Speed control with a rheostat

When the speed of the machine is imposed by the torque, controlling the resistance of the rotor allows to control the torque and so to control the speed of the machine. The main problem is that this kind of control is used for machines with fixed feeding frequency. The variation of the speed corresponds to a variation of the slip. In the equation (166) we have seen that the efficiency of the rotor was equal to $\eta = 1 - s$. In consequence, the speed control by a rheostat is done at the expense of the efficiency [98]. This kind of control was used in the past for some applications, but not for big generators as the ones we are interested in for this thesis.

D.4 Speed control with the slip power recovery (SPR): sub-synchronous cascade and Doubly-Fed Induction Machine (DFIM)

It is possible to imitate the effect of the rheostats by connecting a bridge-rectifier to the rotor of the machine. The DC current out of the bridge can then pass through an inverter and then be re-injected on the network. From the side of the rotor, the bridge-rectifier is analogous to a resistance. In

fact, the current and the voltage are in phase in a rectifier, like for a resistance. The whole system acts as if the resistance of the rotor would have increased. But instead of dissipating the energy in the rheostat, the energy is recovered. From an equivalent circuit point of view, the addition of the inverter connected to the rotor is like adding a variable voltage source at the rotor in phase with the rotor currents. Thus, the equivalent circuit is the same as in Figure C-3 but with a voltage source to the rotor. This system is named sub-synchronous cascade.



- I_1 is the primary current.
- I_2 is the rotor currents.
- R_1 Stator winding resistance.
- X_1 Stator leakage reactance.
- R_2 Rotor winding resistance.
- X_2 Rotor leakage reactance.
- I_M Magnetizing current.
- X_m Magnetizing reactance.
- R_c Iron loss resistance. It represents the core losses so it is slightly dependant of the slip.
- $\frac{V_r'}{s}$ voltage source of the rotor in the stator frame.

Figure D-1: Per phase equivalent circuit of an asynchronous machine with a slip power recovery system referred to as sub-synchronous cascade or a DFIM (sub-synchronous cascade, voltage in phase with currents, DFIM: voltage can have a phase shift with currents). The rotor losses resistance and rotor conversion resistance are separated.

There exist many terms to refer to this technology: it is sometimes referred to as slip power recovery (SPR) or as Kramer Drives or Scherbius Drives.

An improvement on the sub-synchronous cascade is to replace the bridge-rectifier by another AC-DC inverter. Such a drive will have thus an AC-DC inverter connected to the rotor followed by a DC-AC converter connected to the grid. This technology is more expensive than sub-synchronous cascade technology since the AC-DC inverter is more expensive than the bridge-rectifier. The advantage over sub-synchronous cascade is that the power of the frequency inverter can flow in the two directions. By adding power to the rotor through the inverter it is possible to accelerate the asynchronous machine over the synchronism speed. Depending on the power flow in the inverter, it is said that the machine is operated in Synchronous, Hypo-synchronous or Hyper-synchronous mode. The converter processes an amount of power proportional to the slip multiplied by the rated power of the machine. Thanks to the two power inverters it is also possible to add reactive power to the rotor. The machine can be in over-excited mode or under-excited mode. In the per phase equivalent circuit, this technology is no longer represented by a simple resistance, but by a complex reactance; it is no longer represented by a voltage source in phase with the currents but by a voltage source that can have a phase shift with the currents. It is possible to have a control on the magnetization of the machine. The machines which benefit from this technology can also be referred to as Doubly-Fed Induction Machine (DFIM) or sometimes Wound Rotor Induction Generator (WRIG). These designations can induce in error since an Induction Machine Doubly-Fed by the Stator could also suit to the DFIM appellation, and a machine with a rheostat or with slip recovery for speed variation could also be referred to as a WRIG. Even if the DFIM appellation could be error inducing, this is the one that is currently the most used, including in GE to refer to this technology.

The sub-synchronous cascade technology does not make sense in the case with an inverter feeding the stator. In fact, the aim of the technology is to recover the slip power that would be lost if we were to control the speed with rheostats. It recovers the power that would be lost in Joule losses in the rheostats. It cannot recover the normal slip power loss: the Joule losses lost in the rotor windings. On the contrary, a power inverter such as in DFIM could still make some sense in the case of an asynchronous machine fed by the stator. In fact, the power inverter could be used just to control the reactive power of the rotor to diminish it. If the reactive power of the rotor is decreased, the current flowing through the rotor is smaller and the Joule losses at the rotor diminish.

The sub-synchronous cascade and the DFIM technologies can be interesting since the power converter connected to the rotor does not need to be sized to transfer the rated power. In comparison to an induction machine with an inverter feeding the stator, the inverter here can be smaller and deal with lower voltages. In this case, a transformer is added between the inverter and the network to match the voltages (see Figure D-2).

Generally, for big machines, the power inverters are sized so that the speed of the rotor can vary by up to $\pm 10\%$. For big machines, it is impossible to be able to make speed variation above $\pm 25\%$ of the rated speed. In fact, to increase the power flowing through the rotor, the rotor should be sized subsequently. Above a certain point, trying to get more speed variation would translate into designing bigger and bigger rotors which would then translate into machines more and more expensive. If the inverter is sized to be able to start the machine, then the operation above a $\pm 25\%$ slip would need to be transient. Designing a big DFIM with the possibility to work with full speed variation: $\pm 100\%$ of the rated speed would be like designing a big induction motor to work only in starting conditions: the rotor should be oversized creating a very expensive machine.

If the inverter is not big enough to be able to vary the speed from 0% to 100%, a rheostat can be added for the starting operation and other rare cases. The rheostats are cheap, and the addition of the whole: rheostat, inverter, and transformer is currently cheaper than would be the price of a big inverter to feed the stator.

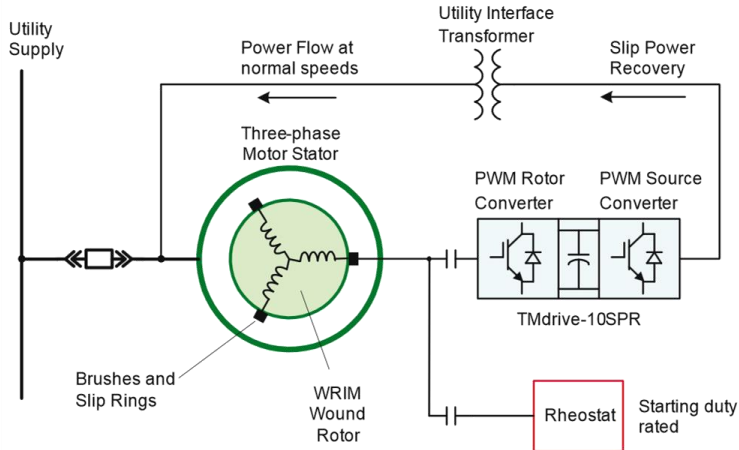


Figure D-2: Scheme of an induction machine with a wound rotor and slip power recovery SPR [99]

For a given project, a sub-synchronous cascade should have a better efficiency than an asynchronous machine with a converter connected to the stator. In fact, the power inverter does not have a 100% efficiency, so in the second case, more energy is lost through the inverter. For this same

project, a DFIM should theoretically be even more efficient than the sub-synchronous cascade. In fact, the control of the reactive power of the rotor allows diminishing a bit the rotor losses. In [99] a case study was made between a DFIM and an induction machine with an inverter connected to the stator. This case study was for an application of a mill of 5 MW running at 80% of the synchronous speed. In their case, the DFIM technology was a bit more efficient. The machine with a stator inverter had a global efficiency of $\eta_{stator\ inverter} = 92.2\%$. The DFIM had an efficiency of $\eta_{DFIM} = 93.2\%$. The machine with speed control by rheostats had an efficiency of $\eta_{rheostat\ controlled} = 75.5\%$, it would be interesting to have other comparisons to confirm this result for bigger machines and compare it over a range of operating points.

D.5 DFIM with a rotary transformer to avoid the brushes and the slip rings

A rotary transformer design has the particularity of having an airgap that allows movement between the primary (stator) and the secondary (rotor) winding. When the secondary winding is mounted on the same shaft as the rotor shaft of an induction machine, a rotary transformer allows to access to the power of the rotor. By connecting the stator of the rotary converter to an inverter the same principle as in normal SPR can be used but without the problem of the slip ring and the brushes. This kind of transformer is convenient for cases where sparks are excluded (for example in explosive environments). In fact, some little fault in the slip ring system can conduce to sparks from time to time in normal DFIM. Rotary transformers are also convenient for the cases where maintenance is extremely expensive (on spacecraft for example).

The main drawback of these machines is the price of the rotary transformer.

To transfer power, the rotor of the rotary transformer needs to have alternative currents, thus an induction machine connected to a rotary transformer at the rotor cannot work at the synchronism speed. Apart from the synchronism speed, all the other speed attainable by a normal SPR system are also attainable with a rotary converter.

In [100] example of a 350 kW prototype built by WEG with a rotary converter is presented.

APPENDIX E.

Principles and Determination of a Reluctance Network

As explained in Table II-1 in II.2.2.4, p 50, an analogy exists between the magnetic circuits and the electrical circuits. As an electrical circuit, a magnetic circuit can be represented by an equivalent circuit. This circuit will be referred to as a reluctance network. This appendix explains the model of a reluctance to represent tubes of flux. Examples of reluctance network are given and the importance of the airgap and MMF representations are stressed and illustrated. In all the examples given, the tool used was Reluctool paired with Cades as presented in II.2.2.5, p 50.

E.1 Reluctance calculation

Reluctances represent tubes in which the flux can pass. They can be defined for air or iron. A tube is defined so that the flux passing through each of its sections remains identical. In Figure E-1, the flux that enters section A is equal to the flux that exits section B. No flux passes through the perimeter of the sections of the tube.

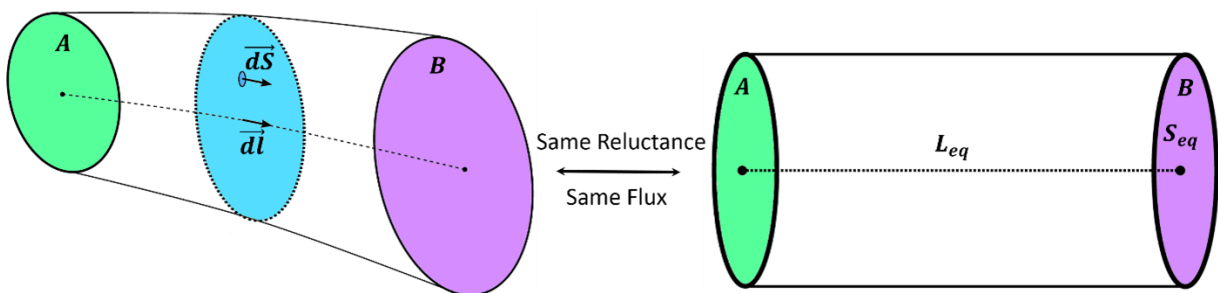


Figure E-1: A tube of flux and the equivalent flux tube associated with it

From Maxwell-Ampere, the MMF can be written:

$$\Theta = \oint_c \vec{H} \, d\vec{l} \quad (169)$$

Θ is the MMF: for the tube, it is the difference of Magnetic Potential between A and B,
 \vec{H} is the magnetic field.

The flux passing through an equipotential section of the tube can be expressed as:

$$\Phi = \iint \vec{B} \, d\vec{S} \quad (170)$$

Φ is the flux,

\vec{B} is the flux density.

With the definition of the flux tube above, the volume of the tube can be seen as a sequence of equipotential sections with flux lines perpendiculars to these sections. This simplifies equations (169) and (170) since it implies that \vec{H} and \vec{dl} are collinear and that \vec{B} and \vec{dS} are collinear too.

For further simplifications, the tube can be related to an equivalent tube with the same flux, a constant flux density B_{eq} , the same reluctance and with an equivalent length L_{eq} and an equivalent section S_{eq} [101].

Equation (170) becomes:

$$\Phi_{\text{tube}} = B_{eq} S_{eq} \quad (171)$$

Φ_{tube} is the flux passing through a section of the considered tube.

Considering the relation $B = \mu H$, equation (169) becomes:

$$\Theta_{\text{tube}} = \Theta_B - \Theta_A = \int_A^B \frac{B_{eq}}{\mu} dl = \frac{\Phi_{\text{tube}}}{\mu S_{eq}} L_{eq} \quad (172)$$

Θ_{tube} is the MMF of the tube, it is the difference of Magnetic Potential between section A and section B.

μ is the permeability of the material in the tube.

The reluctance associated with the tube represents the ratio of the MMF and the magnetic flux. As seen in Table II-1 this is analogous to the definition of the resistance in an electrical circuit.

$$R_{\text{tube}} = \frac{1}{P_{\text{tube}}} = \frac{\Theta_{\text{tube}}}{\Phi_{\text{tube}}} = \frac{L_{eq}}{\mu S_{eq}} \quad (173)$$

R_{tube} is the reluctance of the tube considered.

P_{tube} is the tube's permeance.

In the case of saturation, μ will vary as a function of the flux passing through the tube.

Reorganizing equation (173), we can express the reluctance of the tube as a function of the flux and of the characteristic $H(B)$ of the material which is a characteristic that can be obtained experimentally with an Epstein Frame.

$$R_{\text{tube}} = \frac{L_{eq} H(B)}{\Phi_{\text{tube}}} \quad (174)$$

E.2 Airgap representation in Reluctance Networks:

When a tube is defined in the air, the reluctance of the tube can be computed using equation (173) and μ_0 the vacuum permeability. In many machines, the airgap has a complex shape. Moreover, the shape changes with the rotation of the rotor. A good representation of the airgap is important since most of the magnetic energy is stored in it and is then used to compute the torque.

The MMF (see E.3) and the airgap representation choice will determine whether the reluctance network can be used for multi-static simulations or only for one static calculation. For the airgap, the representation can be done for one rotor position, for different rotor positions or can even be parametrized depending on the rotor position. The choice of the representation will depend on the topology of the airgap, the technology of the machine studied and the intricacy and accuracy desired.

To avoid considering the tooth effect, the author of [56] use Carter's coefficient to come back to a smooth airgap.

To do an airgap representation depending on the rotor position and considering the tooth effect, two different solutions are commonly used. In the first one, the values of airgap reluctances are expressed as functions of the rotor position and of geometric parameters. The second solution is to define the airgap reluctance values through an FFT computation of the airgap radial length, both methods are presented in [40].

The reluctance network designed in [40] for the BDFRM uses the second solution. The BDFRM has both stator and rotor teeth. In [40] each rotor tooth is connected through the airgap to three stator teeth (Figure E-2). The values of the reluctances are determined as functions of the rotor position for a maximum rotation of one stator tooth pitch. For further rotations, the rotor is set back in the initial position and the MMF sources of the stator are rotated by one stator tooth. This way, it is possible to do multi-static simulations for any rotor angular position.

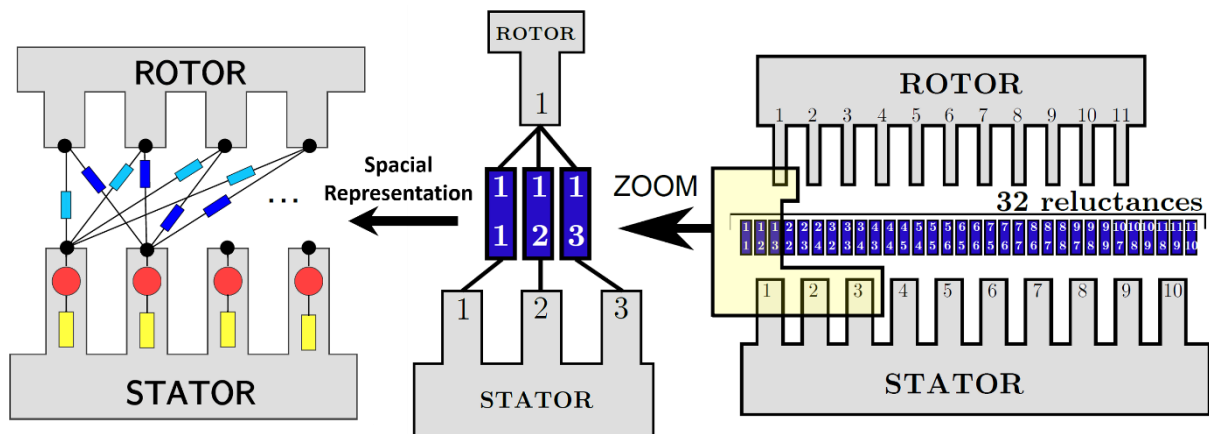


Figure E-2: Reluctance network in the airgap able to consider the rotor rotation of one stator tooth pitch from [40]

E.3 Modeling of Magnetomotive Force

The choice for the representation of the MMF (Magnetomotive Force) will determine whether the reluctance model will be a static simulation or a multi-static simulation. In some cases, to get the tooth effect, the torque ripple, or for some technologies of machines, it is important to be able to do multi-

static simulations. In this case scenario, the MMF of the network needs to be parametrized to be rotating.

As seen in Figure II-4, there is one MMF source for each tooth. From [40], there are three different possibilities to compute the MMF source for each tooth:

- First, considering only the fundamental component, this method makes sense for a static simulation and for some simplified multi-static simulations. MMF sources will be defined for each tooth depending on the tooth angular position and of the electrical angle. The MMF sources will model the distributed current sources of the three-phase winding of the stator. This can be seen in Figure E-3 from [83].

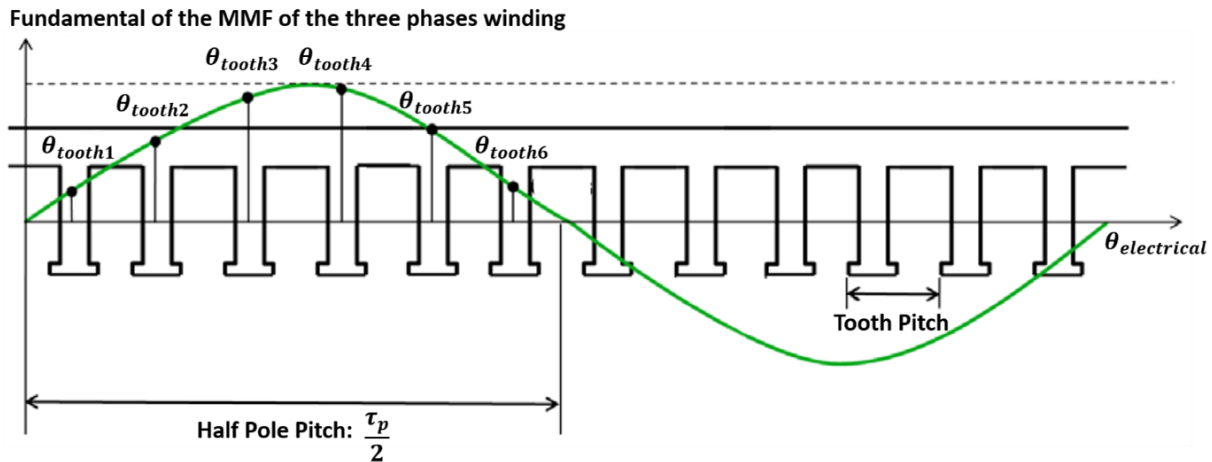


Figure E-3: Definition of the MMF of each rotor tooth from the fundamental harmonic of the MMF created by the stator [83]

- A second and more advanced method is to include some harmonics of the FFT of the MMF of the three-phase winding. This would look like Figure E-3 apart from the fact that the MMF is not a sinusoid anymore.
- Finally, there is the third method that is discrete, the Ampere-turns of each slot are considered with Ampere's Law resulting in a rectangular waveform (Figure E-4). The method will consider most of the harmonics of the MMF. This method is used both in [40] and in [83].

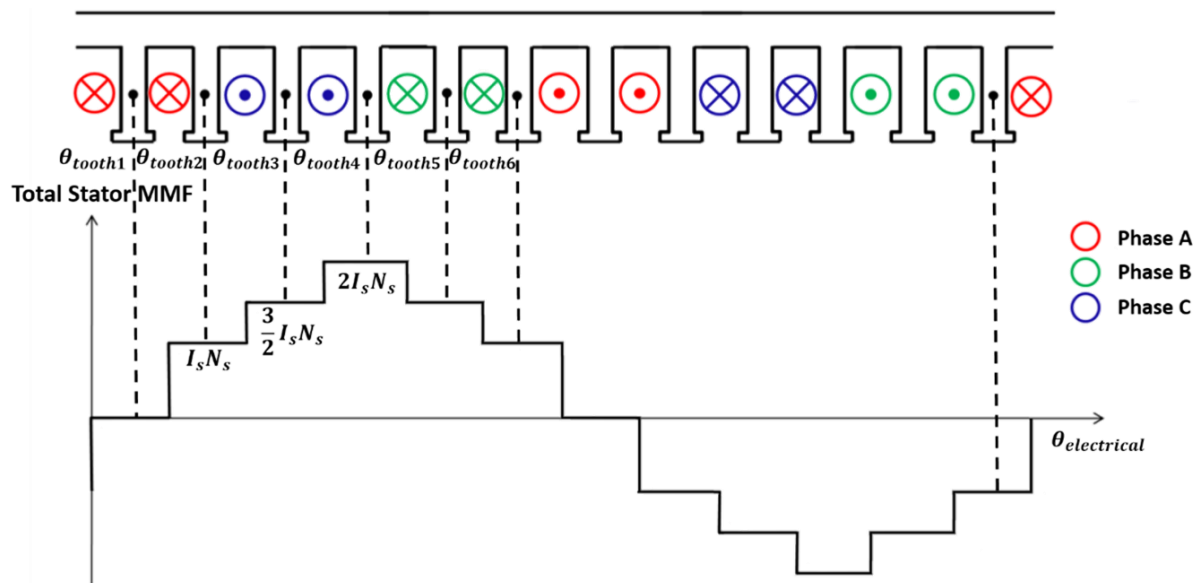


Figure E-4: Definition of the MMF of each rotor tooth with a discrete method and most of the spatial harmonics considered

APPENDIX F.

Semi-Analytical Model of an Asynchronous Machine Used for Sizing with a First Order Optimization Method in Cades

This appendix contains the equations used to optimize an induction machine on Cades. The model was developed in Mathcad. It was then imported into this document. For that reason, the structure, the presentation, and the references of this appendix does not fit with the rest of the document. In Cades, the use of Greek alphabet is not supported. For that reason, the equations developed in this appendix do not use Greek alphabet notations. Therefore, this appendix does not use the same nomenclature as in the rest of this work. All the notations in this appendix are defined along the development of the equations.

The original Mathcad model was developed by Frédéric Wurtz, in French for [55].

In comparison to [55], the model of APPENDIX F was adapted for powerful IMs:

- The slots are now rectangular (and not trapezoidal).
- The stator winding is made of bars, with two bars per slot, a number of conductors per bars and a number of strands per conductors (explanation in A.3, p 164).
- This allows for the possibility of fractional winding and reduction of coil span (see A.7 and A.8) that are now considered by the model.
- The rotor slots are also rectangular to allow for a squirrel cage made of copper bars.
- The leakage inductances have been updated (thanks to [73] and [12]) for the new stator and rotor slots geometries and to consider the case of reduced coil span.
- Saturation is now considered with B(H) curves obtained by interpolation of measured B(H) curves on samples. The B(H) measurements were done results with an Epstein Frame and samples of iron sheets used by GE.
- The iron losses are computed according to Bertotti's model [74]: as a sum of hysteresis losses, Eddy current losses, and excess losses.
- The flux in the airgap is now determined in an iterative loop. On the first iteration, the airgap flux density is computed from the feeding voltage of the stator. On the following iterations, the voltage drop due to the stator current is taken into account. Since the stator current depends on the machine saturation, this is done in an iterative loop until convergence. The iterative loops iterate the calculation on the "airgap voltage" until convergence.
- Objective functions were defined to compute the efficiency and the price of the IM.

Original document from Wurtz Frédéric
Modification and translation to English: Moisson Franckhauser Nicolas

Originally from: Annexe B de la thèse: "Une nouvelle approche pour la conception sous contraintes de machines électriques", F. WURTZ, thèse de l'institut national polytechnique de Grenoble, le 28 mai 1996

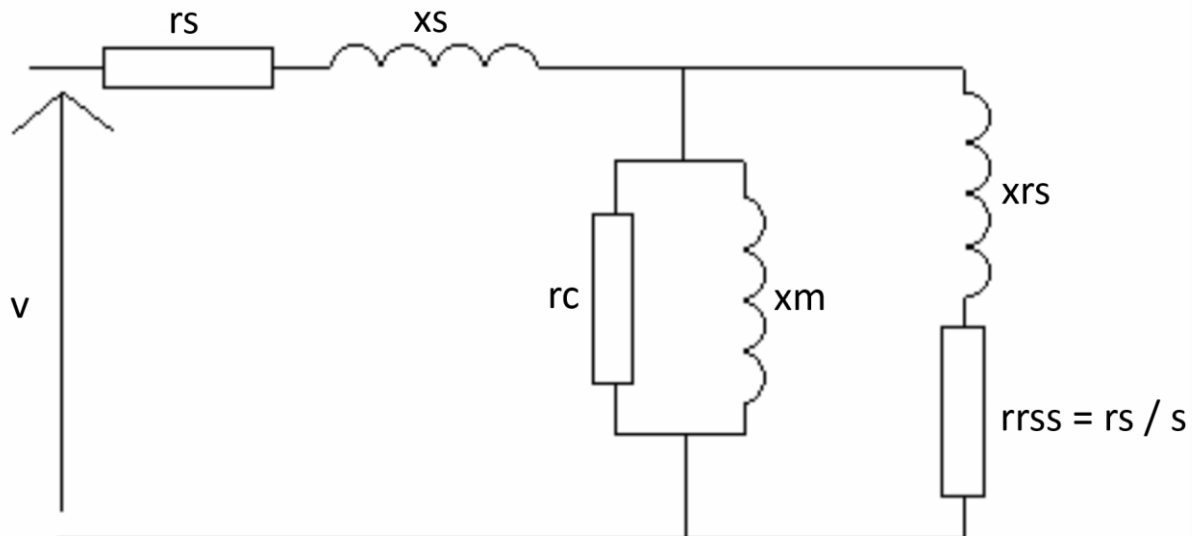
Model of an Asynchronous Machine used for sizing in CADES

F.1. Principle of the structural model:

In this model the parameters of the equivalent scheme are used to compute the performance of the induction machine. These parameters are computed from the construction parameters of the machine.

The equivalent scheme of one phase of the asynchronous machine is presented in the following figure:

Figure F.1: Equivalent scheme of the induction machine.



rs: Resistance of the stator winding
xs: Leakage reactance of the stator winding
rc: Resistance representing the core losses (iron losses)
xm: Magnetizing inductance of the machine
xrs: Leakage reactance of the rotor expressed to the stator
rrss: Reactance of the rotor expressed to the stator divided by the slip
s: Slip
v: Voltage per phase

F.2. Characteristics of the structural model:

- Nonlinear model that consider the no load saturations.
- The iron losses are taken into account thanks to LS method.
- The model takes into account the skewing of the rotor bars.
- The stator winding consists of bars. There can be many bars in the top slot and in the bottom slot.
- The rotor is a squirrel cage made of copper bars.

F.3. List of input parameters, meaning, and initial value.

Variables used for Mathcad software:

(ma is the mathematical limit to refer to 0:	$ma := 1 \cdot 10^{-6}$)
(mm transforms mm to m:	$mm := 10^{-3}$)
(mm ² transform mm ² to m ² :	$mm^2 := mm \cdot mm$)

Initial numerical value for the input in Cades:

This example was developed with the characteristic of the Typical Tidal Poject in Mind

m is the number of phases	$m := 3$ (Fixed)
pa is the number of poles	$pa := 16$
L is the length of the machine	$L := 1795 \cdot mm$
ns is the number of stator slots	$ns := 336$
nr is the number of rotor slots	$nr := 288$
f is the feeding frequency	$f := 10Hz$
wGap is the width of the air gap (in m)	$wGap := 10 \cdot mm$
v is the rms feeding voltage for each phase (each parallel path)	$v := 660V$
s is the slip of the machine under nominal load:	$s := -0.01$
ncps is the number of conductors per slot:	$ncps := 4$
nspc is the number of strands per conductor	$nspc := 22$
npp is the number of stator parallel path	$npp := 1$
The rank of the harmonic considered:	$\gamma := 1$

recs stands for the reduction of coil span
 (recs is expressed as the number of slot reduction for the coil span in comparison to the full pitch
 In the case of a one layer winding recs=0.)

$$\text{recs} := 4$$

tsta is the temperature of the stator winding

$$\text{tsta} := 100\text{ }^{\circ}\text{C}$$

trot is the temperature of the rotor winding

$$\text{trot} := 105\text{ }^{\circ}\text{C}$$

Specific stator input:

dout is the outer diameter of the stator (in m), see Figure F.3

$$\text{dOut} := 4500\text{mm}$$

hStatorYoke is the height of the stator yoke

$$\text{hStatorYoke} := 195\text{mm}$$

mainInsulS is the width of the main insulation of the top or the bottom layer of a stator slot plus the slot corona protection plus the round packing

$$\text{mainInsulS} := 2.87\text{mm}$$

strandInsulS is the width of the insulation around a strand

$$\text{strandInsulS} := 0.2\text{mm}$$

rStrandCorner is the radius of the curve of every corner of the strands

$$\text{rStrandCorner} := 0.65\text{mm}$$

spacer is the width of the spacer between the bottom slot and the top slot

$$\text{spacer} := 5.3\text{mm}$$

wVentS is the width of the ventilation duct for the stator

$$\text{wVentS} := 7\text{mm}$$

wStackIronS is the width of the stack of Iron between two ventilation ducts for the stator:

$$\text{wStackIronS} := 60\text{mm}$$

nVentS is the number of stator ventilation ducts:

$$\text{nVentS} := \frac{L}{\text{wVentS} + \text{wStackIronS}} - 1$$

LirS is the iron length for the stator

$$\text{LirS} := L - \text{nVentS} \cdot \text{wVentS}$$

Input for the stator slots and strands:

The stator slots model can be seen in figure F.2

$$\text{bas} := 15\text{mm} \quad \text{hfs} := 167.92\text{mm}$$

$$\text{os} := 15\text{mm} \quad \text{hes} := 12.08\text{mm}$$

os can be greater than bas to emulate a wedge

The total height of the stator slot is:

$$\text{hts} := \text{hfs} + \text{hes}$$

The inner diameter of the stator is (the stator Bore diameter):

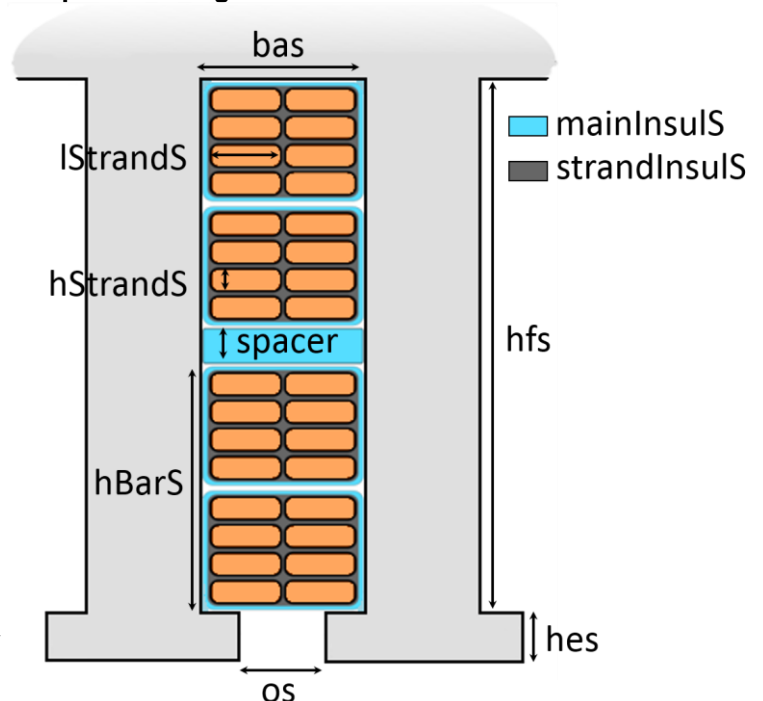
$$\text{dIn} := \text{dOut} - 2 \cdot \text{hStatorYoke} - 2 \cdot \text{hts}$$

The section area of a stator slot in mm² is:

$$\text{aSlotS} := \text{hfs} \cdot \text{bas} + \text{os} \cdot \text{hes}$$

When strands are equally distributed between the bottom and the top slot. They are put aside two by two in the width of the slot and they are as many layer of strand as they are number of strand divided by 4.

Figure F.2: Parameters of a stator slot. Simplification in comparison to figure:



The length of a strand is:

$$l_{\text{StrandS}} := \frac{\text{bas} - 2 \cdot \text{mainInsulS} - 4 \cdot \text{strandInsulS}}{2}$$

The height of a strand is:

$$h_{\text{StrandS}} := \frac{(\text{hfs} - 4 \cdot \text{mainInsulS} - \text{spacer} - \text{nspc} \cdot \text{ncps} \cdot \text{strandInsulS}) \cdot 2}{\text{nspc} \cdot \text{ncps}}$$

The height of the bar composed of all the strands of one layer is:

$$h_{\text{BarS}} := \frac{\text{nspc} \cdot (h_{\text{StrandS}} + 2 \cdot \text{strandInsulS})}{2}$$

Specific rotor input:

$h_{\text{RotorYoke}}$ is the height of the rotor yoke

$$h_{\text{RotorYoke}} := 320\text{mm}$$

mainInsulR is the width of the rotor bar insulation

$$\text{mainInsulR} := 2.4\text{mm}$$

w_{VentR} is the width of the ventilation duct for the rotor

$$w_{\text{VentR}} := 8\text{mm}$$

$w_{\text{StackIronR}}$ is the width of the stack of Iron between two ventilation ducts for the rotor.

$$w_{\text{StackIronR}} := 60\text{mm}$$

n_{VentR} is the number of rotor ventilation ducts:

$$n_{\text{VentR}} := \frac{L}{w_{\text{VentR}} + w_{\text{StackIronR}}} - 1$$

l_{irR} is the iron length for the rotor

$$l_{\text{irR}} := L - n_{\text{VentR}} \cdot w_{\text{VentR}}$$

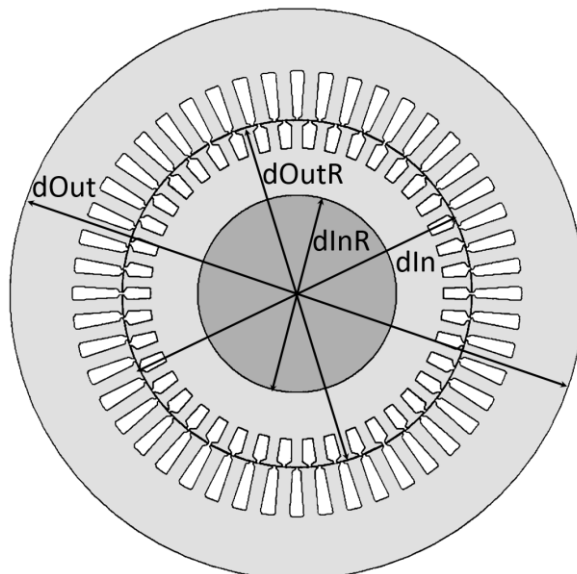
l_i is the ideal length of the machine:

This is the equivalent length for magnetic computation the machine would have if the ventilation ducts of the stator and the rotor were not there.

$$l_i := L - \left(\frac{n_{\text{VentS}} \cdot w_{\text{VentS}}}{1 + 5 \cdot \frac{w_{\text{Gap}}}{w_{\text{VentS}}}} + \frac{n_{\text{VentR}} \cdot w_{\text{VentR}}}{1 + 5 \cdot \frac{w_{\text{Gap}}}{w_{\text{VentR}}}} \right)$$

The different diameter that have been defined are presented in the figure F.3

Figure F.3: Definition of the diameters that will be used.



The model of rotor slot can be seen in figure F.4: **Figure F.4: Parameters of a rotor slot.**

$$\underline{\text{bar}} := 16.08 \text{ mm}$$

$$\text{hfr} := 110 \text{ mm}$$

$$\text{orr} := 16.08 \text{ mm}$$

$$\text{her} := 0 \text{ mm}$$

The total height of the stator slot is:

$$\text{htr} := \text{hfr} + \text{her}$$

The outer diameter of the rotor is:

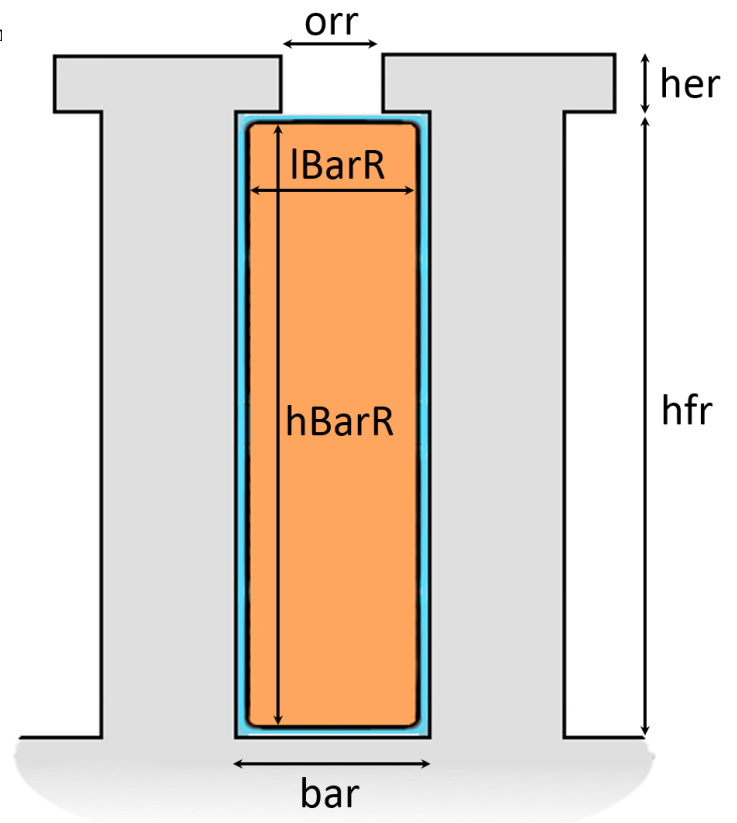
$$\text{dOutR} := \text{dIn} - 2 \cdot \text{wGap}$$

The inner diameter of the rotor is:

$$\text{dInR} := \text{dOutR} - 2 \cdot \text{htr} - 2 \cdot \text{hRotorYoke}$$

The section area of a rotor slot in mm² is:

$$\text{aSlotR} := \text{hfr} \cdot \text{bar} + \text{orr} \cdot \text{her}$$



Data for the rotor conductors:

hBarR is the height of the rotor bar:

$$\text{hBarR} := \text{hfr} - 2 \cdot \text{mainInsulR}$$

lBarR is the length of the rotor bar:

$$\text{lBarR} := \text{bar} - 2 \cdot \text{mainInsulR}$$

scrs is the section area of the conductor in the rotor slot:

$$\text{scrs} := \text{hBarR} \cdot \text{lBarR}$$

Data of the rotor cage:

nSkew is the inclination of the rotor bars (expressed in slot step)

$$nSkew := 1$$

rhoR is the resistivity of the rotor cage. Here the resistivity of copper.

$$\rho R := 0.017 \cdot 10^{-6} \text{ Ohm.m}$$

alphrot is the coefficient of resistivity in function of the temperature.

$$\alpha_{hrot} := 0.00380 \text{ K}^{-1}$$

han is the height of the short circuit ring.

$$han := 130 \text{ mm}$$

ban is the width of the short circuit ring.

$$ban := 40 \text{ mm}$$

ascr is the section area of the short circuit ring (in m²)

$$ascr := han \cdot ban$$

dam is the average diameter of the rotor cage

$$dam := d_{OutR} - h_{tr}$$

diffGap is the difference of the normal air gap width and the air gap width at the level of the short circuit ring. diffGap is imposed > 0

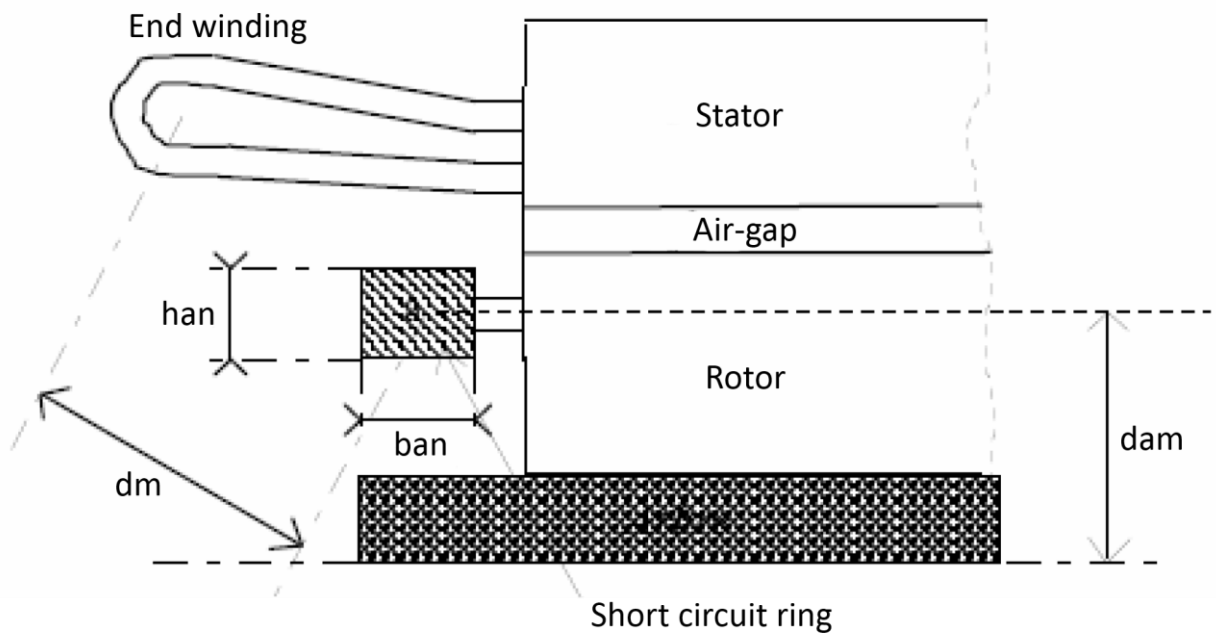
$$diffGap := h_{tr} - han$$

dm is the distance between the middle of the end winding of the stator and the short circuit ring (dm is computed in the worst-case scenario where they are in front of each other):

$$dm := w_{Gap} + \frac{(h_{ts} + h_{tr})}{2}$$

han, ban, a, dam and dm are represented in the figure F.5.

Figure F.5: Visualization of the parameters han, ban, dam, and dm (from [Wurtz])



F.4. Determination of the parameters of the equivalent scheme:

Computation of geometric parameters:

p is the number of pair of pole

$$p := \frac{pa}{2}$$

q is the number of slot per pole and per phase

$$q := \frac{ns}{(m \cdot pa)}$$

ntsppS is the number of turn in series per parallel path for the Stator

$$ntsppS := \frac{ns \cdot ncps}{m \cdot np \cdot 2}$$

nsp is the number of slot per pole:

$$nsp := \frac{ns}{pa}$$

span is the coil span expressed in number of slots:

$$span := nsp - recs$$

The pulsation is:

$$\omega := 2 \cdot \pi \cdot f$$

wToothS is the width of a stator tooth:

$$wToothS := \pi \cdot \frac{dIn}{ns} - os$$

Computation of the filling factor of the stator slots fills:

To do so the useful section area of the copper in a stator slot scSlotS is computed:

$$scStrS := lStrandS \cdot hStrandS - rStrandCorner^2 \cdot (4 - \pi)$$

$$scSlotS := scStrS \cdot ncps \cdot nspc$$

$$fills := \frac{scSlotS}{aSlotS}$$

Computation of the winding factor for the stator:

To do so the following 2 parameters are computed:

The coil span (in m):
$$dspan := \frac{(\pi \cdot dIn \cdot span)}{ns}$$

The pole pitch (in m):
$$taup := \frac{(\pi \cdot dIn \cdot ns)}{(ns \cdot 2 \cdot p)}$$

The winding factor of the stator is then:

This winding factor takes into account the distribution factor and the shortening factor

$$kwS := \frac{\sin\left[\frac{(\gamma \cdot \pi)}{(2 \cdot m)}\right]}{\left[q \cdot \sin\left[\frac{(\gamma \cdot \pi)}{(2 \cdot m \cdot q)}\right]\right]} \cdot \sin\left(\gamma \cdot \frac{ds\ pan}{\tau\ a\ u\ p} \cdot \frac{\pi}{2}\right)$$

Computation of the skewing factor:

Computation from [TAIEB] page 52, [Alger] page 228 and [Cochran] formula 10.151.

This coefficient is going to be used to model the effect of the rotor bar inclination.

This coefficient depends on the harmonic number considered:

$$kSkew := \frac{\sin\left(\gamma \cdot p \cdot \pi \cdot \frac{nSkew}{nr}\right)}{\left(\gamma \cdot p \cdot \pi \cdot \frac{nSkew}{nr}\right)}$$

Computation of the transformation ratio to bring the rotor impedance in the reference of the stator:

From [KOSTENKO] page 444

$$k := \frac{m \cdot nts\ ppS^2 \cdot kwS^2}{nr \cdot nts\ ppR^2 \cdot kwR^2 \cdot kSkew^2} \quad \text{with} \quad nts\ ppR := \frac{1}{2} \quad \text{and} \quad kwR := 1$$

See formula (18-23) from [Kostenko], or page 53 from [TAIEB].

Where:

ntsppR: Number of turns in series per phase for the rotor. ntsppR is 1/2 for a squirrel cage rotor.

kwR: is the winding factor for the rotor. The winding factor is 1 for a squirrel cage rotor.

The transformation ratio as computed takes into account the skewing of the rotor bars [Cochran], [Jong], [Alger].

F.5. Taking into account the mechanical losses:

The mechanical losses are taken into account thanks to a viscous friction coefficient.

smecav is the viscous coefficient to consider the mechanical losses:

$$\text{smecav} := 0.0$$

This coefficient is not used, it could be used for the optimization if there would be a way to estimate the mechanical losses of the machine.

F.6. Computation of the parameters of the equivalent scheme:

F.6.1. Computation of the resistance of the primary winding rs

Computation from [TAIEB] page 43

The resistivity of copper is defined:

$$\rho_{\text{Cu}} := 0.017 \cdot 10^{-6} \text{ Ohm.m}$$

alphsta is the coefficient of the variation of resistivity in function of temperature:

$$\text{alphsta} := 0.0038 \text{ K}^{-1}$$

LTu is the length of a turn without the length of the end winding (in m):

$$\text{LTu} := 2 \cdot L$$

LEndWind is an estimation of the length of the end winding part (cf. [VASSENT] page 72):

$$\text{LEndWind} := \frac{\pi}{(2 \cdot p)} \cdot (d_{\text{In}} + 2 \cdot \text{hts}) + 2 \cdot \text{hts}$$

LTurn is the total length of a turn:

$$\text{LTurn} := \text{LTu} + 2 \cdot \text{LEndWind}$$

rhot is the resistivity of the stator winding in function of the temperature:

$$\text{rhot} := \rho_{\text{Cu}} \cdot [1 + \text{alphsta} \cdot (\text{tsta} - 20)]$$

rspp is the resistance of one parallel path:

$$\text{rspp} := \text{rhot} \cdot \frac{n_{\text{tspp}} \cdot \text{LTurn}}{s_{\text{cStr}} \cdot n_{\text{spc}}}$$

rs is the final equivalent resistance of the stator for one phase:

$$\text{rs} := \frac{\text{rspp}}{n_{\text{pp}}}$$

F.6.2. Computation of the magnetizing reactance xm

Computation from [TAIEB] page 48

The coil span and the pole pitch: dspan and taup have already been defined in 4°

Carter coefficient models the average impact of the slotting on the magnetizing inductance [ALGER].

kcS is the Carter coefficient for the stator:

$$kcS := \frac{ts}{\left[ts - \frac{os^2}{(5 \cdot wGap + os)} \right]} \quad \text{with} \quad ts := \pi \cdot \frac{dIn}{ns} \quad \text{the tooth pitch of the stator}$$

kcR is the Carter coefficient for the rotor:

$$kcR := \frac{tr}{\left[tr - \frac{orr^2}{(5 \cdot wGap + orr)} \right]} \quad \text{with} \quad tr := \pi \cdot \frac{dOutR}{nr} \quad \text{the tooth pitch of the rotor}$$

kc the final Carter coefficient is obtained through the product of the two previous one:

$$kc := kcR \cdot kcS$$

The vacuum permeability is defined as: $\mu_z := 4 \cdot \pi \cdot 10^{-7} \text{ H} \cdot \text{m}^{-1}$

The magnetizing inductance can then be computed thanks to the formula:

$$xm := \frac{2 \cdot m \cdot f \cdot kwS^2 \cdot nts \cdot ppS^2 \cdot Li \cdot dIn \cdot \mu_z}{p^2 \cdot wGap \cdot kc \cdot \gamma^2}$$

F.6.3. Computation of the rotor resistance in the stator reference rrs

Computation from [Kostenko].

The resistance of one rotor bar rb is computed:

$$rb := \rho_R \cdot [1 + \text{alphrot} \cdot (\text{trot} - 20)] \cdot \frac{L}{scrs}$$

The resistance of the portion of the short circuit ring between two bars is computed:

$$rShoCir := \pi \cdot \rho_R \cdot [1 + \text{alphrot} \cdot (\text{trot} - 20)] \cdot \frac{dam}{(nr \cdot ascr)} \cdot \frac{1}{\left(2 \cdot \sin\left(\frac{\pi \cdot p}{nr} \cdot \gamma \right) \right)^2}$$

See formula 18-24 from [Kostenko].

F.6.4. Taking into account the skin effect for the rotor bars:

The analytical formulas that take into account the skin effect only exist for conductors with specific shapes. We are taking it into account for rectangular shapes: as it was done in [Wurtz].

Let's define:

$$\text{eps p} := \text{hBarR} \cdot \sqrt{\left(\pi \cdot \text{mu z} \cdot \frac{\text{lBarR}}{\text{bar}} \cdot \frac{\gamma \cdot f \cdot |s|}{\text{rhoR}} \right)}$$

See formula 23-19 from [Kostenko] or formula 13.204 from [Cochran].

$$\text{krr} := \text{eps p} \cdot \frac{\sinh(2 \cdot \text{eps p}) + \sin(2 \cdot \text{eps p})}{\cosh(2 \cdot \text{eps p}) - \cos(2 \cdot \text{eps p})}$$

See formula 23-18 from [Kostenko] or formula 10.64 from [Cochran].

Finally, the rotor resistance in the rotor reference is rr:

$$\text{rr} := \text{rb} \cdot \text{krr} + \text{rShoCir} \cdot 2 \quad (\text{See formula 18-22 from [Kostenko]})$$

rrs is the rotor resistance referred to the stator side $\text{rrs} := \text{k} \cdot \text{rr}$

F.6.5. Computation of the stator leakage inductance xs

kxs is the coefficient that is going to be multiplied by the permeance coefficient so that to compute the reactances:

$$\text{kxs} := \text{mu z m w nts ppS}^2 \cdot 4 \cdot \frac{\text{Li}}{\text{ns}}$$

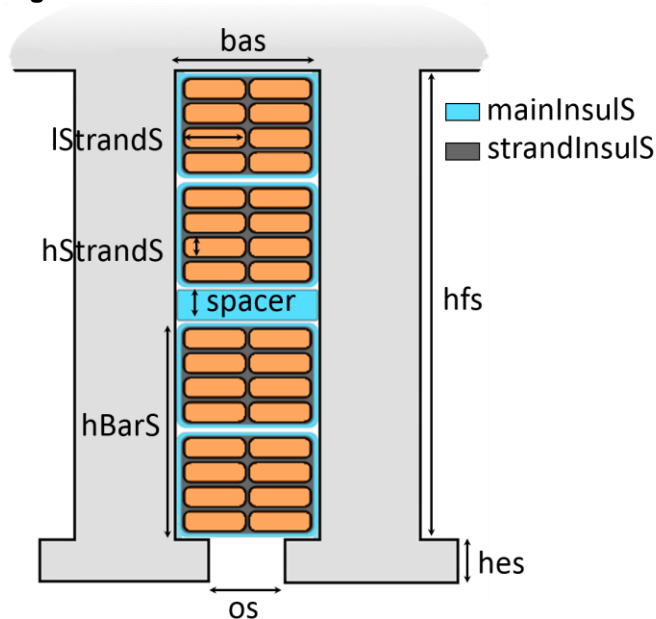
(See formula 5.14 from [Kostenko])

(See formula 38 from [TI])

First, the leakage reactance of the stator slots is computed:

The scheme of the slot was given in Figure F.2, it is reminded in figure F.6:

Figure F.6: Parameter of a stator slot



The permeance of the stator slot is computed

$$\lambda_{\text{slotS}} := \frac{2 \cdot h_{\text{barS}}}{3 \cdot \text{bas}} \cdot \left(1 - \frac{3}{16} \cdot m \cdot \frac{\text{recs}}{\text{nsp}} \right) + \left(\frac{\text{mainInsulS}}{\text{bas}} + \frac{\text{hes}}{\text{os}} \right) \cdot \left(1 - \frac{1}{4} \cdot m \cdot \frac{\text{recs}}{\text{nsp}} \right) + \frac{2 \cdot \text{mainInsulS} + \text{spacer}}{4 \cdot \text{bas}}$$

(See formula 5-14 from [Kostenko], or formula 11 from [TI]).

Thus, the leakage reactance of the stator slot is computed: $x_{\text{slotS}} := k_{\text{xs}} \cdot \lambda_{\text{slotS}}$

Then the stator harmonic part of the leakage reactance is computed

σ_{NuS} is the sum of all the winding coefficient for each unpair harmonic divided by the winding coefficient of the first harmonic multiplied by the harmonic number:

$$\sigma_{\text{NuSPlus}} := \sum_{y=2}^{42} \left[\frac{\frac{\sin \left[\frac{(2 \cdot y + 1) \cdot \pi}{2 \cdot m} \right]}{q \cdot \sin \left[\frac{(2 \cdot y + 1) \cdot \pi}{2 \cdot m \cdot q} \right]} \cdot \sin \left[(2 \cdot y + 1) \cdot \frac{\text{dspan}}{\text{taup}} \cdot \frac{\pi}{2} \right]}{(2 \cdot y + 1)} \right]^2$$

$$\sigma_{\text{NuSMinus}} := \sum_{y=1}^{13} \left[\frac{\frac{\sin \left[\frac{3 \cdot (2 \cdot y + 1) \cdot \pi}{2 \cdot m} \right]}{q \cdot \sin \left[\frac{3 \cdot (2 \cdot y + 1) \cdot \pi}{2 \cdot m \cdot q} \right]} \cdot \sin \left[3 \cdot (2 \cdot y + 1) \cdot \frac{\text{dspan}}{\text{taup}} \cdot \frac{\pi}{2} \right]}{3 \cdot (2 \cdot y + 1)} \right]^2$$

$$\sigma_{\text{NuS}} := \sigma_{\text{NuSPlus}} - \sigma_{\text{NuSMinus}}$$

The permeance coefficient λ_{daos} is then computed as follows

$$\lambda_{\text{daos}} := \frac{3 \cdot q \cdot \text{taup} \cdot \sigma_{\text{NuS}}}{\pi^2 \cdot w_{\text{Gap}} \cdot k_{\text{cS}}}$$

And the harmonic part of the stator leakage reactance can finally be computed:

$$x_{\text{os}} := \lambda_{\text{daos}} \cdot k_{\text{xs}}$$

The stator end part leakage is finally computed

KWKS is a coefficient from experience $\text{KWKS} := 1.2$

$$\lambda_{\text{endS}} := \frac{[q \cdot (0.44 \cdot \text{taup} + 0.15) \cdot \text{KWKS}]}{\text{LirS}}$$

The stator end part leakage reactance x_{ends} is:

$$x_{ends} := \lambda_{EndS} \cdot k_{xs}$$

Finally, the total leakage reactance for the stator x_s is the sum of all of the stator leakage reactance

$$x_s := x_{SlotS} + x_{os} + x_{ends}$$

F.6.6. Computation of the leakage inductance of the rotor expressed to the stator side x_{rs}

k_{xr} is the coefficient that will be multiplied with the permeance coefficient so that to compute the reactances:

$$k_{xr} := \mu_z \cdot w \cdot L_i$$

First, the slot leakage inductance of the rotor is computed

The rotor slots were already presented in Figure F.4. It is reminded in Figure F.7.

Taking into account the skin effect:

So that to compute the permeance, a permeance variation is introduced at the level of the conductor to consider the skin effect.

For that we define a k_x coefficient:

(see [TAIEB], [Kostenko], formula 23-18), [Cochran] figure 10.9 the ratio referred as "of bar portion of slot").

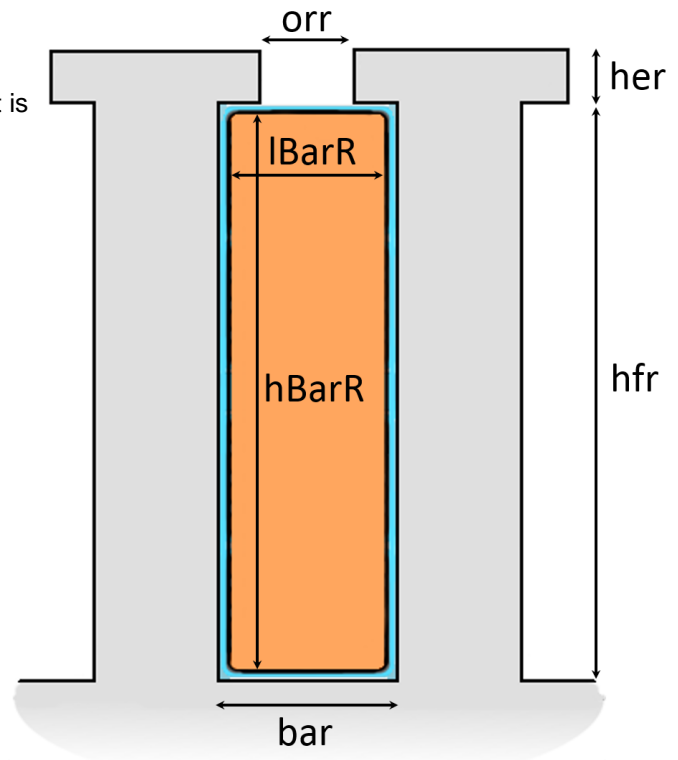
$$k_x := \frac{3}{(2 \cdot \epsilon_p)} \cdot \frac{\sinh(2 \cdot \epsilon_p) - \sin(2 \cdot \epsilon_p)}{\cosh(2 \cdot \epsilon_p) - \cos(2 \cdot \epsilon_p)}$$

The permeance coefficient of the rotor slot is defined as follows

$$\lambda_{SlotR} := \frac{h_{BarR}}{3 \cdot bar} \cdot k_x + \frac{mainInsulR}{bar} + \frac{her}{orr}$$

Thus $x_{SlotR} := k_{xr} \cdot \lambda_{SlotR}$

Figure F.7: Parameter of a rotor slot. The slot was simplified from figure F.4



(See formula 5-14 from [Kostenko] or formula 11 from [TI])

The winding coefficient for the rotor is 1 for a squirrel cage, thus it does not make sense to compute an harmonic part leakage reactance for a squirrel cage machine.

The rotor end part leakage is finally computed

KWKR is a coefficient defined from experience

$$KWKR := 1.8$$

$$\lambda_{\text{EndR}} := \frac{[q \cdot (0.44 \tau_p + 0.15) \cdot KWKR]}{L_{\text{irR}}}$$

The rotor end part leakage reactance x_{endr} is:

$$x_{\text{endr}} := \lambda_{\text{EndR}} \cdot k_{\text{xr}}$$

The leakage reactance due to the skewing of the rotor is computed thanks to:

[Alger] formula 7.60, [Cochran] formula 13.159, [Jong], [Christofides 65] formula 7

$$x_{\text{skew}} := \left(\frac{1}{k_{\text{Skew}}^2} - 1 \right) \cdot x_{\text{r}}$$

N.B: This reactance is already expressed to the stator side.

Finally, the total leakage reactance for the rotor x_{r} is the sum of all of the stator leakage reactance

$$x_{\text{r}} := x_{\text{SlotR}} + x_{\text{endr}}$$

The total leakage reactance of the rotor expressed to the stator side is x_{rs} :

$$x_{\text{rs}} := k \cdot x_{\text{r}} + x_{\text{skew}}$$

F.8. Taking into account the no load saturation factor and the iron losses:

Description of the magnetic steels of the stator and the rotor:

The density of the stator magnetic steel is: $\text{densMSS} := 7600 \text{ kg / m}^3$

The density of the rotor magnetic steel is: $\text{densMSR} := 7600 \text{ kg / m}^3$

Method from [Cochran]

The saturation factor k_{sat} is the ratio between all the ampere turn needed for the flux in the air gap and in the magnetic steel divided by the ampere turn need for the flux in the air gap.

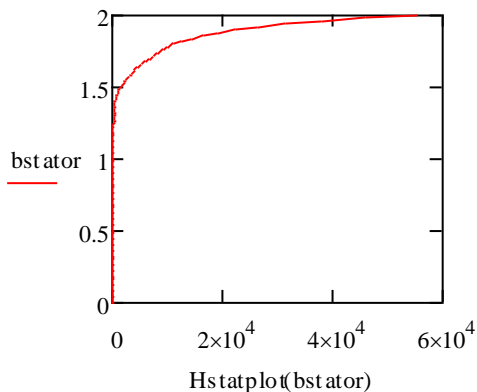
k_{sat} is then used to divide the magnetizing inductance x_{m} for the equivalent scheme of the machine

In order to compute k_{sat} the magnetic iron characteristic need to be known (Flux density in function of Ampere turn)

The iron characteristics are defined thanks to spline of third order polynomials computed from the measures made with an Epstein frame of samples of these irons.

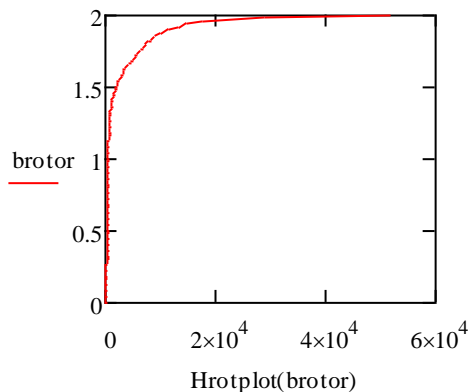
Hstatplot(bstator) := hstat(bstator)

Characteristics of the stator iron



Hrotplot(brotor) := hrot(brotor)

Characteristics of the rotor iron



this represents the equivalent magnetizing curve in the yoke in the following conditions:

- the induction in the yoke is ortho-radial,
- its modulus is sinusoidally-varying (=0 on the interpolar axis).

The iron losses are determined thanks to Bertotti computation

The stator coefficients are:

$$khSms := 0.0167968 \text{ W.s.Kg}^{-1} \cdot \text{T}^{-\alpha}$$

The loss coefficient of the magnetic steel of the stator for the hysteric part of the iron losses

$$kcSms := 0.00009011 \text{ W.s}^2 \cdot \text{Kg}^{-1} \cdot \text{T}^{-2}$$

$$keSms := 0 \text{ W.s}^{1.5} \cdot \text{Kg}^{-1} \cdot \text{T}^{-1.5}$$

$$\alpha haS := 2$$

alphaS could be determined thanks to a SPLINE

The rotor coefficients are:

$$khRms := 0.0702994 \text{ W.s.Kg}^{-1} \cdot \text{T}^{-\alpha}$$

$$kcRms := 0.0001768 \text{ W.s}^2 \cdot \text{Kg}^{-1} \cdot \text{T}^{-2}$$

$$keRms := 0.0020437 \text{ W.s}^{1.5} \cdot \text{Kg}^{-1} \cdot \text{T}^{-1.5}$$

$$\alpha haR := 2$$

alphaR could be determined thanks to a SPLINE

Detail of the computation of the saturation factor and the iron losses:

In the method used to compute the saturation factor and the iron losses, the air-gap voltage will be used to compute the flux per pole. From the flux per pole, and taking the assumption that the flux is sinusoidal in the air gap it will be possible to determine the flux circulation in the magnetic steel and to compute the resulting magnetic field in the different part of the machines. From this magnetic field, it will be possible to compute the saturation factor and the iron losses which will be translated into a resistance in the equivalent scheme r_c . This saturation factor and iron losses reactance will have an impact on the air gap voltage, therefore a loop will be introduced to do the computation until convergence.

To compute the induction in the different part of the machine, we need to compute the sections in the different part of the teeth and the yoke prior to the loop (if we were to put these computations in the loop, computing power would be used again and again for no purpose).

Computation of the different sections in the teeth and the yoke:

Surface of the air gap per pole:

$$ag := \tau_{aup} \cdot Li$$

Computation of the first section of the stator tooth sbdsa:

$$sbtsa := (dIn \cdot \pi - ns \cdot os) \cdot \frac{LirS}{pa}$$

Computation of the second section of the stator tooth sbdsb:

$$sbtsb := [(dIn + 2 \cdot hes) \cdot \pi - ns \cdot os] \cdot \frac{LirS}{pa}$$

Computation of the third section of the stator tooth sbdsb:

$$sbtsb := [(dIn + 2 \cdot hes) \cdot \pi - ns \cdot bas] \cdot \frac{LirS}{pa}$$

Computation of the fourth section of the stator tooth sbdsb:

$$sbtsd := [(dIn + 2 \cdot (hes + hfs)) \cdot \pi - ns \cdot bas] \cdot \frac{LirS}{pa}$$

Computation of the section in the stator yoke

$$sbcsa := hStatorYoke \cdot LirS$$

Computation of the mean path length in the stator yoke

$$lsy := (dOut - hStatorYoke) \cdot \frac{\pi}{2 \cdot pa}$$

Computation of the first section of the rotor tooth sbdsb:

$$sbtra := (dOutR \cdot \pi - nr \cdot orr) \cdot \frac{LirR}{pa}$$

Computation of the second section of the rotor tooth sbdsb:

$$sbtrb := [(dOutR - 2 \cdot her) \cdot \pi - nr \cdot orr] \cdot \frac{LirR}{pa}$$

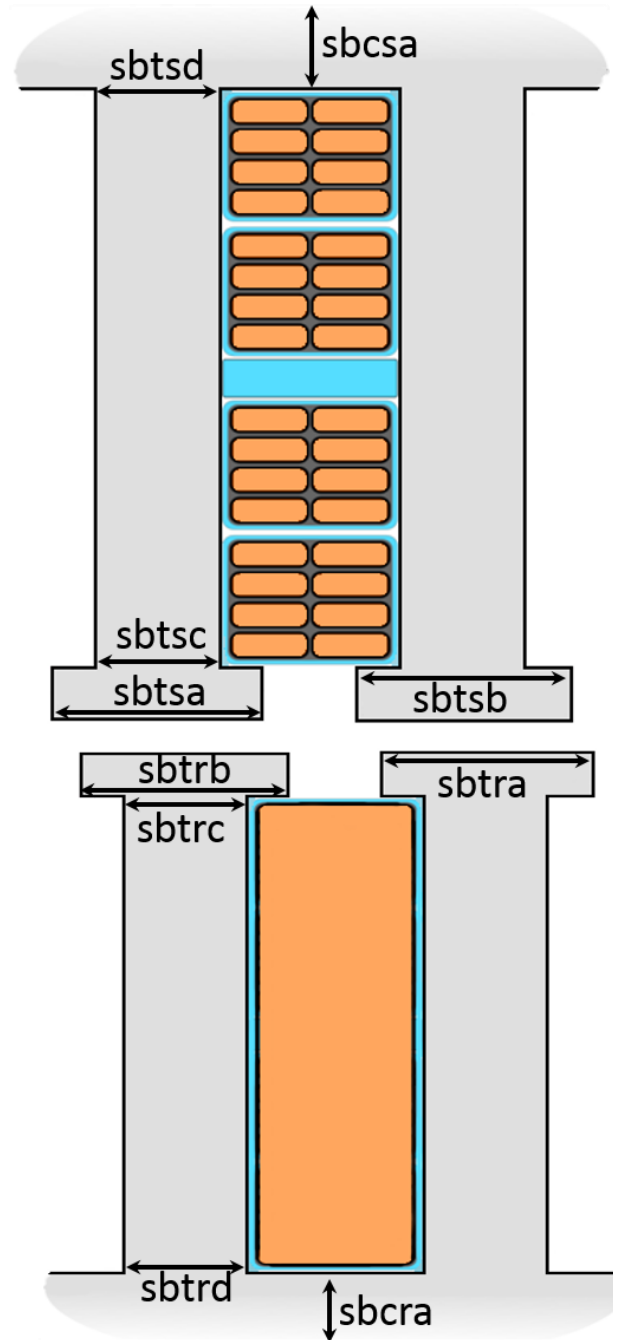
Computation of the third section of the rotor tooth sbdsb:

$$sbtrc := [(dOutR - 2 \cdot her) \cdot \pi - nr \cdot bar] \cdot \frac{LirR}{pa}$$

Computation of the fourth section of the rotor tooth sbdsb:

$$sbtrd := [(dOutR - 2 \cdot (her + hfr)) \cdot \pi - nr \cdot bar] \cdot \frac{LirR}{pa}$$

Figure F.8: Definition of the sections where the flux density is computed



Computation of the section in the rotor yoke

$$sbcra := hRotorYoke \cdot LirR$$

Computation of the mean path length in the rotor yoke

$$lry := (dInR + hRotorYoke) \cdot \frac{\pi}{2 \cdot pa}$$

Computation loop for the iron losses and the saturation factor

The loop will be done until we can find a stable value of the air gap voltage. Thus, two voltages are initialized for the loop boolean condition: vairgap and vairgapNew

vairgapNew := v The first air gap voltage in the loop will be taken as the feeding stator voltage

vairgap := 0 vairgap is initialized to zero so that the first boolean condition of the loop is true

while (vairgapNew-vairgap)² > 0.0001

$$\underline{vairgap} := vairgapNew$$

At the end of the loop, the new air gap voltage will be computed, as long as this air gap voltage is more than 0.01 volt different from the previous airgap voltage the computation will be done once again.

$$phip := \frac{vairgap}{2 \cdot \pi \cdot f \cdot kwS \cdot nts \cdot ppS} \cdot \sqrt{2}$$

Computation of the mutual flux per pole from the feeding voltage:

For the first iteration of the loop, we are using $v=rs \cdot is + nts \cdot ppS \cdot kwS(1) \cdot dphip/dt$ and the resistive term is neglected, it will not be neglected anymore after the first iteration of the loop.

The maximum flux density in the air gap can now be computed with the assumption that the flux density in the air gap is sinusoidal

$$bmaxAG := \frac{phip}{ag} \cdot \frac{\pi}{2}$$

Computation of the number of Ampere-turns needed so that to impose the maximum air gap flux density in the air gap alone:

$$nig := \frac{kc \cdot wGap \cdot bmaxAG}{4 \cdot \pi \cdot 10^{-7}}$$

In the following equations, so that to compute the Ampere-turns needed to imposed the flux density in the magnetic steel we are assuming that all the flux density in passing through the iron and that there is no leakage.

Computation of the flux density in the stator magnetic steel and computation of the Ampere-turns needed to impose these inductions:

Computation of the flux density in the first section of the stator tooth

$$btsa := \frac{phip}{sbtsa} \cdot \frac{\pi}{2}$$

Computation of the flux density in the second section of the stator tooth

$$btsb := \frac{phip}{sbtsb} \cdot \frac{\pi}{2}$$

Computation of the average flux density between the first and the second section of the stator tooth

$$btmsab := \frac{(btsa + btsb)}{2}$$

Computation of the hysteresis losses between the first and the second section of the stator tooth

$$Phbtmsab := khSms \cdot btmsab^{\alpha_{haS}} \cdot f \cdot densMSShes \cdot \frac{sbtsa + sbtsb}{2}$$

Computation of the Eddy current losses between the first and the second section of the stator tooth

$$Pcbtmsab := kcSms \cdot btmsab^2 \cdot f^2 \cdot densMSShes \cdot \frac{sbtsa + sbtsb}{2}$$

Computation of the Excess losses between the first and the second section of the stator tooth

$$Pebtmsab := keSms \cdot btmsab^{1.5} \cdot f^{1.5} \cdot densMSShes \cdot \frac{sbtsa + sbtsb}{2}$$

Computation of the Ampere-turns needed so that to impose the flux density between the first and the second section of the stator tooth

$$athes := hes \cdot \frac{hstat(btsa) + 4 \cdot hstat(btmsab) + hstat(btsb)}{6}$$

Computation of the flux density in the third section of the stator tooth

$$btsc := \frac{phip}{sbtsd} \cdot \frac{\pi}{2}$$

Computation of the flux density in the fourth section of the stator tooth

$$btsc := \frac{phip}{sbtsd} \cdot \frac{\pi}{2}$$

Computation of the average flux density between the third and the fourth section of the stator tooth

$$btmscd := \frac{(btsc + btsc)}{2}$$

Computation of the hysteresis losses between the third and the fourth section of the stator tooth

$$Phbtmscd := khSms \cdot btmscd^{\alpha_{haS}} \cdot f \cdot densMSShfs \cdot \frac{sbtsd + sbtsd}{2}$$

Computation of the Eddy current losses between the third and the fourth section of the stator tooth

$$Pcbtmscd := kcSms \cdot btmscd^2 \cdot f^2 \cdot densMSShfs \cdot \frac{sbtsd + sbtsd}{2}$$

Computation of the Excess losses between the third and the fourth section of the stator tooth

$$Pebtmscd := keSms \cdot btmscd^{1.5} \cdot f^{1.5} \cdot densMSShfs \cdot \frac{sbtsd + sbtsd}{2}$$

Computation of the Ampere-turns needed so that to impose the flux density between the third and the fourth section of the stator tooth

$$athfs := hfs \cdot \frac{hstat(bts c) + 4 \cdot hstat(btmscd) + hstat(bts d)}{6}$$

Computation of the number of Ampere-turns needed so that to impose the flux density in the stator tooth

$$nist := athes + athfs$$

Computation of the flux density in the stator yoke

$$bcsa := \frac{\phi_{ip}}{sbcsa \cdot 2} \quad \text{The division by 2 is because only half of the flux in the air gap pass in the yoke on the interpolar axis}$$

Computation of the hysteresis losses in the stator yoke

$$Phbcsa := kh_{Sms} \cdot bcsa^{\alpha_{haS}} \cdot f \cdot dens_{MSS} \cdot LirS \cdot \frac{\pi \cdot [d_{Out}^2 - (d_{In} + 2 \cdot hts)^2]}{pa}$$

Computation of the Eddy current losses in the stator yoke

$$Pcbcsa := kc_{Sms} \cdot bcsa^2 \cdot f^2 \cdot dens_{MSS} \cdot LirS \cdot \frac{\pi \cdot [d_{Out}^2 - (d_{In} + 2 \cdot hts)^2]}{pa}$$

Computation of the Excess losses in the stator yoke

$$Pebcsa := ke_{Sms} \cdot bcsa^{1.5} \cdot f^{1.5} \cdot dens_{MSS} \cdot LirS \cdot \frac{\pi \cdot [d_{Out}^2 - (d_{In} + 2 \cdot hts)^2]}{pa}$$

Computation of the number of Ampere-turns needed so that to impose the flux density in the stator yoke

$$nisy := lsy \cdot hstat(bcsa)$$

Computation of the flux density in the rotor magnetic steel and computation of the Ampere-turns needed to impose these inductions:

Computation of the flux density in the first section of the rotor tooth

$$btra := \frac{\phi_{ip}}{sbtra} \cdot \frac{\pi}{2}$$

Computation of the flux density in the second section of the rotor tooth

$$btrb := \frac{\phi_{ip}}{sbtrb} \cdot \frac{\pi}{2}$$

Computation of the average flux density between the first and the second section of the rotor tooth

$$btmrab := \frac{(btra + btrb)}{2}$$

Computation of the hysteresis losses between the first and the second section of the rotor tooth

$$Phbtmrab := kh_{Rms} \cdot btmrab^{\alpha_{haR}} \cdot f \cdot dens_{MSR} \cdot her \cdot \frac{sbtra + sbtrb}{2}$$

Computation of the Eddy current losses between the first and the second section of the rotor tooth

$$Pcbtmrab := kc_{Rms} \cdot btmrab^2 \cdot f^2 \cdot dens_{MSR} \cdot her \cdot \frac{sbtra + sbtrb}{2}$$

Computation of the Excess losses between the first and the second section of the rotor tooth

$$P_{\text{btmrb}} := k_{\text{eRms}} \cdot b_{\text{tmrb}}^{1.5} \cdot f^{1.5} \cdot \text{densMSR} \cdot \text{her} \cdot \frac{s_{\text{btra}} + s_{\text{btrb}}}{2}$$

Computation of the Ampere-turns needed so that to impose the flux density between the first and the second section of the rotor tooth

$$\text{ather} := \text{her} \cdot \frac{\text{hrot}(b_{\text{tra}}) + 4 \cdot \text{hrot}(b_{\text{tmrb}}) + \text{hrot}(b_{\text{trb}})}{6}$$

Computation of the flux density in the third section of the rotor tooth

$$b_{\text{trc}} := \frac{\text{phip}}{s_{\text{btrc}}} \cdot \frac{\pi}{2}$$

Computation of the flux density in the fourth section of the rotor tooth

$$b_{\text{trd}} := \frac{\text{phip}}{s_{\text{btrd}}} \cdot \frac{\pi}{2}$$

Computation of the average flux density between the third and the fourth section of the rotor tooth

$$b_{\text{tmrcd}} := \frac{(b_{\text{trc}} + b_{\text{trd}})}{2}$$

Computation of the hysteresis losses between the third and the fourth section of the rotor tooth

$$P_{\text{hbtmrcd}} := k_{\text{hRms}} \cdot b_{\text{tmrcd}}^{\text{alphaR}} \cdot f \cdot \text{densMSR} \cdot \text{hfr} \cdot \frac{s_{\text{btrc}} + s_{\text{btrd}}}{2}$$

Computation of the Eddy current losses between the third and the fourth section of the rotor tooth

$$P_{\text{cbtmrcd}} := k_{\text{cRms}} \cdot b_{\text{tmrcd}}^2 \cdot f^2 \cdot \text{densMSR} \cdot \text{hfr} \cdot \frac{s_{\text{btrc}} + s_{\text{btrd}}}{2}$$

Computation of the Excess losses between the third and the fourth section of the rotor tooth

$$P_{\text{ebtmrcd}} := k_{\text{eRms}} \cdot b_{\text{tmrcd}}^{1.5} \cdot f^{1.5} \cdot \text{densMSR} \cdot \text{hfr} \cdot \frac{s_{\text{btrc}} + s_{\text{btrd}}}{2}$$

Computation of the Ampere-turns needed so that to impose the flux density between the third and the fourth section of the rotor tooth

$$\text{athfr} := \text{hfr} \cdot \frac{\text{hrot}(b_{\text{trc}}) + 4 \cdot \text{hrot}(b_{\text{tmrcd}}) + \text{hrot}(b_{\text{trd}})}{6}$$

Computation of the number of Ampere-turns needed so that to impose the flux density in the rotor tooth

$$\text{nirt} := \text{ather} + \text{athfr}$$

Computation of the flux density in the rotor yoke

$$b_{\text{cra}} := \frac{\text{phip}}{s_{\text{bcra}} \cdot 2} \quad \text{The division by 2 is because only half of the flux in the air gap pass in the yoke on the interpolar axis}$$

Computation of the hysteresis losses in the stator yoke

$$P_{\text{hbca}} := k_{\text{hRms}} \cdot b_{\text{cra}}^{\text{alphaR}} \cdot f \cdot \text{densMSR} \cdot \text{LirR} \cdot \frac{\pi \cdot [(d_{\text{OutR}} - 2 \cdot \text{htr})^2 - d_{\text{InR}}^2]}{p_{\text{a}}}$$

Computation of the Eddy current losses in the stator yoke

$$P_{\text{cbca}} := k_{\text{cRms}} \cdot b_{\text{cra}}^2 \cdot f^2 \cdot \text{densMSR} \cdot \text{LirR} \cdot \frac{\pi \cdot [(d_{\text{OutR}} - 2 \cdot \text{htr})^2 - d_{\text{InR}}^2]}{p_{\text{a}}}$$

Computation of the Excess losses in the stator yoke

$$P_{ebcra} := k_{eRms} \cdot b_{cra}^{1.5} \cdot f^{1.5} \cdot \text{densMSR} \cdot L_{irR} \cdot \frac{\pi \cdot [(d_{OutR} - 2 \cdot h_{tr})^2 - d_{InR}^2]}{p_a}$$

Computation of the number of Ampere-turns needed so that to impose the flux density in the rotor yoke

$$n_{iry} := l_{ry} \cdot h_{rot}(b_{cra})$$

From this point, it is possible to compute the saturation factor ksatsat:

$$k_{sat} := \frac{2 \cdot n_{ig} + 2 \cdot n_{ist} + n_{isy} + 2 \cdot n_{irt} + n_{iry}}{2 \cdot n_{ig}}$$

In Cades, the ksatsat equation is actually divided into two equations:

$$k_{ic} := 1 + \frac{n_{isy} + n_{iry}}{2 \cdot n_{ig}} \quad k_{sat} := \frac{n_{ist} + n_{irt}}{n_{ig}} + k_{ic}$$

The variable k_{ic} was introduced so that to make the symbolic computation and the generation of code into Cades easier.

In fact, the expression of ksatsat is going to appear in all the macroscopic equations computed from the equivalent scheme.

These expressions are cosphi, pu, pabs,... . The symbolic computation of these variables can become enormous. It is necessary to introduce intermediate parameters. In particular, these parameters will be taken from the equivalent scheme. It looks like it would have been interesting to introduce ksatsat as an intermediate parameter. The problem is that all the intermediate parameters are exclusively computed from input parameters of the model. The symbolic expression of ksatsat would have been really big.

Thus, it is important to create intermediate parameters that will serve in the expression of ksatsat. The first idea would have been to take n_{ist}, n_{isy}, n_{irt}, n_{iry} and n_{ig} as intermediate parameters. It would have resulted in symbolic expressions of cosphi, pu, pabs that would have been bigger. The creation of k_{ic} allows the number of parameters of these expressions to be reduced.

Ph is the sum of all the hysteresis losses in the Machine

$$P_h := P_{hbtmsab} + P_{hbtmscd} + P_{hbcsa} + P_{hbtmrab} + P_{hbtmr cd} + P_{hb cra}$$

Pc is the sum of all the Eddy current losses in the Machine

$$P_c := P_{cbtmsab} + P_{cbtmscd} + P_{cbcsa} + P_{cbtmrab} + P_{cbtmr cd} + P_{cb cra}$$

Pe is the sum of all the Excess losses in the Machine

$$P_e := P_{ebtmsab} + P_{ebtmscd} + P_{ebcsa} + P_{ebtmrab} + P_{ebtmr cd} + P_{eb cra}$$

ironLosses is the result of the computation of the iron losses in W:

$$\text{ironLosses} := P_h + P_c + P_e$$

r_m is the equivalent resistance to the iron losses previously computed. It comes from $\text{ironLosses} = 3 \cdot \text{vaigap}^2 / r_m$

$$r_m := 3 \cdot \frac{\text{vaigap}^2}{\text{ironLosses}}$$

Computation of the equivalent scheme equations

$$r_{rs\text{Slip}} := \frac{r_{rs}}{s}$$

$$x_{mk} := \frac{x_m}{k_{sat}}$$

The impedance of the stator is:

$$z_s := r_s + i \cdot x_s$$

The impedance of the rotor expressed to the stator side is:

$$z_r := r_{rs\text{Slip}} + i \cdot x_{rs}$$

The magnetizing impedance is:

$$z_m := \frac{i \cdot x_{mk} \cdot r_m}{i \cdot x_{mk} + r_m}$$

The total impedance of the machine is thus:

$$z := z_s + \frac{z_r \cdot z_m}{z_r + z_m}$$

From this point the amplitude of the stator current per phase can be computed:

$$i_s := \frac{v}{|z|}$$

The cos phi of the machine can also be computed:

$$\cos \phi := \frac{\text{Re}(z)}{|z|}$$

And finally the new air gap voltage can be computed from the feeding voltage minus the voltage drop in the stator winding

$$\text{vaigapNew} := v \cdot \left| \frac{z_m \cdot z_r}{z_s \cdot (z_m + z_r) + z_m \cdot z_r} \right|$$

A variable named `compteur` can be incremented so that to give an indication of how many iterations were necessary to get a convergence.

$$\text{compteur} := \text{compteur} + 1$$

end This is the end of the while loop

F.9. Full computation of the machine performance:

Once again, the parameters of the equivalent circuit can be defined, this time taking into account the real flux density in the air-gap

$$z_s := r_s + i \cdot x_s$$

$$r_{rs\ Slip} := \frac{r_s}{s}$$

$$x_{mk} := \frac{x_m}{k_{sat}}$$

$$z_r := r_{rs\ Slip} + i \cdot x_{rs}$$

$$z_m := \frac{i \cdot x_{mk} \cdot r_m}{x_{mk} \cdot i + r_m}$$

then:

$$z := z_s + \frac{z_r \cdot z_m}{z_r + z_m}$$

the norm of z is:

$$n_z := \frac{|z_r \cdot z_m + z_s \cdot (z_m + z_r)|}{|z_m + z_r|}$$

The amplitude of the stator current per phase is:

$$i_s := \frac{v}{n_z}$$

The amplitude of the rotor current expressed in the stator side is:

$$i_{rs} := \frac{|z_m|}{|z_r \cdot z_m + z_s \cdot (z_m + z_r)|} \cdot v$$

Originally we wrote:
$$i_{rs} = \left| \frac{z_m}{z_m + z_r} \right| \cdot i_s$$

This equation was obtained thanks to the current divider rule in the equivalent scheme. The equation chosen eqirs seems to generate a simpler symbolic code.

The total electromagnetic torque produced by the machine can be expressed as:

$$T_{em} := 3 \cdot r_{rs\ Slip} \cdot i_{rs}^2 \cdot \frac{P}{(2 \cdot \pi \cdot f)}$$

The total mechanical power of the machine is then computed:

$$P_t := \left[3 \cdot (1 - s) \cdot r_{rs} \text{Slip} \cdot i_{rs}^2 \right]$$

The power factor of the machine is still defined as:

$$\cos \phi := \frac{\text{Re}(z)}{nz}$$

The no load current is (We consider that $g_0 = m a$):

$$I_{\text{noLoad}} := \frac{V}{nz}$$

The resistive viscous mechanical torque is:

$$t_{\text{mecav}} := s_{\text{mecav}} \cdot w \cdot \frac{1 - s}{p}$$

The mechanical losses from the resistive viscous mechanical torque are:

$$p_{\text{mecav}} := t_{\text{mecav}} \cdot \frac{1 - s}{p} \cdot w$$

The useful mechanical torque of the machine is:

$$T_u := 3 \cdot r_{rs} \text{Slip} \cdot i_{rs}^2 \cdot \frac{p}{2 \cdot \pi \cdot f} - t_{\text{mecav}}$$

The useful power of the machine is:

$$P_u := P_t - p_{\text{mecav}}$$

The active power of the machine is expressed as:

$$p_{\text{abs}} := 3 \cdot V \cdot i_s \cdot \cos \phi$$

The efficiency of the machine is then:

$$\text{eff} := \frac{P_u}{p_{\text{abs}}}$$

j_s is the current density in the stator winding:

$$j_s := \frac{i_s}{s_{\text{cStrS}} \cdot n_{\text{pp}}}$$

Computation of the current density in the rotor bars

$$k_{ci} := \frac{n_{ts} p p_S k_w S \cdot m}{n_{ts} p p_R k_w R \cdot nr} \quad (\text{See formula 19-12c from [Kostenko]. This formula brings back the currents absorbed through the stator to their real value in the rotor}).$$

$$j_{rs} := \frac{i_{rs}}{s_{crs}} \cdot k_{ci}$$

Computation of the Joules losses in the stator:

$$p_{jous} := 3 \cdot r_s \cdot i_s^2$$

Computation of the Joules losses in the rotor:

$$p_{jour} := 3 \cdot s \cdot r_{rs} \cdot i_{rs}^2$$

Computation of the iron losses to verify that they are equal to the one computed in the loop

Computation **of the magnetizing current in the rm branch:**

zram is the equivalent impedance of the two parallel branches of the rotor and the magnetizing inductance.

$$z_{ram} := \frac{i \cdot z_r \cdot x_{mk}}{z_r + i \cdot x_{mk}}$$

imc is the current in the branch of the iron losses resistance

$$i_{mc} := \left| \frac{z_{ram}}{z_{ram} + r_m} \right| \cdot i_s$$

$$ironLossesEnd := 3 \cdot r_m \cdot i_{mc}^2$$

F.10. Definition of the objective function:

Depending on the objective of the optimization we can define different objective functions. In this example, we will define three different objective functions. The first one will depend on the efficiency of the machine design, a second one will be based on the price of the materials of the design (the assumption is made that the price of the machine would be roughly proportional to the price of its materials, which is not true. The last objective function will be a ponderation of the two previous functions.

In order to define the weight of the machine we can define the density of copper, the density of the stator sheets, the density of the rotor sheets and the density of the shaft steel.

densCu is the density of copper: $densCu := 8960 \text{ kg.m}^{-3}$

The density of the stator magnetic sheets was already defined: $densMSS := 7600 \text{ kg.m}^{-3}$

The density of the rotor magnetic sheets was already defined: $densMSR := 7600 \text{ kg.m}^{-3}$

densSteel is the density of the steel shaft: $densSteel := 7850 \text{ kg.m}^{-3}$

The copper mass weightCu is defined as:

$$\text{weightCu} := \left(\frac{l\text{StrandS} \cdot h\text{StrandS} \cdot n\text{cps} \cdot n\text{spc} \cdot n\text{s} \cdot L\text{Turn}}{2} + h\text{BarR} \cdot l\text{BarR} \cdot n\text{r} \cdot L + \text{ascr} \cdot \text{dam} \right) \cdot \text{densCu}$$

The mass of the stator electrical sheets weightSheetsR is defined as:

$$\text{weightSheetsS} := \left(\frac{\pi \cdot d\text{Out}^2}{4} - \frac{\pi \cdot d\text{In}^2}{4} - a\text{SlotS} \cdot n\text{s} \right) \cdot L\text{irS} \cdot \text{densMSS}$$

The Mass of the rotor electrical sheets weightSheetsS is defined as:

$$\text{weightSheetsR} := \left(\frac{\pi \cdot d\text{OutR}^2}{4} - \frac{\pi \cdot d\text{InR}^2}{4} - a\text{SlotR} \cdot n\text{r} \right) \cdot L\text{irR} \cdot \text{densMSR}$$

The mass of the shaft weightShaft is defined as:

$$\text{weightShaft} := \frac{\pi \cdot d\text{InR}^2}{4} \cdot L \cdot \text{densSteel}$$

The price per kg of the materials are defined to compute the materials price of each design

The price of copper is (in): $\text{priceCu} := 8 \quad \$.kg^{-1}$

The price of the stator sheets are (in \$.kg⁻¹): $\text{priceSheetsS} := 1.2 \quad \$.kg^{-1}$

The price of the rotor sheets are (in \$.kg⁻¹): $\text{priceSheetsR} := 1.6 \quad \$.kg^{-1}$

The price of the shaft steel is (in \$.kg⁻¹): $\text{priceSteel} := 0.7 \quad \$.kg^{-1}$

It is now possible to compute the price of the raw materials:

$$\text{priceMaterials} := \text{weightCu} \cdot \text{priceCu} + \text{weightSheetsR} \cdot \text{priceSheetsR} + \text{weightSheetsS} \cdot \text{priceSheetsS} + \text{weightShaft} \cdot \text{priceSteel}$$

The first objective function based on the efficiency of the design can be expressed:

$$\text{fob_eff} := (1 - \text{eff})$$

The second objective function based on the price of the design can be expressed:

$$\text{fob_price} := \text{priceMaterials}$$

A third objective function can be defined as a ponderation of the two previous functions. The definition of the ponderation coefficient will have a big impact on the result of the optimization. Another interesting idea could be to plot the best efficiency as a function of the price of the machine.

$$\text{fob_ponderation} := \text{coef_eff} \cdot (1 - \text{eff}) + \text{coef_price} \cdot \text{priceMaterials}$$

Bibliography:

[Wurtz] - Frédéric Wurtz, "Une Nouvelle Approche pour la Conception Sous Contraintes de Machines Electriques", PhD, Institut National Polytechnique de Grenoble - INPG, 1996.

[Alger] - Philip L. Alger, "Induction Machines", ed. Gordon and Breach Science Publishers - 150 Fifth Avenue, New-York, 518 pages, 1970.

[Cochran] - Paul L. Cochran, "Polyphase Induction Motors - Analysis, Design, and Application", ed. MARCEL DEKKER, 675 pages, 1989, ISBN 0-8247-4.

[Christofides 65] - Christofides, "Origins of load losses in induction motors with cast aluminium rotors", IEE Proceedings, vol. 112, december 1965, pp. 2317-2332.

[Jong] - H. C. J. de Jong, "Skew Leakage in Induction Machines", ETEP Vol. 4, No. 1, January/February 1994, pp. 43 - 46.

[Kostenko] - M. Kostenko et L. Piotrovski, "Machines Electriques - TOME II", éditions Mir - Moscou 1969.

[TAIEB] - Taieb Brahim Abdelhalim, "Contribution à la modélisation de la machine asynchrone à cage par logiciel d'éléments finis 2D et 3D", Thèse de Docteur, Institut National Polytechnique de Grenoble, juin 1992.

[TI] - André Belot, "Calcul des fuites et inductances de fuites de l'induit", issu des Techniques de l'ingénieur, page D440-1 D440-16.

[VASSENT] - Vassent Eric, "Contribution à la modélisation des moteurs asynchrones par la méthode des éléments finis", Thèse de Docteur, Institut National Polytechnique de Grenoble, Novembre 1990.

APPENDIX G.

Example of Improvements Using FEM and a Method Comparable to Design of Experiment for an Induction Machine Design

As explained in II.2.3.6, p 58, the first optimization of an IM on the TTP specifications was done with dimension constraints that were too challenging. The maximal outer diameter was 4.5 m, the maximal length was 1.8 m, and the power of the machine 22 MW. The semi-analytical model paired with an SQP algorithm was not able to meet all the constraints. Under these conditions, the algorithm was not trying to optimize the objective function but simply to verify all the constraints. The algorithm managed to design a machine getting close to all the constraints but the one on the power factor. To verify the semi-analytical model used, it was then tried to reproduce the geometry with FEM on Flux2D.

The semi-analytical model was right that the constraints were not reasonable. Thus, in the following, the reader should keep in mind that the comparison is made on an IM that is very saturated and has a lot of leakages. The designed was pushed beyond what would be normally acceptable to reach a 22 MW rated power.

When the design was simulated on Flux2D, the stator currents were too high (according to the analytical model, a maximum of 5 A/mm² was expected, where it should be limited to 3 A/mm² by constraint), and there was a lot of flux leakage. With a few iterations, using a method analogous to DOE (see II.2.2.2.4, p 49), the geometrical parameters of the IM were slightly changed so as to maintain the rated power and diminish the reactive power.

The parameters that were modified were the number of turns in series per parallel path and per phase, the number of teeth and their width and length, for both the stator and the rotor. The airgap diameter was increased (maintaining the stator outer diameter and decreasing the stator rim height) and the other parameters that were changed were depending on the airgap diameter.

It would not have been easy to modify much more parameters with such a method, indeed each iteration was taking a few minutes to simulate and a then some more time to analyze. Playing on five parameters, it took 17 iterations and more than a day to pass from the initial to the final design. As it can be seen in Table G-1, the stator current density and the power factor were notably improved. The power factor was improved with wider rotor slots and a resulting lower flux leakage in the rotor. The stator currents were improved with a bigger copper cross section, and lower currents due to lower flux leakage. The iron losses were not calculated, so the efficiency was not calculated either. But due to the lower currents and lower reactive power, we can expect the new design to be more efficient than the original design.

Table G-1: Comparison of the initial and final IM design after 17 iterations of FE simulations with the variation of a few parameters.

	Rated Power	Reactive Power	Rotor Current	Stator Current	Power Factor
Initial IM	22.18 MW	28.30 MVar	4.88 A/mm ²	5.67 A/mm ²	0.617
Final IM	23.46 MW	16.08 MVar	4.91 A/mm ²	4.72 A/mm ²	0.825

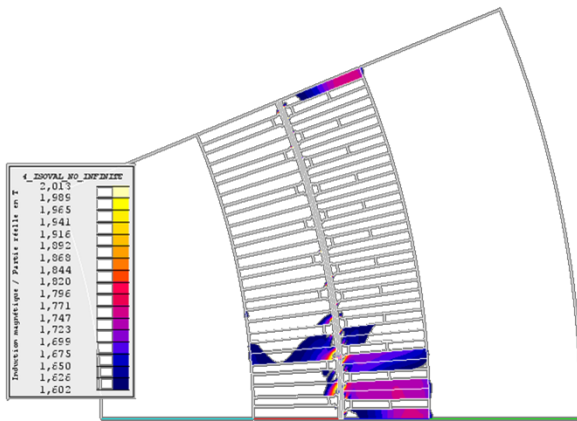


Figure G-1: View on Flux2D of one pole of the initial design obtained by an optimization with the semi-analytical model of APPENDIX F. The flux density is visualized for sectors with high saturation: between 1.6 and 2.01 Tesla.

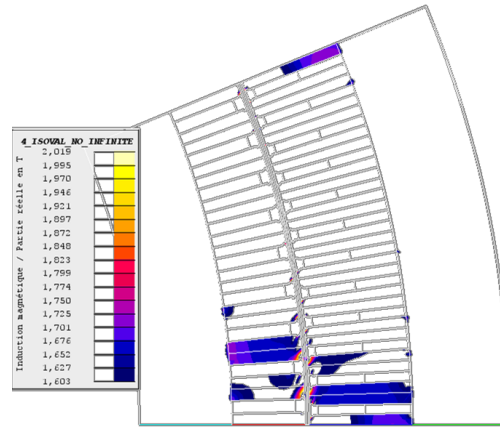


Figure G-2: View on Flux2D of one pole of the final design obtained after 17 iterations of FE simulations with the variation of a few parameters. The flux density is visualized for sectors with high saturation: between 1.6 and 2.01 Tesla.

As it can be seen in Figure G-1 and Figure G-2, the proportions of the stator and rotor slots have changed. In both figures, the maximal flux density in the teeth is very high: above 1.8 T. In usual design, we aim at flux densities in the 1.6 T range. This is due to the airgap diameter or the length of the machine being too small for the required torque. For the same reason, to increase the copper section area in the slots, their lengths were increased instead of their widths. We ended up with a design where the teeth were too thin and too long. With a machine with a bigger airgap surface area (bigger airgap diameter or bigger length), the same torque would be obtained with a smaller flux density. With the bigger diameter, it would then be possible to design slots shorter in length and bigger in width (as it was obtained in APPENDIX H).

Table G-2: Parameters of the final design fed with 6600 V supply at 9.6 Hz and a rotor slip of 3% for the results of Table G-1. This design will be used for the comparison between FEM and the semi-analytical model (see II.2.3.6, p 58).

General parameters	
POLES PAIRS	8
MACHINE LENGTH [mm]	1795
Stator parameters	
INNER STATOR DIAMETER [mm]	3750
OUTER STATOR DIAMETER [mm]	4500
NUMBER OF STATOR SLOTS	336
QSTATOR PER POLE AND PER PHASE	7
STATOR COIL PITCH	17
NUMBER OF PARALLEL PATHS	1
NUMBER CONDUCTOR PER SLOT	4
STATOR SLOT WIDTH [mm]	15
STATOR SLOT HEIGHT [mm]	180
STATOR PRE-SLOT HEIGHT [mm]	16.46
STATOR VENTILATION DUCTS NUMBER [-]	26
STATOR VENTILATION DUCTS WIDTH [mm]	7
STATOR CORE STACKING FACTOR [mm]	0.93
Rotor parameters	
INNER ROTOR DIAMETER [mm]	3000
OUTER ROTOR DIAMETER [mm]	3730
NUMBER OF ROTOR SLOTS	288
QROTOR PER POLE AND PER PHASE	6
ROTOR COIL PITCH	14
NUMBER OF PARALLEL PATHS	2
ROTOR SLOT WIDTH [mm]	16.08
ROTOR SLOT HEIGHT [mm]	110
ROTOR PRE-SLOT HEIGHT [mm]	26.9
ROTOR VENTILATION DUCTS NUMBER [-]	26
ROTOR VENTILATION DUCTS WIDTH [mm]	8
ROTOR CORE STACKING FACTOR [mm]	0.93

APPENDIX H.

From imaginary to real machines using the Semi-Analytical model presented in APPENDIX F and a 1st order optimization.

H.1 Methodology

The semi-analytical model of APPENDIX F was coded into Cades (Cades is presented in II.2.2.3, and the implementation of the semi-analytical model into Cades is presented in II.2.3.5). Thanks to this software, it was possible to do multiple optimizations, with different specifications and objectives, to plot parametrized optimizations and Pareto curves, for imaginary and real machines (as explained and shown in II.2.3.7, p 60).

These optimizations were done with a Sequential Quadratic Programming (SQP) algorithm. This algorithm is a 1st order algorithm (as defined in II.2.2.2.2, p 47) available in Cades.

In order to get from the analytical sizing given in Table II-3, p 55, to a “real” machine optimized with Cades given in Table H-1 and Table H-2, multiple optimizations, parametrized optimizations and Pareto curves with imaginary and real machines were done (as shown in Figure II-6 and Figure II-7, p 62 and 63).

In this appendix, we will describe the steps to create a parametrized optimization or a Pareto curve with imaginary machines and then create the same optimization or Pareto curve with real machines. We will describe these steps for the parametrized optimization of the optimum efficiency as a function of the flux densities in the teeth (presented in Figure II-6, p 62). Finally, the optimization leading to the “best real” design will be given in Table H-1 and Table H-2.

H.1.1 Close attention needs to be paid to avoid mistaking local optimums for global optimums

The concept of local optimums and global optimums was presented in Figure II-3, p 48 for a problem with only one dimension. Complex semi-analytical models generally have a high number of dimensions (the semi-analytical model presented in APPENDIX F has 29 inputs that are degrees of liberty for a total of 81 inputs). Thus, it is not possible to visualize local optimums the same way they can easily be seen in Figure II-3 when there is only one degree of liberty. However, the user of 1st order optimization algorithm needs to be aware of this problem. Sometimes, the 1st order optimization algorithm can even get stuck in a position that does not respect all the constraints but that still is a local optimum.

To avoid being stuck on local optimums, a first idea is to start the first iteration of the optimization algorithm not too far from the global optimum. This is the main reason why a first geometry was designed with an analytical method in II.2.3.3, p 54 before launching the first optimization. The first design obtained was used as the 1st iteration of the 1st order optimization.

The previous idea can be kept when plotting a parametrized optimization or a Pareto curve. When the global optimum is found for a given set of constraints, the design obtained can be used as a first step for the optimization of the next point of the optimization or Pareto curve.

Despite the precautions taken with the previous advice it is still possible to get stuck in local optimums. During the optimizations using the semi-analytical model of APPENDIX F, this was a recurring problem. The best solution against this eventuality is to launch several optimizations in a row for a given set of specifications and constraints, each with a slightly different starting point. This is the solution that gave the best results during this Ph.D. With Cades, it is possible to automatize some work with Python scripts. With such scripts, it is easy to launch successive optimizations, each with a few inputs parameters defined randomly in a range. All the results can then be scanned to look for the best one.

In the results presented in Figure II-6 and Figure II-7 for example, each point of the parametrized optimization or Pareto curve with imaginary machines was the best point found amid 50 different optimizations. The inputs parameters that were set randomly were: the slip, the number of pole pairs, the frequency, the number of parallel paths, the number of conductors per slot, and the number of strands per conductor.

H.1.2 From imaginary machines to real machines for optimizations and Pareto curves

The concept of imaginary machines was introduced in this work in II.2.3.7.1, p 61. As already explained, imaginary machines are machines that do not make physical sense: some of their parameters that should be discrete are continuous. However, they are very good indicators of what can be expected from real machines. The main advantage of using imaginary machines is that the set of imaginary machines can be explored much faster with a 1st order optimization algorithm than the set of real machines.

Using this advantage, in this work parametrized optimizations and Pareto curves were plotted using imaginary machines (for example in Figure II-6 and Figure II-7). It was then possible, using the results from the optimizations with imaginary machines, to plot the parametrized optimizations or Pareto curves with real machines. The related process will be detailed here until the same figure as Figure II-6 is obtained.

The parametrized optimization presented in Figure II-6, gives the maximum efficiency that can be reached under the specifications and constraints of the TTP, depending on saturation (the flux density) in the teeth of the Induction Machine. With the semi-analytical model of APPENDIX F, using a 1st order optimization algorithm such as the SQP algorithm available in Cades, taking care of avoiding the multiple local optimums (following the advice given in H.1.1), it only takes a few hours to obtain following parametrized optimization in Figure H-1.

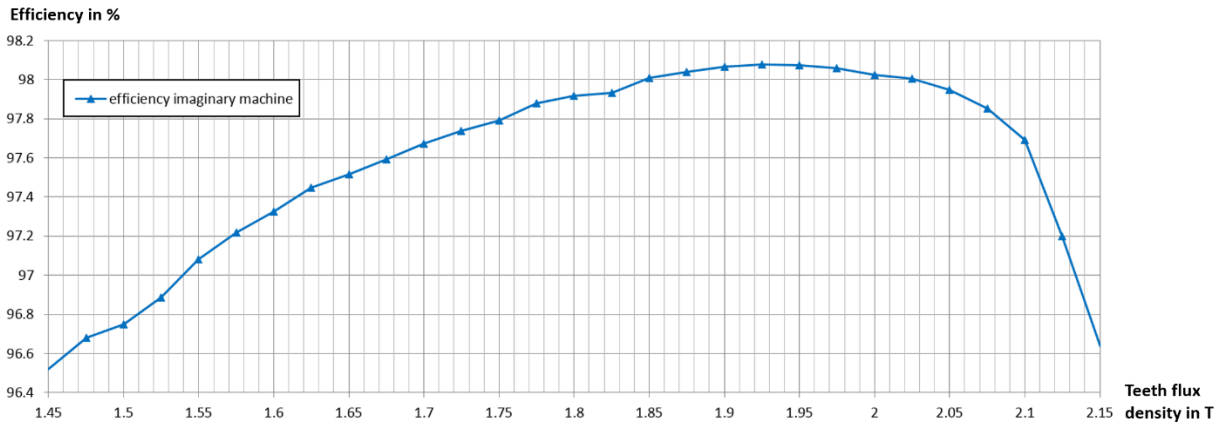


Figure H-1: Parametrized optimization: maximum efficiency reached after optimizations as a function of the imposed teeth flux density for the specifications of the TTP

With the optimization results for each point of the parametrized optimization in Figure H-1, it is possible to get the value of each parameter that should be discrete. For example, the number of poles, the number of slots per pole and per phase, the number of parallel paths, the coil span reduction, the number of conductors per slot, and the number of strands per conductor. The number of poles and the number of slots per pole and per phase for the imaginary machines of the parametrized optimization in Figure H-1 can be seen in Figure H-2.

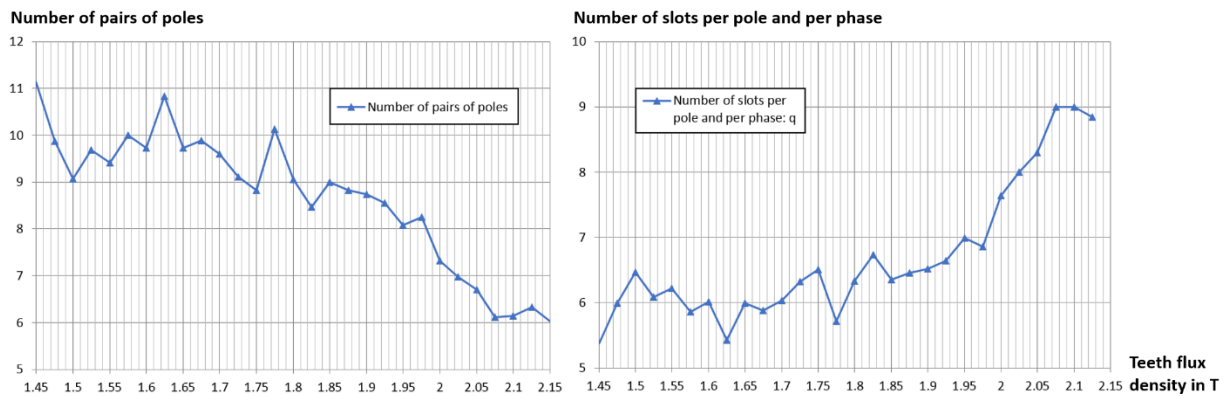


Figure H-2: Evolution of two discrete parameters (p and q) of the imaginary machines of the parametrized optimization from Figure H-1

It is then possible to relaunch the parametrized optimization. This time, instead of being degrees of liberties, the discrete parameters are imposed to the closest integer from the imaginary machine results. Taking the example of the number of pole pairs and number of slots per pole and per phase that are given in Figure H-2, we obtain Figure H-3.

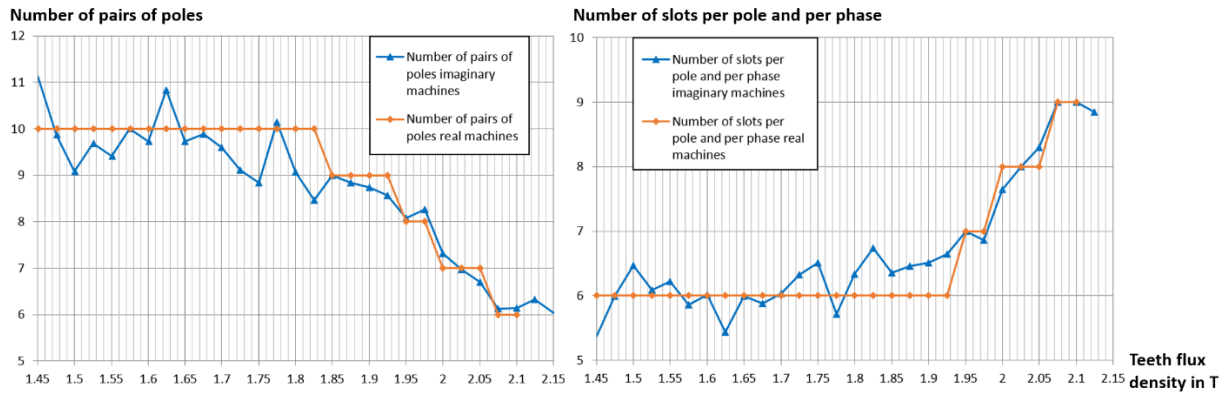


Figure H-3: Evolution of two discrete parameters (p and q) for the imaginary machines and real machines of the parametrized optimization from Figure H-5

The optimizations for the parametrized optimization with real machines are made using the same advice to avoid local optimums as for the imaginary machines: many optimizations are launched with slightly different 1st step, only the best result is selected. Since the number of turns in series are fixed, the feeding voltage is freed from meeting the maximum voltage of the power converter (**6600 V**). The voltage can now be lower than **6600 V** if it needs to be. This way, the optimization algorithm will be able to adapt the voltage to the new number of turns in series. Without freeing the voltage, the optimum efficiencies of the real machines would not follow nearly as well the optimum efficiencies of the imaginary machines. It is interesting to see the voltage evolution in Figure H-4. For some points of the parametrized optimization, the voltage of the real machines will use the degree of liberty and be lower than the voltage of imaginary machines. For other points, the voltage of real machines will reach the maximum value (it would probably higher than **6600 V** if it was possible).

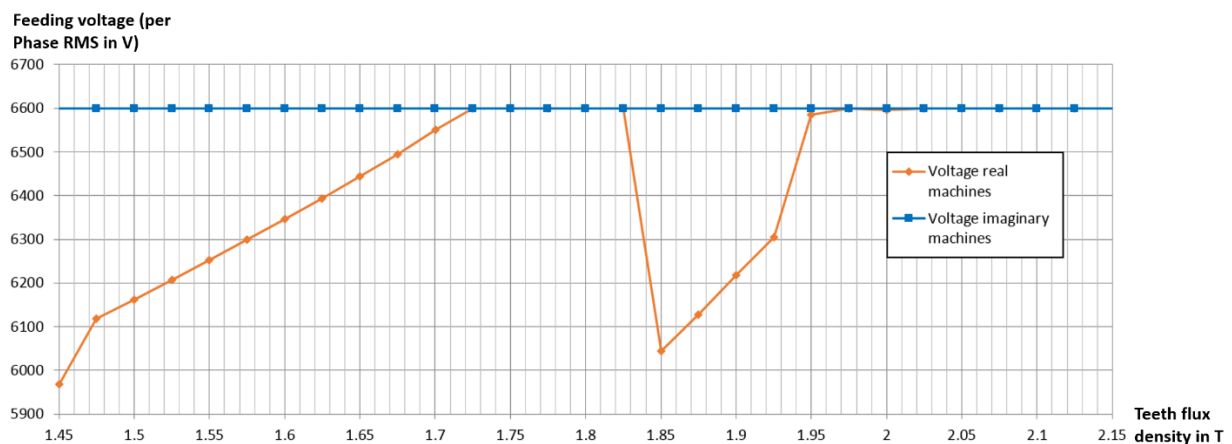


Figure H-4: Evolution of the feeding voltage for the imaginary machines and real machines of the parametrized optimization from Figure H-5

Finally, the parametrized optimization is obtained for the real machines. It can be compared to the parametrized optimization of the imaginary machines. As it can be seen in Figure H-5 (identical to Figure II-6), the parametrized optimization of the real machines is very close to the imaginary machine one. The difference between the two curves is inferior to 0.1 % most of the time and reached a maximum of 0.4 % difference in efficiency. For the points with a 0.4 % difference in efficiency, it might be because the optimum found for the real machines is a local optimum.

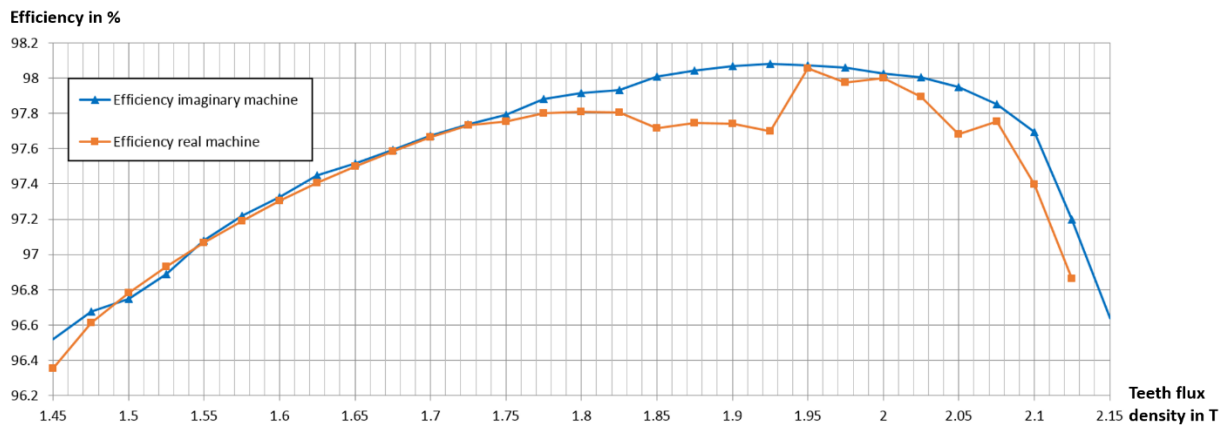


Figure H-5: Parametrized optimization: maximum efficiency reached after optimizations as a function of the imposed teeth flux density for the specifications of the TTP (identical to Figure II-6)

H.2 Analyses of the results and interpretations

To begin with, many optimizations lead to solutions meeting all the constraints. The efficiency (parameter: *eff* in Table H-2) went from 90.5% (with the analytical design given in Table II-3, p 55) to a bit over 98 %. Several constraints limits were reached, if we were to modify these constraints the maximal efficiency could change.

The machine diameter and length (*dOut* and *l*) went from the values calculated in the first sizing (see Table II-3) to their maximum constraint: $dOut = 5.2$ and $l = 2.1$). This is not surprising since increasing the copper and iron sheets size diminishes the losses. In other optimizations, the maximal constraints for the length of the machine were much stricter and did not lead to any machine meeting all the constraints. To decrease the rotor resistance, the maximal width of the copper short-circuit ring was also reached (*ban* and *han*).

The algorithm also diminished the airgap radial width to the minimum width specified ($wGap = 0.01$). This is not surprising neither: when the airgap diminishes, the magnetizing currents diminish too. The minimum airgap radial width is generally set by mechanical and production limits. Diminishing the airgap radial width also increases the iron losses due to the teeth harmonics, but the analytical model does not take these losses into account.

The initial power factor (*cosPhi*) was very low: $cosPhi = 0.277$. During the optimization, the minimal power factor constraint of $cosPhi = 0.8$ was reached.

The slip of such a big IM (*s*) was estimated to be around 2 %, to increase the efficiency, the algorithm diminished it close to 1 %. This is not surprising: as shown in equation (166), in APPENDIX C dealing with the IM, the efficiency cannot be higher than $1 - s$. A minimal slip is still required for currents to develop in the rotor squirrel cage and electromagnetic interaction to appear.

The geometry obtained from the first sizing was not delivering the rated power output (*Pu*) of the specifications. The initial design was reaching 4.8 MW and the minimal constraint of 20 MW was achieved by the optimization.

The best efficiency for the specifications of the TTP was found for very high saturation. This is linked to the fact that the machine rotates very slowly, which leads to low iron losses. Despite this optimum when to tooth saturation is above 1.9 T, we will select the design where the teeth flux

density is much closer to usual machines: $1.7 T$. This design has many advantages: the efficiency is only slightly lower than the best efficiency (97.7 % instead of 98.1 %), the stator voltage is only slightly below the rated voltage of the power converter (6550 V for a power converter rated at 6600 V). Thus, the power converter for this design will only need to be oversized by a few percent. There will be a small margin to increase the voltage and the machine saturation during operation in any case.

In the following part, we will give the full results of the optimization that was done to maximize the efficiency of the IM in the parametrized optimization of Figure H-5, with a flux density in the teeth of $1.7 T$. The constraints were fixed for the specifications of the TTP given in Table II-2, p 53, and based on experience.

H.3 Results of the optimizations for one set of constraints

In Table H-1 and Table H-2, the inputs and outputs of the optimization leading to the best efficiency are presented for the first and the last iterations.

Table H-1: Inputs parameters of an optimization with the semi-analytical model of APPENDIX F. In gray, the parameters that were fixed, in red, the parameters that reached the constraint upper limit, and in blue the parameters that reached the constraint lower limit.

Inputs parameters	First iteration	Last iteration
alphrot	0.0038	0.0038
alphsta	0.0038	0.0038
ban	0.04	0.1
bar	0.01608	0.01423
bas	0.015	0.02211
coefcrs	0.0	0.0
coefl	0.0	0.0
coefpu	-1.0	-1.0
coefrend	1000000.0	1000000.0
coefweight	1.0	1.0
densSheetsR	8600.0	8600.0
densSheetsS	8600.0	8600.0
densSteel	8600.0	8600.0
dOut	5.2	5.2
f	10.0	10.0
han	0.13	0.2
her	0.0	0.0
hes	0.01208	0.01208
hfr	0.11	0.1331
hfs	0.16792	0.2273
hRotorYoke	0.32	0.1660
hStatorYoke	0.195	0.1310
KWKR	1.8	1.8
KWKS	1.2	1.2
I	1.795	2.1
lambda	1.0	1.0
m	3.0	3.0

mainInsulR	0.0024	0.0024
mainInsulS	0.0024	0.0024
ncps	12.0	12.0
npp	3.0	3.0
nr	490.0	490.0
ns	360.0	360.0
nSkew	1.0	1.0
nspc	4.0	4.0
pa	20.0	20.0
priceCu	0.0	0.0
priceRendPercentage	0.0	0.0
priceShaftSteel	0.0	0.0
priceSheetsR	0.0	0.0
priceSheetsS	0.0	0.0
recs	2.0	2.0
rho	1.7E-8	1.7E-8
rhoal	1.7E-8	1.7E-8
s	0.02	0.01175
smecav	0.0	0.0
spacer	0.0053	0.0053
strandInsulS	2.0E-4	2.0E-4
trot	105.0	105.0
tsta	100.0	100.0
v	6600.0	6551.0
wGap	0.01	0.01
wStackIronR	0.06	0.06
wStackIronS	0.06	0.06
wVentR	0.0080	0.0080
wVentS	0.0070	0.0070

Table H-2: Outputs parameters of an optimization of the semi-analytical model of APPENDIX F. In red, the parameters that reached the constraint upper limit, and in blue the parameters that reached the constraint lower limit.

Outputs parameters	First iteration	Last iteration
a	0.0052	0.0200
ag	1.355	1.430
aSlotR	0.0018	0.00189
aSlotS	0.0027	0.00529
ather	0.0000	0.0000
athes	1.504	61.73
athfr	24601	368.8
athfs	17.06	395.44
bb	0.0113	0.0094310
bcra	0.5331	1.0000
bcsa	0.8626	1.2500

be	0.0161	0.01423
bmaxAG	0.5855	0.6315
btmrab	2.101	1.496
btmrcd	2.287	1.598
btmsab	1.139	1.689
btmscd	1.071	1.520
btra	2.101	1.496
btrb	2.101	1.496
btrc	2.101	1.496
btrd	2.474	1.700
btsa	1.145	1.700
btsb	1.134	1.679
btsc	1.134	1.679
btsd	1.007	1.361
cosphi	0.5570	0.8000
dam	4.320	4.306
denc	18.0	18.0
dIn	4.450	4.459
dInR	3.570	3.841
dOutR	4.430	4.439
dspan	0.6287	0.6226
eff	0.9053	0.9766
epsilon	0.0000	1.0E-10
epsp	0.5697	0.5455
fills	0.3396	0.5878
fob	-19 128 661	-19 989 809
fob_easy	362 870	131 827
fob_rend	905 274	976 633
fob_weight	268 145	108 460
hBarR	0.1052	0.1283
hbarS	0.0189	0.01755
hreffp	0.1052	0.1283
hStrandS	0.0013	0.008373
htr	0.1100	0.1331
hts	0.1800	0.2394
ib	1460	1 211
imc	0.2953	0.4260
ironLosses	4 119	7 374
is	1916	1 302
jrs	2 929 577	2 769 139
js	8 357 123	1 673 776

k	1.097	1.252
kc	1.318	1.362
kci	2.381	2.767
kcR	1.195	1.125
kcS	1.103	1.211
kic	1.010	1.017
krr	1.009	1.008
ks	0.9131	0.9698
ksat	5.019	1.138
kSkew	0.9996	0.9993
kSlotRhw	6.841	9.354
kSlotShw	12.000	10.83
kToothSlotR	1.984	3.000
kToothSlotS	3.931	2.520
kwR	1.0	1.0
kwS	0.9134	0.9416
kx	0.9973	0.9978
kxr	0.0001	1.611E-4
kxs	0.2500	0.3094
lambdaEndr	4.185	2.859
lambdaEnds	2.751	1.879
lambdaaos	0.2800	0.3309
lambdaSlotR	2.324	3.167
lambdaSlotS	1.788	1.241
lBarR	0.0113	0.009431
LEndWind	1.200	1.255
Li	1.745	2.041
LirR	1.480	1.731
LirS	1.502	1.755
lry	0.3395	0.3147
lStrandS	0.0042	0.007784
lsy	0.4368	0.3981
LTu	3.590	4.2
LTurn	5.989	6.709
muz	0.0000	1.257E-6
nig	6.142	6.843
nirt	24.601	368.8
niry	94.96	149.6
nist	1.268	457.2
nisy	30.41	82.00
nsr	0.5000	0.5000

ntsppS	240.0	240.0
nVentR	30.0	30.0
nVentS	30.0	30.0
nz	3.445	5.032
orr	0.0161	0.01423
os	0.0150	0.02211
p	9.0000	10.0
pabs	21 130 236	20 468 089
phip	0.5051	0.5747
pjour	390 381	237 574
pjous	1 607 075	233 332
pmecav	0.0000	0.0000
PriceRend	0.0000	0.0000
priceTot	0.0000	0.0000
Pt	19 128 661	19 989 809
Pu	19 128 661	19 989 809
q	7.0000	6.0
rb	0.0000	3.903E-5
rhot	0.0000	2.217E-8
rm	15 739	13547
rr	0.0001	4.312E-5
rrs	0.0610	0.05400
rrsSlip	3.052	4.598
rs	0.1459	0.04589
rShoCir	0.0000	1.891E-6
rspp	0.2919	0.1377
sbkra	0.4737	0.2874
sbcra	0.2928	0.2299
sbtra	0.3776	0.6034
sbtrb	0.3776	0.6034
sbtrc	0.3776	0.6034
sbtrd	0.3207	0.5310
sbtsa	0.6932	0.5310
sbtsb	0.6995	0.5377
sbtsd	0.6995	0.5377
sbtsd	0.7875	0.6631
scr	0.0012	0.001210
scrB	0.0012	0.001210
scre	0.0009	0.003111
scSlotS	0.0009	0.003111
scStrS	0.0000	6.482E-5

sigmaNuS_outputCpp	0.0019	0.003136
span	17.0000	16.0
taup	0.7767	0.7005
tauSlotR	0.0480	0.05692
tauSlotS	0.0740	0.07783
Tem	3 106 552	3 219 288
tme cav	0.0000	0.0
tr	0.0240	0.02846
ts	0.0370	0.03891
Tu	3 106 552	3 219 288
vairgapNew	4 648	5 770
vairgapSolNR	4 648	5 770
w	56.55	62.83
weight	268 145	108 460
weightCu	11 723	20 392
weightShaft	154 522	209 260
weightSheetsR	48 683	38 518
weightSheetsS	53 218	49 551
wsm	6.283	6.283
wToothS	0.0220	0.01681
xendr	0.0005	4.608E-4
xends	0.6877	0.5815
xm	26.14	25.73
xmk	5.209	22.62
xos	0.0700	0.1024
xr	0.0008	9.712E-4
xrs	0.9060	1.252
xs	1.205	1.068
xskew	0.0207	0.03529
xSlotR	0.0003	5.104E-4
xSlotS	0.4469	0.3839
z_imag	2.861	3.019
z_real	1.919	4.026
zm_imag	5.209	22.62
zm_real	0.0017	0.03777
zr_imag	0.9060	1.252
zr_real	3.052	4.598
zram_imag	1.657	1.953
zram_real	1.773	3.981
zs_imag	1.205	1.068
zs_real	0.1459	0.04589

H.4 Evolution of a few interesting parameters during the optimization

Cades allows access to the evolution of parameters during the optimization process. Figure H-6, Figure H-7, and Figure H-8 show how the power factor, the slip, and the efficiency evolved during the optimization presented in Table H-1 and Table H-2.

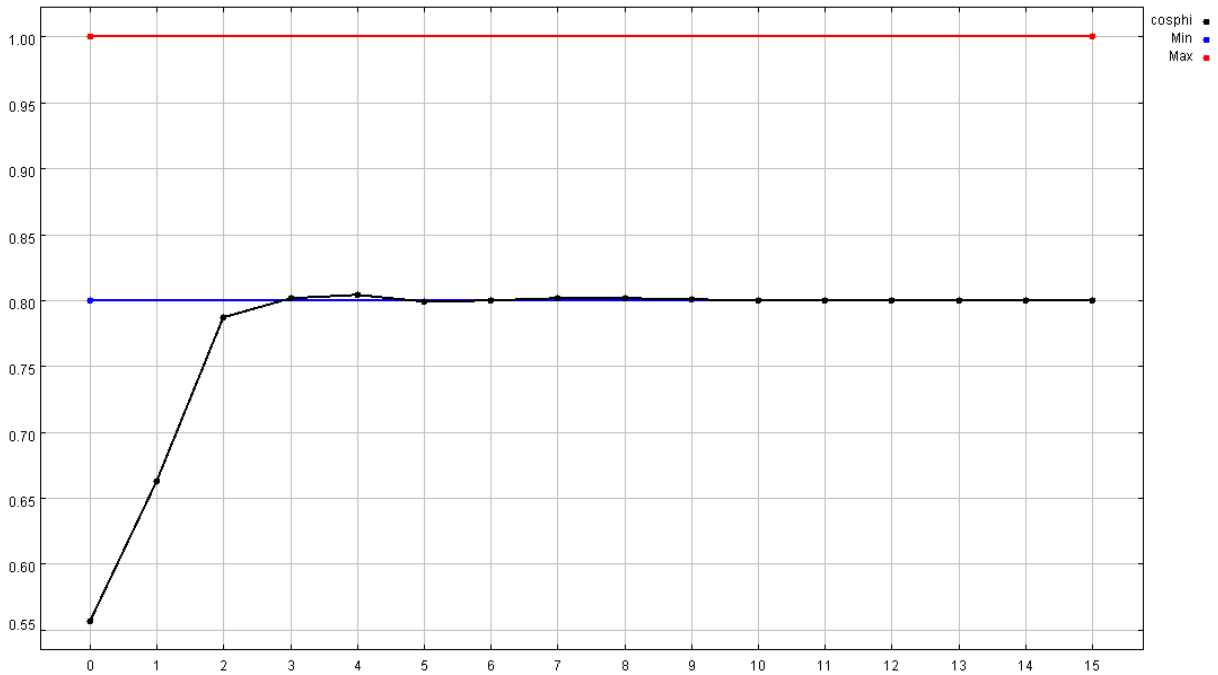


Figure H-6: Evolution of the power factor of the IM depending on the iteration of the optimization. The red line is the upper limit constraint and the blue line is the lower limit constraint.

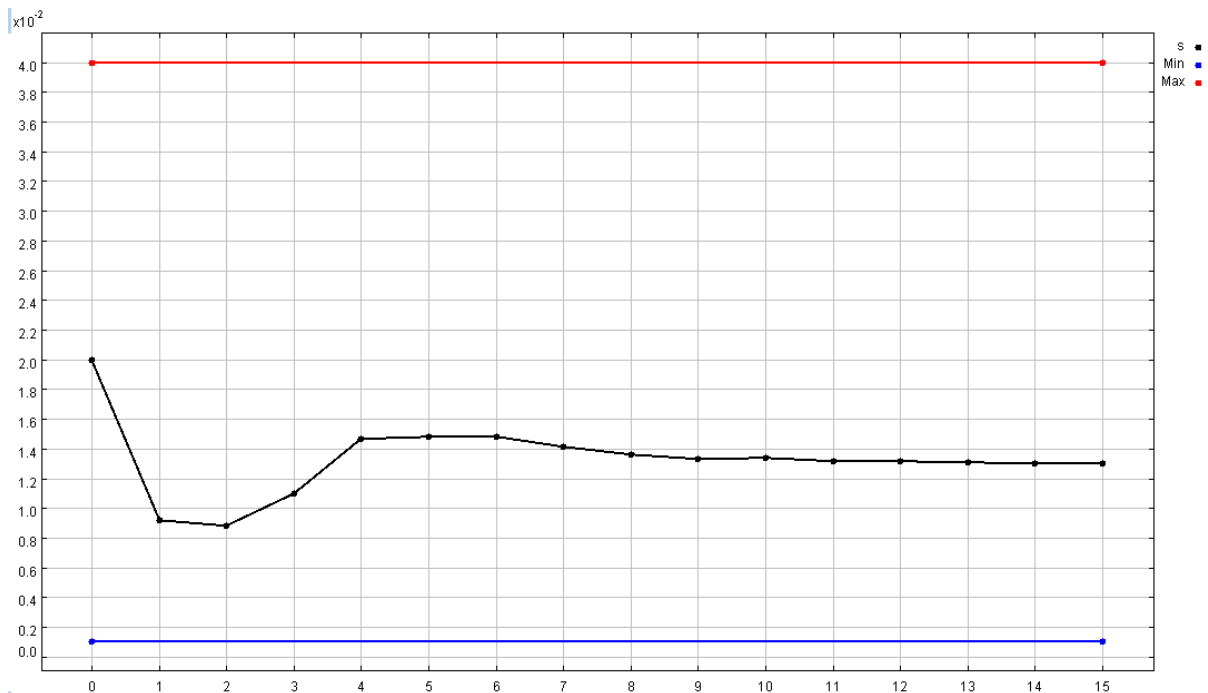


Figure H-7: Evolution of the slip of the IM depending on the iteration of the optimization. The red line is the upper limit constraint and the blue line is the lower limit constraint.

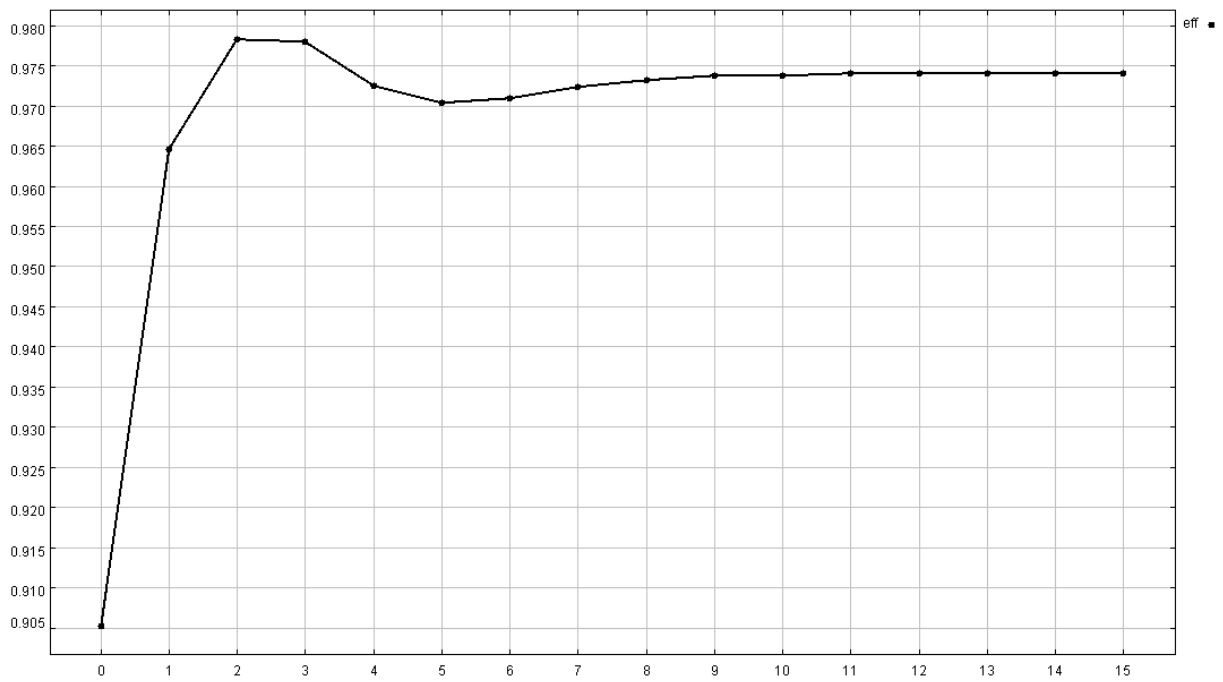


Figure H-8: Evolution of the efficiency of the IM depending on the iteration of the optimization. The red line is the upper limit constraint and the blue line is the lower limit constraint.

APPENDIX I.

Harmonic analyses of a BDFM

In the harmonic analysis of a BDFM, in III.2, p 76, the harmonics tables were only presented with the fundamentals to minimize the table sizes. In this appendix, the tables presented for the harmonic analysis of a BDFM will be reported with more information (with harmonics with amplitudes as small as 5 % of the main harmonic). The analysis of the nested-loops rotor impact on the airgap flux density harmonic, but also the rotor position, and saturation can be found in III.2.

Table I-1: Harmonic analysis of the flux density in the airgap due to the PW, an extension of Table III-2, p 79.

PW voltage: 100 V, frequency: 100 Hz, rotor nested-loops in open-circuit, rotor speed: 750 rpm				
Harmonic Spatial Order	Amplitude (T) / (pu): Table I-1 reference		Phase (Rad)	Frequency (Hz)
6	0.00307	1.000	2.585	100
114	0.00023	0.075	-2.585	1400
126	0.00023	0.075	2.584	1600
138	0.00034	0.112	-2.585	-100
150	0.00017	0.055	2.584	100

Table I-2: Harmonic analysis of the flux density in the airgap due to the CW, an extension of Table III-3, p 79.

CW voltage: 40 V, frequency: 25 Hz, rotor nested-loops in open-circuit, rotor speed: 750 rpm				
Harmonic Spatial Order	Amplitude (T) / (pu): Table I-1 reference		Phase (Rad)	Frequency (Hz)
4	0.00386	1.257	-2.106	25
116	0.00029	0.094	2.106	1475
124	0.00029	0.095	-2.107	1525
140	0.00039	0.128	2.106	-25
148	0.00024	0.080	-2.107	25

Table I-3: Harmonic analysis of the flux density in the airgap due to the PW and nested-loops interactions, an extension of Table III-4, p 80.

PW voltage: 100 V, frequency: 100 Hz, CW in open-circuit, rotor speed: 750 rpm				
Harmonic Spatial Order	Amplitude (T) / (pu): Table I-1 reference		Phase (Rad)	Frequency (Hz)
4	0.001994	0.650	-2.543	25
6	0.002755	0.898	2.589	100
14	0.000325	0.106	0.699	150
30	0.000165	0.054	-2.573	-100
116	0.000203	0.066	2.543	1475
126	0.000267	0.087	2.577	1600
138	0.000359	0.117	-2.582	-100
140	0.000164	0.053	2.543	-25
148	0.000161	0.053	-2.544	25

Table I-4: Harmonic analysis of the flux density in the airgap due to the CW and nested-loops interactions, an extension of Table III-5, p 80.

CW voltage: 40 V, frequency: 25 Hz, PW in open-circuit, rotor speed: 750 rpm				
Harmonic Spatial Order	Amplitude (T) / (pu): Table I-1 reference		Phase (Rad)	Frequency (Hz)
4	0.00369	1.202	-2.114	25
6	0.00378	1.233	2.049	100
16	0.00051	0.165	1.962	225
20	0.00027	0.088	-1.074	-25
26	0.00019	0.063	1.901	350
114	0.00044	0.144	-2.049	1400
124	0.00039	0.128	-2.094	1525
138	0.00031	0.102	-2.050	-100
140	0.00046	0.152	2.100	-25
150	0.00030	0.082	2.048	100

Table I-5: Harmonic analysis of the flux density in the airgap due to the PW with the CW in cascaded mode through the nested-loops, an extension of Table III-6, p 80.

PW voltage: 100 V, frequency: 100 Hz, CW in short-circuit, rotor speed: 750 rpm				
Harmonic Spatial Order	Amplitude (T) / (pu): Table I-1 reference		Phase (Rad)	Frequency (Hz)
4	0.000319	0.104	-2.306	25
6	0.001793	0.585	2.703	100
14	0.000531	0.173	0.704	150
16	0.000290	0.095	-0.767	225
20	0.000266	0.087	2.411	-25
24	0.000156	0.051	0.711	275
26	0.000113	0.037	-0.765	350
28	0.000156	0.051	-2.421	25
30	0.000327	0.107	-2.474	-100
42	0.000191	0.062	2.469	100
66	0.000100	0.033	-2.471	-100
106	0.000097	0.031	-0.704	1350
114	0.000171	0.056	0.954	1400
114	0.000104	0.034	2.471	100
116	0.000257	0.084	2.403	1475
124	0.000186	0.061	0.715	1525
126	0.000383	0.125	2.513	1600
138	0.000407	0.133	-2.555	-100
140	0.000134	0.044	-0.703	-25
148	0.000169	0.055	-2.401	25

Table I-6: Harmonic analysis of the flux density in the airgap due to the CW with the PW in cascaded mode through the nested-loops, an extension of Table III-7, p 80.

CW voltage: 40 V, frequency: 25 Hz, PW in short-circuit, rotor speed: 750 rpm				
Harmonic Spatial Order	Amplitude (T) / (pu): Table I-1 reference		Phase (Rad)	Frequency (Hz)
4	0.00339	1.104	-2.146	25
6	0.00200	0.652	1.945	100
14	0.00041	0.135	-1.989	150
16	0.00080	0.260	1.917	225
20	0.00054	0.175	-1.170	-25
26	0.00031	0.100	1.879	350
28	0.00031	0.102	1.160	25
30	0.00033	0.108	1.205	-100
42	0.00019	0.063	-1.208	100
114	0.00060	0.196	-1.939	1400
124	0.00058	0.188	-2.028	1525
126	0.00024	0.077	-1.211	1600
140	0.00060	0.195	2.056	-25
150	0.00038	0.125	1.939	100

Table I-7: Harmonic analysis of the flux density in the airgap during a load case without saturation of the BDFM, an extension of Table III-8, p 81.

PW voltage: 100 V, frequency: 100 Hz, CW voltage: 40 V, frequency: 25 Hz, rotor speed: 750 rpm				
Harmonic Spatial Order	Amplitude (T) / (pu): Table I-1 reference		Phase (Rad)	Frequency (Hz)
4	0.00370	1.207	-2.160	25
6	0.00352	1.149	2.302	100
14	0.00024	0.078	-0.143	150
16	0.00055	0.180	1.682	225
20	0.00032	0.103	-1.538	-25
26	0.00021	0.070	1.624	350
114	0.00044	0.143	-1.843	1400
116	0.00020	0.067	2.906	1475
124	0.00041	0.134	-1.852	1525
126	0.00023	0.074	3.126	1600
138	0.00033	0.109	-2.733	-100
140	0.00048	0.155	1.950	-25
150	0.00030	0.097	1.894	100

Table I-8: Harmonic analysis of the flux density in the airgap due to the PW, an extension of Table III-9, p 81.

PW voltage: 100 V, frequency: 100 Hz, rotor nested-loops in open-circuit, rotor speed: 750 rpm				
Harmonic Spatial Order	Amplitude (T) / (pu): Table III-2 reference		Phase (Rad)	Frequency (Hz)
6	0.00307 T	1.000 pu	2.585 rad	100 Hz
114	0.00023	0.075	1.604	1400
126	0.00023	0.075	0.490	1600
138	0.00034	0.112	-2.585	-100
150	0.00017	0.055	2.584	100

Table I-9: Harmonic analysis of the flux density in the airgap due to the PW and nested-loops interactions. Rotor position at $t = 0$ is rotated by $+13^\circ$. Extension of Table III-11, p 82.

PW voltage: 100 V, frequency: 100 Hz, CW in open-circuit, rotor speed: 750 rpm				
Harmonic Spatial Order	Amplitude (T) / (pu): Table III-2 reference		Phase (Rad)	Frequency (Hz)
4	0.00199	0.650	1.4711	25
6	0.00276	0.898	2.589	100
14	0.00033	0.106	2.4438	150
30	0.00016	0.054	-2.573	-100
116	0.00020	0.066	2.7175	1475
126	0.00027	0.087	0.48264	1600
138	0.00036	0.117	-2.5823	-100
140	0.00016	0.053	-1.4717	-25
148	0.00016	0.053	1.4705	25

Table I-10: Harmonic analysis of the flux density in the airgap due to the CW and nested-loops interactions. Rotor position at $t = 0$ is rotated by $+13^\circ$. Extension of Table III-12, p 83.

CW voltage: 40 V, frequency: 25 Hz, PW in open-circuit, rotor speed: 750 rpm				
Harmonic Spatial Order	Amplitude (T) / (pu): Table III-2 reference		Phase (Rad)	Frequency (Hz)
4	0.00369	1.202	-2.114	25
6	0.00378	1.233	-0.220	100
16	0.00051	0.165	-2.576	225
20	0.00027	0.088	-1.074	-25
26	0.00019	0.063	1.377	350
114	0.00044	0.144	-1.875	1400
124	0.00039	0.128	2.095	1525
138	0.00031	0.102	0.219	-100
140	0.00046	0.152	2.100	-25
150	0.00030	0.099	-0.221	100

Table I-11: Harmonic analysis of the flux density in the airgap due to the PW with the CW in cascaded mode through the nested-loops. Rotor position at $t = 0$ is rotated by $+13^\circ$. Extension of Table III-13, p 83.

PW voltage: 100 V, frequency: 100 Hz, CW in short-circuit, rotor speed: 750 rpm				
Harmonic Spatial Order	Amplitude (T) / (pu): Table III-2 reference		Phase (Rad)	Frequency (Hz)
4	0.00032	0.104	1.708	25
6	0.00179	0.585	2.703	100
14	0.00053	0.173	2.449	150
16	0.00029	0.095	-3.036	225
20	0.00027	0.087	-1.604	-25
24	0.00016	0.051	0.187	275
26	0.00011	0.037	0.980	350
28	0.00016	0.051	1.594	25
30	0.00033	0.107	-2.474	-100
42	0.00019	0.062	2.469	100
66	0.00010	0.033	-2.472	-100
106	0.00010	0.031	1.740	1350
114	0.00017	0.056	-1.140	1400
114	0.00010	0.034	2.471	100
116	0.00026	0.084	2.578	1475
124	0.00019	0.061	2.635	1525
126	0.00038	0.125	0.419	1600
138	0.00041	0.133	-2.555	-100
140	0.00013	0.044	1.566	-25
148	0.00017	0.055	1.614	25

Table I-12: Harmonic analysis of the flux density in the airgap due to the CW with the PW in cascaded mode through the nested-loops. Rotor position at $t = 0$ is rotated by $+13^\circ$. Extension of Table III-14, p 83.

CW voltage: 40 V, frequency: 25 Hz, PW in short-circuit, rotor speed: 750 rpm				
Harmonic Spatial Order	Amplitude (T) / (pu): Table III-2 reference		Phase (Rad)	Frequency (Hz)
4	0.00339	1.104	-2.146	25
6	0.00200	0.652	-0.324	100
14	0.00041	0.135	2.025	150
16	0.00080	0.260	-2.621	225
20	0.00054	0.175	-1.170	-25
26	0.00031	0.100	1.355	350
28	0.00031	0.102	1.160	25
30	0.00033	0.108	-2.809	-100
42	0.00019	0.063	2.806	100
114	0.00060	0.196	-1.764	1400
124	0.00058	0.188	2.161	1525
126	0.00024	0.077	0.709	1600
140	0.00060	0.195	2.056	-25
150	0.00038	0.125	-0.330	100

Table I-13: Harmonic analysis of the flux density in the airgap during a load case without saturation of the BDFM. Rotor position at $t = 0$ is rotated by $+13^\circ$. Extension of Table III-15, p 84.

PW voltage: 100 V, frequency: 100 Hz, CW voltage: 40 V, frequency: 25 Hz, rotor speed: 750 rpm				
Harmonic Spatial Order	Amplitude (T) / (pu): Table III-2 reference		Phase (Rad)	Frequency (Hz)
4	0.00315	1.027	-2.213	25
6	0.00030	0.098	0.433	100
14	0.00092	0.301	2.264	150
16	0.00107	0.348	-2.731	225
20	0.00023	0.076	1.635	525
20	0.00079	0.256	-1.313	-25
24	0.00030	0.098	-0.058	275
26	0.00041	0.135	1.255	350
28	0.00046	0.150	1.303	25
30	0.00065	0.211	-2.642	-100
34	0.00017	0.057	-2.332	400
36	0.00022	0.072	-1.026	475
42	0.00038	0.124	2.638	100
44	0.00022	0.072	1.834	-25
52	0.00017	0.056	-1.837	25
66	0.00020	0.064	-2.641	-100
78	0.00017	0.055	2.640	100
102	0.00017	0.055	-2.639	-100
104	0.00021	0.070	0.636	1275
106	0.00017	0.055	1.925	1350
114	0.00075	0.244	-1.630	1400
114	0.00020	0.067	2.639	100
116	0.00038	0.125	2.567	1475
124	0.00075	0.244	2.275	1525
124	0.00019	0.061	1.309	25
126	0.00061	0.200	0.530	1600
138	0.00050	0.164	-2.601	-100
140	0.00072	0.235	1.968	-25
148	0.00021	0.068	1.772	25
150	0.00046	0.148	-0.459	100

Table I-14: Harmonic analysis of the flux density in the airgap during a load case without saturation of the BDFM. Extension of Table III-16, p 85.

PW voltage: 17 500 V, frequency: 100 Hz, CW voltage: 7 000 V, frequency: 25 Hz, rotor speed: 750 rpm				
Harmonic Spatial Order	Amplitude (T) / (pu): Table III-2 reference extrapolation if linear		Phase (Rad)	Frequency (Hz)
2	0.050645	0.094	2.8975	-50
4	0.63573	1.184	-2.1605	25
6	0.58894	1.097	2.2993	100
8	0.082959	0.155	-2.7238	175
14	0.1157	0.216	0.83226	150
16	0.054836	0.102	0.17355	225
20	0.044123	0.082	-1.519	-25
114	0.070448	0.131	-1.9733	1400
124	0.075012	0.140	-2.0226	1525
126	0.037987	0.071	2.8274	1600
138	0.055167	0.103	-2.5797	-100
140	0.081748	0.152	2.0629	-25
150	0.047518	0.089	2.0462	100

Table I-15: Harmonic analysis of the flux density in the airgap during a load case without saturation of the BDFM. Extension of Table III-17, p 85.

PW voltage: 30 000 V, frequency: 100 Hz, CW voltage: 12 000 V, frequency: 25 Hz, rotor speed: 750 rpm				
Harmonic Spatial Order	Amplitude (T) / (pu): Table III-2 reference extrapolation if linear		Phase (Rad)	Frequency (Hz)
2	0.12102	0.225	2.6059	-50
4	1.0339	1.926	-2.1804	25
6	0.80702	1.504	2.2866	100
8	0.20951	0.390	-2.5105	175
10	0.091817	0.171	-0.96647	250
14	0.22749	0.424	0.98439	150
16	0.097714	0.182	-0.53439	225
20	0.055343	0.103	-1.229	-25
24	0.077178	0.144	-1.9831	275
114	0.083549	0.156	-1.9197	1400
124	0.13591	0.253	-2.0845	1525
126	0.056838	0.106	2.7416	1600
138	0.0692	0.129	-2.6321	-100
140	0.13331	0.248	2.0884	-25
150	0.052585	0.098	1.9647	100

APPENDIX J.

Determination of the Parameters of the Equivalent Circuit of an Induction Machine Using No-Load and Blocked Rotor Tests.

Tests to determine the parameters of the equivalent scheme of an induction machine are well known. They are reminded in this appendix.

The equivalent scheme of an Induction Machine was given in Figure C-3 and is reminded in Figure J-1:

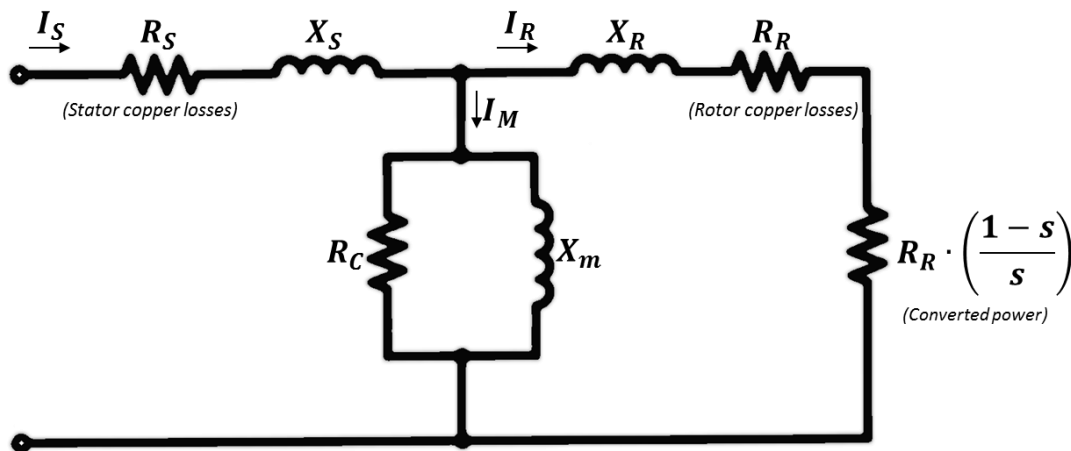


Figure J-1: Equivalent circuit of an Induction Machine with a squirrel cage rotor

In the case of a real machine, the stator resistance R_S could be determined with a DC test. With a DC test, there is no current induced in the rotor and the leakage and magnetizing reactances and the iron losses resistance disappear.

J.1 Determination of the magnetizing inductance and stator leakage reactance: no-load test

The magnetizing reactance X_m cannot be easily separated from the stator leakage reactance X_S . The magnetizing reactance will vary depending on the machine saturation. Saturation is dependent of the flux density in the machine which is linked to the feeding voltage of the stator. Thus, it is interesting to determine the magnetizing reactance as a function of the feeding voltage.

During a no-load test, the rotor rotates at the synchronism speed. The slip is equal to $s = 0$. Since the rotor rotates at the same speed as the magnetic field, there are no induced currents in the rotor cage. This can also be seen in the equivalent circuit: with $s = 0$, the resistance $R_R \cdot \left(\frac{1-s}{s}\right)$ tends toward infinity, so I_R tends toward 0.

The equivalent circuit of a no-load test can be simplified as in Figure J-2:

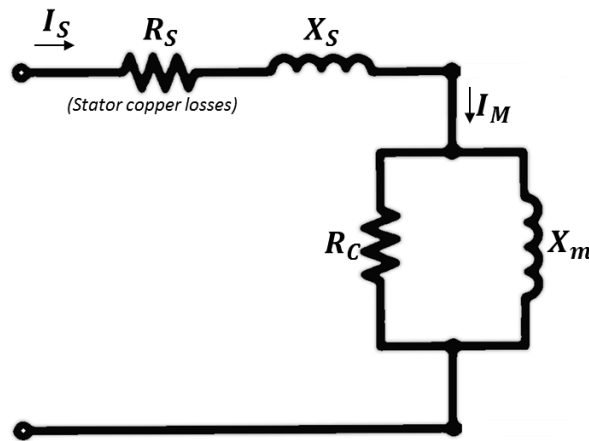


Figure J-2: Simplified equivalent scheme of an Induction Machine during a no-load test ($s = 0$).

From the equivalent scheme in Figure J-2, if the iron losses are neglected, we can write:

$$Q_{NL} = I_{NL}^2 \cdot (X_S + X_m) \quad (175)$$

Q_{NL} is the no-load test reactive power.

I_{NL} is the no-load test current amplitude.

With equation (175), we see that a no-load test allows to determine the sum of the magnetizing reactance X_m and the stator leakage reactance X_S .

The sum of the magnetizing reactance X_m and stator leakage reactance X_S obtained with a no-load test and depending on the stator voltage can be seen in Figure II-5, p 59.

J.2 Determination of the sum of stator and rotor leakage reactance: blocked-rotor test

During a blocked-rotor test, the slip of the IM is equal to $s = 1$. The magnetizing reactance becomes big in comparison to the rotor reactance (most of the time there is at least a factor 10: 1 between the magnetizing reactance X_m and the rotor leakage reactance X_R). In the equivalent circuit representation, the current is not passing anymore in the magnetizing branch and passes through the rotor. The equivalent circuit can be simplified as in Figure J-3.

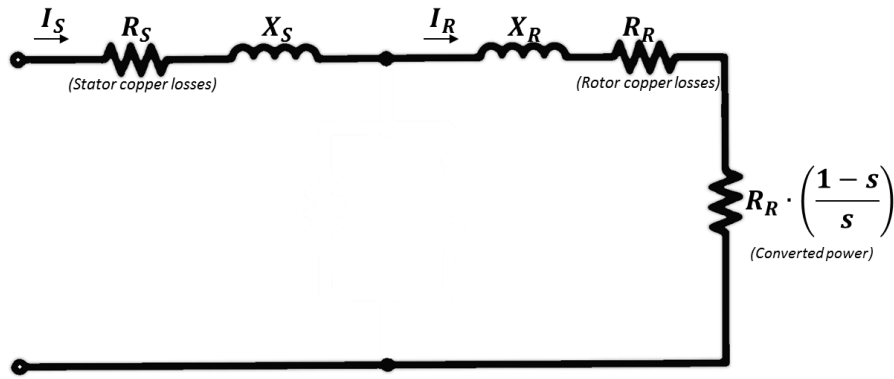


Figure J-3 Simplified equivalent scheme of an IM during a blocked-rotor test ($s = 1$).

Since $s = 1$, the resistance to express the converter power is equal to $R_R \cdot \left(\frac{1-s}{s}\right) = 0$

From the simplified equivalent scheme, it is possible to write the following equation:

$$P_{BR} = I_{BR}^2 \cdot (R_S + R_R) \quad (176)$$

P_{BR} is the active power measured during the blocked-rotor test.

I_{BR} is the current amplitude measured during the blocked-rotor test.

Equation (176) allows to determine the sum of the stator resistance R_S and rotor resistance R_R in the equivalent scheme. Since the stator resistance could already be determined with a DC test, the rotor resistance of the equivalent circuit can be determined with this equation.

The total reactance of the blocked-rotor test can be expressed from the equivalent circuit parameters, as in equation (177):

$$Z_{BR} = \sqrt{(R_S + R_R)^2 + (X_S + X_R)^2} \quad (177)$$

With Z_{BR} the total blocked-rotor reactance.

The total reactance of the blocked-rotor test can also be expressed depending on the blocked-rotor test voltage and current:

$$Z_{BR} = \frac{V_{BR}}{I_{BR}} \quad (178)$$

With V_{BR} the voltage amplitude of the blocked-rotor test.

I_{BR} the current amplitude of the blocked-rotor test.

Combining equations (177) and (178) leads to:

$$X_S + X_R = \sqrt{\frac{V_{BR}^2}{I_{BR}^2} - (R_S + R_R)^2} \quad (179)$$

We could also have written:

$$X_S + X_R = \frac{Q_{BR}}{I_{BR}^2} \quad (180)$$

With Q_{BR} the blocked-rotor test reactive power.

From equation (179) or (180) it is possible to determine the sum of the stator leakage reactance X_S and the rotor leakage reactance X_R . With the blocked-rotor test, it is not possible to separate the two leakage reactances. It is usual to attribute 50% of the leakage to the stator and 50% to the rotor.

In the analytical model of APPENDIX F, the leakage reactances are considered constant. They do not depend on the flux density in the machine and saturation. But saturation changes the flux path in the machine and has an impact on the leakage reactance.

APPENDIX K.

Determination of the equivalent circuit parameters of the BDFM from electrical tests.

As seen in III.3, p 85, the behavior of the BDFM can be described by an equivalent circuit. In this appendix, it will be described how from a few electrical tests it is possible to determine the parameters of the equivalent circuit. It will then be possible to carry out these tests on FE models or on real machines so as to have a simple electrical circuit, easy to solve, describing the behavior of the machine in the cross-coupling mode. As already explained in III.3.3, p 97, other methods exist for the extraction of the parameters of the equivalent circuit. Their main disadvantage is that these methods use the measurements of the torque ([82]), or use tests at different frequencies ([84] and [85]). The method that will be described here can be performed with the measurements of currents and voltages only. The power winding only needs to be fed at 50 Hz, thus there is no need of a special power converter to implement the tests described in this appendix.

In cross-coupling mode, the electrical circuit derived will stay relevant as long as saturation in the machine will stay comparable to the one during the tests. In fact, the machine saturation will have an impact on the auto and mutual inductances. In the electrical circuit, these changes will impact the leakage inductances and the magnetizing inductances.

In Figure K-1 the per phase equivalent circuit of the BDFM is reminded (Figure K-1 is identical to Figure III-9, p 97).

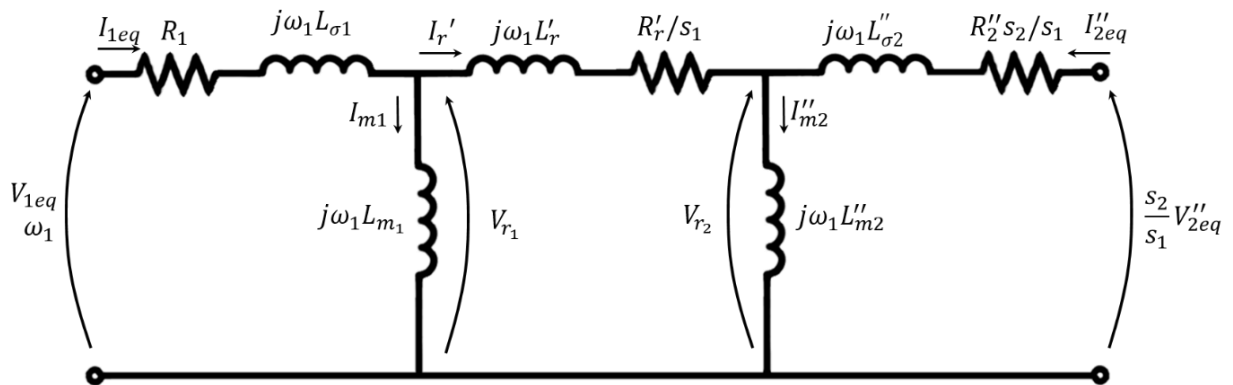


Figure K-1: Per phase equivalent scheme of a BDFM operating in cross-coupling mode. All the parameters, the voltages, and the currents are expressed on the power winding side. Identical to Figure III-9, p 97.

With:

R_1 the resistance of the power winding phase.

$L_{\sigma s1}$ is the leakage inductance of the power winding phase.

L_{m1} is the magnetizing inductance of the power winding phase.

$L'_r = L_r N_1^2$ is the apparent leakage inductance of the rotor expressed in the power winding reference frame.

$R'_r = R_r N_1^2$ is the apparent rotor resistance.

$I'_r = \frac{I_r}{N_1}$ is the rotor apparent current expressed in the power winding reference frame.

$L''_{m2} = \frac{N_1^2}{N_2^2} L_{m2}$ is the apparent magnetizing inductance of the control winding expressed in the power winding reference frame.

$I''_{m2} = \frac{N_2}{N_1} I_{m2}$ is the apparent magnetizing current of the control winding expressed in the power winding reference frame.

$L''_{\sigma s2} = \frac{N_1^2}{N_2^2} L_{\sigma s2}$ is the apparent leakage inductance of the control winding expressed in the power winding reference frame.

$R''_2 = \frac{N_1^2}{N_2^2} R_2$ is the apparent control winding resistance expressed in the power winding reference frame.

$I''_{2eq} = \frac{N_2}{N_1} I_2^* e^{i\angle M_{s2r}}$ is the apparent control winding current expressed in the power winding reference frame.

$V''_{2eq} = \frac{N_1}{N_2} V_2^* e^{i\angle M_{s2r}}$ is the apparent control winding voltage adjusted by the slips and expressed in the power winding reference frame.

On a real BDFM, the values of R_1 and R_2 can be determined with two basic DC tests. During the design, the resistances are also easy to get through straightforward computations, as for example in IV.3.5.3, equation (139), p 148.

To determine the inductances of the equivalent circuit we will use special tests that will allow us to simplify the equivalent circuit. Two no load tests and four blocked rotor tests will be done to obtain all the equations for the extraction of the BDFM parameters.

K.1 No load tests

For the no-load tests, it is important to carry them out with the conditions of the cross-coupling state of the BDFM verified. Thus, for the power winding, we want both the rotor to be rotating at the cross-coupling speed (speed condition in equation (34), p 32 reminded in (181)) and at the speed of synchronism for the power winding if it was an asynchronous machine (equation (182)).

So, to be in the no-load test condition, we want the rotation speed to verify the cross-coupling speed condition:

$$\omega_{rm} = \frac{\omega_1 + \omega_2}{p_1 + p_2} \quad (181)$$

And, the synchronism speed condition of the PW:

$$\omega_{rm} = \frac{\omega_1}{p_1} \quad (182)$$

Equations (181) and (182) are met when:

$$\frac{\omega_1}{p_1} = \frac{\omega_1 + \omega_2}{p_1 + p_2} \quad (183)$$

Which leads to:

$$\omega_2 = \omega_1 \cdot \frac{p_2}{p_1} \quad (184)$$

Equation (184) is interesting because it shows that if we are at the cross-coupling speed condition for the BDFM and at the no-load condition for the power winding, then we are also at the no-load condition for the control winding. In fact:

$$\omega_2 = \omega_1 \cdot \frac{p_2}{p_1} \Rightarrow \omega_1 = \omega_2 \cdot \frac{p_1}{p_2} \quad (185)$$

It seems possible to carry out the no-load tests for the machine at the same time for the two windings. This is interesting especially in the case we want to implement these tests in saturated conditions. In fact, saturation in the BDFM arises from the sum of flux density induced by the two windings. It would not be possible to feed only one winding and to get the same saturation as the one obtained in rated conditions.

In the no-load test, the two magnetic fields created by the two stator windings are rotating at the exact same speed which also happens to be the mechanical speed of the rotor.

Since the rotor is rotating at the same speed as the magnetic fields, no currents will arise in the rotor. The equivalent circuit can be simplified as shown in Figure K-2:

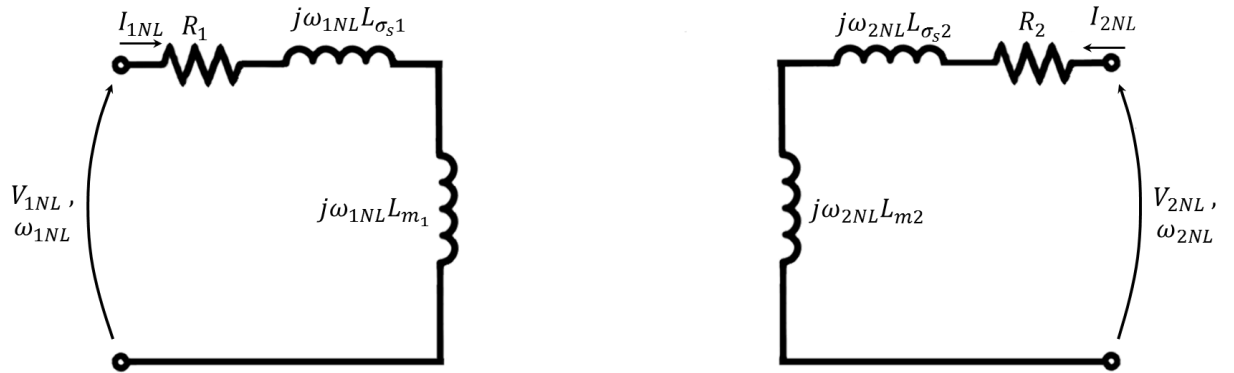


Figure K-2 : Equivalent circuit of the BDFM at no load conditions.

It is interesting to note that for the no-load test, we are not trying to express the results of the CW to the PW side. The magnetizing inductance of the CW will be determined in the CW reference.

From this circuit, we can derive two equations that will give us a link between the sum of the leakage and magnetizing inductances, resistances, and the no-load voltages and no-load currents:

$$\begin{cases} V_{1NL} = I_{1NL} \cdot (R_1 + j(X_{\sigma_s1} + X_{m1})) \\ V_{2NL} = I_{2NL} \cdot (R_2 + j(X_{\sigma_s2} + X_{m2})) \end{cases} \quad (186)$$

To these two equations, we will now add the equations of the blocked rotor test.

K.2 Blocked Rotor test:

In the blocked rotor test, for the equivalent circuit to be relevant, it is once again important to be in the cross-coupling speed condition of the BDFM. This translates into:

$$\omega_{rm} = \frac{\omega_1 + \omega_2}{p_1 + p_2} = 0 \quad (187)$$

Which leads to:

$$\omega_2 = -\omega_1 \quad (188)$$

Four blocked rotor tests will be used to get enough equations to extract all the parameters of the equivalent circuit. To simplify the equivalent circuit, in the first test, the power winding will be fed and the control winding will be short-circuited (self-cascaded mode in blocked rotor test). In the second test, we will have the inverse: the control winding will be fed and the power winding will be short-circuited. Finally, we will also do a blocked rotor test with the power fed and the control opened (induction mode in blocked rotor test) and the last blocked rotor test will be with the control fed and the power in open circuit.

For the first two tests, the short circuit on one size will allow us to use Thevenin and Norton to obtain quickly the equivalent impedance and to solve the system faster.

For the first blocked rotor test, the power winding is fed and the control winding is short-circuited. The equivalent circuit is shown in Figure K-3.

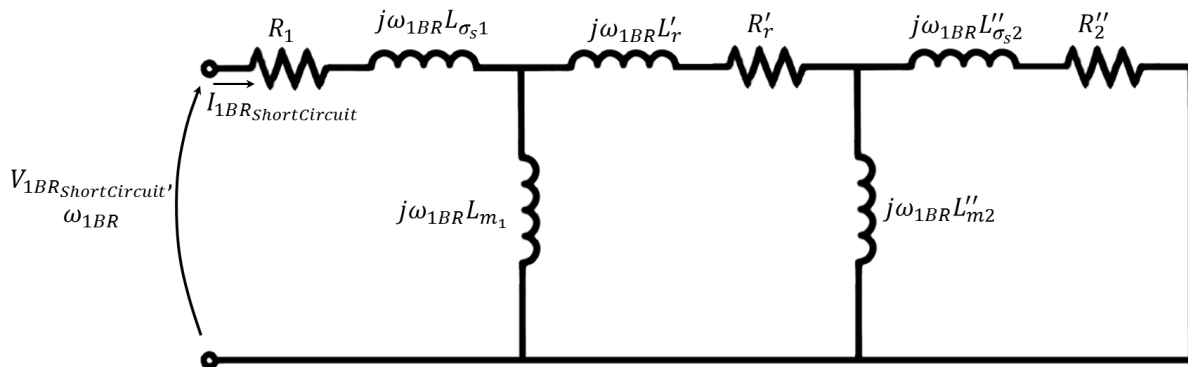


Figure K-3: Equivalent circuit of the BDFM for a blocked rotor test with the control winding short-circuited and with the cross-coupling condition of the BDFM met.

First note: since the control winding is short-circuited, the relation $\omega_2 = -\omega_1$ from equation (188), is unavoidably verified. In fact, in self-cascaded mode, the cross-coupling conditions are automatically met. The short-circuited winding induced current are necessarily meeting the cross-coupling speed condition of the BDFM.

Second note: with a rotor not rotating we have: $s_1 = 1$ and $s_2 = 1$. The equivalent circuit has thus been simplified: the slips do not appear in it anymore.

We will now simplify this equivalent circuit. We will start with Figure K-4 by giving to each branch an equivalent impedance.

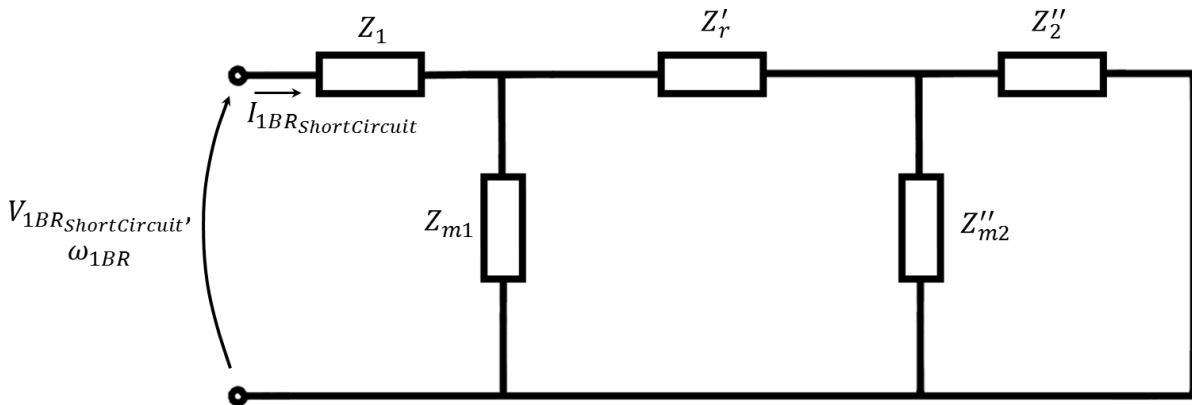


Figure K-4: Equivalent circuit of the BDFM with blocked rotor a control winding short-circuited. Equivalent impedance 1.

The impedances Z''_2 and Z''_{m2} in parallel in Figure K-4 are replaced by the equivalent impedance in Figure K-5.

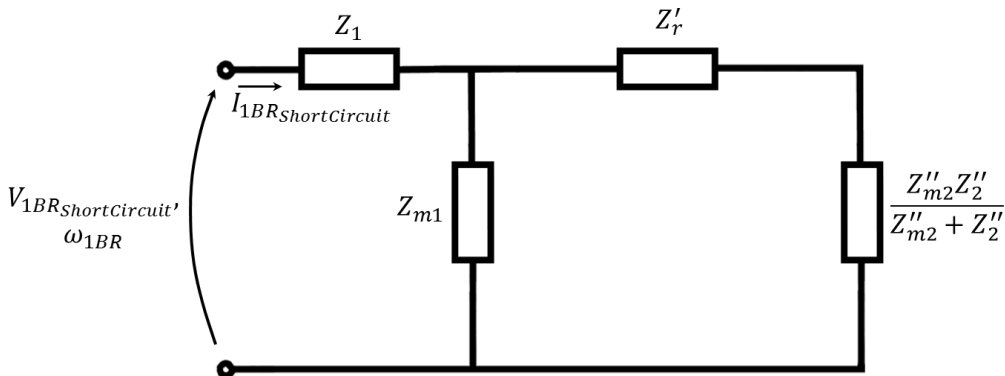


Figure K-5: Equivalent circuit of the BDFM with blocked rotor a control winding short-circuited. Equivalent impedance 2.

The impedances Z''_{m1} and $Z'_r + \frac{Z''_{m2}Z''_2}{Z''_{m2} + Z''_2}$ in parallel in Figure K-5 are replaced by the equivalent impedance in Figure K-6.

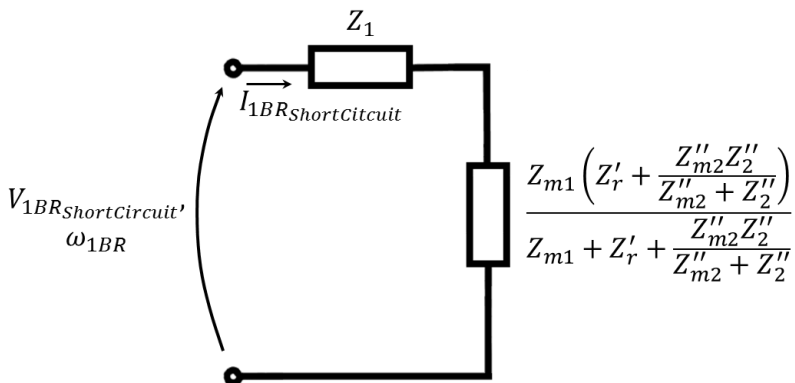


Figure K-6: Equivalent circuit of the BDFM with blocked rotor a control winding short-circuited. Equivalent impedance 3.

With Figure K-6 we can easily write a new equation:

$$V_{1BR_{ShortCircuit}} = I_{1BR_{ShortCircuit}} Z_{eqBR1}$$

With

$$Z_{eqBR1_{ShortCircuit}} = Z_1 + \frac{Z_{m1} \left(Z_r' + \frac{Z_{m2}'' Z_2''}{Z_{m2}'' + Z_2''} \right)}{Z_{m1} + Z_r' + \frac{Z_{m2}'' Z_2''}{Z_{m2}'' + Z_2''}} \quad (189)$$

It is possible to apply the exact same reasoning in the reference frame of the control winding with the second blocked rotor test. In the end, we will have the two equations for the rotor test:

$$\begin{cases} V_{1BR_{ShortCircuit}} = I_{1BR_{ShortCircuit}} \left(Z_1 + \frac{Z_{m1} \left(Z_r' + \frac{Z_{m2}'' Z_2''}{Z_{m2}'' + Z_2''} \right)}{Z_{m1} + Z_r' + \frac{Z_{m2}'' Z_2''}{Z_{m2}'' + Z_2''}} \right) \\ V_{2BR_{ShortCircuit}} = I_{2BR_{ShortCircuit}} \left(Z_2 + \frac{Z_{m2} \left(Z_r' + \frac{Z_{m1}'' Z_1''}{Z_{m1}'' + Z_1''} \right)}{Z_{m2} + Z_r' + \frac{Z_{m1}'' Z_1''}{Z_{m1}'' + Z_1''}} \right) \end{cases} \quad (190)$$

It can be noted that the second equation of (190) was expressed in the reference frame of the CW instead of the reference frame of the PW. To do so one will just need to follow the explanations already given in Figure K-1.

The two equations derived from the two blocked rotor tests with one circuit fed and the other one in open circuit are easier to obtain. In fact, the equivalent circuit will be the same as the one in Figure K-4 without the Z_2'' loop. Using the same simplification technique as shown above it is possible to get to the equations:

$$\begin{cases} V_{1BR_{OpenCircuit}} = I_{1BR_{OpenCircuit}} \left(Z_1 + \frac{Z_{m1} (Z_r' + Z_{m2}'')}{Z_{m1} + Z_r' + Z_{m2}''} \right) \\ V_{2BR_{OpenCircuit}} = I_{2BR_{OpenCircuit}} \left(Z_2 + \frac{Z_{m2} (Z_r' + Z_{m1}'')}{Z_{m2} + Z_r' + Z_{m1}''} \right) \end{cases} \quad (191)$$

To summarize, the equivalent circuit of the BDFM presented in Figure III-9 and reminded in Figure K-1 have 8 unknowns: 3 resistances and 5 inductances.

We have now 6 equations, they can be decomposed in 12 equations: 6 equations for the real part and 6 equations for the imaginary part. During a design, the 2 stator resistances are easy to compute. With a real BDFM, the 2 stator resistances are easy to obtain with DC measurements. With only 6 unknowns left, there are enough independent equations to extract all the parameters of the equivalent circuit.

The 6 independent equations from (186), (190) and (191), are reminded together in (192).

$$\left\{ \begin{array}{l}
V_{1NL} = I_{1NL} \cdot (R_1 + j(X_{\sigma_{s1}} + X_{m1})) \\
V_{2NL} = I_{2NL} \cdot (R_2 + j(X_{\sigma_{s2}} + X_{m2})) \\
V_{1BR_{ShortCircuit}} = I_{1BR_{ShortCircuit}} \left(Z_1 + \frac{Z_{m1} \left(Z'_r + \frac{Z''_{m2} Z''_2}{Z''_{m2} + Z''_2} \right)}{Z_{m1} + Z'_r + \frac{Z''_{m2} Z''_2}{Z''_{m2} + Z''_2}} \right) \\
V_{2BR_{ShortCircuit}} = I_{2BR_{ShortCircuit}} \left(Z_2 + \frac{Z_{m2} \left(Z'_r + \frac{Z''_{m1} Z''_1}{Z''_{m1} + Z''_1} \right)}{Z_{m2} + Z'_r + \frac{Z''_{m1} Z''_1}{Z''_{m1} + Z''_1}} \right) \\
V_{1BR_{OpenCircuit}} = I_{1BR_{OpenCircuit}} \left(Z_1 + \frac{Z_{m1} (Z'_r + Z''_{m2})}{Z_{m1} + Z'_r + Z''_{m2}} \right) \\
V_{2BR_{OpenCircuit}} = I_{2BR_{OpenCircuit}} \left(Z_2 + \frac{Z_{m2} (Z'_r + Z''_{m1})}{Z_{m2} + Z'_r + Z''_{m1}} \right)
\end{array} \right. \quad (192)$$

It can be noticed that if we were to get rid of the denominators in these equations, the system would become of the sixth order. For this reason, we did not try to solve this system directly and obtain a general expression of the solution. However, it is possible to find a solution for this system with analytical values using specific algorithms. For example, a Newton Raphson algorithm. During this PhD, we used the solve function of Excel that gave us quick results. But the solution with Excel was not very flexible. It was hard to debug and to improve because of the way complex equations are written in Excel. We also tried a genetic algorithm in MATLAB. The results obtained with this solution were sufficiently accurate, but were very long to obtain. Finally, the most efficient solution was to create an optimization problem with a 1st order algorithm. The objective function to be minimized was the sum of squared errors of equations in (192). Since the problem had many local optimums, 50 optimizations with random start were launched for each extraction. Since each optimization was only taking seconds, the whole process was only a few minutes long.

APPENDIX L.

Computation of the power state of the BDFM through the electrical state of the equivalent scheme.

In APPENDIX K, the method to extract the equivalent scheme parameters from electrical tests was explained. The equivalent scheme is interesting to compute the state of the machine in function of the inputs voltages of the two windings. The results given by the equivalent scheme should stay accurate if saturation of the BDFM is identical to the one during the electrical tests for the parameters extraction. Of course, this assumption is a strong one. Under nominal load, as soon as the state of the machine will vary, saturation will vary. In fact, under load operation, saturation is due to the sum of the flux induced by the two stators windings.

Anyway, in unsaturated mode, the equivalent scheme parameters will stay the same. The equivalent scheme will then help us to understand the power exchange between the two stators through the rotor.

In the following section, we demonstrate how the power output of the BDFM can be derived from the two stator voltages and the equivalent scheme parameters.

Before starting the demonstration, let's remind ourselves that the equivalent scheme will describe how the BDFM works when it is operated in the cross-coupling conditions (refer to the rotor speed condition in equation (34), p 32). If the speed of the rotor changes, the machines will work as two separates induction machines.

L.1 Resolution of the equivalent scheme electrical state

In the Figure L-1, the equivalent scheme of the BDFM is reminded. Knowing the input voltages and all the parameters of the equivalent scheme it is possible to express all the currents.

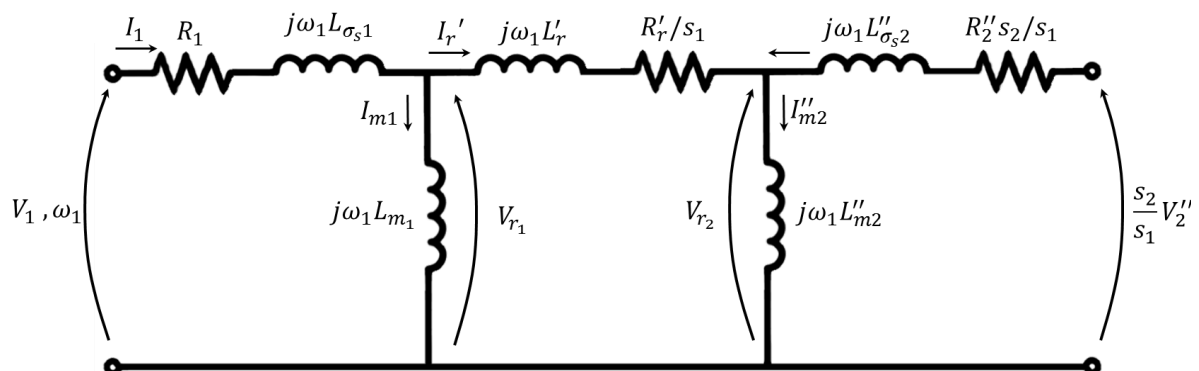


Figure L-1: Per phase equivalent scheme of a BDFM operating at the cross-coupling speed. All the parameters are expressed on the power winding side. This equivalent scheme and the expression of the parameters on the power winding side was already presented in Figure I.

To simplify the expression of the equation for the resolution all the parameters in series will be expressed as one impedance as shown in Figure L-2:

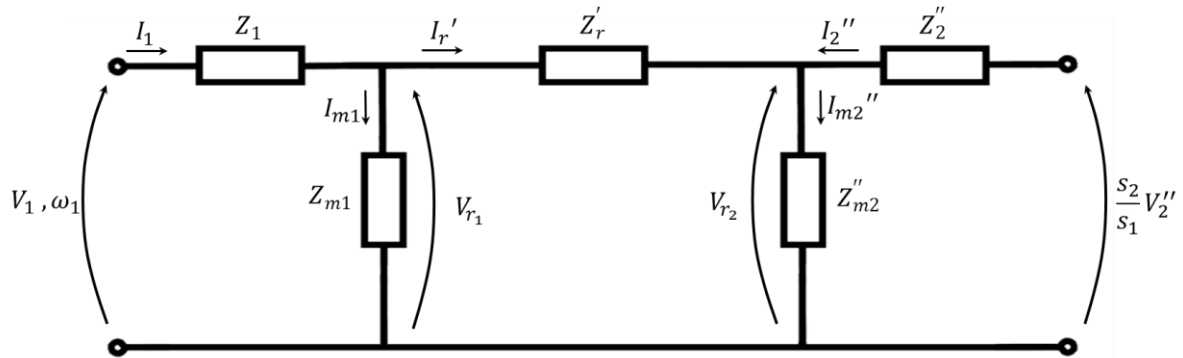


Figure L-2: Equivalent scheme of the BDFM expressed in the power winding reference frame.

In the Figure L-2,

$$Z_1 = R_1 + j\omega_1 L_{\sigma s1}$$

$$Z_{m1} = j\omega_1 L_{m1}$$

$$Z'_r = \frac{R'_r}{s_1} + j\omega_1 L'_r$$

$$Z''_{m2} = j\omega_1 L''_{\sigma s2}$$

$$Z''_2 = R''_2 \frac{s_2}{s_1} + j\omega_1 L''_{\sigma s2}$$

Note: if the BDFM is operated in cross-coupling mode, the voltages of the two windings in the equivalent scheme have the same frequency if they are expressed in the same reference frame (either the power side or the control side).

We will now use the equivalent circuit of Figure L-2 to determine the electrical state of the equivalent scheme from the two stator voltages. The expressions of the equivalent parameters are known. The five unknowns are: the currents I_1 , I_{m1} , I'_r , I''_{m2} , and I''_2 . From the equivalent circuit, using the Kirchhoff law it is possible to write five equations:

$$\begin{cases} V_{1eq} = Z_1 I_{1eq} + Z_{m1} I_{m1} & (1) \\ \frac{s_2}{s_1} V_{2eq} = Z''_2 I''_{2eq} + Z''_{m2} I''_{m2} & (2) \\ Z_{m1} I_{m1} = I'_r Z'_r + Z''_{m2} I''_{m2} & (3) \\ I_{1eq} = I'_r + I_{m1} & (4) \\ I''_{2eq} + I'_r = I''_{m2} & (5) \end{cases} \quad (193)$$

Using equation (4) and (5) into (3) it is possible to eliminate I_{m1} and I''_{m2} :

(3) becomes:

$$Z_{m1} (I_{1eq} - I'_r) = I'_r Z'_r + Z''_{m2} (I'_r + I''_{2eq}) \quad (194)$$

With the previous equation, I'_r can be expressed depending on I_{1eq} and I''_{2eq} . This will allow us to replace I'_r in the equations (1) and (2). Thus, we will have a problem of two equations and two unknowns.

$$I'_r = \frac{I_{1eq}Z_{m1} - I''_{2eq}Z''_{m2}}{Z_{m1} + Z'_r + Z''_{m2}} \quad (195)$$

The problem now becomes:

$$\begin{cases} V_{1eq} = Z_1 I_{1eq} + Z_{m1} \cdot \left(I_{1eq} - \frac{I_{1eq}Z_{m1} - I''_{2eq}Z''_{m2}}{Z_{m1} + Z'_r + Z''_{m2}} \right) & (1) \\ \frac{s_2}{s_1} V''_{2eq} = Z''_2 I''_{2eq} + Z''_{m2} \cdot \left(I''_{2eq} + \frac{I_{1eq}Z_{m1} - I''_{2eq}Z''_{m2}}{Z_{m1} + Z'_r + Z''_{m2}} \right) & (2) \end{cases} \quad (196)$$

It can be written in a matrix form:

$$\begin{bmatrix} V_{1eq} \\ \frac{s_2}{s_1} V''_{2eq} \end{bmatrix} = \begin{bmatrix} Z_1 + Z_{m1} - \frac{Z_{m1}^2}{Z_{m1} + Z'_r + Z''_{m2}} & \frac{Z_{m1}Z''_{m2}}{Z_{m1} + Z'_r + Z''_{m2}} \\ \frac{Z_{m1}Z''_{m2}}{Z_{m1} + Z'_r + Z''_{m2}} & Z''_2 + Z''_{m2} - \frac{Z''_{m2}^2}{Z_{m1} + Z'_r + Z''_{m2}} \end{bmatrix} \times \begin{bmatrix} I_{1eq} \\ I''_{2eq} \end{bmatrix} \quad (197)$$

Using Matrix to solve equations:

If $AX = B$ then $X = A^{-1}B$

$$\text{If } A = \begin{bmatrix} a & b \\ c & d \end{bmatrix} \quad \text{then} \quad A^{-1} = \begin{bmatrix} a & b \\ c & d \end{bmatrix}^{-1} = \frac{1}{ad-bc} \begin{bmatrix} d & -b \\ -c & a \end{bmatrix} \quad (198)$$

Finally, applying (198) to (197) the feeding currents of the equivalent scheme can be expressed as:

$$\begin{bmatrix} I_{1eq} \\ I''_{2eq} \end{bmatrix} = \frac{1}{\left(Z_1 + Z_{m1} - \frac{Z_{m1}^2}{Z_{m1} + Z'_r + Z''_{m2}} \right) \left(Z''_2 + Z''_{m2} - \frac{Z''_{m2}^2}{Z_{m1} + Z'_r + Z''_{m2}} \right) - \left(\frac{Z_{m1}Z''_{m2}}{Z_{m1} + Z'_r + Z''_{m2}} \right) \left(\frac{Z_{m1}Z''_{m2}}{Z_{m1} + Z'_r + Z''_{m2}} \right)} \begin{bmatrix} Z''_2 + Z''_{m2} - \frac{Z''_{m2}^2}{Z_{m1} + Z'_r + Z''_{m2}} & -\frac{Z_{m1}Z''_{m2}}{Z_{m1} + Z'_r + Z''_{m2}} \\ -\frac{Z_{m1}Z''_{m2}}{Z_{m1} + Z'_r + Z''_{m2}} & Z_1 + Z_{m1} - \frac{Z_{m1}^2}{Z_{m1} + Z'_r + Z''_{m2}} \end{bmatrix} \times \begin{bmatrix} V_{1eq} \\ \frac{s_2}{s_1} V''_{2eq} \end{bmatrix} \quad (199)$$

So I_{1eq} and I''_{2eq} can be expressed and then the other currents are easy to obtain as:

$$\begin{cases} I_{1eq} = \frac{\left(Z''_2 + Z''_{m2} - \frac{Z''_{m2}^2}{Z_{m1} + Z'_r + Z''_{m2}} \right) V_{1eq} - \frac{Z_{m1}Z''_{m2}}{Z_{m1} + Z'_r + Z''_{m2}} \frac{s_2}{s_1} V''_{2eq}}{\left(Z_1 + Z_{m1} - \frac{Z_{m1}^2}{Z_{m1} + Z'_r + Z''_{m2}} \right) \left(Z''_2 + Z''_{m2} - \frac{Z''_{m2}^2}{Z_{m1} + Z'_r + Z''_{m2}} \right) - \left(\frac{Z_{m1}Z''_{m2}}{Z_{m1} + Z'_r + Z''_{m2}} \right)^2} \\ I''_{2eq} = \frac{\left(Z_1 + Z_{m1} - \frac{Z_{m1}^2}{Z_{m1} + Z'_r + Z''_{m2}} \right) \frac{s_2}{s_1} V''_{2eq} - \frac{Z_{m1}Z''_{m2}}{Z_{m1} + Z'_r + Z''_{m2}} V_{1eq}}{\left(Z_1 + Z_{m1} - \frac{Z_{m1}^2}{Z_{m1} + Z'_r + Z''_{m2}} \right) \left(Z''_2 + Z''_{m2} - \frac{Z''_{m2}^2}{Z_{m1} + Z'_r + Z''_{m2}} \right) - \left(\frac{Z_{m1}Z''_{m2}}{Z_{m1} + Z'_r + Z''_{m2}} \right)^2} \\ I'_r = \frac{I_{1eq}Z_{m1} - I''_{2eq}Z''_{m2}}{Z_{m1} + Z'_r + Z''_{m2}} \\ I_{m1} = I_{1eq} - I'_r \\ I''_{m2} = I'_r + I''_{2eq} \end{cases} \quad (200)$$

With equation (200), the electrical state of the equivalent circuit is known. In the second part of this annex, the power state of the BDFM will be expressed from the electrical state of the equivalent circuit.

L.2 The power state of the BDFM

To express the power flow in the BDFM, one should be careful that the power state of the equivalent scheme is not equal to the power state of the BDFM. As explained in III.3.2.4, p 94, in particular in equations (70) and (76), the equivalent scheme is just a representation with mathematical tricks of what happens in the BDFM.

The active power that flows in the power winding can be written for the equivalent scheme and for the BDFM:

$$\begin{cases} P_{1eq} = 3\Re(V_{1eq}I_{1eq}^*) \\ P_1 = 3\Re(V_1I_1^*) \\ V_{1eq} = V_1e^{i\angle -M_{s1r}} \\ I_{1eq} = I_1e^{i\angle -M_{s1r}} \end{cases} \quad \text{so} \quad P_{1eq} = P_1 \quad (201)$$

\Re for the real part.

P_{1eq} is active power of the grid winding in the equivalent scheme.

P_1 is the BDFM active power of the grid winding.

V_{1eq} and V_1 are the voltages applied to the power winding in the equivalent scheme and the BDFM respectively, the relation between V_{1eq} and V_1 was already explained in III.3.2.5, p 96.

i_{1eq}^* is the complex conjugate of i_{1eq} the power winding current in the equivalent scheme.

the relation between I_{1eq} and I_1 was already explained in III.3.2.5, p 96.

The active power that flows in the control winding can be written for the equivalent scheme and for the BDFM:

$$\begin{cases} P_{2eq}'' = 3\Re\left(\frac{S_2}{S_1}V_{2eq}''I_{2eq}''^*\right) \\ P_2 = 3\Re(V_2I_2^*) \\ V_{2eq}'' = \frac{N_1}{N_2}V_2^*e^{i\angle M_{s2r}} \\ I_{2eq}'' = \frac{N_2}{N_1}I_2^*e^{i\angle M_{s2r}} \end{cases} \quad \text{so} \quad P_{2eq} = \frac{s_2}{s_1}P_2 \quad (202)$$

The relation between V_{2eq}'' and V_2 was already explained in III.3.2.5, p 96.

the relation between I_{2eq}'' and I_2 was already explained in III.3.2.5, p 96.

The Joule Losses of the power winding in the equivalent scheme are equal to the Joule Losses of the power winding in the BDFM. They are expressed as:

$$\begin{cases} P_{Joules1eq} = 3|I_{1eq}^2|R_1 \\ P_{Joules1} = 3|I_1^2|R_1 \\ I_{1eq} = I_1 e^{i\angle -M_{s1r}} \end{cases} \quad \text{so} \quad P_{Joules1eq} = P_{Joules1} \quad (203)$$

The Joule losses of the control winding can be written for the equivalent scheme and for the BDFM:

$$\begin{cases} P_{Joules2eq} = 3|I_{2eq}''^2|R_2' \frac{s_2}{s_1} \\ P_{Joules2} = 3|I_2^2|R_2 \\ I_{2eq}'' = \frac{N_2}{N_1} I_2^* e^{i\angle M_{s2r}} \\ R_2' = \frac{N_1^2}{N_2^2} R_2 \end{cases} \quad \text{so} \quad P_{Joules2eq} = \frac{s_2}{s_1} P_{Joules2} \quad (204)$$

The Joule losses of the rotor can be written for the equivalent scheme and for the BDFM:

$$\begin{cases} P_{JoulesReq} = 3|I_r'^2|R_r' \frac{1}{s_1} \\ P_{JoulesR} = 3|I_r^2|R_r \\ I_r' = \frac{I_r}{N_1} \\ R_r' = N_1^2 R_r \end{cases} \quad \text{so} \quad P_{JoulesReq} = \frac{1}{s_1} P_{JoulesR} \quad (205)$$

$P_{Joules1eq}$ and $P_{Joules2eq}$ are the Joule losses in the power and control part of the equivalent scheme.

Power conservation equations can be written for both the equivalent scheme and the BDFM, we get:

$$\begin{cases} P_{1eq} + P_{2eq}'' = P_{Joules1eq} + P_{Joules2eq} + P_{JoulesReq} \\ P_1 + P_2 = P_{Joules1} + P_{Joules2} + P_{JoulesR} + P_{meca} \end{cases} \quad (206)$$

P_{meca} is the mechanical power of the BDFM.

By subtracting the first term of equation (206) to the second term of equation (206), we obtain:

$$\begin{aligned} P_2 - P_{2eq}'' &= P_{Joules2} - P_{Joules2eq} + P_{JoulesR} - P_{JoulesReq} + P_{meca} \\ \text{So} & \\ P_{meca} &= P_2 - P_{2eq}'' - P_{Joules2} + P_{Joules2eq} - P_{JoulesR} + P_{JoulesReq} \end{aligned} \quad (207)$$

With equations (202), (204), (205), (206), and (207) we can obtain several expressions of P_{meca} :

$$\begin{cases}
P_{meca} = 3\Re(V_{2eq}'' I_{2eq}''^*) \left(1 - \frac{s_2}{s_1}\right) + 3|I_{2eq}''|^2 |R_2''| \left(\frac{s_2}{s_1} - 1\right) + 3|I_r''|^2 |R_r'| \left(\frac{1}{s_1} - 1\right) \\
P_{meca} = 3\Re(V_2 I_2^*) \left(1 - \frac{s_2}{s_1}\right) - 3|I_2^2| |R_2| \left(1 - \frac{s_2}{s_1}\right) - 3|I_r^2| |R_r| \left(1 - \frac{1}{s_1}\right) \\
P_{meca} = 3\Re(V_1 I_1^*) + 3\Re(V_2 I_2^*) - 3|I_1^2| |R_1| - 3|I_2^2| |R_2| - 3|I_r^2| |R_r|
\end{cases} \quad (208)$$

APPENDIX M.

An iterative process for the improvement of the BDFM design with FE magneto-harmonic simulations

In Table M-1, the extensive results of the iterative process for the improvement of the analytical BDFM design are presented. In the first part of Table M-1, the parameters to be optimized are presented for the 10 iterations (the iteration 0 is the analytical design). The parameters that do not change from an iteration to the next one are colored in light grey. The parameters that do change from an iteration to the next one are in black and bold. The power state results of the BDFM are given in green when they make sense from a physical point of view, and are given in black when they do not make sense from a physical point of view (for example, when the resistances are not verifying equations (140), (141), and (142), p 149).

Table M-1: Evolution of the optimized parameters and results of the no saturation load test of the BDFM during the iterative process to improve upon the analytical design (iteration 0).

Iteration	0	1	2	3	4	5	6	7	8	9	10
Evolution of the parameters to be optimized.											
V PW [V]	7200	7200	7200	7200	7200	7200	7200	7200	7600	7600	7600
V CW [V]	6600	6600	6600	6600	6600	6600	6600	6600	6135	6135	6135
PhiV CW [deg]	0	0	270	270	270	270	270	300	300	300	300
Stator Back diameter	5400	5400	5400	5400	5400	5800	5800	5800	5800	6500	6500
Stator Bore diameter	4710	4710	4710	4710	4910	5310	5310	5310	5310	6010	6010
Rotor Bore diameter	4690	4690	4690	4690	4890	5290	5290	5290	5290	5990	5990
Rotor back diameter	4000	4000	4000	4000	4300	4700	4700	4700	4700	5400	5400
R PW [Ohm]	0.019	0.019	0.019	0.04	0.04	0.035	0.035	0.035	0.035	0.035	0.027
R CW [Ohm]	0.025	0.025	0.025	0.05	0.05	0.044	0.044	0.044	0.044	0.044	0.034
R Rotor [Ohm]	0.007	0.007	0.007	0.014	0.014	0.012	0.012	0.012	0.012	0.012	0.009
Nr	480	480	480	480	480	480	480	480	480	480	480
Loops/Nest	3	3	3	3	3	3	3	3	3	3	3
Stator Slot height	232	100	100	100	100	100	100	100	100	100	100
Rotor Slot height	194	100	100	100	100	100	100	100	100	100	100
Stator Slot width	9.86	9.86	9.86	9.86	10.28	11.12	11.12	11.12	11.12	14.23	14.23
Rotor Slot width	11.8	11.8	11.8	11.8	12.3	13.31	13.31	13.31	13.31	17.07	17.07

Evolution of the power state of the BDFM under a load case without saturation											
PW total power [MW]	-0.89	-3.36	-7.00	-4.17	-4.44	-4.85	-5.54	-5.51	-5.79	-6.67	-8.40
PW total S [MVA]	-13.0	-19.2	-15.6	-13.7	-13.3	-12.6	-12.8	-14.3	-15.8	-16.5	-17.7
CW total power [MW]	-1.97	-3.75	-2.93	-2.10	-2.23	-2.45	-2.71	-3.17	-2.92	-3.35	-4.21
CW total S [MVA]	9.4	10.7	-13.7	11.9	11.6	11.2	11.5	10.8	9.4	-9.8	10.4
Power factor PW	0.07	0.17	0.17	0.29	0.29	0.17	0.29	0.36	0.34	0.38	0.43
Power factor CW	0.21	0.33	0.33	0.17	0.17	0.33	0.17	0.28	0.30	0.32	0.38
BDFM total power [MW]	-2.87	-7.11	-9.93	-6.27	-6.67	-7.29	-8.26	-8.67	-8.70	-10.02	-12.60
BDFM total S [MVA]	-22.4	-30.0	-1.9	-25.6	-24.9	-23.8	-24.4	-25.1	-25.2	-6.7	-28.1

Bibliography

- [1] Sutter John D., Berlinger Joshua, “Final draft of climate deal formally accepted in Paris”. CNN. Cable News Network, Turner Broadcasting System, Inc. Retrieved 12 December 2015. <http://edition.cnn.com/2015/12/12/world/global-climate-change-conference-vote/> (Cit. on pp. 7).
- [2] “Spécial COP 21 – Les engagements nationaux de la France”. Gouvernement.fr, 2015 <http://www.gouvernement.fr/special-cop-21-les-engagements-nationaux-de-la-france-3390> (Cit. on pp. 7).
- [3] *Mémemento sur l’Energie. Energy Handbook*. CEA, 2016. <http://www.cea.fr/multimedia/Documents/publications/ouvrages/memento-sur-energie-2016.pdf> (Cit. on pp. 8).
- [4] *Renewable Energy Statistics*. Eurostat, 2016. http://ec.europa.eu/eurostat/statistics-explained/index.php/Renewable_energy_statistics (Cit. on pp. 8).
- [5] G. D. Ciocan, O. Teller, and F. Czerwinski, “Variable Speed Pump-Turbines Technology”. University POLITEHNICA of Bucharest Scientific Bulletin – D Series: Mechanical Engineering, vol 74, no. 1, pp 33-42, 2012. https://www.scientificbulletin.upb.ro/rev_docs_arhiva/full67d_700564.pdf (Cit. on pp. 8, 11).
- [6] *White Paper - Electrical Energy Storage*. International Electrotechnical Commission, Geneva, Switzerland 2011. <http://www.iec.ch/whitepaper/pdf/iecWP-energystorage-LR-en.pdf> (Cit. on pp. 9).
- [7] Uptin Saiidi, “Let the countdown begin: Elon Musk has 100 days to build a battery system or could lose \$50 million”. CNBC, 29.09.2017, updated 01.10.2017 <https://www.cnbc.com/2017/09/29/elon-musk-battery-plant-south-australia-100-days.html> (Cit. on pp. 10).
- [8] Colin Packham, James Regan, “Tesla wins giant battery contract in Australia, has 100-day deadline”. REUTERS, 07.07.2017 <https://www.reuters.com/article/us-australia-power-tesla/tesla-wins-giant-battery-contract-in-australia-has-100-day-deadline-idUSKBN19S0EV> (Cit. on pp. 10).
- [9] Rod Adams, “There's Less To Tesla's Big Australian Battery Deal Than Meets The Eye”. Forbes, 07.07.2017 <https://www.forbes.com/sites/rodadams/2017/07/07/megahype-over-tesla-battery-capable-of-providing-nameplate-power-for-less-than-80-minutes/#c17d80c4919f> (Cit. on pp. 10).

- [10] C. Roselund, "Tesla inaugurates 20 MW / 80 MWh battery system in Southern California". PV Magazine, February 1, 2017.
<https://www.pv-magazine.com/2017/02/01/tesla-inaugurates-20-mw-80-mwh-battery-system-in-southern-california/>
 (Cit. on pp. 10).
- [11] *Office of Electricity Delivery & Energy Reliability*. U.S. Department of Energy's Global Energy Storage Database Last access: 07.07.2017.
<http://www.energystorageexchange.org/>
 (Cit. on pp. 10).
- [12] Thomas Lugand "Contribution to the Modeling and Optimization of the Double-Fed Induction Machine for Pumped-Storage Hydro Power Plant Applications". Ph.D., INPG / ALSTOM, 2013.
 (Cit. on pp. 11, 57, 189).
- [13] A. Schwery, E. Fass, J-M. Henry, W. Bach, and A. Mirzaian. "Pump Storage Power Plants, ALSTOM's long experience and Technological Innovation". In: Hydro. 2005.
 (Cit. on pp. 11).
- [14] A. Schwery. "Varspeed Pump Storage Power Plants: Technology and Operation". In: IEEE presentation. Feb. 2006.
 (Cit. on pp. 11, 12).
- [15] J.W. Kolar, and T. Friedli, "Comprehensive Evaluation of Three-Phase AC-AC PWM Converter Systems". Swiss Federal Institute of Technology (ETH) Zurich, Power Electronic Systems Laboratory. IECON 2010.
<https://www.ethz.ch/content/dam/ethz/special-interest/itet/power-electronic-systems-lab/images/Publications/Tutorials/iecon-2010-tutorial-matrix-converters-latest-version-010211-smaller.pdf>
 (Cit. on pp. 15, 16, 17).
- [16] V. G. Agelidis, D. M. Baker, W. B. Lawrance, and C. V. Nayar, "A multilevel PWM inverter topology for photovoltaic applications". Proceedings of the IEEE International Symposium on Industrial Electronics, Vol. 2, pp. 589-594, July 1997, Portugal, Guimaraes.
 (Cit. on pp. 16).
- [17] M. Ahmed; N.A. Rahim, W.P. Hew, "Three-phase three-level voltage source inverter with low switching frequency based on the two-level inverter topology". Proceedings of IET Electric Power Applications, Volume 1, Issue 4, pp. 637 - 641, July 2007.
 (Cit. on pp. 16).
- [18] ABB Switzerland Ltd, "Grimsel 2, Switzerland. The world's largest power converter for variable speed pumped hydropower". ABB Switzerland Ltd, Power Converter Solutions.
https://library.e.abb.com/public/0ee456abcf33cf89c1257d6900347076/Reference_Grimsel_RevA.pdf?_sm_au_=iPVKSM6rJ0VDMnns
 (Cit. on pp. 17).
- [19] Cigré WG B4.55's report "HVDC connection of offshore wind power plants". May 2015
http://www.ee.co.za/article/hvdc-connection-offshore-wind-power-plants.html?_sm_au_=iPV7PbZqHLbSR3W6
 (Cit. on pp. 17).

- [20] Rick West, "PV String to 3-Phase Inverter with Highest Voltage Capabilities, Highest Efficiency and 25 Year Lifetime".
National Renewable Energy Laboratory, 2012, San Luis Obispo, California.
http://www.nrel.gov/docs/fy13osti/57247.pdf?_sm_au_=iPVKSM6rJOVDMnns
(Cit. on pp. 17).
- [21] P.K. Steimer, S.Aubert, and S. Linder, "New dimensions in converter fed synchronous machines: CFMS for pumped storage plants". ABB Switzerland Ltd, 2013.
(Cit. on pp. 18).
- [22] Steve Taranovich, "Power Si vs. GaN vs. SiC which process and supplier are best for my design?". EDN March 2013, Issue 3. p. 38 – 47, 2013.
http://radio-hobby.org/uploads/journal/EDN/2013/EDN_03_2013.pdf
(Cit. on pp. 18).
- [23] S. Brothers and F. Lydall, "Siemens Brothers & Co. Ltd. and Francis Lydall. Improvements in polyphase induction motors". In British Patent No.: 16839, 1902.
(Cit. on pp. 20, 28).
- [24] L. Hunt, "A new type of induction motor".
Journal of the Institution of Electrical Engineers, vol. 39, no. 186, Sep. 1907, pp. 648-667.
(Cit. on pp. 20).
- [25] L. Hunt, "The Cascade Induction Motor, Electrical Engineers".
Journal of the Institution of, vol. 52, no. 230, 1914, pp. 406-426.
(Cit. on pp. 20).
- [26] F. Creedy, "Some developments in multi-speed cascade induction motors".
Journal of the Institution of Electrical Engineers, vol. 59, no. 301, May 1921, pp. 511-532.
(Cit. on pp. 20, 125).
- [27] A. Broadway and L. Burbridge, "Self-cascaded machine: a low-speed motor or high-frequency brushless alternator".
Proceedings of the Institution of Electrical Engineers, vol. 117, no. 7, 1970, p. 1277.
(Cit. on pp. 20, 32).
- [28] A. Broadway, "Cageless induction machine".
Proceedings of the Institution of Electrical Engineers, vol. 118, no. 11, 1971, p. 1593.
(Cit. on pp. 20).
- [29] A. Broadway, B. Cook, and P. Neal, "Brushless cascade alternator".
Proceedings of the Institution of Electrical Engineers, vol. 121, no. 12, 1974, p. 1529.
(Cit. on pp. 20).
- [30] S. Williamson and M. S. Boger, "Impact of inter-bar currents on the performance of the brushless doubly-fed motor".
IEEE Transactions on industry applications, vol. 35, no. 2, Apr. 1999.
(Cit. on pp. 21).
- [31] B. Koch, R. Spée, and B. Clever, "A comparison of stack preparation methods for bar insulation in diecast rotors".
IEEE Industry Applications Society, Annual Meeting, New Orleans, Louisiana, Oct. 1997.

(Cit. on pp. 21, 65, 104).

- [32] P. C. Roberts, "A study of Brushless Doubly-Fed (Induction) Machines. Contributions in machine analysis, design and control". Ph.D., Emmanuel College, University of Cambridge, 2004. (Cit. on pp. 21, 33, 34, 36, 64, 65, 66, 67, 76, 82, 86, 97, 100, 104, 105, 118, 119, 124, 141).
- [33] A. M. Oliveria, P. Kuo-Peng, N. Sadowski, F. Runcos, R. Carlson, and P. Dular, "Finite-element analysis of a double-winding induction motor with a special rotor bar topology". IEEE Trans. Magn., vol. 40, no. 2, pp. 770–773, Mar. 2004. (Cit. on pp. 21, 68).
- [34] H. Gorginpour, B. Jandaghi, and H. Oraee, "Finite element analysis of brushless doubly-fed machine under stator winding faults". In Proc. 2nd Power Electron., Drive Syst. Technol. Conf., pp. 169–174, Feb. 16–17, 2011. (Cit. on pp. 21, 68).
- [35] X. Wang, T. D. Strous, D. Lahaye, H. Polinder, and J. A. Ferreira, "Finite Element Modeling of Brushless Doubly-Fed Induction Machine Based on Magneto-Static Simulation". In Int. Conf. Elect. Machines & Drives (IEMDC), 2015. (Cit. on pp. 21, 68).
- [36] T. D. Strous, X. Wang, H. Polinder, and J. A. Ferreira, "Finite Element Based Multi-Objective Optimization of a Brushless Doubly-Fed Induction Machine". 2015 IEEE International Electric Machines & Drives Conference (IEMDC), Coeur d'Alene, ID, 2015, pp. 1689-1694. (Cit. on pp. 21, 68, 135).
- [37] Hamed Gorginpour, Hashem Oraee, and Richard A. McMahon, "A Novel Modeling Approach for Design Studies of Brushless Doubly-Fed Induction Generator Based on Magnetic Equivalent Circuit". IEEE Trans. Energy Conversion, vol. 28, no. 4, December 2013. Drive Syst. Technol. Conf., pp. 169–174, Feb. 16–17, 2011. (Cit. on pp. 21, 68, 135).
- [38] F. J. Poza Lobo "Modélisation, Conception et Commande d'une Machine Asynchrone sans Balais Doublement Alimentée pour la Génération à Vitesse Variable". PhD, engineering Sciences. Institut National Polytechnique de Grenoble - INPG, 2003. French. (Cit. on pp. 21, 22, 97, 127).
- [39] E. Schulz and R. Betz, "Optimal rotor design for brushless doubly-fed reluctance machines". In 38th IAS Annual Meeting on Conference Record of the Industry Applications Conference, 2003., vol. 1. IEEE, 2003, pp. 256-261. (Cit. on pp. 22, 23).
- [40] T. Staudt, "Brushless Doubly-Fed Reluctance Machine Modeling, Design and Optimization". Ph.D., Institut National Polytechnique de Grenoble – INPG, 2015. (Cit. on pp. 23, 50, 51, 67, 68, 187, 188).
- [41] L. Xu, F. Liang, and T. Lipo, "Transient model of a doubly excited reluctance motor". IEEE Transactions on Energy Conversion, vol. 6, no. 1, Mar. 1991, pp. 126-133. (Cit. on pp. 23).

- [42] F. Liang, L. Xu, and T. Lipo, "D-q analysis of a variable speed doubly AC excited reluctance motor". *Electric Machines and Power Systems*, vol. 19, 1991, pp. 125-138.
(Cit. on pp. 23).
- [43] Y. Liao, L. Xu, and L. Zhen, "Design of a doubly-fed reluctance motor for adjustable-speed drives". *IEEE Transactions on Industry Applications*, vol. 32, no. 5, 1996, pp. 1195-1203.
(Cit. on pp. 23, 28).
- [44] R. E. Betz and M. G. Jovanovic, "Introduction to Brushless Doubly-Fed Reluctance Machines. The Basic Equations".
University of Newcastle, NSW, 2308, Australia., Aalborg, Denmark, Tech. Rep., 1998.
(Cit. on pp. 23).
- [45] R. E. Betz and M. G. Jovanovic, "Introduction to the Space Vector Modeling of the Brushless Doubly-Fed Reluctance Machine".
Electric Power Components and Systems, vol. 31, no. 8, Aug. 2003, pp. 729-755.
(Cit. on pp. 23).
- [46] C.-M. Ong, "Dynamic Simulation of Electric Machinery".
1st ed., P. Hall, Ed., New Jersey, 1997, p. 688.
(Cit. on pp. 24).
- [47] S. Williamson, A. C. Ferreira, and A. K. Wallace, "Generalised theory of the brushless doubly-fed machine. Part 1: Analysis".
Electric Power Applications, IEE Proceedings, Volume:144, Issue:2 p. 111-122, 1997.
(Cit. on pp. 28, 32).
- [48] B. S. Marwa, K. M. Larbi, B. F. Mouldi, and R. Habib, "Modeling and analysis of double stator induction machine supplied by a multi-level inverter".
Electrotechnical Conference (MELECON), 16th IEEE Mediterranean, Mar. 2012.
(Cit. on pp. 29).
- [49] R. A. McMahon, X. Wan, E. Abdi-Jalebi, P. J. Tavner, P. C. Roberts, and M. Jagiela, "The BDFM as a generator in wind turbines".
Power Electronics and Motion Control Conference. EPE-PEMC 2006.
(Cit. on pp. 35, 36, 82).
- [50] M. S. Boger, A. K. Wallace, and R. Spée, "Investigation of appropriate pole number combinations for brushless doubly-fed machines applied to pump drives".
IEEE Transactions on Industry Applications, 1996.
(Cit. on pp. 36, 65, 130).
- [51] E. Abdi-Jalebi, R. A. McMahon, P. Malliband, S. Shao, M. Ezekiel Mathekga, P. J. Tavner, S. Abdi, A. Oraee, T. Long, and M. Tatlow, "Performance analysis and testing of a 250 kW medium-speed brushless doubly-fed induction generator".
Renewable Power Generation, IET (Volume:7, Issue: 6), 2013.
(Cit. on pp. 37, 39, 68, 124, 135, 141).
- [52] Stephane Brisset. "Démarches et outils pour la conception optimale des machines électriques". *Energie électrique. Université des Sciences et Technologie de Lille - Lille I*, 2007.
<https://tel.archives-ouvertes.fr/tel-00264041v2>
(Cit. on pp. 44).

- [53] R. Carlson, F. Wurtz, "The Concepts of Sizing and Optimization Model: applied to the Optimal Design of a Permanent Magnet Generator". ACEMP'2011: International Aegean Conference on Electric Machines and Power Electronics & Electromotion, 08-10 September 2011, Istanbul, Turkey. (Cit. on pp. 46).
- [54] B. Delinchant, D. Duret, and L. Estrabaut, "An optimizer using the software component paradigm for the optimization of engineering systems". COMPEL: The International Journal for Computation and Mathematics in Electrical and Electronic Engineering, 26(2):368379, 2007. (Cit. on pp. 48, 49).
- [55] Frédéric Wurtz, "Une Nouvelle Approche pour la Conception Sous Contraintes de Machines Electriques". PhD, Institut National Polytechnique de Grenoble - INPG, 1996. (Cit. on pp. 48, 56, 57, 189).
- [56] Li Li. "Etude et mise au point d'une nouvelle famille d'alternateur pour véhicules hybrides et électriques". PhD. Energie électrique. Université Grenoble Alpes, 2011. (Cit. on pp. 48, 187).
- [57] G. F. Üler, O. A. Mohamed, and C. S. Koh : "Utilizing genetic algorithms for the optimal design of electromagnetic devices". IEEE transactions on Magnetics, 30: 4296–4298, April 1994. (Cit. on pp. 49).
- [58] J. A. De Vasconcelos : "Optimisation de forme de structures électromagnétiques". Thèse de doctorat, Ecole Centrale de Lyon, 1994. (Cit. on pp. 49).
- [59] S. L. Ho, Shiyong Yang., G. Ni, and H. C. Wong, "A Particle Swarm Optimization Method with Enhanced Global Search Ability for Design Optimizations of Electromagnetic Devices". COMPUMAG, Conference on the Computation of Electromagnetic Fields, 15, June 2005. (Cit. on pp. 49).
- [60] G.Q. Bao, D. Zhang, J.H. Shi, and J.Z. Jiang, "An Improved Particle Swarm Algorithm for Transverse Flux Permanent Flux Permanent Motor Optimization". COMPUMAG, Conference on the Computation of Electromagnetic Fields, 15, June 2005. (Cit. on pp. 49).
- [61] J-L. Coulomb, "Electrognétisme et problèmes couplés - Chapitre 8". Livre, Lavoisier, 2002. (Cit. on pp. 49).
- [62] N. Ida and J. a. P. A. Bastos, *Electromagnetics and Calculations of Fields*. 2nd ed. New York: Springer Verlag, 1997. (Cit. on pp. 50).
- [63] B. du Peloux de Saint Romain : "Modélisation des actionneurs électromagnétiques par réseaux de réductances. Création d'un outil métier dédié au prédimensionnement par optimisation". Thèse de doctorat, G2elab-INPG, Oct. 2006. (Cit. on pp. 50).

- [64] T. P. Do : “Simulation dynamique des actionneurs et capteurs électromagnétiques par réseaux de réluctances : modèles, méthodes et outils”.
Thèse de doctorat, G2elab, INPG, Mar. 2010.
(Cit. on pp. 50).
- [65] M. V. K. Chari and P. Silvester, “Finite-Element Analysis of Magnetically Saturated D-C Machines”.
In *IEEE Transactions on Power Apparatus and Systems*, vol. PAS-90, no. 5, pp. 2362-2372, Sept. 1971.
(Cit. on pp. 51).
- [66] A. Hrennikoff, “Solution of problems of elasticity by the framework method”.
Journal of applied mechanics. 8.4: 169–175, 1941.
(Cit. on pp. 51).
- [67] R. Courant, “Variational methods for the solution of problems of equilibrium and vibrations”. *Bulletin of the American Mathematical Society*. 49: 1–23, 1943.
(Cit. on pp. 51).
- [68] M. Liwshitz-Garik and C.C: Wipple, “Alternating Current Machines”. Van Nostrand, 1961.
(Cit. on pp. 53).
- [69] H. Barr, A. Bonnett and C. Yung, “Understanding the design of stators and rotors of squirrel cage induction motors”. 2008 55th IEEE Petroleum and Chemical Industry Technical Conference, Cincinnati, OH, 2008, pp. 1-11.
(Cit. on pp. 53).
- [70] A. Boblietti, A. Cavagnino, M. Lazzari and S. Vaschetto, “Preliminary induction motor electromagnetic sizing based on a geometrical approach”.
IEEE: IET Electric Power Applications, 2012.
(Cit. on pp. 53, 54, 55, 56, 60).
- [71] Jesús A. De Loera, Raymond Hemmecke, Matthias Köppe, Robert Weismantel, “Integer Polynomial Optimization in Fixed Dimension”.
2006, *Mathematics of Operations Research*. <http://dx.doi.org/10.1287/moor.1050.0169>
(Cit. on pp. 56).
- [72] J. Perho, “Reluctance Network for Analysing Induction Machines”.
Acta Polytechnica Scandinavica, Electrical Engineering Series, No. 110, Espoo 2002. 147 p.
Published by the Finnish Academies of Technology.
(Cit. on pp. 56).
- [73] A. Foggia, “Méthodes de calcul des inductances de fuites”.
Techniques de l’Ingénieur, Energies | Conversion de l’énergie, 1999. Réf D3440, V1.
(Cit. on pp. 57, 189).
- [74] G. Bertotti, “General properties of power losses in soft ferromagnetic materials”.
In *IEEE Transactions on Magnetics*, vol. 24, no. 1, pp. 621-630, Jan 1988.
(Cit. on pp. 57, 189).

- [75] F. Wurtz, P. Kuo-Peng, and E. S. De Carvalho, "The concept of Imaginary Machines for design and Setting of Optimization Problems: Application to a synchronous generator". 2012 XXth International Conference on Electrical Machines, Marseille, 2012, pp. 1463-1468. <http://ieeexplore.ieee.org/stamp/stamp.jsp?tp=&arnumber=6350071&isnumber=6349821> (Cit. on pp. 61).
- [76] R. A. McMahon, P. C. Roberts, X. Wang, P. J. Tavner, "Performance of BDFM as generator and motor". In IET Proceedings, Electric Power Applications, vol. 153, no. 2, pp. 289-299, 2006. (Cit. on pp. 64, 82, 114, 141, 142).
- [77] Wang, P. C. Roberts, and R. A. McMahon, "Optimization of BDFM Stator Design Using an Equivalent Circuit Model and a Search Method". In Proc. 3rd IET International Power Electronics, Machines and Drives Conference (PEMD), March 2006, pp. 606-610. (Cit. on pp. 64, 68, 82, 124).
- [78] R. McMahon, P. Tavner, E. Abdi, P. Malliband and D. Barker, "Characterising rotors for brushless doubly-fed machines (BDFM)". *The XIX International Conference on Electrical Machines - ICEM 2010*, Rome, 2010, pp. 1-6. <http://ieeexplore.ieee.org/stamp/stamp.jsp?tp=&arnumber=5607908&isnumber=5607489> (Cit. on pp. 68, 124, 135, 142).
- [79] Xianming Deng, Guojun Tang, Haizhong Zhang and Xiao Zhang, "Finite element method analysis of the electromagnetic field of Brushless Doubly-Fed Machine". *2008 International Conference on Electrical Machines and Systems*, Wuhan, pp. 346-350. <http://ieeexplore.ieee.org/stamp/stamp.jsp?tp=&arnumber=4770714&isnumber=4770630> (Cit. on pp. 76).
- [80] T. D. Strous, N. H. van der Blij, H. Polinder and J. A. Ferreira, "Brushless Doubly-Fed Induction Machines: Magnetic field modelling". *2014 International Conference on Electrical Machines (ICEM)*, Berlin, 2014, pp. 2702-2708. <http://ieeexplore.ieee.org/stamp/stamp.jsp?tp=&arnumber=6960570&isnumber=6960148> (Cit. on pp. 76).
- [81] T. D. Strous, X. Wang, H. Polinder and J. A. B. Ferreira, "Brushless Doubly-Fed Induction Machines: Magnetic Field Analysis". In *IEEE Transactions on Magnetics*, vol. 52, no. 11, pp. 1-10, Nov. 2016. <http://ieeexplore.ieee.org/stamp/stamp.jsp?tp=&arnumber=7506287&isnumber=7593001> (Cit. on pp. 76).
- [82] P. C. Roberts, R. A. McMahon, P. J. Tavner, J. M. Maciejowski, and T. J. Flack, "Equivalent circuit for the brushless doubly-fed machine (BDFM) including parameter estimation and experimental verification". *IEE Proc. Electr. Power Appl.*, vol. 152, no. 4, pp. 933-942, Jul. 2005. (Cit. on pp. 82, 86, 97, 247).
- [83] S. Perez, "Contribution au dimensionnement optimal d'alternateur à griffes sans aimant - Apport des alliages FeCo". PhD, INPG, 2013. (Cit. on pp. 85, 86, 97, 188).

- [84] A. Ramchandran, G.C. Alexander, and R. Spee, "Off-line parameter estimation for the doubly-fed machine". Proc. Conf. on Industrial electronics, control, instrumentation, and automation, 1992, Vol. 3, pp. 1294–1298.
(Cit. on pp. 86, 98, 247).
- [85] A. Ramchandran, and G.C. Alexander, "Frequency-domain parameter estimations for the brushless doubly-fed machine". Conf. Record of PCC 1993. Power Conversion Conference, Yokohama, 1993: IEEE, 1993, pp. 346–351.
(Cit. on pp. 86, 98, 247).
- [86] Eric VASSENT, "Contribution à la modélisation des moteurs asynchrones par la méthode des éléments finis". Ph.D. 1990 - INPG (Contribution to the modeling of asynchronous motors by the finite element method).
(Cit. on pp. 107).
- [87] Christophe GUERIN, "Détermination des pertes par courant de Foucault dans les cuves de transformateurs - Modélisation de régions minces et prise en compte de la saturation des matériaux magnétiques en régime harmonique". Ph.D. 1994 - INPG (Determining of eddy current losses in the transformers curves – Modeling of narrow regions and taking into consideration of magnetic materials in harmonic regime).
(Cit. on pp. 107).
- [88] Eric VASSENT, "Simulation of induction machine operation using complex magnetodynamic finite elements". IEEE Transactions on magnetics, vol. 25, No 4, July 1989.
(Cit. on pp. 107).
- [89] R. Resmi, C. Arun Agoram, P. Adithya, V. Vanitha, "Design and Analysis of Brushless Doubly-Fed Induction Generator". In *Procedia Technology*, vol. 21, pp. 604-610, 2015.
(Cit. on pp. 135).
- [90] R. McMahan, P. Tavner, E. Abdi, P. Malliband and D. Barker, "Characterising brushless doubly-fed machine rotors".
In *IET Electric Power Applications*, vol. 7, no. 7, pp. 535-543, Aug. 2013.
(Cit. on pp. 141).
- [91] F. Poopak Roshanfekar, "Roebel windings for hydro generators".
Master Thesis, Chalmers University of Technology, Göteborg, Sweden, 2007.
(Cit. on pp. 164).
- [92] N. Moisson-Franckhauser, "Effect of Static or Dynamic Eccentricities on the Unbalanced Magnetic Pull in Doubly-Fed Induction Machines". 2017 15th International Conference on Electrical Machines, Drives and Power Systems (ELMA), Sofia, 2017, pp. 383-388.
doi: 10.1109/ELMA.2017.7955469
(Cit. on pp. 166).
- [93] S. Nagano, T. Kitajima, K. Yoshida, Y. Kazao, Y. Kabata, D. Murata, K. Nagakura, "Development of World's Largest Hydrogen-Cooled Turbine Generator".
Power Engineering Society Summer Meeting, 2002 IEEE.
(Cit. on pp. 172).

- [94] H. Mahmoudi, A. Lagrioui, "Flux-Weakening Control of Permanent Magnet Synchronous Machines".
Journal of Theoretical and Applied Information Technology, Vol. 34 No. 2, 2011.
<http://www.jatit.org/volumes/Vol34No2/2Vol34No2.pdf>
(Cit. on pp. 173).
- [95] Sesanga N'Tshuika, "Optimisation de Gammes: application à la conception des Machines Synchrones à concentration de flux". PhD, 2011.
(Cit. on pp. 173).
- [96] M. Dessoude, *Moteurs Asynchrones – Choix et problèmes connexes*.
Technique de l'ingénieur, d3490, 1996.
(Cit. on pp. 177, 179).
- [97] J. L. Kirtley Jr. *Designing Squirrel Cage Rotor Slots with High Conductivity*.
Massachusetts Institute of Technology.
(Cit. on pp. 178).
- [98] M. Poloujadoff, *Machine Asynchrones – Régimes permanent*.
Technique de l'ingénieur, d3480, 1998.
(Cit. on pp. 178, 179, 181).
- [99] P. Blaiklock and W. Horvath, "Saving Energy". TMEIC, General Electric, 2009.
(Cit. on pp. 183, 184).
- [100] F. Runcos and M. Ruviano, "A brushless doubly-fed induction machine with flat plane rotary transformers". Technical Notes, WEG, 2012.
(Cit. on pp. 184).
- [101] T. RAMINOSOA, "Optimisation des performances des machines synchro-reluctantes par réseaux de perméances".
Génie Electrique, Institut National Polytechnique de Lorraine, Oct. 2006.
(Cit. on pp. 186).

ABSTRACTS

English version:

Pumped-hydro storage plants (PSP) are important assets to stabilize electric grids.

Variable speed technologies can improve the cycle efficiency and the power adjustability of PSPs. Current technologies such as fully-fed machines or Doubly-Fed Induction Machines (DFIM) have drawbacks. In this work, the focus will be on an unconventional design of variable speed machine: the Brushless Doubly-Fed Induction Machine (BDFM). The objectives are to better understand the working principles of this machine to size it, optimize it, and compare it to other types of variable speed machines.

Following a review of sizing and optimization techniques for conventional machines, similar approaches are investigated for the BDFM. Two different methods for faster Finite-Element (FE) simulations of the BDFM are presented: a fast one without saturation considerations and another one based on the principle of magneto-harmonic simulations. A careful harmonic analysis combined with a comparison of cross-coupling tests between FE simulations and results of equivalent circuit found in the literature will lead to a modification of the BDFM equivalent circuit. A new method to determine the parameters of this equivalent circuit from electrical tests is presented. The parameters determination from the geometry will also be considered for the elaboration of a derivable semi-analytical model. Such a model, paired with a 1st order optimization algorithm could be extremely powerful during the sizing of a BDFM. The potential of such an approach is shown in this work with the exemple of the optimization of an Induction Machine.

Version Française :

Les Stations de Transfert d'Énergie par Pompage (STEP) sont des structures importantes pour stabiliser le réseau électrique.

Les technologies à vitesse variable peuvent améliorer l'efficacité et la souplesse d'utilisation des STEPs. Les technologies actuelles telles que les machines alimentées à fréquence variable, ou les Machines Asynchrone à Double Alimentations (MADA) présentent des inconvénients. Dans ce travail, nous nous concentrons sur une structure non conventionnelle de machine à vitesse variable : la Machine à Induction à Double Alimentation sans Balais (BDFM). Les objectifs sont de mieux comprendre le fonctionnement de cette machine pour la dimensionner, l'optimiser et finalement la comparer aux structures existantes.

Après un examen des techniques de dimensionnement et d'optimisation des machines classiques, des approches similaires sont étudiées pour les BDFM. Deux méthodes différentes pour des simulations éléments finis plus rapides de la BDFM sont présentées : une première, la plus rapide mais qui ne considère pas le phénomène de saturation et une seconde basée sur le principe des simulations magnéto-harmoniques. Une analyse harmonique minutieuse combinée à une comparaison de cas en charges (couplage-croisés) entre des simulations FE et les résultats obtenus avec des schémas équivalents obtenus dans la littérature conduit à une modification du circuit équivalent de la BDFM. Une nouvelle méthode pour déterminer les paramètres de ce circuit grâce à des essais électriques est ensuite présentée. La détermination des paramètres à partir de la géométrie est également abordée pour aboutir à un modèle semi-analytique dérivable. Un tel modèle, couplé à un algorithme d'optimisation du 1er ordre pourrait être extrêmement puissant lors du dimensionnement d'une BDFM. Le potentiel d'une telle approche est montré dans ce travail grâce à l'optimisation d'une machine à induction.